CAL/USAAVLABS SYMPOSIUM PROCEEDINGS

AERODYNAMIC PROBLEMS
ASSOCIATED WITH
V/STOL AIRCRAFT

VOLUME II

PROPULSION AND INTERFERENCE AERODYNAMICS

22-24 June 1966

Statler-Hilton Hotel

Buffalo, New York

CAL/USAAVLABS

SYMPOSIUM PROCEEDINGS

AERODYNAMIC PROBLEMS
ASSOCIATED WITH
V/STOL AIRCRAFT

Published in Four Volumes as Follows:

This is **VOLUME II** and contains those technical papers presented

Thursday, 23 June 1966

Statler-Hilton Hotel

Buffalo, New York

D D C

SEP 7 1967

C

FOREWORD

The rapid advances made in helicopter and V/STOL aircraft development in the past few years have spotlighted areas in which significant aerodynamic problems have been encountered, and in some cases the problems still exist. Fortunately, a technological maturity has now been attained in the industry, making possible investigations through knowledgeable scientific approaches that have produced an enlightened understanding of the problems and, in many cases, have led to practical solutions. The next generation of flight vehicles, currently in the design and development stages, are offering challenges to the aerodynamicist and engineer, and it is evident that future vehicle developments will demand an ever-increasing rate of technological advance in the knowledge and understanding of aerodynamic phenomena.

Several years have passed since a technical specialists' meeting was held to direct attention specifically to the low-speed aerodynamic problem areas of helicopters and V/STOL vehicles. Therefore, in the interest of disseminating up-to-date information, the cosponsors of this symposium, the U.S. Army Aviation Materiel Laboratories (USAAVLABS) and Cornell Aeronautical Laboratory, Inc. (CAL), believe such a meeting among technical specialists in the field would be timely. It is hoped that this symposium will, through the presentation of selected technical papers, establish the state of the art of aerodynamic analysis in the basic problem areas and spotlight those critical areas where research is urgently needed. The ultimate objective is to identify those advances required in the state of the art that can assure the availability of the analytical tools needed to develop and analyze the next generation of helicopters and V/STOL aircraft.

In keeping with these objectives, five technical sessions, each dealing with specific basic areas of aerodynamic analysis associated with V/STOL aircraft, have been formed. In addition, a panel session has also been scheduled in which outstanding members of industry and government from three countries will present their recommendations for areas of research that need to be pursued if the state of the art is to advance at the required rate.

It is believed that the formal presentation of the selected papers and the panel presentations and recommendations will stimulate constructive discussions among the specialists in attendance. While a significant amount of time has been allotted during the sessions for this to be accommodated, it is hoped the sessions will, in addition, stimulate discussions and serious thought between the attendees and the technical members of the various organizations who were unable to attend. In order to foster this latter objective, the informal discussions (questions and answers, etc.) will be recorded, printed, and mailed to each attendee for inclusion in his copy of the proceedings.

The proceedings of the symposium have been bound in four volumes -- a separate volume for the technical sessions of each day, and one volume for the panel sessions. We are indebted to the authors for preparing their manuscripts in a form that could be directly reproduced. This material was published as provided by the authors and was neither checked nor edited by CAL or USAAVLABS.

The cosponsors of the symposium are grateful to the many people who contributed to its success. In particular, our thanks go to Colonel Harry L. Bush, Commanding Officer of the U.S. Army Aviation Materiel Laboratories, and Mr. Ira G. Ross, President of Cornell Aeronautical Laboratory, Inc., who opened the sessions; to Mr. Charles W. Harper, our keynote speaker; to Major General William Bunker, Deputy Commanding General, U.S. Army Materiel Command, for his address at the symposium banquet; to the five session chairmen --

Arthur Jackson, Hamilton Standard

Franklyn J. Davenport, Vertol Division of The Boeing Company

John W. White, U.S. Army Aviation Materiel Laboratories

Irven H. Culver, Lockheed-California Company

Sean C. Roberts, Mississippi State University

and to the two panel chairmen --

Larry M. Hewin, Technical Director, USAAVLABS

Harold A. Cheilek, Vice President - Technical Director, CAL

and, most especially, of course, to the authors and panel members without whom there could not have been this symposium on low-speed aerodynamic problems.

SYMPOSIUM TECHNICAL CHAIRMAN

Richard P. White, Jr., CAL
John E. Yeates, USAAVLABS

CONTENTS
VCLUME II
PROPULSION AND INTERFERENCE AERODYNAMICS

TECHNICAL SESSION III

PROPULSION AERODYNAMICS

Thursday Morning
23 June 1966

SESSION CHAIRMAN

J.W. White
U.S. Army Aviation Materiel Laboratories

PREDICTED AND MEASURED PERFORMANCE OF
TWO FULL-SCALE DUCTED PROPELLERS

by

A. R. Kriebel
M. R. Mendenhall

Vidya Division, Itek Corporation
Palo Alto, California, USA

INTRODUCTION

A theoretical aerodynamic analysis of a ducted propeller at angle of attack is presented in References 1 and 2. This potential flow analysis can be used to predict the force and moment on the duct in terms of the propeller thrust. The usefulness of any theory is dependent on evaluation by comparison with valid data. Much of the previous data (summarized in Ref. 1) are restricted to hovering or axial flight and/or low Reynolds number with flow separation from the duct. Full-scale test data for two ducted-propeller configurations at angle of attack, presented herein, allow a correlation study and a good evaluation of the potential flow theory. The duct force and moment are predicted by use of Reference 2 and compared with experiment. The analysis is extended to predic the duct pressure distribution and boundary-layer separation which are also compared with experiment.

The analysis is based on a combination of two previous potential flow theories for a ring-wing at a small angle of attack, Reference 3, and for a lightly loaded ducted propeller in axial flow, Reference 4. In Reference 2, the duct thrust, normal force, and pitching moment were predicted by representing the propeller as a uniformly loaded actuator disk. Estimates of the normal force and pitching moment on propeller blades operating in a duct were small compared with those on the duct. Small amounts

of duct taper, camber, and thickness were estimated to have little effect on the duct force and moment; hence, the duct is represented herein as a thin cylinder to predict its force and moment.

For comparison with test data, the theory is usually used to predict the thrust, normal force, and pitching moment on the cylinder in terms of the measured total thrust (on both the disk and cylinder). The predicted duct thrust can then be compared with the value deduced from the measured duct pressure distribution. The predicted duct normal force and pitching moment are compared with the values measured for the ducted propeller unit.

The work described herein was sponsored by the Ames Research Center of NASA under Contract No. NAS2-2647.

EXPERIMENTAL PROGRAM

Two full-scale ducted propellers have been tested at angle of attack in the NASA Ames Research Center 40- by 80-foot wind tunnel. The first of these was the "Doak" ducted propeller mounted on the tip of a semispan wing (Ref. 5). This unit, which is referred to herein as the 4-foot model, consists of a duct with a chord-to-diameter ratio of 0.608 and a profile thickness-to-chord ratio of 0.158; an eight-bladed propeller with fixed blade pitch of 15° at the tip; a set of seven inlet guide vanes of variable pitch; and a set of nine stators aft of the propeller. A photograph and a sketch of the cross section of this ducted propeller are shown in Figures 1(a) and 2(a). Complete details of the 4-foot model and the test methods are described in Reference 5. The second unit tested was the "Bell X22-A" ducted propeller mounted on the tip of a stub wing. This unit, referred to as the 7-foot model, consists of a duct with a chord-to-diameter ratio

2

of 0.525 and a profile thickness-to-chord ratio of 0.172; a
three-bladed variable pitch propeller; and six streamlined support
struts aft of the propeller. For some of the tests, ar. elevon
extended across the duct exit plane with a thickness of 0.44
feet and a chord of approximately 5 feet. A photograph and a
sketch of the cross section of this model are shown in Figures
1(b) and 2(b). The test setup and techniques were similar to
those used with the 4-foot model.

For the 4-foot model the data included direct measure-
ment of lift, drag, and pitching moment reported in Reference 5
and duct surface pressure at 27 orifice stations around the duct
profile and at 10 azimuth locations. Total pressure was measured
along the duct radii directly ahead of the inlet vanes, directly
behind the propeller, and across the duct exit plane with pres-
sure rakes at 10 azimuth locations.

Data for the 7-foot model included direct measurements
of forces and moments and duct surface-pressure measurements at
19 orifice stations around the duct profile for 3 azimuth loca-
tions. Since the duct pressure data were taken at only 3 azi-
muth locations, pressure integrations were made to obtain duct
thrust only at zero angle of attack.

In addition to the data described above, stalling of the
4-foot model duct was deduced from observation of tufts, sound
level, and pitching moment as described in Reference 5.

METHOD OF PREDICTION

Potential Flow Model

For a ducted propeller at angle of attack, the analysis
of Reference 2 predicts the thrust, normal force, and pitching
moment on the duct in terms of the propeller thrust. The analysis
represents the propeller and stator blading and the centerbody
as a uniformly loaded actuator disk. There is no swirl in the

3

slipstream, and the circulation about each propeller and stator blade is assumed to be invariant with radius and time. The boundary layer and frictional drag of the duct are neglected. The ducted propeller is assumed isolated in the free stream.

Calculative examples have been run to investigate the effects of duct camber and radial variation of disk loading in order to arrive at a simple, yet realistic analytical flow model. As a result of this work, the following assumptions will be employed:

(a) The actuator disk loading is applied only to the annular area swept out by the propeller blades and not to the aft part of the centerbody or inner duct surface.

(b) The duct thrust is taken as that due to leading-edge suction on a thin cylinder.

(c) The effects of duct camber and thickness are neglected except in computing the duct pressure distribution and boundary layer. (It is shown in Ref. 2 that this is a good approximation for the duct force and moment.)

(d) The propeller and stators are represented as a uniformly loaded actuator disk. The centerbody, support wing, and elevon are neglected.

Duct Force and Moment

To predict the duct force and moment, the duct is represented as a thin cylinder through the actual duct trailing edge as shown in Sketch A.
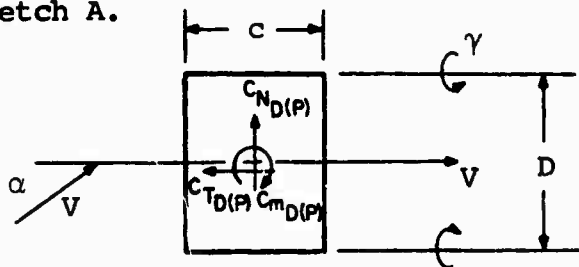
Sketch A.- Flow model for predicting
duct force and moment.

4

All the trailing vorticity is placed on the extension of the cylinder. This approximation requires the free-stream crossflow to be small compared with the slipstream velocity ($V \sin \alpha \ll V_j$). The pressure jump across the actuator disk Δp is equal to the increased total pressure in the slipstream as given by

$$\frac{\Delta p}{q} = \frac{V_j^2}{V^2} - 1 = \left(\frac{V \cos \alpha + \gamma}{V}\right)^2 - 1$$

$$= 2 \frac{\gamma}{V} \cos \alpha + \frac{\gamma^2}{V^2} - \sin^2 \alpha \qquad (1)$$

The propeller thrust is taken as

$$T_{P(D)} = A_p \Delta p \qquad (2)$$

where A_p is the annular area swept out by the propeller blades. Hence, the propeller thrust coefficient is

$$C_{T_{P(D)}} = \frac{T_{P(D)}}{Aq} = \frac{A_p}{A} \cdot \frac{\Delta p}{q} \qquad (3)$$

The coefficients for the duct force components and pitching moment are given by Equations (20) through (23) of Reference 2 as

$$C_{N_{D(P)}} = f_1 \sin \alpha \left(\cos \alpha + f_2 \frac{\gamma}{V}\right) \qquad (4)$$

$$C_{T_{D(P)}} = f_3 \sin^2 \alpha + f_4 \left(\frac{\gamma}{V}\right)^2 \qquad (5)$$

$$C_{m_{D(P)}} = 4f_5 \sin \alpha \cos \alpha + (f_5 f_6 + f_7) \frac{\gamma}{V} \sin \alpha \qquad (6)$$

where the f_n coefficients are given versus the duct chord-to-diameter ratio c/D in Table I, Reference 2.

5

Use of blade element theory in Reference 2 indicated that the normal force and pitching moment on the propeller are generally small compared with those on the duct. Therefore, we shall take the coefficients for the ducted propeller unit as

$$C_{T_{DP}} = C_{T_{P(D)}} + C_{T_{D(P)}} \tag{7}$$

$$C_{N_{DP}} = C_{N_{D(P)}} \tag{8}$$

$$C_{m_{DP}} = C_{m_{D(P)}} \tag{9}$$

The strength of the vortex cylinder surrounding the slipstream is found by substituting Equations (1), (3), and (5) into (7) and solving for

$$\frac{\gamma}{V} = - \frac{\cos \alpha}{\frac{A}{A_P} f_4 + 1} + \sqrt{\left(\frac{\cos \alpha}{\frac{A}{A_P} f_4 + 1} \right)^2 + \frac{\frac{A}{A_P} C_{T_{DP}} - \left(\frac{A}{A_P} f_3 - 1 \right) \sin^2 \alpha}{\frac{A}{A_P} f_4 + 1}}$$

$$\tag{10}$$

The general procedure for prediction will be to determine γ/V from Equation (10) using a measured value of $C_{T_{DP}}$, and then to evaluate the preceding expressions. This value of $/V$ is also used to predict the duct surface-pressure distribution and boundary layer.

Duct Pressure Distributions

The duct pressure distribution is obtained by first predicting the bound vorticity and velocity distribution over the thin duct camberline, then including the effect of duct thickness to obtain the surface velocity distribution, and finally using Bernoulli's law to get the duct surface pressure.

6

The flow model used to predict the duct surface pressure is shown in Sketch B.

Numbers 1 through 4 designate the camberline or duct surfaces indicated.
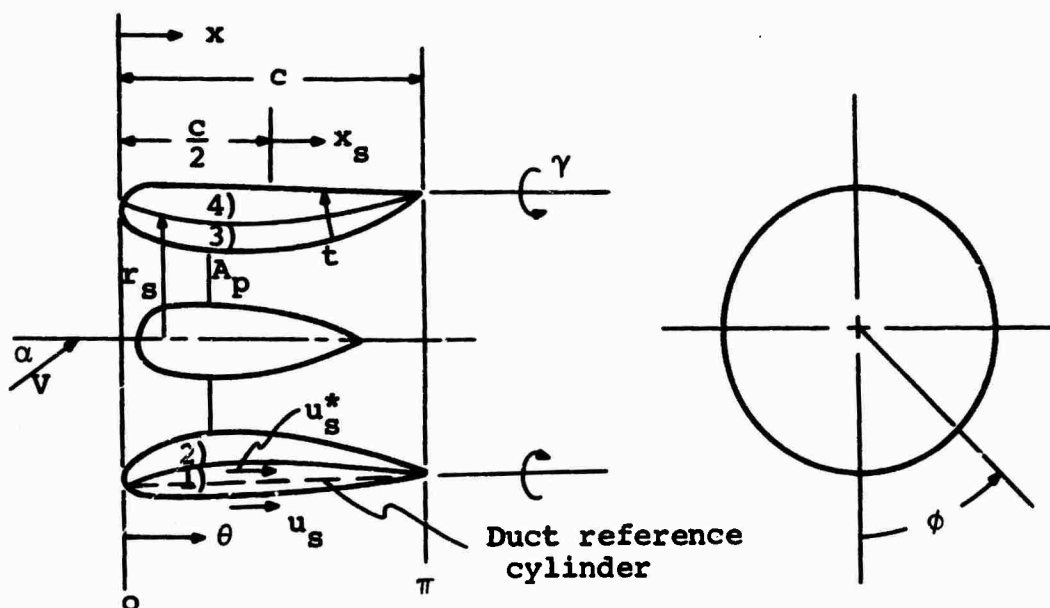
Sketch B.- Flow model for predicting duct pressure distribution.

Duct-bound vorticity

All the bound and trailing vorticity is placed on a reference cylinder through the duct trailing edge. The distribution of duct-bound vorticity is composed of elementary γ_D vortex rings which are axially symmetric and elementary γ_α rings with strength proportional to $\cos \phi$. The axially symmetric part of the flow field, composed of $V \cos \alpha$ plus that induced by the γ_D rings and the γ cylinder, is set tangent to the duct camberline. This boundary condition is actually imposed at the duct reference cylinder and it determines the strength of the γ_D rings.

The γ_α rings, together with the axial vortex filaments which trail from them, are required to cancel the velocity across

7

the duct reference cylinder due to the free-stream crossflow $V \sin \alpha$.

The slope of the duct camberline is expressed as a four-term cosine series

$$\epsilon = \frac{dr_s}{dx_s} = \sum_0^3 R_n \cos n\theta \tag{11}$$

where

$$\cos \theta = - \frac{2x_s}{c}$$

Integration gives the duct camberline shape as

$$\frac{r_s - R}{c} = R_0 \left(\frac{1 + \cos \theta}{2} \right) + R_1 \left(\frac{1 - \cos^2 \theta}{4} \right)$$

$$+ R_2 \left(\frac{1}{6} + \frac{1}{2} \cos \theta - \frac{1}{3} \cos^3 \theta \right)$$

$$+ R_3 \left(- \frac{1}{4} + \frac{3}{4} \cos^2 \theta - \frac{1}{2} \cos^4 \theta \right) \tag{12}$$

The R_n coefficients are determined such that Equation (12) fits the geometric camberline at $x/c = 0$, $1/4$, $1/2$, $3/4$, and 1. The actual duct profiles and the approximate analytical profiles are compared in Figure 3. An effective camber due to thickness ϵ_t as subtracted from Equation (11) is described in Reference 6. This effect is due to the radial velocity induced by the source rings used to generate duct thickness.[1] We shall take ϵ_t for a

---

[1]Evaluation of the axial velocity induced by the source rings from Reference 6 indicates that it is nearly the same as for a straight, 2-dimensional wing with the same thickness as the duct. This approximation will be employed in the present analysis.

8

NACA 0018 thickness distribution using Equation (44), Reference 6.[2] Thus, the slope of the effective camberline is specified as

$$\epsilon_e = \epsilon - \epsilon_t = \sum_0^3 R_n^* \cos n\theta \qquad (13)$$

To set the flow tangent to the camberline, we specify that

$$v_\gamma + v_{\gamma_D} = \epsilon_e \left(V \cos \alpha + u_\gamma + u_{\gamma_D} \right) \qquad (14)$$

The u and v terms are the axial and radial velocity components induced along the duct reference cylinder by the γ cylinder extending from the duct trailing edge and the γ_D rings bound to the duct reference cylinder. These terms are expressed as a six-term cosine series as follows. The components induced by the vortex cylinder can be found from Reference 7 in terms of elliptic integrals. Fourier analysis by machine then give

$$\frac{u_\gamma}{\gamma} = \sum_0^5 B_n^* \cos n\theta \qquad (15)$$

$$\frac{v_\gamma}{\gamma} = \sum_0^5 B_n \cos n\theta \qquad (16)$$

---

[2]The duct profiles for the two ducts do not correspond to any standard airfoil section. However, it was found that the NACA 0018 is a good approximation to the actual thickness distribution of both configurations, particularly over the forward portion of the airfoil where the pressure distributions are of greatest interest.

If the duct-bound vorticity is put in terms of a Glauert series as[3]

$$\frac{\gamma_D}{\gamma} = C_o \cot \frac{\theta}{2} + \sum_1^5 C_n \sin n\theta \qquad (17)$$

then the corresponding induced axial velocity component is from Equation (18), Reference 2

$$\frac{4D}{c} \frac{u_{\gamma_D}}{\gamma} = \left(\ell n \frac{16D}{c} - 1\right)\left(C_o + \frac{C_1}{2}\right) + \left(C_o + \frac{C_2}{2}\right)\cos \theta$$
$$+ \frac{C_3 - C_1}{4}\cos 2\theta + \frac{C_4 - C_2}{6}\cos 3\theta$$
$$+ \frac{C_5 - C_3}{8}\cos 4\theta \qquad (18)$$

The radial velocity component can be found from Equation (14) of Reference 4 as

$$\frac{v_{\gamma_D}}{\gamma} = \frac{C_o}{2} - \sum_{k=o}^{\infty} \frac{C_\ell}{2} P_{o\ell} + \sum_{k=1}^{\infty} \cos k\theta \left(-\frac{C_k}{2} + \sum_{\ell=o}^{\infty} \frac{C_\ell}{2} P_{k\ell}\right) \qquad (19)$$

The $P_{k\ell}$ coefficients appearing in Equation (19) are evaluated in Tables 2.1 through 2.4 of Reference 4.

The six unknown C_n coefficients appearing for γ_D are determined by: (1) substituting the foregoing cosine series for the terms in Equation (14), (2) expanding the right-hand side as

---

[3] Between the actuator disk and duct trailing edge γ_D includes the vorticity shed from the disk onto the inner duct surface. The Kutta condition of no flow across the duct trailing edge is satisfied because γ_D is nonsingular at $\theta = \pi$ in Equation (17).

a cosine series, and (3) equating each of the six harmonics of Equation (14). The resulting six linear algebraic equations are then solved by machine for the six c_n. The remaining part of the duct vorticity γ_α is the same as determined by Weissinger for a ring-wing at angle of attack, and is given by Equation (8) of Reference 2 as

$$\frac{\gamma_\alpha}{V \sin \alpha \cos \phi} = c_o \cot \frac{\theta}{2} + \sum_1^5 c_n \sin n\theta \qquad (20)$$

Weissinger's values for the c_n coefficients are given in Table 1, Reference 2. The axial velocity induced by γ_α along the duct reference cylinder is given by Equation (19) of Reference 2 as

$$\frac{4Du_{\gamma_\alpha}}{cV \sin \alpha \cos \phi} = \left(\ell n \frac{16D}{c} - 3\right) \left(c_o + \frac{c_1}{2}\right) + \frac{1.46c}{4D} \left(c_o + \frac{c_2}{2}\right)$$

$$+ \left[c_o - \frac{1.46c}{4D} \left(c_o + \frac{c_1}{2}\right) + \frac{c_2}{2}\right] \cos \theta$$

$$+ \frac{c_3 - c_1}{4} \cos 2\theta + \frac{c_4 - c_2}{6} \cos 3\theta$$

$$+ \frac{c_5 - c_3}{8} \cos 4\theta \qquad (21)$$

Finally, the velocity distribution over the four duct camberline surfaces shown in Sketch B can be evaluated by substitution of preceding expressions into

$$u_s{}^* = \pm \frac{\gamma_D + \gamma_\alpha}{2} + V \cos \alpha + u_\gamma + u_{\gamma_D} + u_{\gamma_\alpha} \qquad (22)$$

11

where the plus sign refers to the inner surfaces 2 and 3 and the minus sign the outer surfaces 1 and 4. At the sides of the duct, γ_α induces a tangential velocity component. We shall not consider the component, since it vanishes at the vertical plane of symmetry to which we shall restrict the pressure distribution predictions.

Duct surface velocity

To obtain the duct surface velocity from the velocity distribution over the camberline (Eq. (22)), we apply corrections to the discontinuous (vorticity) and continuous terms in Equation (22). These correction factors are deduced as follows from theoretical results for two-dimensional (c/D = 0) thick airfoils in Reference 8. For a thin flat plate at angle of attack, the bound vorticity is

$$\frac{\gamma_D}{V} = 2\alpha \cot \frac{\theta}{2} \tag{23}$$

At $\alpha = 1/(2\pi)$ the lift coefficient is unity and

$$\frac{\gamma_D}{2V} = \frac{1}{2\pi} \cot \frac{\theta}{2} \tag{24}$$

This chordwise distribution is listed in Table I for comparison with values for a NACA 0018 airfoil from Reference 8. It is evident that thickness has little effect on the bound vorticity except near the airfoil nose where $x < 0.1c$. Hence, we shall correct the singular $(\cot(\theta/2))$ terms in γ_D and γ_α by replacing $\cot(\theta/2)$ by the corresponding value for a NACA 0018 airfoil when $x < 0.1c$. For example, at the leading edge $(1/2\pi) \cot(\theta/2)$ is replaced by 1.342. The surface velocity distribution for a two-dimensional NACA 0018 airfoil at $\alpha = 0$ is shown in the last column of Table I. In this case, the continuous part of the camberline velocity distribution is V and the

12

continuous part of the surface velocity distribution is $VF(x)$, where $F(x)$ is given by the last column in Table I. By analogy, we shall obtain the continuous part of the duct surface velocity by multiplying the continuous part of camberline velocity by $F(x)$. Thus, we obtain the duct surface-velocity distribution from the duct camberline distribution (Eq. (22)) as

$$u_s = \pm \left(\frac{\gamma_D + \gamma_\alpha}{2}\right)_c + \left(V \cos \alpha + u_\gamma + u_{\gamma_D} + u_{\gamma_\alpha}\right) F(x)$$

(25)

The first parenthesized term is corrected only when $x < 0.1c$ as described previously.

Duct pressure distribution

The duct surface-pressure coefficient is obtained from Equation (25) by Bernoulli's law as

$$C_p = 1 - \frac{u_s^2}{V^2}$$

(26)

However, on the inner duct surface downstream of the actuator disk, the total pressure is increased by Δp and C_p is increased by $\Delta p/q$ due to the pressure jump across the disk.

Duct Boundary-Layer Model and Assumptions

Our purpose in computing the duct boundary layer is to predict those conditions under which separation will occur on the windward inside surface before the propeller. We shall use the axisymmetric Truckenbrodt method to obtain the momentum thickness (θ) and shape factor (H) of the boundary layer and then we shall use an empirical rule $(H = 1.8)$ to predict turbulent separation.

13

The Truckenbrodt method (Refs. 9 or 10) has been compared to known results in both laminar and turbulent flow and found to give excellent agreement. We have computed the laminar boundary-layer parameters for Howarth flow on a flat plate and they agree within 5 percent of the exact Howarth solution. We have also computed turbulent boundary-layer parameters for a NACA 65(216)-222 profile at 10.1^o angle of attack using the measured velocity distribution. The computed momentum thickness, shape factor, and separation point all agree well with measured results.

We shall make use of the following assumptions in calculating the duct boundary layers:

(1) The boundary-layer momentum thickness is small in comparison with the duct radius so that the presence of the boundary layer does not appreciably alter the potential flow around the duct.

(2) The predicted surface velocity (Eq. (25)) is taken as the boundary-layer-edge velocity distribution.

(3) The velocity profiles in the boundary layer are approximated by a one-parameter family of curves.

As a transition criterion, it is assumed that the boundary layer changes from laminar to turbulent at a Reynolds number of about 400 based on momentum thickness and local surface velocity.[4] In cases with high adverse pressure gradients near the leading edge, the laminar boundary layer separated (H = 4.04) before Re_θ = 400. Assuming that the separated region acts as a turbulence trip, the point of transition is located at the first indication of laminar separation. In Reference 11, it is reported

---

[4] The transition criterion is based on a measured critical Reynolds number on a flat plate, $Vx/\nu = 3\times10^5$ (Ref. 10). This corresponds to $V\theta/\nu \approx 365$ in a laminar boundary layer on a flat plate. Since the location of turbulent separation is insensitive to small variations in transition location, transition was assumed to occur when $350 < u_s\theta/\nu < 425$.

14

that small laminar separation bubbles, which did not show up in the pressure distribution, did serve as turbulence trips.

The shape factor (H) is used to estimate the location of boundary-layer separation from the duct. The usual criteria for boundary-layer separation is that turbulent separation occurs when H has attained a value between 1.8 and 2.4, and laminar separation occurs when H = 4.04.

The Truckenbrodt solution to the boundary layer is based on integration of the energy equation. The energy equation is written in the form

$$\frac{1}{2} \frac{1}{u_s^3 r_s} \frac{d}{dx} \left(u_s^3 r_s \delta^{**} \right) = \frac{d + t}{\rho u_s^3} \tag{27}$$

where δ^{**} is the energy thickness of the boundary layer, d is the dissipation term, and t is the energy of turbulent motion term. The right side of Equation (27) is the shear stress work in the boundary layer. Truckenbrodt's final expression for momentum thickness as a function of boundary-layer-edge conditions is

$$\frac{\theta(z)}{s} = \frac{1}{\left(\frac{u_s}{V}\right)^3 \left(\frac{r_s}{s}\right)} \left[C_1^* + \left(\frac{c_{f_t}}{2}\right)^{1+n} \int_{z_1/s}^{z/s} \left(\frac{u_s}{V}\right)^{3+2n} \left(\frac{r_s}{s}\right)^{1+n} d\left(\frac{z}{s}\right) \right]^{1/1+n}$$

(28)

where

$$C_1^* = \left\{ \frac{c_{f_\ell}}{2} \left[\int_0^{z_1/s} \left(\frac{u_s}{V}\right)^5 \left(\frac{r_s}{s}\right)^2 d\left(\frac{z}{s}\right) \right]^{1/2} \right\}^{1+n}$$

15

$$c_{f_\ell} = \text{laminar flat-plate drag coefficient from the Blasius relation based on } q \text{ and } s.$$

$$c_{f_t} = \text{turbulent flat-plate drag coefficient from the Schultz-Grunow relation based on } q \text{ and } s.$$

laminar flow: $n = 1$

turbulent flow: $n = 1/6$

The actual calculation of momentum thickness is carried out in a surface coordinate system where z is measured from the leading edge along the surface of the duct and s is the surface length of the duct. The point of transition of the boundary layer from laminar to turbulent is denoted by z_1. After the boundary layer is computed in the surface coordinate system, the results are transferred into a coordinate system based on axial distance x and chord length c.

Boundary-layer parameters were computed on the inside surface of both ducts using measured and predicted velocity distributions. Computation of these parameters using the measured velocity distribution was started at the leading edge. When the predicted velocity distribution was used to compute the boundary-layer parameters, the computation was started either at the leading edge or at the stagnation point on the outside surface.

RESULTS

The predicted force and moment coefficients are given by Equations (3) through (10) in terms of the parameters A_p/A, c/D, and f_n. Values for these parameters are listed in Table II for both ducts. The f_n are found by interpolation from Table 1, Reference 2. The total measured force and moment coefficients are deduced from force balance data. Individual duct and propeller thrust coefficients are determined from integrat.ons of measured pressure distributions over the duct surface ar.d total pressure rake data just aft of the propeller.

16

Division of Thrust in Axial Flow

Four-foot model

For a series of axial flow runs with the 4-foot model duct, the measured thrust coefficients are listed in Table III. The sum of the individual duct and propeller measured thrusts $C_{T_{D(P)}}$ and $C_{T_{P(D)}}$ is equal to the total measured thrust $C_{T_{DP}}$ within 7 percent. The values of γ/V and $C_{T_{D(P)}}$ predicted from the measured $C_{T_{P(D)}}$ are listed next. Finally, the values of γ/V and $C_{T_{D(P)}}$ predicted from the measured $C_{T_{P(D)}}$ are shown. The latter values are obtained by use of Equations (3), (1), and (5) in succession rather than by the usual method (Eqs. (10) and (5)).

Seven-foot model

Measured values of $C_{T_{DP}}$ and $C_{T_{D(P)}}$ are shown in Table III together with the predicted value of $C_{T_{D(P)}}$. The effect of increased propeller blade pitch is indicated by the last three runs.

Duct Force and Moment at Angle of Attack

Four-foot model

Normal force and pitching moment coefficients predicted versus the total thrust coefficient are shown in Figures 4 and 5, together with measured values. The data generally lie well below the predicted curves, particularly the normal-force coefficient. The measured duct normal force (deduced from the pressure distribution) is considerably smaller than the measured total normal force as shown in Table IV.

Seven-foot model

Similar predicted and measured coefficients for the larger duct are shown in Figures 6 and 7. The data are all for the same propeller pitch and with the elevon either off or

17

aligned with the duct axis. The elevon appears to have most
effect on the measured normal force at the highest angles of
attack.

Duct Pressure Distributions in Axial Flow

Following the procedure described previously, the first
step in predicting the duct pressure distribution is to fit Equa-
tion (12) to the duct camberline and solve for the four camber-
line coefficients R_n. The computed values for R_n are given
in Table II for both ducts. The thickness distributions for both
ducts were approximated by a NACA 0018 profile. The resulting
duct profiles (Fig. 3) fit the nose radius of curvature for both
ducts. However, the hook in the camberline near the leading
edge of the larger duct is not well represented. Attempts to fit
the hook with the four-term series caused a very poor fit over
most of the camberline.

The effective camber due to thickness (ϵ_t in Eq. (13))
is given by Reference 6 for a NACA 0008 profile and $c/D = 1/2$.
Multiplication by 18/8 gives, for an 0018 profile and $c/D = 1/2$,

$$\epsilon_t = 0.001 + 0.040 \cos \theta + 0.013 \cos 2\theta - 0.001 \cos 3\theta$$

This distribution was used for both ducts. The resulting R_n^*
coefficients for the effective camberline (Eq. (13)) are given
in Table II.

Fourier analysis by machine gives the series coeffi-
cients B_n and B_n^* which appear in Equations (15) and (16) for
the velocity components induced by the vortex cylinder trailing
from the duct. Machine computed values are given in Table V for
the two ducts.

The $P_{k\ell}$ coefficients which appear in Equation (19) are
found by interpolation from Tables 2.3 and 2.4 of Reference 4.
Values for the two ducts are given in Tables VI and VII.

18

The C_n coefficients in Equation (17) for the duct-bound vorticity γ_D must be computed for each case since they depend upon γ/V. However, for no duct camber ($R_n^* = 0$) the C_n depend only upon c/D, and these values are given in Table V.

The c_n coefficients in Equation (20) for the duct-bound vorticity γ_α can be found by interpolation from Table 1 of Reference 2. Values for the two ducts are given in Table V.

Four-foot model

Duct pressure distributions computed for the smaller duct in axial flow are shown in Figure 8 at three thrust levels. Measured data are shown by the vertical lines to indicate the variation with azimuth. The discontinuous change in predicted pressure on the inner duct surface is caused by the pressure jump across the assumed uniformly loaded actuator disk.

Seven-foot model

For a series of axial flow runs with the larger model, the measured and predicted duct pressure distributions are shown in Figure 9. The first three runs are for propeller blade pitch $\beta = 19^o$, and the last is for $\beta = 29^o$.

Duct Pressure Distributions at Angle of Attack

Four-foot model

Pressure distributions measured and predicted for the smaller duct at angle of attack are shown in Figure 10. The corresponding pressure distribution for $\alpha = 0$ is shown in Figure 8(b).

Total pressure distributions measured vertically across the duct exit plane are shown in Figure 11. These data show that the propeller loading was not uniform and that the flow was separated from the lower inner duct surface 2 even at low angles of attack.

19

Seven-foot model

Pressure distributions measured and predicted for the 7-foot model duct at angle of attack are shown in Figures 12 and 13. The effect of angle of attack at a high advance ratio is shown in Figures 12 and 9(b); and at a low advance ratio in Figure 13 and 9(c). All the data at angle of attack were taken 13° off the vertical plane of symmetry ($\phi = 0$ in Sketch B).

Duct Boundary Layers

With the foregoing duct surface geometry and both measured and predicted surface-pressure distributions, duct boundary layers were computed using the method previously described. Bernoulli's equation was used to relate surface velocity and pressure distributions. The boundary layers were computed only on the lower inner surface[5] of the computed duct profile.

Four-foot model

For the smaller duct in axial flow at various advance ratios, the boundary-layer momentum thickness, shape factor, and surface-velocity distributions are shown in Figure 14. The momentum thickness was assumed zero at the leading edge in each case. The turbulent boundary layers computed from the predicted velocity distributions did not separate from the duct ahead of the propeller. However, when the measured velocity distribution was used for the hovering flight condition $(J = 0)$ and a second high thrust condition $(J = 0.178)$, the boundary layer separated slightly ahead of the propeller.

The boundary layer results for the duct at $\alpha = 80^{\circ}$ and $J = 0.166$ are shown in Figure 15, where the measured and predicted surface-velocity distributions (from Fig. 10(d)) are also

---

[5]The computed duct shape is the superposition of a NACA 0018 thickness distribution on the duct camberline shape from Equation (12).

compared. The momentum thickness and shape factor were computed from 'he leading edge using both predicted and measured velocity distributions. The boundary layer computed from the predicted velocity distribution separates before that from the measured velocity distributions. For the predicted velocity, the boundary layer was also computed from the stagnation point at $x/c = 0.60$ with almost no change in the results.

For the larger duct at high advance ratio ($J \simeq 0.52$) and various angles of attack, the boundary-layer momentum thickness, shape factor, and surface velocity distribution are shown in Figure 16. Using predicted velocity distributions, the boundary layers were computed from the leading edge at $\alpha = 0^{\circ}$ and 20°, and from $x/c = 0.05$ near the outside stagnation point at $\alpha = 40^{\circ}$. The measured velocity distribution was also used for $\alpha = 0^{\circ}$ and 40°. Only the last of these computed boundary layers separated. This result agrees with the measured pressure distributions where separation is evident at $\alpha = 40^{\circ}$ (Fig. 12(b)).

For the measured pressure distributions at lower advance ratio (Fig. 13), separation was computed at $x/c = 0.21$ for $\alpha = 20^{\circ}$ and $x/c = 0.18$ for $\alpha = 40^{\circ}$. The effect of separation was not evident in the measured pressure distribution except at higher angles of attack.

Duct Stall Boundary

The location of boundary-layer separation on the smaller duct, as computed from measured and predicted velocity distributions, is shown by the points in Figure 17(a). The upper-dashed curve is the boundary corresponding to separation midway between the leading edge and the propeller (at $x/c \simeq 0.15$). This boundary is estimated from the points computed with measured velocity distributions. The other dashed curves correspond to separation at other values of x/c as estimated from the computed points. Also shown in this figure is the stall boundary

21

deduced from the measured pitching moment, sound level, and
visualization of tufts on the inner duct lip (Ref. 5).

For both ducts in axial flow, the location of boundary-
layer separation computed from measured velocity distributions
is shown in Figure 17(b).

All of the computed separation points on both ducts are
shown in Figure 18. The points are plotted versus a Reynolds
number based on a length ℓ obtained from a straigh line through
the separation point on a $u(x)$ plot as indicated in Sketch C
and Figure 18.
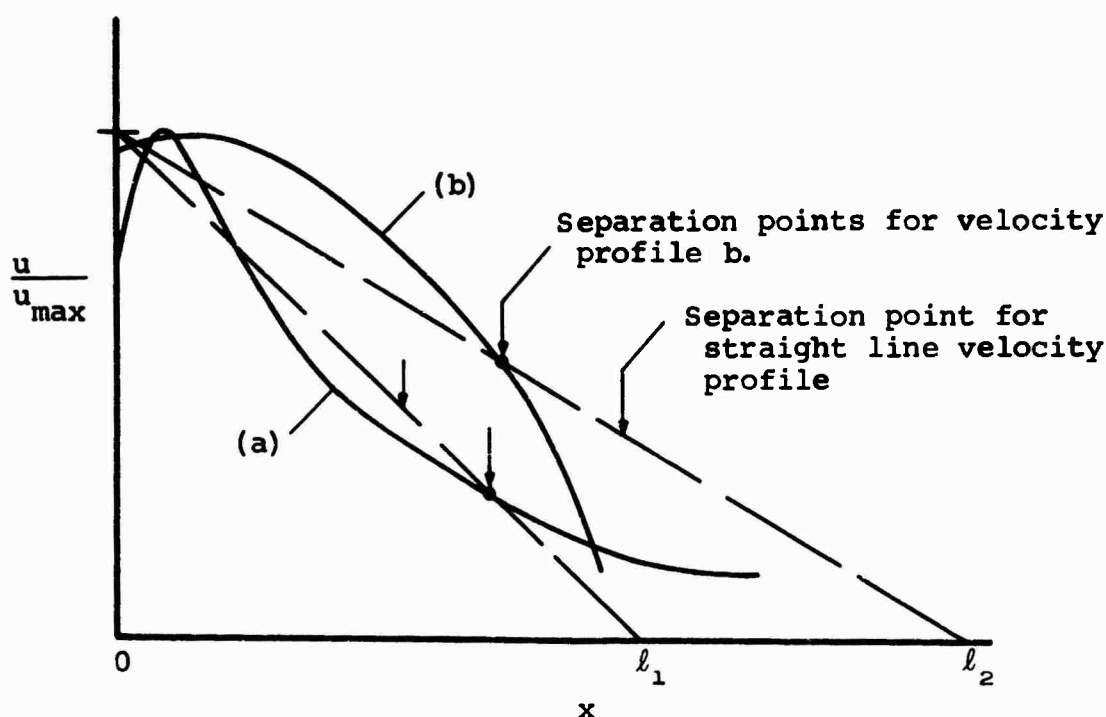
Sketch C.- Linear approximation to duct velocity distributions.

The curved line in Figure 18 shows that the separation points
for a series of straight line velocity profiles, computed by the
Truckenbrodt method as before, are all at nearly a constant
velocity ratio, $u_{sep}/u_{max} \simeq 0.65$. The points which lie below
the curve are for velocity profiles which are concave downward,

for example, curve (a) in Sketch C, or the dashed curve in Figure 15. On the other hand, the points which lie above the curve are for convex upward profiles such as curve (b) in Sketch C, or the lower dashed cruve in Figure 14.

DISCUSSION

Division of Thrust in Axial Flow

In axial flow, the 4-foot model duct thrust predicted both from the measured total thrust and the measured propeller thrust (Table III) agrees with the measured value within +10/-12 percent. This agreement seems satisfactory in view of the fact that the theory neglected the observed non-uniformity of propeller blade loading and the prevalence of flow separation from the duct diffuser in addition to many other real effects.

For the 7-foot model duct in axial flow, the measured duct thrust generally exceeds the predicted value (Table III). The flow separated from the inner duct surface upstream of the propeller when $C_{T_{DP}} > 2$ according to the boundary-layer predictions using the measured pressure distributions (Fig. 17). The predictions did not account for the hook in the duct camberline near the leading edge or the duct frictional drag. However, calculations indicate that both of these effects are appreciable only at low thrust levels. Calculations also indicate that the thrust on the 7-foot model (but not the 4-foot model) duct is predicted more accurately when the pressure rise across the actuator disk is assumed to act on the aft part of the inner duct surface.

Duct Force and Moment at Angle of Attack

The main difference between the measured and predicted performance of the two ducted propellers is the normal force at angle of attack. The measured values for the 4-foot model duct

23

(Fig. 4) are generally much smaller than for the 7-foot model duct (Fig. 6), particularly at high thrust levels. The predicted normal force is nearly the same for the two ducts and generally in good agreement with the data for the larger duct without the elevon (Fig. 6(a)). The data and predictions both indicate that there was considerable flow separation from the 4-foot model duct at angle of attack. However, it appears that the very low normal force measured for the smaller duct at high thrust level was caused largely by the concentration of propeller thrust loading toward the hub. Except for this effect, one might expect the normal force on the smaller unit to be greater than predicted for the duct alone because of the large centerbody and large number of stator and propeller blades. Theoretical estimates[6] indicate that concentration of the propeller loading toward the hub does cause the duct normal force to decrease significantly at high thrust level but has little effect on the duct thrust. The pitching moment appears to be well predicted for both ducts (Figs. 5 and 7).

Duct Pressure Distributions in Axial Flow

The pressure distributions for the 4-foot model duct (Fig. 8) appear to be reasonably well predicted. At the higher thrust levels, and particularly for the hovering flight condition, the pressure on the inner duct surface aft of the propeller is lower than predicted. This is probably due to the fact that the propeller loading is concentrated near the hub so that the full disk pressure jump is not applied suddenly to the duct surface.

The pressure distributions for the larger duct (Fig. 9) are accurately predicted on the outer surface. However, on the

---

[6]Kriebel, A. R.: Investigation of Dynamic Stability Derivatives of Ducted Propellers, 1st Quarterly Progress Rpt., Vidya Project No. 9270, Contract NOw 65-0348-c, June 1965.

24

more critical inner surface, the pressure is predicted less accurately than for the smaller duct. This is particularly true when the blade pitch and thrust coefficient are high (Fig. 9(c)). Although the presence of the elevon appears to have little effect on the duct pressure distribution, increased blade pitch at a fixed thrust lowers the measured pressure over the inner duct surface. The effect is complicated by the fact that separation of the boundary layer slightly ahead of the propeller was computed for all of the pressure distributions shown at the higher blade pitch. Such separation and possible reattachment after the propeller would probably be affected by the loading of the propeller blade tips.[7]

The discontinuity in duct pressure predicted for a uniform actuator disk loading is not evident for either ducted propeller. This can be attributed to the low loading of the propeller blade tips for the smaller unit as mentioned earlier. For the larger unit the blade tips were apparently more highly loaded, but the computed duct boundary layer separated near the propeller except when the blade loading was low. The separation of the duct boundary layer may have caused the pressure discontinuity on the inner duct wall to be smoothed out similar to a shock wave-boundary layer interaction. The predicted pressure gradient on the inner duct surface can be improved by smoothing out the discontinuity across the actuator disk.

---

[7] Recently, rake data were obtained approximately 10 inches upstream of the duct exit for $\alpha = 0$, $\beta = 29^\circ$, $J = 0$, 0.22, 0.45, 0.62. The measured total pressure was very uniform for each one of these runs except within the duct boundary layer (about 2 in. thick) and toward the centerline ($r \leq 18$ in. where $\Delta p \simeq 0$). The low dynamic head in the central part of the slipstream is believed to have: (1) caused the velocity over the inner duct surface to be higher than predicted, and (2) reduced the effectiveness of the elevon.

25

Duct Pressure Distributions at Angle of Attack

The predicted pressure distributions at angle of attack are in overall qualitative agreement for both ducts (Figs. 10, 12, and 13). However, the accuracy is poorest on the most critical surface 2. For surface 2 the pressure is underpredicted more for the smaller than for the larger duct. This is in agreement with the fact that the normal force on the smaller duct was over-predicted whereas the normal force on the larger model was not. For the smaller duct the inaccuracy of prediction is ascribed to the prevelence of flow separation from the duct and the nonuniformity of the propeller loading.

For the larger duct at low thrust coefficient (Fig. 12(a)), the pressure gradient on the uppermost surface 4 is more adverse than predicted. This is believed to be ʌ ʌsed by the hook near the leading edge of the actual camberline (Fig. 3) which cannot be accurately represented by the four-term series expression for the camberline. The corresponding suction peak is much smaller for the smaller duct. As the angle of attack is increased to 40° in Figure 12(b), the flow separates from surface 4. The flow is also separated from surface 2 in Figure 19(b) as shown by the measured pressure distribution and the boundary-layer calculations.

At higher thrust coefficient (Fig. 13), the stagnation point moves onto surface 4 and the pressure gradient becomes favorable. The computed separation on surface 2 was near the propeller and the separation bubble did not appear in the data until α exceeded the values shown here. Hence, the predicted pressure distributions are relative accurate.

Duct Boundary-Layer Calculations

In Figure 14, the difference in pressure gradient upstream of the propeller causes the boundary layer corresponding to the measured pressure to separate ahead of the propeller while

26

the predicted pressure boundary-layer does not. However, when the boundary layer separates farther forward similar results are obtained using measured and predicted pressure distributions (Fig. 15).

Starting point

In Figure 15, the boundary layer computed from the leading edge is compared with that computed from the outside surface stagnation point. Up to the leading edge the pressure gradient is highly favorable and the momentum thickness at the leading edge is quite small. There is only a small difference in momentum thickness on the inside surface and negligible difference ($< 0.01c$) between the computed separation points. Therefore, the additional effort required to compute the boundary layer from the stagnation point does not seem required.

Seven-foot model

The measured pressure distribution on the duct at $\alpha = 40^{\circ}$ (Fig. 12(b)) indicates a separated region at $x/c \approx 0.05$. The boundary layer computed from the leading edge using the measured pressure distribution separates at $x/c = 0.032$. Since this pressure distribution clearly indicates a separation region, the computed result is encouraging in terms of the method used to predict the boundary layer. No separation was computed using the predicted pressure distribution, but this distribution was inaccurate because of the flow separation.

Four-foot model

A summary of all the computed separation points for the smaller duct is shown in Figure 17(a). The dashed curves indicate the location of separation on the windward inner duct surface 2 as estimated from the computed points. These curves are obviously rough estimates because of the small number of points. The

27

upper dashed curve, which can be estimated more accurately than the others, gives the estimated flight conditions (angle of attack versus advance ratio) for separation about midway between the duct lip and propeller $(x/c = 0.15)$. The stall boundary deduced in Reference 5 from sound, tuft, and pitching moment data lies somewhat above the upper dashed curve, hence, this stall boundary apparently corresponded to separation very near the leading edge of the duct. The lowest dashed curve indicates that separation is expected to occur before the propeller except for low angle of attack and high advance ratio. The dashed curve for separation at $x/c = 0.24$ indicates that this is the calculated location of separation for hovering flight (any α at $J = 0$) and that there are values of α for $J > 0$ which fix the separation point at $x/c = 0.24$. A "duct stall boundary" could be defined to correspond with a fixed location of separation before the propeller. This boundary would then correspond with any one of the curves indicated in Figure 12(a) depending on the chosen location of separation.

Boundary-Layer Separation in Axial Flow

The computed separation points for both ducts in axial flow are compared in Figure 17(b). When the total thrust coefficient is near 20 it can be seen that the boundary layer on the larger duct separates slightly farther forward, however, the larger duct carries a considerably larger fraction of the thrust (Table III). The computed boundary layers on both ducts in axial flow are separated ahead of the propeller when $C_{T_{DP}} > 2$. Without unsteady effects due to finite propeller blades, the boundary layer was computed beyond the propeller for both ducts in axial flow using the measured velocity distribution. Separation occurred on the smaller duct at $x/c = 0.65$ for $C_{T_{DP}} = 0.684$ and on the larger duct at $x/c = 0.65$ for $C_{T_{DP}} = 0.890$. Thus, the

28

computed boundary layers on the inner surface of both ducts separate even for thrust coefficients smaller than unity.

Boundary-Layer Separation Summary

The computed separation results for both ducts are compared in Figure 18. The solid line gives the velocity ratio for separation as predicted for a constant adverse velocity gradient indicated in Figure 18. The points which lie above the curve are for increasingly adverse velocity gradients such that $u(x)$ is convex upward. The points below the curve are for $u(x)$ curves which are sharply peaked near the leading edge and convex downward. It can be seen that all of the computed separation points lie within a rather narrow band of velocity ratio, $0.6 \leq \frac{u_{sep}}{u_{max}} \leq 0.8$. By use of Figure 18, one can predict the location of separation for a typical duct velocity profile rather closely.

CONCLUSIONS AND RECOMMENDATIONS

The ability of previously developed theory for a ducted propeller at angle of attack to predict the duct-to-propeller thrust ratio, the normal force, and the pitching moment has been evaluated by use of wind tunnel data for two large-scale ducted propellers. The theoretical predictions were extended to include the pressure distribution, boundary layer, and stall boundary for the duct.

The experimental data presented herein show that the flow over a ducted propeller at angle of attack is generally very complex with much free vorticity generated by non-uniform blade loading and separation of the flow from the duct and centerbody. Specifically, the rake data for the 4-foot model show that the blade loading was concentrated near the t and that the flow was generally separated from the inner duct surface.

The theoretical flow model concentrates the free vorticity into a thin duct boundary layer and a single vortex

29

cylinder trailing from the duct. Nevertheless, this simple model succeeds in predicting at least qualitatively the force and moment, the pressure distribution, and the separation of the boundary layer over the entire operating range of propeller thrust and free-stream angle of attack.

The following specific conclusions are drawn from the experimental data and theoretical calculations reported herein.

(1) The duct thrust force and pitching moment, as predicted for a thin cylinder surrounding an actuator disk, correspond reasonably well with the measured data. In hovering flight the 4-foot model duct carries about 50 percent of the total thrust and the 7-foot model duct about 60 percent. For the larger model, the duct thrust is predicted more accurately with the assumption that the pressure rise across the actuator disk acts on the inner duct surface aft of the propeller. This is not the case for the smaller duct, apparently because the propeller loading is low near the blade tips.

(2) The duct normal force at angle of attack is well predicted for the 7-foot model and considerably overpredicted for the 4-foot model. This difference is also believed to be caused by the concentration of propeller loading nearer the hub for the smaller model, since theoretical estimates indicate that the duct normal force decreases with reduced loading of the propeller blade tips.

(3) The duct pressure distributions predicted for axial flow correspond reasonably well with the measured data. However, when the thrust level and blade pitch are both high, the pressure on the inner surface of the 7-foot duct is lower than predicted, and the predicted discontinuity in pressure across the propeller is not evident in the data. These differences are believed to be caused by low loading of the central part of the propeller and separation of the duct boundary layer as predicted before the propeller except at low thrust.

30

(4) The predicted duct pressure distributions at angle of attack are in qualitative agreement with the data, but they are not always quantitatively accurate, particularly in the critical region for flow separation, inside the windward duct lip.

(5) For both ducts in axial flow, separation of the boundary layer on the inner surface is predicted to occur before the propeller except when the advance ratio is high and the thrust coefficient is low. Separation is predicted slightly farther forward on the 7-foot model duct than on the 4-foot model duct for the same thrust coefficient in axial flow, however, t e duct-to-propeller thrust ratio is higher for the larger duct. The prediction of flow separation from the inner duct lip of the 4-foot model duct at angle of attack corresponds well with the stall boundary deduced experimentally from tufts, sound level, and pitching moment.

The general conclusion of this study is that the difference between the measured performance of the two ducted propellers and the theoretical predictions is caused mainly by diff rences in blade loading distribution and the prevalence of flow separation from the inner duct surface. More data and theory are needed to define and predict the distribution of blade loading, the duct boundary layer, and the interaction between the propeller blade tips and a region of flow separation.

It is recommended that total pressure rake data be obtained to determine the radial distribution of blade loading together with data to locate transition and separation of the duct boundary layer. Such data could be obtained for hovering flight quite readily without the use of a wind tunnel.

31

REFERENCES

1. Kriebel, A. R., Sacks, A. H., and Nielsen, J. N.: Theoretical Investigation of Dynamic Stability Derivatives of Ducted Propellers. Vidya Rpt. 63-95, Jan 9, 1963, AD 403 146.

2. Kriebel, A. R.: Theoretical Investigation of Static Coefficients, Stability Derivatives, and Interference for Ducted Propellers. Vidya Rpt. No. 112, Mar. 31, 1964, AD 602 269 (published in part in Jour. of Aircraft, AIAA, vol. 1, no. 4, July-Aug. 1964).

3. Weissinger, J.: Remarks on Ring Airfoil Theory. Institute für Angewandts Mathematick der Techischen Hochschule Karlsruhe, Jan. 1958, European Office Air Research and Development Command, Contract AF 61(514)-1207, Air Force Office of Scientific Research, AFOSR TN 58-224, AD 154 127.

4. Ordway, D. E., Sluyter, M. M., and Sonnerup, B. O. U.: Three-Dimensional Theory of Ducted Propellers. TAR-TR-602, Therm Advanced Research Div. of Therm, Ithica, New York, Aug. 1960.

5. Mort, K. W. and Yaggy, P. F.: Aerodynamic Characteristics of a 4-Foot-Diameter Ducted Fan Mounted on the Tip of a Semispan Wing. NASA TN D-1301, April 1962.

6. Hough, G. R.: The Aerodynamic Loading on Streamlined Ducted Bodies. TAR-TR-625, Therm Advanced Research Div. of Therm, Ithica, New York, Dec. 1962.

7. Kuchemann, D. and Weber, J.: Aerodynamics of Propulsion. McGraw-Hill Book Co., Inc., New York, 1953.

8. Abbott, I. H. and von Doenhoff, A. E.: Theory of Wing Sections. Dover Publications, Inc., New York, 1959.

9. Truckenbrodt, E.: A Method of Quadrature for Calculation of the Laminar and Turbulent Boundary Layer in Case of Plane and Rotationally Symmetrical Flow. NACA TM 1379, May 1955.

10. Schlichting, H.: Boundary-Layer Theory. McGraw-Hill Book Co., Inc., New York, 1955.

11. Bureau Technique Zborowski: Theoretical Investigation and Examination by Measuring Tests in What Degree the Economy of Flying Vehicles is Influenced by Pre-Cambered Skeletons of Airfoils Closed in Themselves. Contract DA-91-508-EUC-393, Aug. 10, 1959.

LIST OF SYMBOLS

A area of duct exit plane, $\pi D^2/4$

A_P propeller disk area, $\pi/r\left(D_P^2 - L_H^2\right)$

B_n Fourier series coefficients for v_γ, Equation (16)

B_n^* Fourier series coefficients for u_γ, Equation (15)

c chord length of duct

c_n Glauert series coefficients for γ_α, Equation (20)

C_m pitching moment coefficient, M/RAq

C_n Glauert series coefficients for γ_D, Equation (17)

C_N normal force coefficient, N/Aq

C_p pressure coefficient, $1 - u_s^2/V^2$

C_T thrust coefficient, T/Aq

D diameter of duct exit plane and duct reference cylinder

D_H maximum diameter of hub

D_P diameter of propeller, ft

f_n functions of c/D, Equations (4), (5), and (6)

H boundary-layer shape factor, δ^*/θ

J propeller advance ratio, V/nD_P

ℓ length derived from duct velocity profile (Fig. 30)

M aerodynamic pitching moment about the duct midchord diameter, positive clockwise, Sketch A

33

n	propeller rotational speed, rev/sec
N	normal force, Sketch A
P_t	measured total pressure
P_{t_∞}	free-stream total pressure
$P_{k\ell}$	coefficients from Reference 4, Tables VI and VII, Equation (19)
q	free-stream dynamic pressure, $\rho V^2/2$
r_s	local radius of duct surface, Sketch B
R	radius of duct exit plane, $D/2$
Re_θ	Reynolds number based on momentum thickness θ, $u_s(\theta)/\nu$
Re_∞	free-stream Reynolds number per foot, V/ν
R_n	Fourier series coefficients of duct camberline, Equation (11)
R_N^*	Fourier series coefficients for effective camberline of thick duct, Equation (13)
t	duct thickness, Sketch B
T	thrust force, Sketch A
u	local velocity in the duct boundary layer
u_s, u_s^*	local velocity at duct surface, and at duct camberline, Sketch B
u_γ, v_γ	axial and radial velocity components induced at duct reference cylinder by trailing vortex cylinder, Equations (15) and (16)
$u_{\gamma_D}, v_{\gamma_D}$	axial and radial velocity components induced at duct reference cylinder by vorticity bound to duct reference cylinder, Equations (18) and (19)
u_{γ_α}	axial velocity generated at duct reference cylinder by angle of attack, Equation (20)

34

V	free-stream velocity, Sketch A, ft/sec
V_j	axial velocity component in slipstream, Sketch A
x, x_s	axial distances defined in Sketch B
y	distance from duct wall within the duct boundary layer
α	free-stream angle of attack, Sketch A
β	propeller blade pitch angle measured at the blade tip for the 4-foot propeller and at 3/4 blade radius for the 7-foot propeller
γ	strength of vortex cylinder extending from duct trailing edge, Sketch A
γ_D	axially symmetric component of duct bound vorticity, Equation (17)
γ_α	component of duct bound vorticity proportional to $\cos \phi$, Equation 20
ρ	free-stream density
δ^*	displacement thickness of duct boundary layer, $$\int_o^\infty \left(1 - \frac{u}{u_s}\right) dy$$
δ_e	deflection angle of elevon, degrees
ν	kinematic viscosity of air
Δp	rise in static and total pressure across actuator disk, $T_{P(D)}/A_P$
$\epsilon, \epsilon_e, \epsilon_t$	slope of duct camberline, effective slope, effective slope due to duct thickness, Equations (11) and (13)
θ	transformed axial distance, $x_s = -(c/2)\cos \theta$, Sketch B, or momentum thickness of duct boundary layer, $$\int_o^\infty \frac{u}{u_s}\left(1 - \frac{u}{u_s}\right) dy$$
ϕ	azimuthal angle, Sketch B

Subscripts

DP	for the ducted propeller combination
D(P)	for the duct in the presence of the propeller (or actuator disk)
ℓ	laminar
max	maximum
P	for the propeller
P(D)	for the propeller (or actuator disk) shrouded by the duct
sep	separation
t	turbulent

TABLE I

EFFECT OF PROFILE THICKNESS ON
SURFACE VELOCITY DISTRIBUTION

x/c	$\dfrac{\gamma_D}{2V} = \dfrac{1}{2\pi} \cot \dfrac{\theta}{2}$ $t = 0,\ c_\ell = 1$ (Eq. (24))	$\dfrac{\gamma_D}{2V}$ NACA 0018, $c_\ell = 1$ (p. 325, Ref. 8)	$\dfrac{u_s}{V} = F(x)$ NACA 0018, $\alpha = 0$ (p. 325, Ref. 8)
0	∞	1.342	0
0.005	2.25	1.178	0.682
.025	.994	.861	1.103
.05	.695	.662	1.228
.1	.478	.479	1.276
.2	.319	.320	1.275
.4	.195	.184	1.205
.6	.130	.113	1.116
.8	.079	.063	1.025
1.0	0	0	0

TABLE II

SHAPE PARAMETERS FOR THE TWO DUCTED PROPELLERS

Parameter	4-foot model	7-foot model
D_P (in.)	48.0	84.7
$D_{H_{max}}$ (in.)	16.0	17.5
D (in.)	54.3	93.3
c (in.)	33.0	49.0
t_{max} (in.)	5.2	8.4
$(t/c)_{max}$	0.158	0.172
x_P/c	.293	.286
A_P/A	.70	.79
c/D	.608	.525
f_1	3.30	3.10
f_2	0.54	0.53
f_3	1.95	1.90
f_4	0.93	0.92
f_5	.29	.22
f_6	1.49	1.50
f_7	1.92	1.87
$f_5 f_6 + f_7$	2.35	2.20
R_O	-0.007	-0.040
R_1	- .007	- .068
R_2	- .040	- .058
R_3	.039	- .013
R_O^*	- .008	- .041
R_1^*	- .047	- .108
R_2^*	- .053	- .071
R_3^*	.040	- .012

TABLE III

MEASURED AND PREDICTED THRUST COEFFICIENTS FOR AXIAL FLOW

(a) 4-foot model.

J	$C_{T_{DP}}$ Measured	$C_{T_{P(D)}}$ Measured	$C_{T_{D(P)}}$ Measured	γ/V (Eq. (10))	$C_{T_{D(P)}}$ from measured $C_{T_{DP}}$ (Eq. (5))	γ/V (Eqs. (1),(3))	$C_{T_{D(P)}}$ from measured $C_{T_{P(D)}}$ (Eq. (5))
0.541	0.890	0.766	0.186	0.425	0.168	0.447	0.186
.471	1.53	1.15	.403	.630	.367	.623	.360
.419	2.25	1.62	.671	.820	.625	.820	.625
.342	4.15	2.74	1.39	1.22	1.38	1.22	1.38
.220	12.7	7.52	5.03	2.39	5.32	2.42	5.45
.178	19.4	10.8	7.98	3.05	8.62	3.06	8.70
0	306.0	142.0	147.0	13.3	164.0	13.3	164.0

39

TABLE III.- CONCLUDED.

(b) 7-foot model.

Elevon $\beta°$	J	$C_{T_{DP}}$ Measured	$C_{T_{D(P)}}$ Measured	γ/V (Eq. (10))	$C_{T_{D(P)}}$ from measured $C_{T_{DP}}$ (Eq. (5))
Aligned 19°	0.682	0.0826	-0.030	0.049	0.0022
	.525	.684	.099	.322	.095
	.437	1.21	.279	.500	.230
	.311	3.46	1.07	1.04	.99
	.214	8.80	3.70	1.86	3.19
Out 19°	.617	0.220	0.025	0.130	0.016
	.438	1.19	.335	.495	.225
	.219	8.46	3.47	1.82	3.05
Out 29°	.432	3.26	1.34	0.995	0.912
	.216	18.1	10.26	2.83	7.38
	.077	173.0	104.4	9.62	85.2

TABLE IV

COMPARISON OF MEASURED TOTAL NORMAL FORCE $C_{N_{DP}}$ AND
MEASURED DUCT NORMAL FORCE $C_{N_{D(P)}}$ FOR
FOR THE 4-FOOT MODEL

J	α (deg)	$C_{N_{DP}}$ Measured	$C_{N_{D(P)}}$ Measured
0.542	20	1.28	0.66
.540	40	2.29	1.20
.542	60	2.65	1.53
0.178	20	1.55	1.16
.178	40	3.39	1.83
.176	60	5.42	2.06

TABLE V

COMPUTED FOURIER COEFFICIENTS FOR THE TWO DUCTS

Parameter	4-foot model duct	7-foot model duct
B_c	-0.2305	-0.2487
B_1	.2850	.2910
B_2	- .1630	- .1625
B_3	.1068	.1065
B_4	- .0795	- .0796
B_5	.0638	.0640
$B_0{}^*$	.1427	.1509
$B_1{}^*$	- .0821	- .0774
$B_2{}^*$	.0170	.0147
$B_3{}^*$	- .0042	- .0035
$B_4{}^*$	.0016	.0014
$B_5{}^*$	- .0008	- .0007

Parameter (for $R_n{}^* = 0$)	4-foot model duct	7-foot model duct
C_0	0.4922	0.5259
C_1	.7402	.7270
C_2	- .3142	- .3154
C_3	.2107	.2107
C_4	- .1589	- .1591
C_5	.1277	.1280
c_0	.955	.995
c_1	- .280	- .247
c_2	- .027	- .020
c_3, c_4, c_5	0	0

TABLE VI

$P_{k\ell}$ COEFFICIENTS FOR 4-FOOT MODEL DUCT (EQ. (19))

k \ ℓ	0	1	2	3	4	5	6
0	0.09287	0	0.04638	0	0.00006	0	0.00000
1	.18573	0.11179	0	-0.01906	0	0.00012	0
2	.03786	0	.02539	0	-.00650	0	.00004
3	.00022	-.00635	0	.00958	0	-.03314	0
4	-.00026	0	-.00325	0	.00497	0	-.00185
5	-.00002	.00003	0	-.00198	0	.00306	0
6	.00000	0	.00001	0	-.00122	0	.00208

TABLE VII

$P_{k\ell}$ COEFFICIENTS FOR 7-FOOT MODEL DUCT (EQ. (19))

k \ ℓ	0	1	2	3	4	5	6
0	0.07745	0	0.03874	0	-0.00002	0	0.00000
1	.15490	0.09140	0	-0.01403	0	0.00008	0
2	.02791	0	.01860	0	-.00466	0	.000025
3	-.00007	-.00468	0	.00690	0	-.00226	0
4	-.00016	0	-.00234	0	.00359	0	-.00134
5	-.000005	.00002	0	-.00136	0	.00222	0
6	.00000	0	.00001	0	-.00088	0	.00151
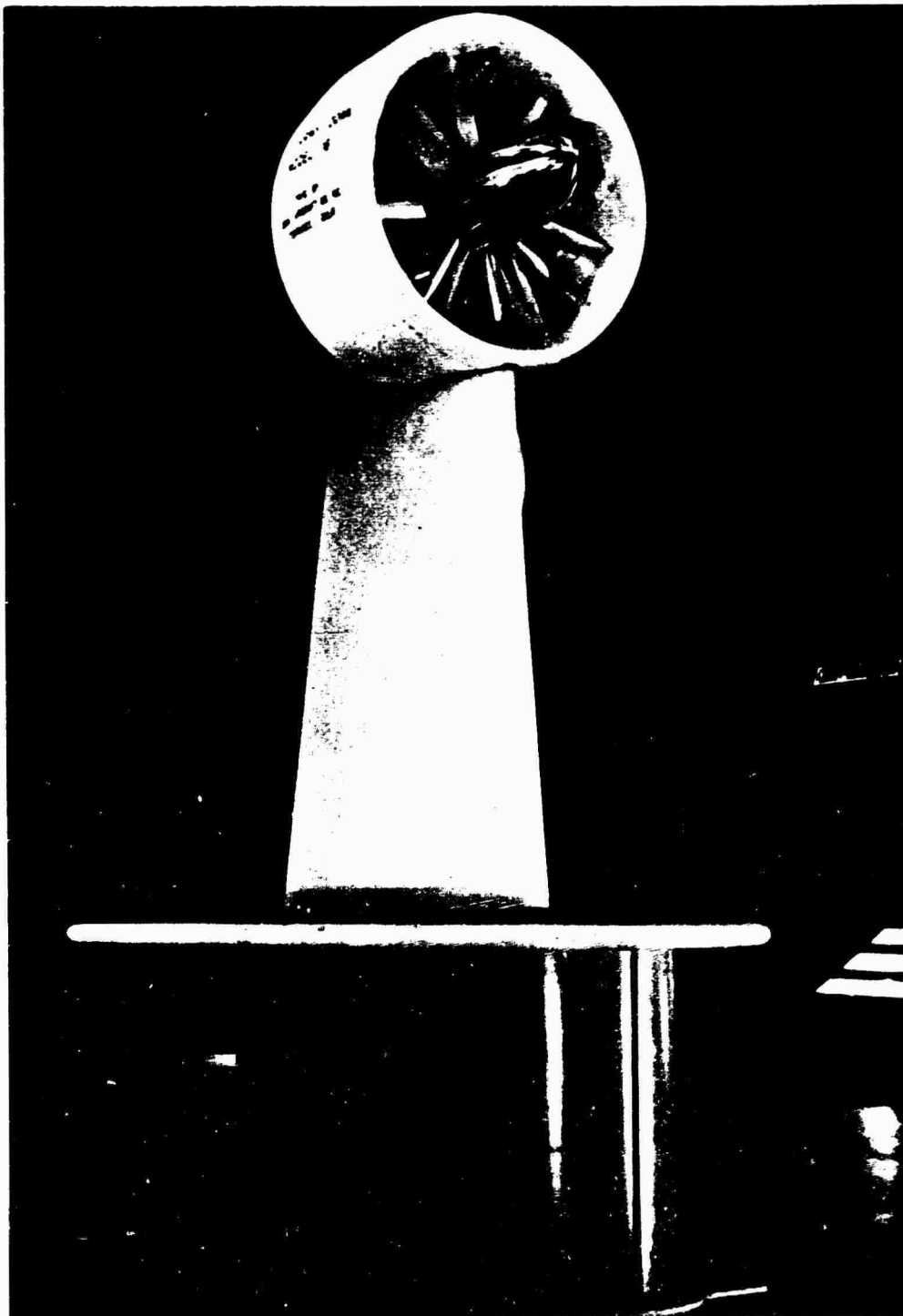
(a) 4-foot model.

Figure 1.- Ducted propellers mounted in the Ames
40- by 80-foot wind tunnel.

44
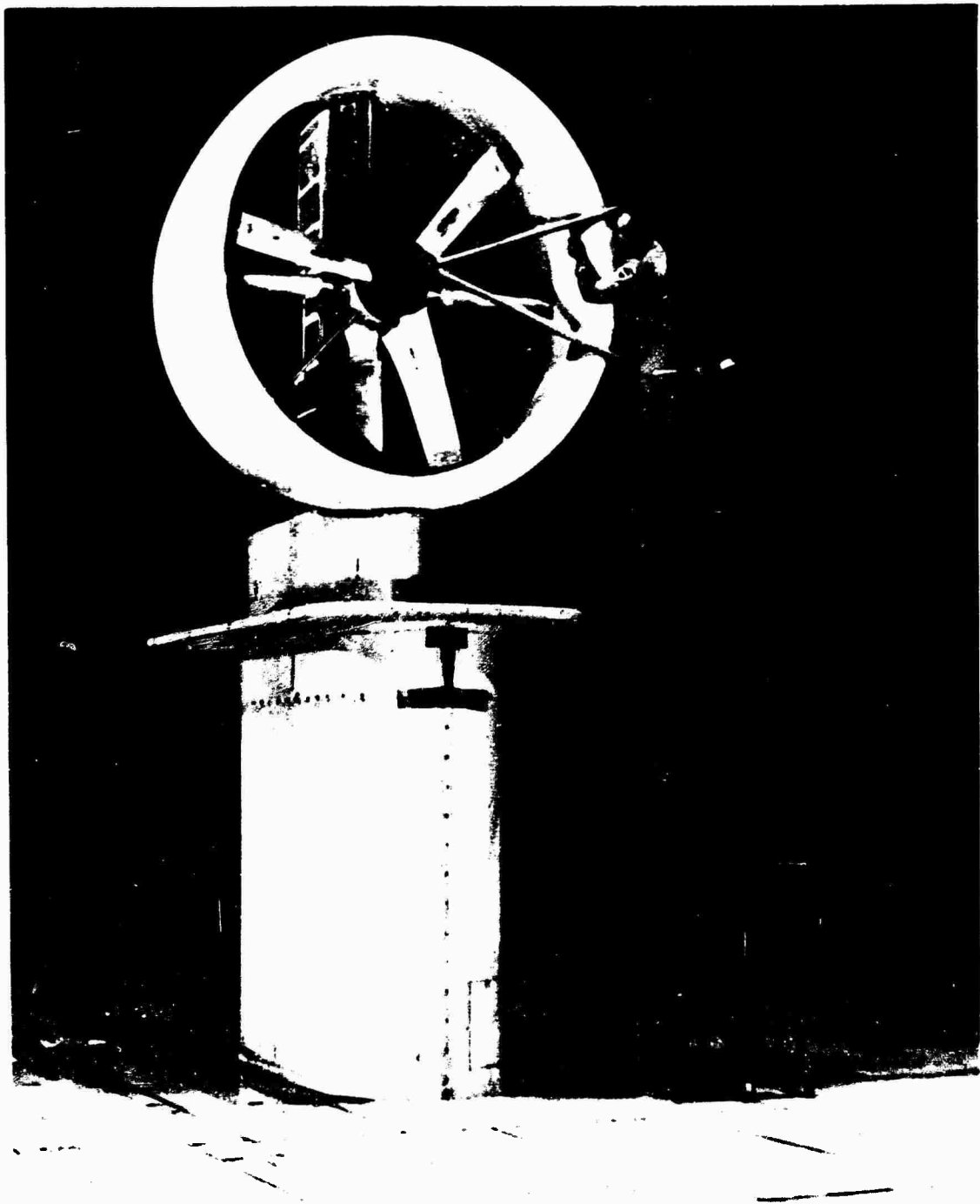
(b) 7-foot model.

Figure 1.- Concluded.

45
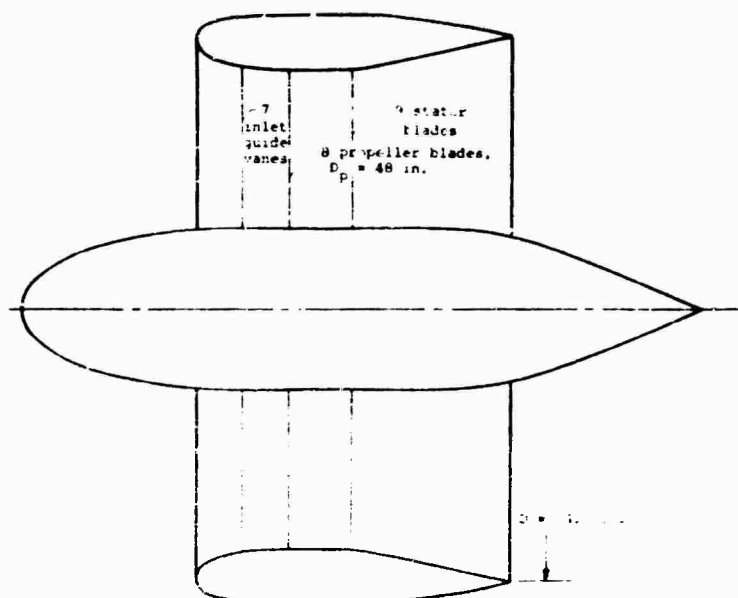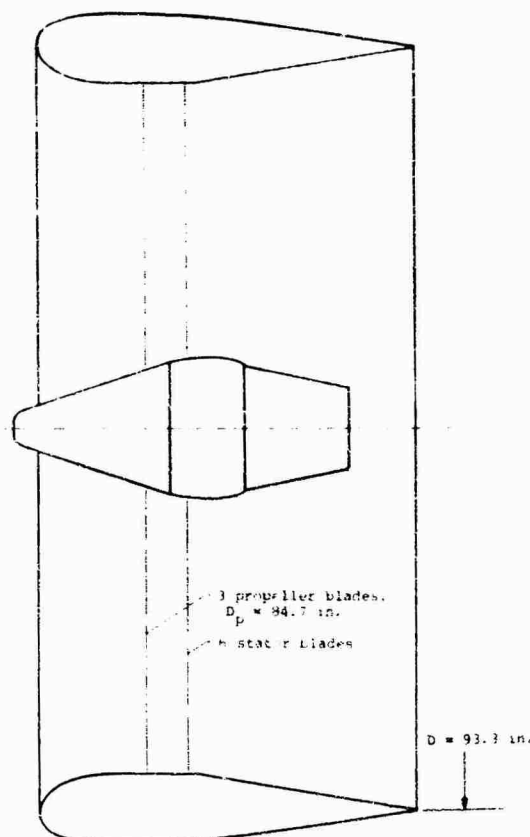
(a) 4-foot model.

(b) 7-foot model.

Figure 2.- Ducted propeller cross sections.
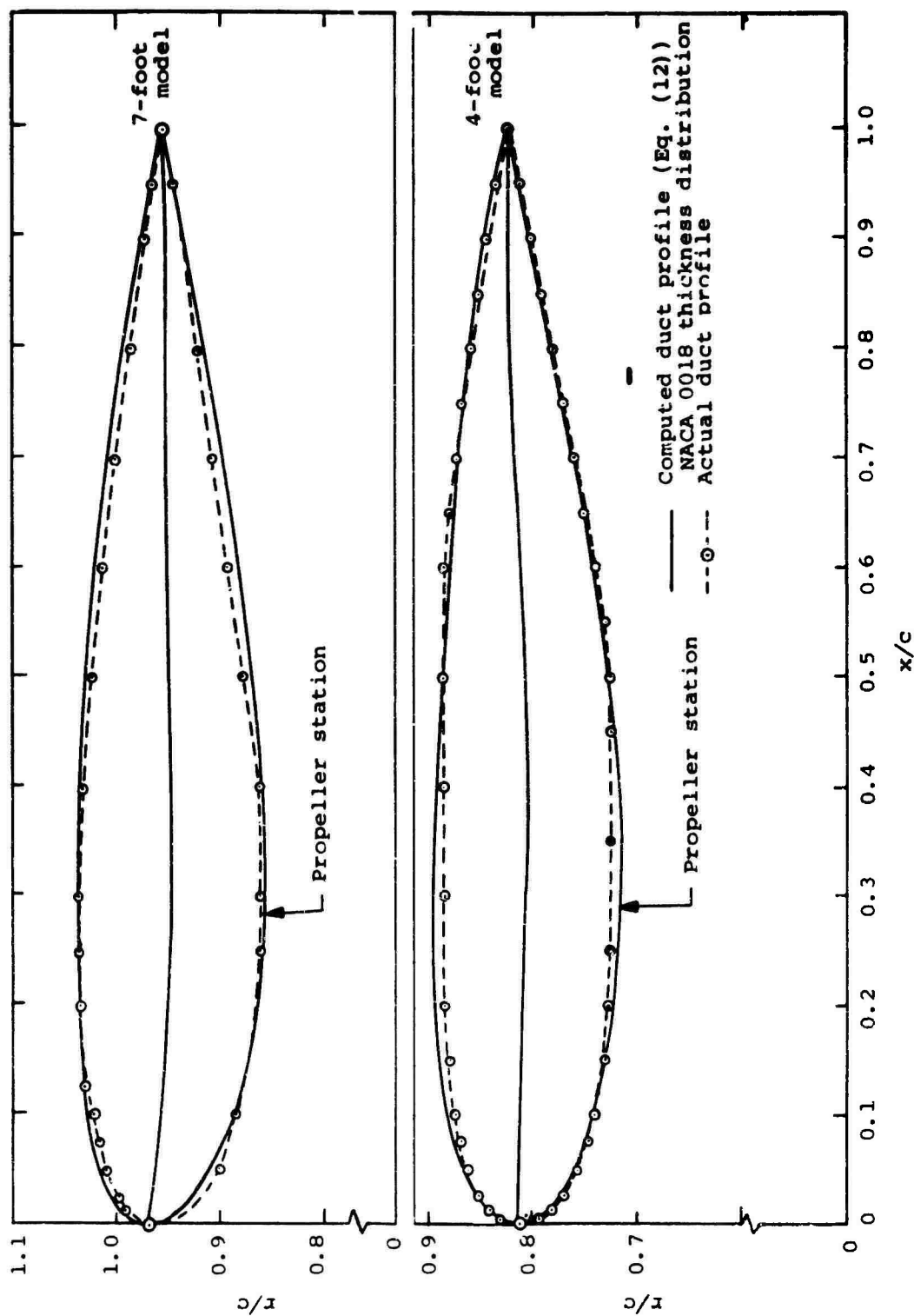
Figure 3.- Comparison of actual and computed duct profiles.

47
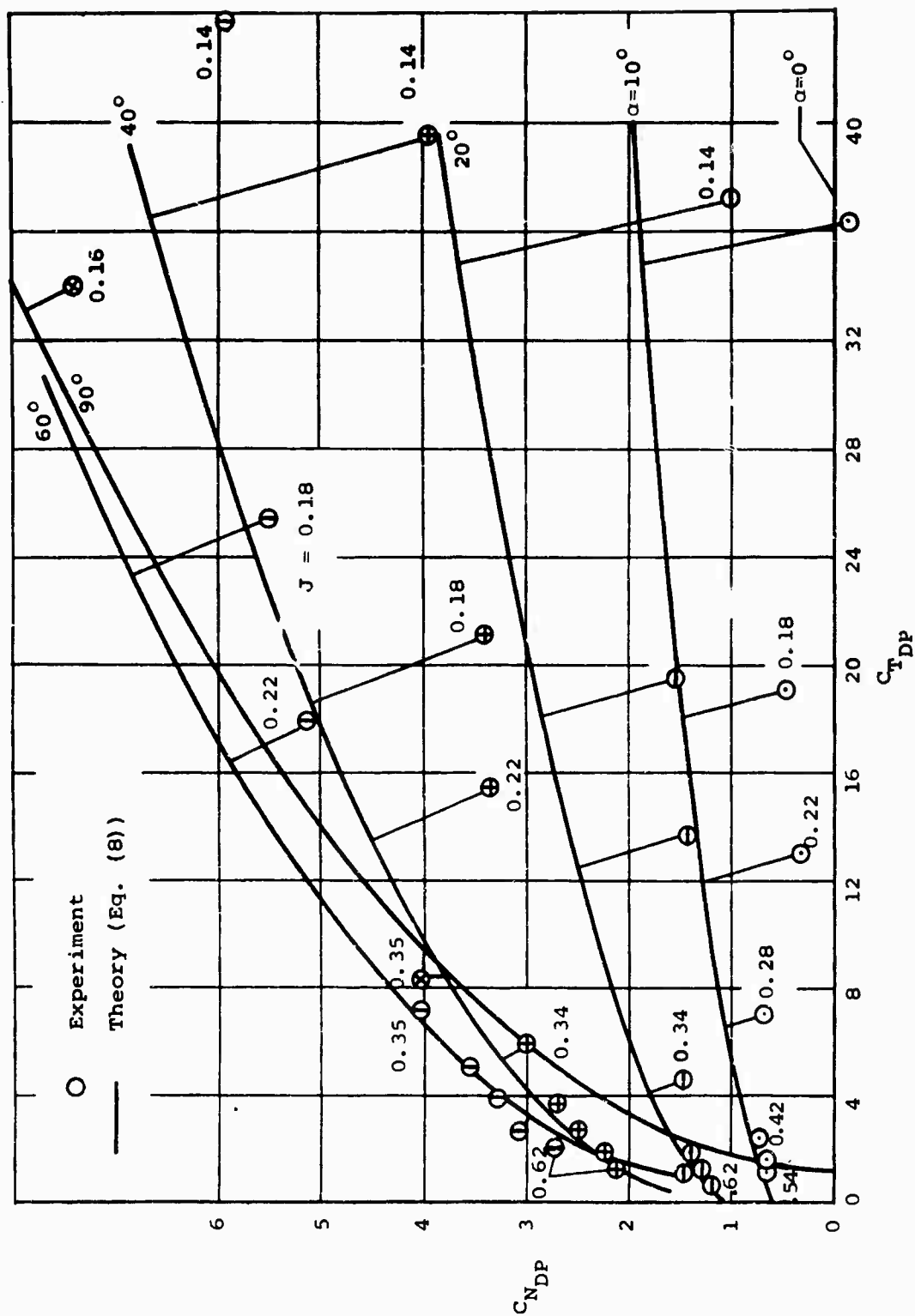
Figure 4.- Normal force versus thrust for the 4-foot model at $\alpha \gtrless 0$.

48
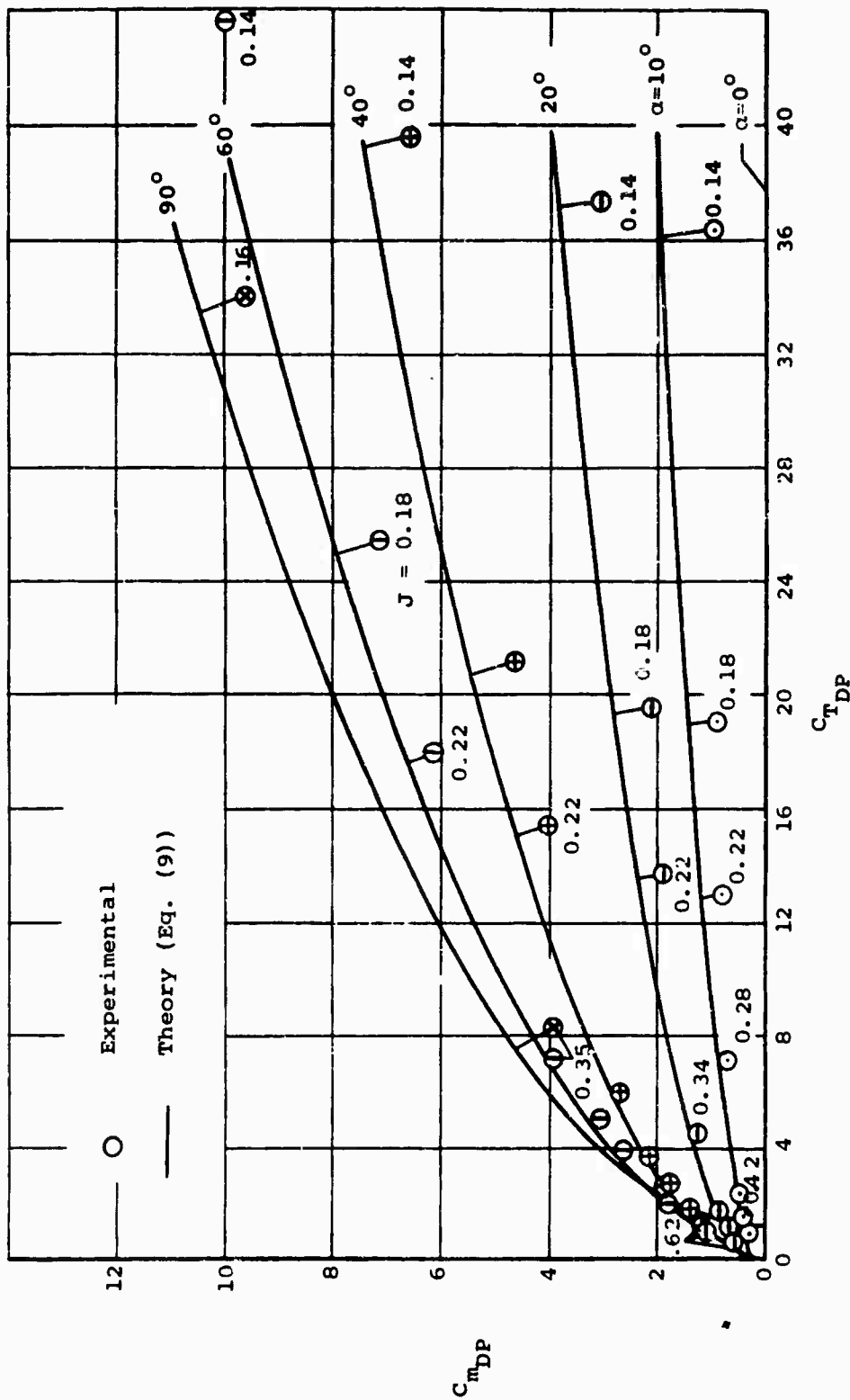
Figure 5.- Pitching moment versus thrust for the 4-foot model at $\alpha > 0$.
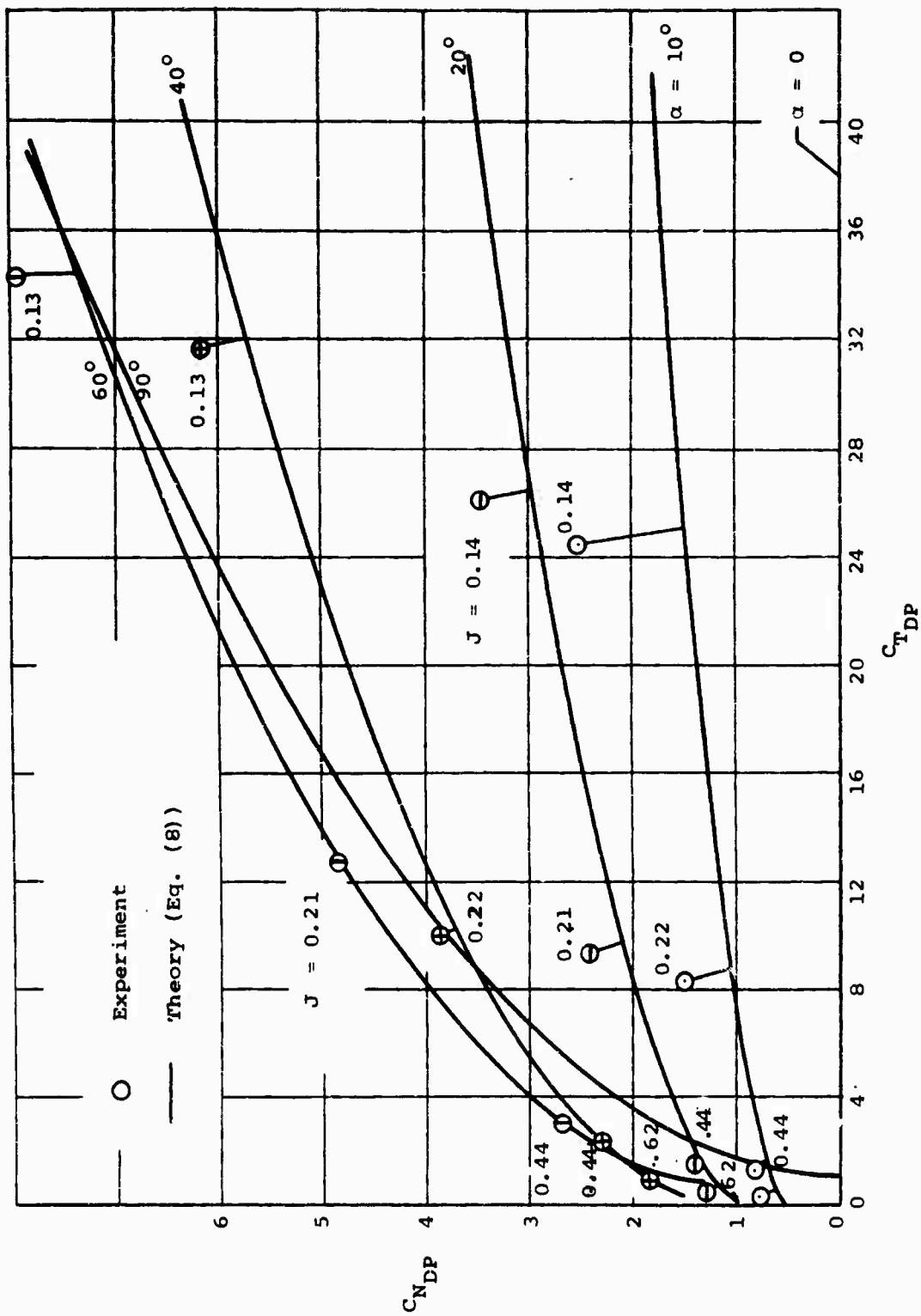
(a) Elevon off.

Figure 6.- Normal force versus thrust for the 7-foot model at $\alpha = 0$ with $\beta = 19°$.

50
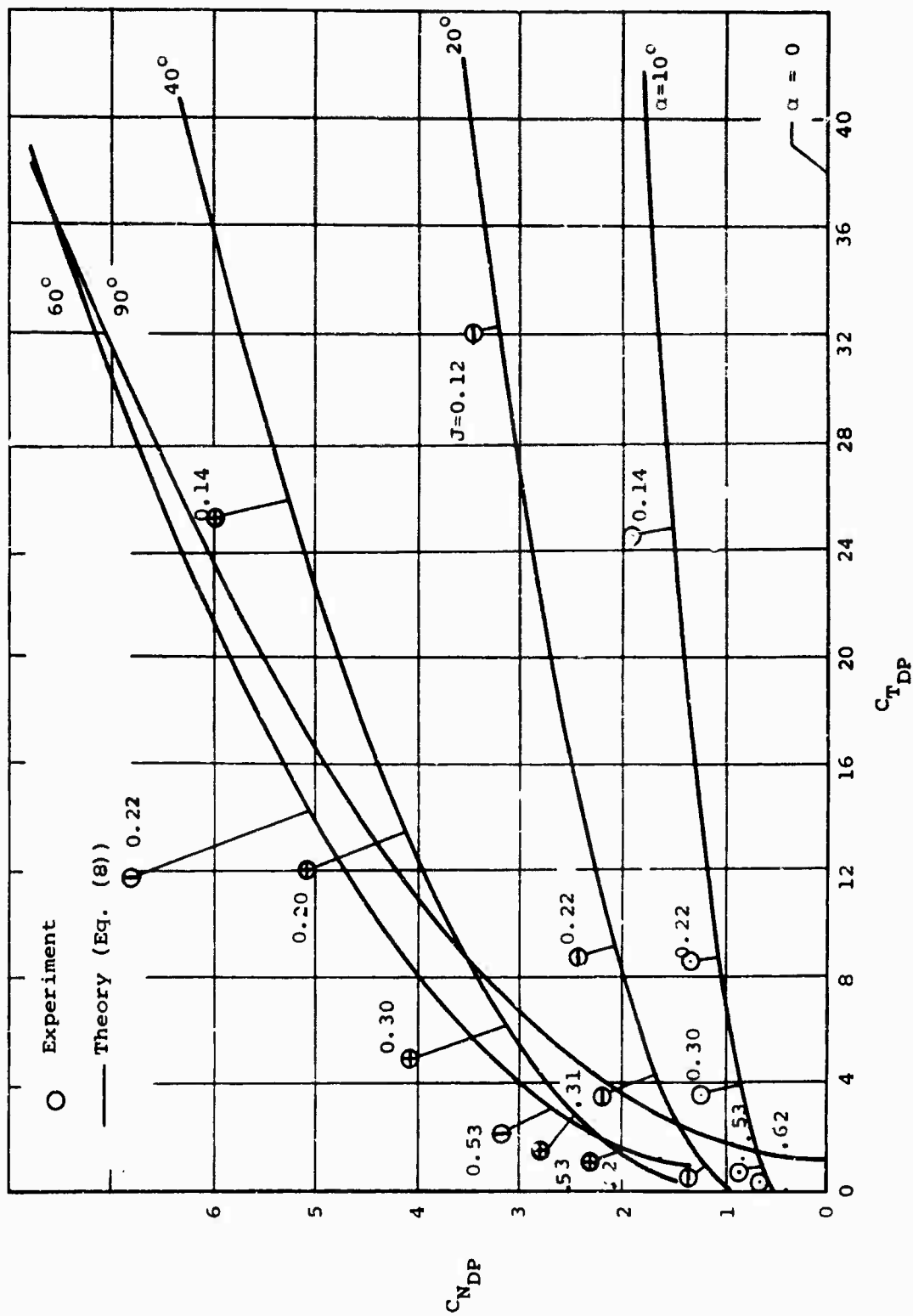
(b) $\eta_e = 0$

Figure 6.- Concluded.

51
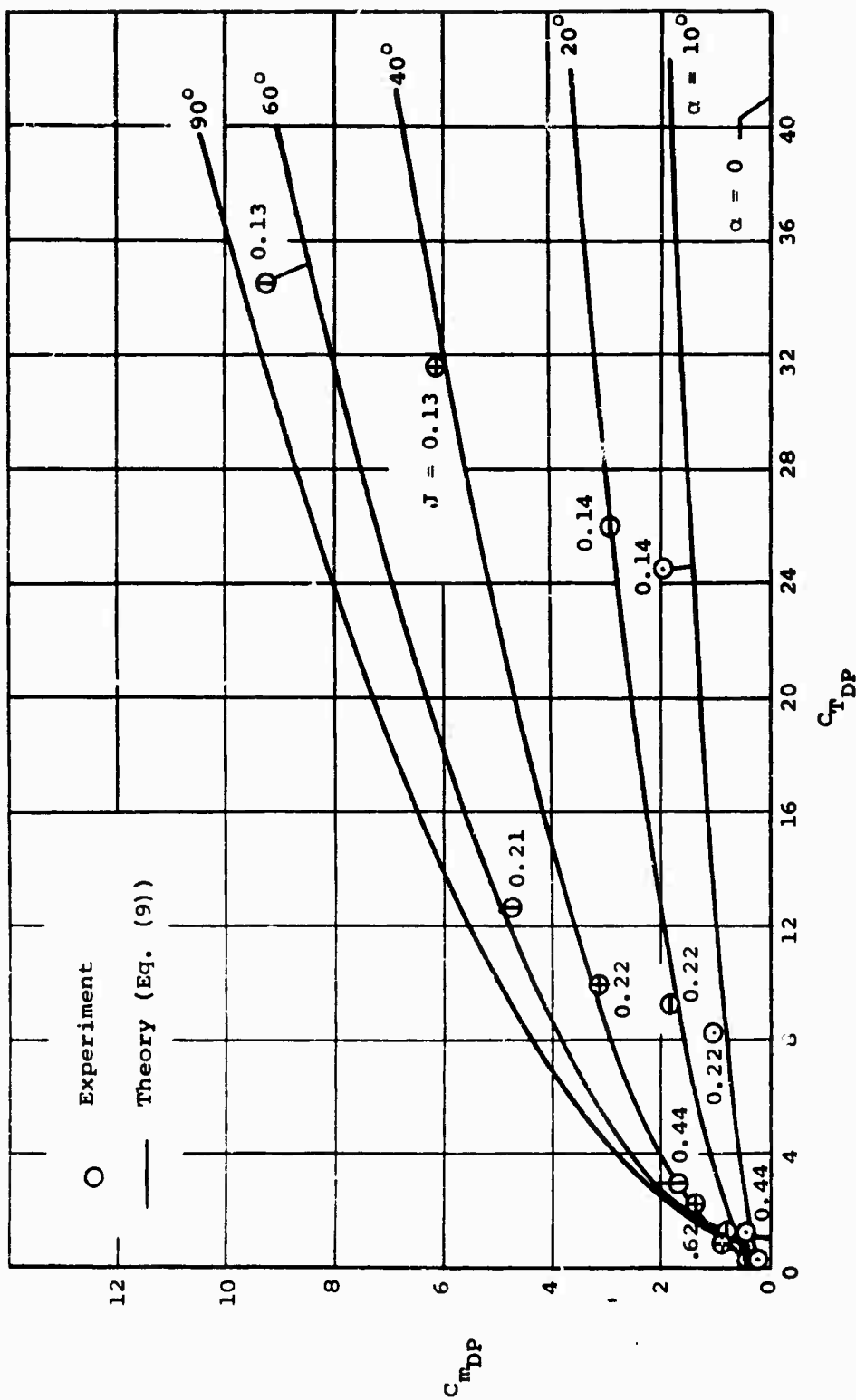
Figure 7.- Pitching moment versus thrust for the 7-foot model at $\alpha = 0$ with $\beta = 19°$.
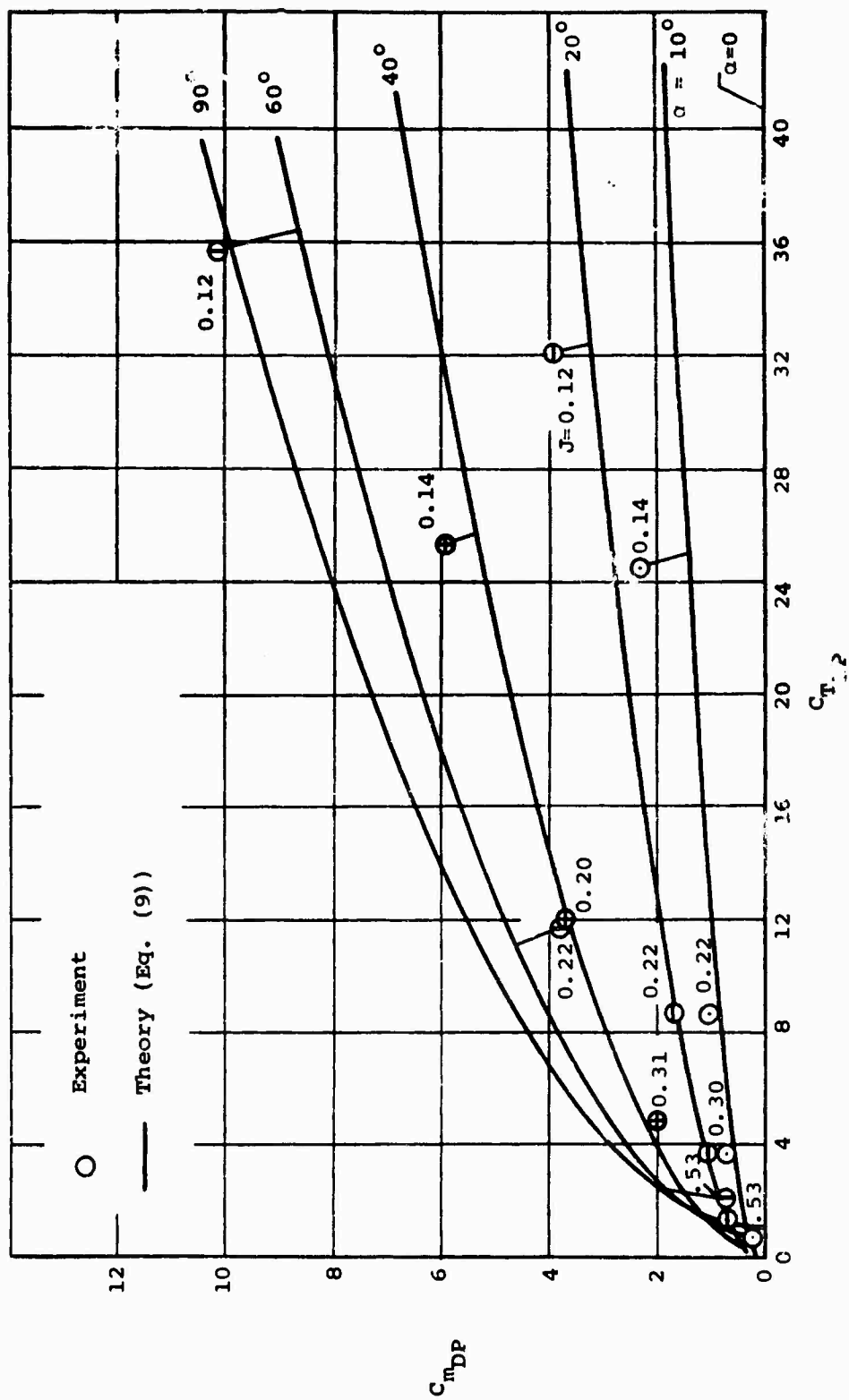
(a) Elevon off.

(b) $\varepsilon_e = 0$

Figure 7.- Concluded.

53
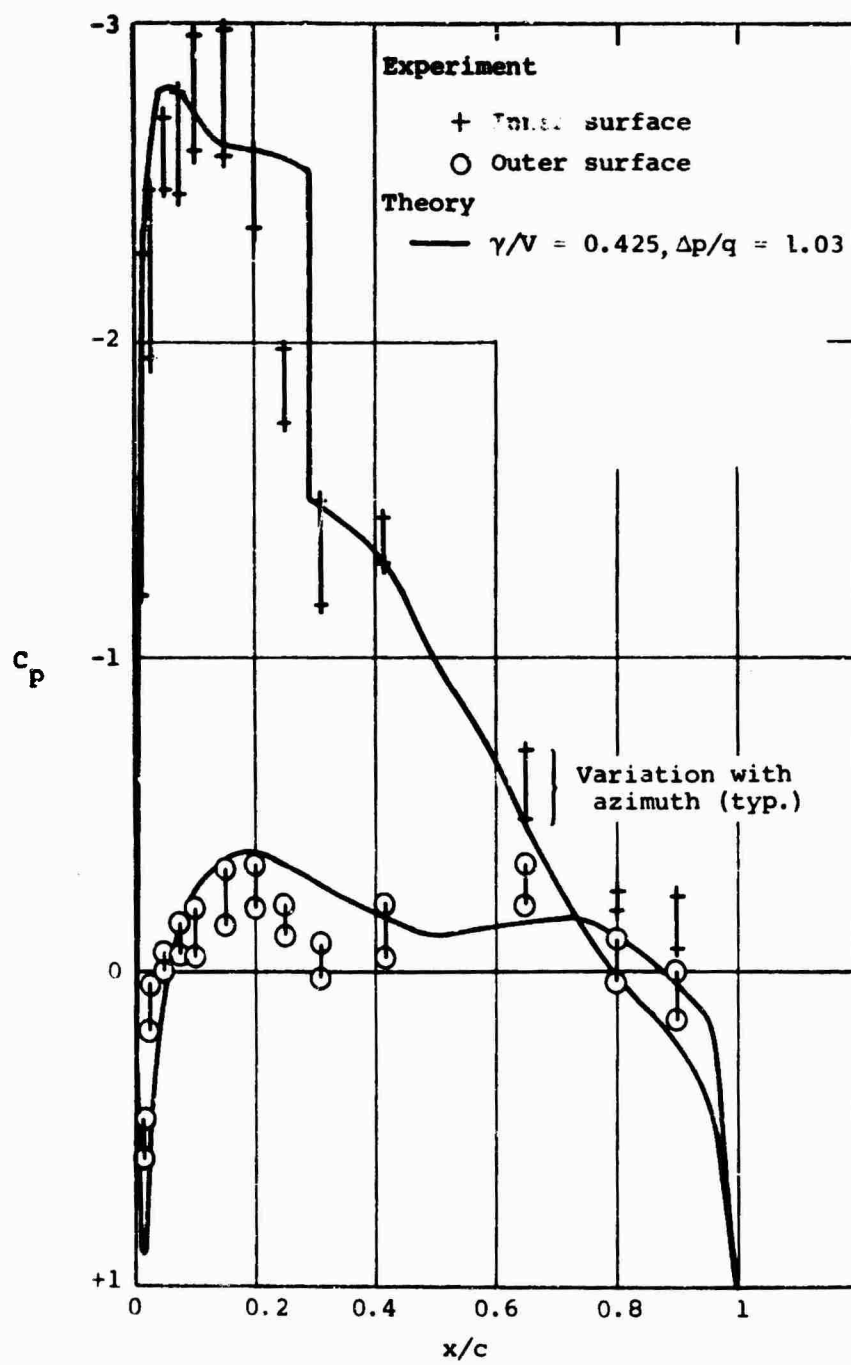
(a) $J = 0.541$, $C_{T_{DP}} = 0.890$

Figure 8.- Pressure distributions for the 4-foot model duct at $\alpha = 0$.
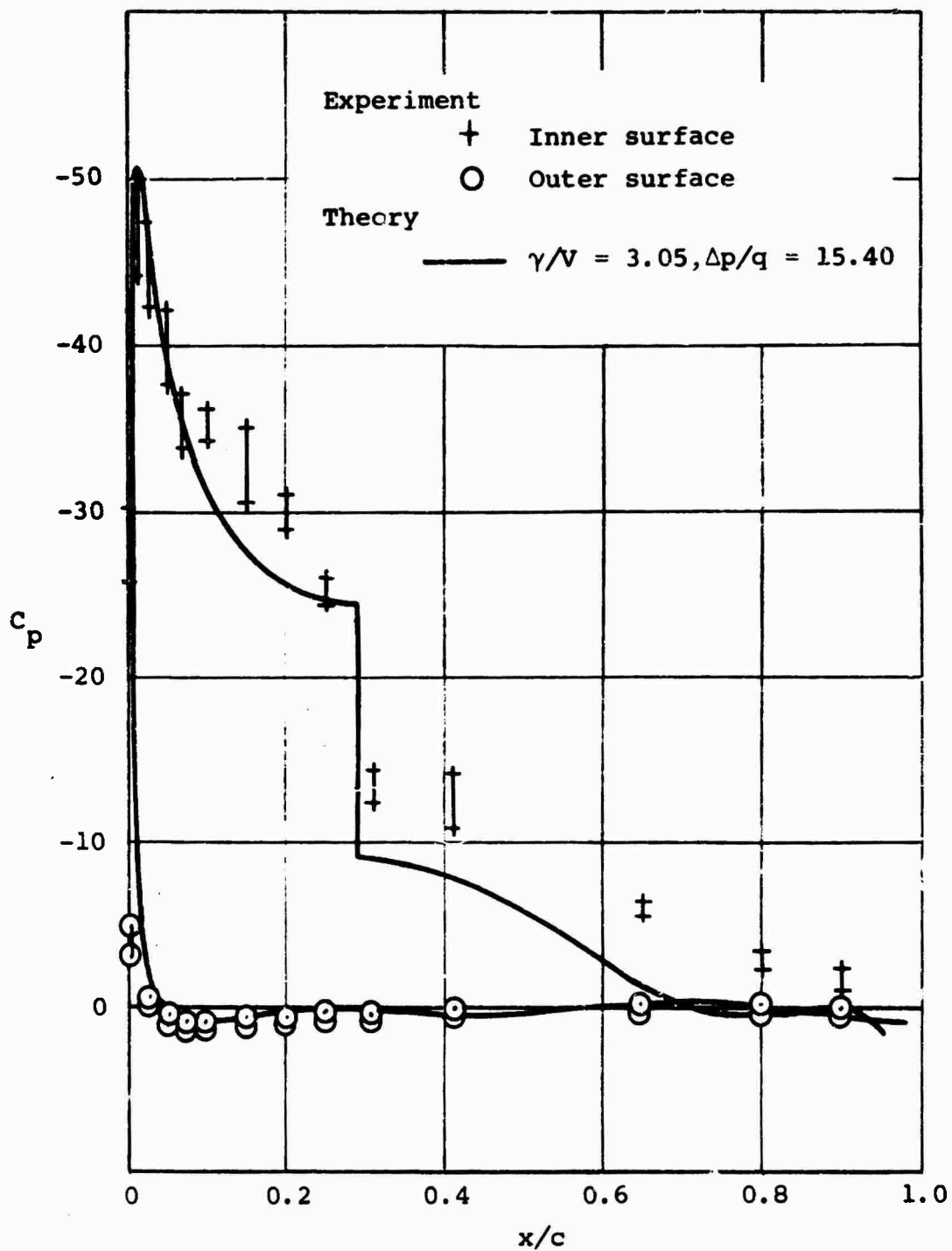
(b) $J = 0.178$, $C_{T_{DP}} = 19.4$

Figure 8.- Continued.
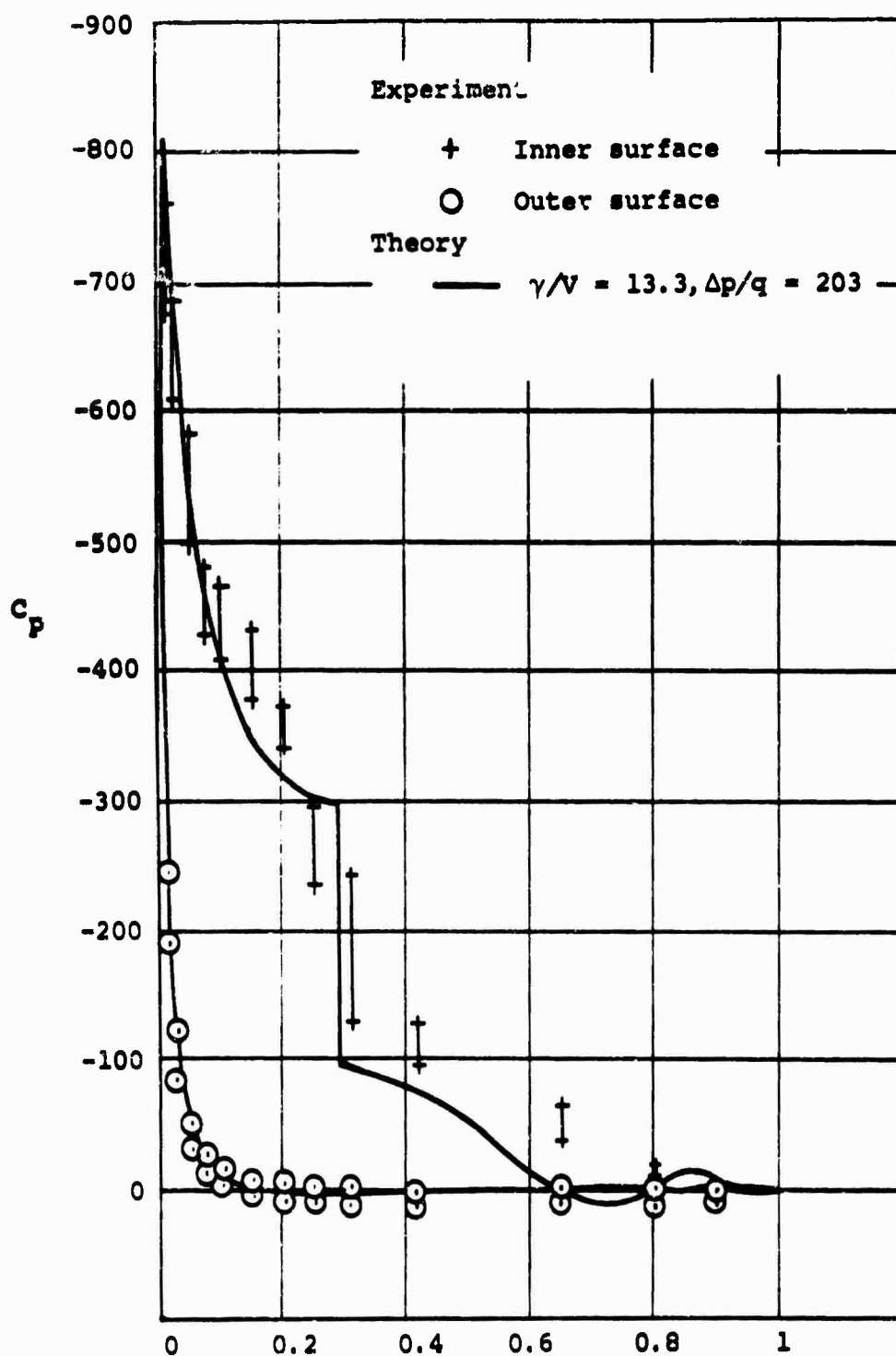
(c) $J \approx 0$, $C_{T_{DP}} = 306$

Figure 8.- Concluded.

56
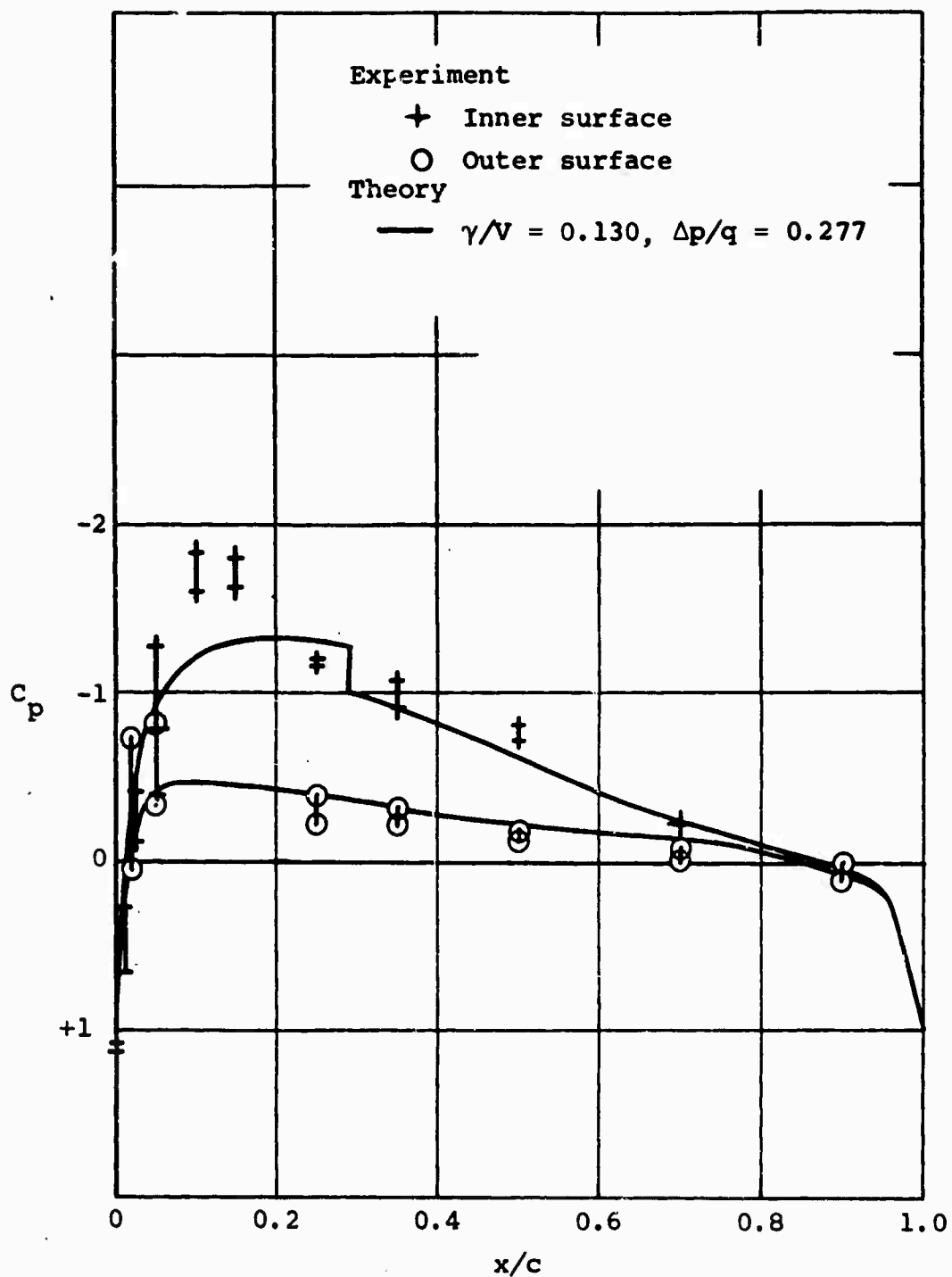
(a) $J = 0.617$, $C_{T_{DP}} = 0.220$, $\beta = 19^o$, elevon off.

Figure 9.- Pressure distributions for the 7-foot model duct
$\alpha = 0$.

57
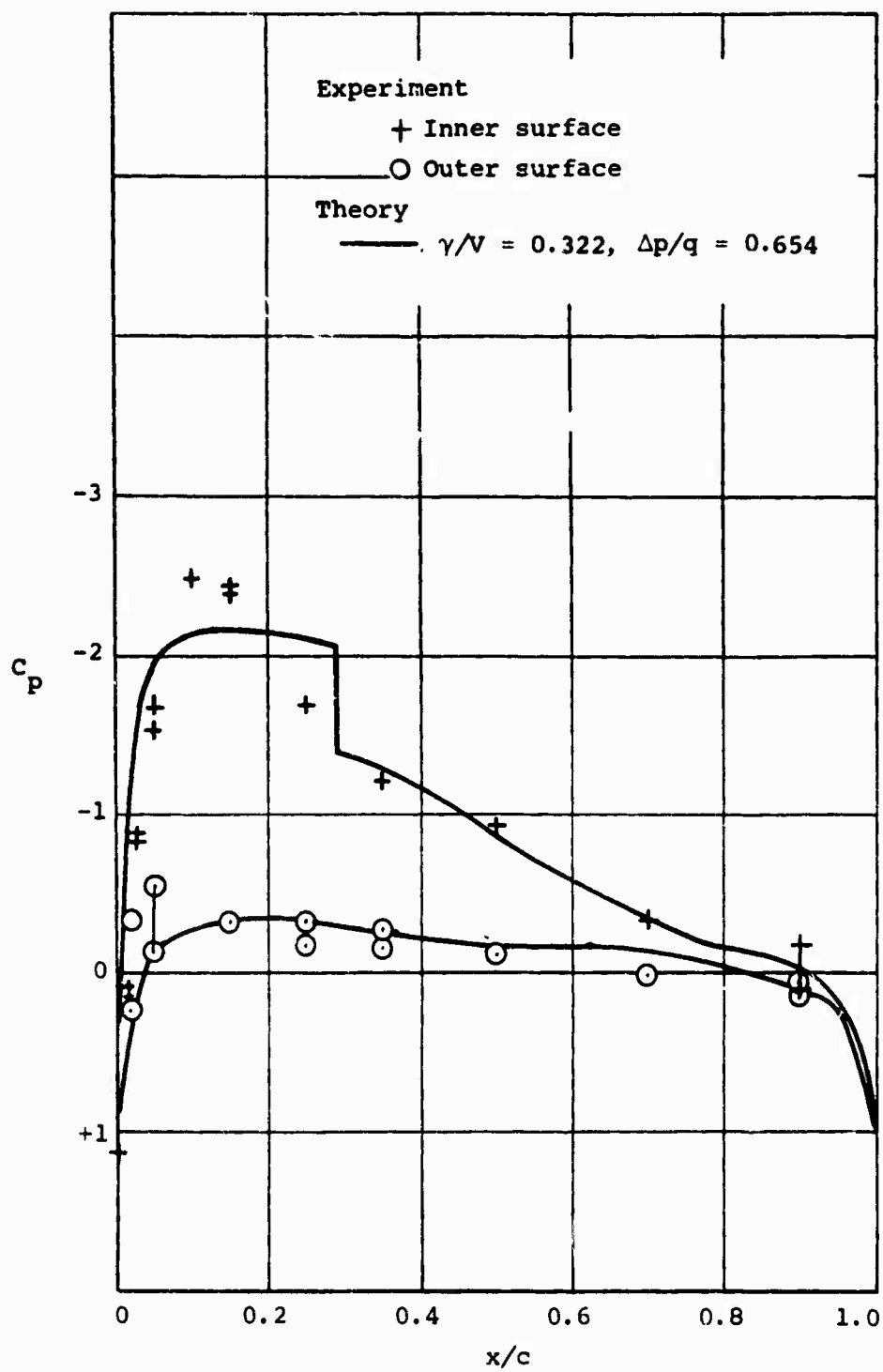
(b) $J = 0.525$, $C_{T_{DP}} = 0.684$, $\beta = 19°$, $\delta_e = 0$.

Figure 9.- Continued.

58
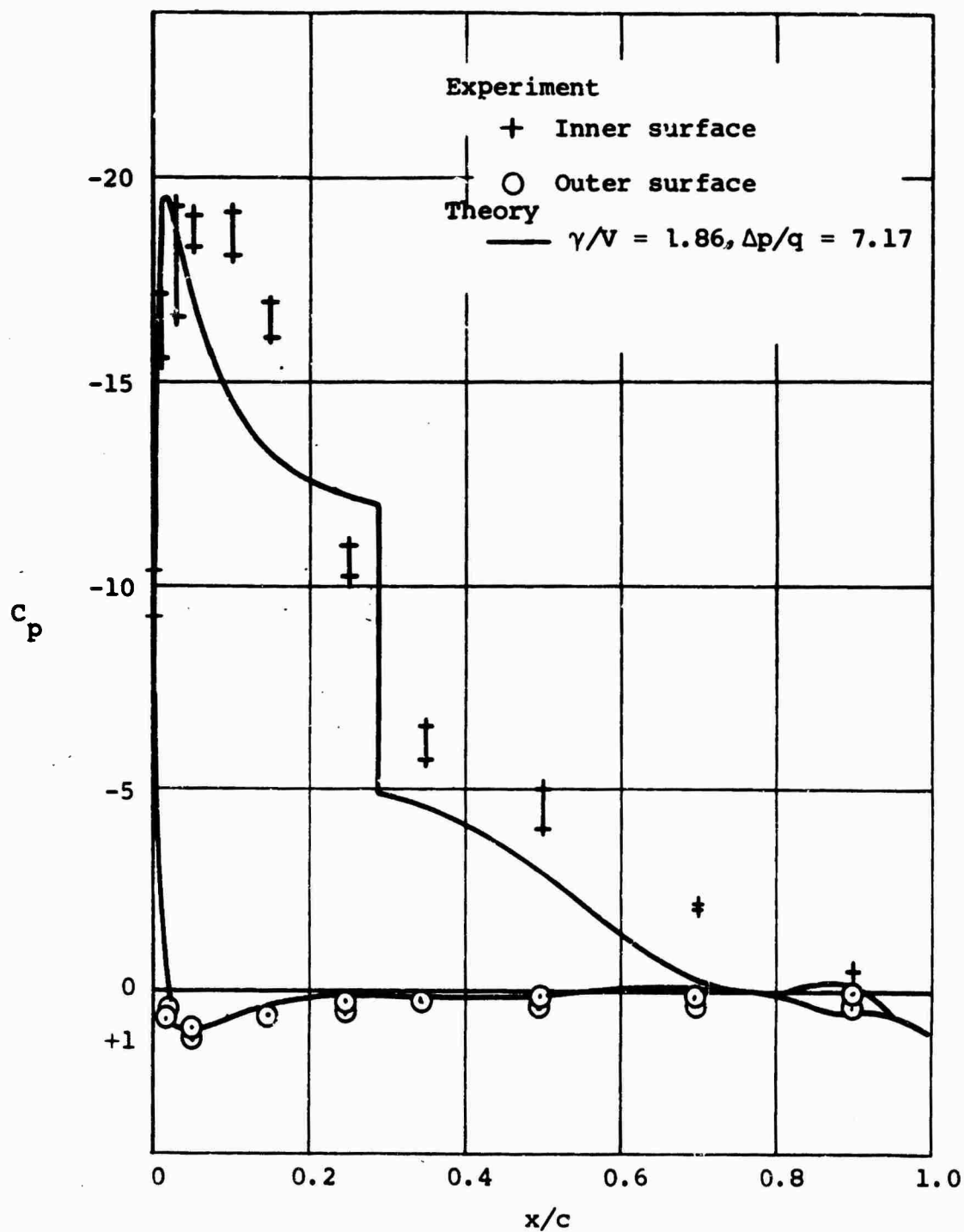
(c) $J = 0.214$, $C_{T_{DP}} = 8.80$, $\beta = 19^\circ$, $\delta_e = 0$.

Figure 9.- Continued.

59

(d) $J = 0.077$, $C_{T_{DP}} = 173$, $\beta = 29^{\circ}$, $\delta_e = 0$.
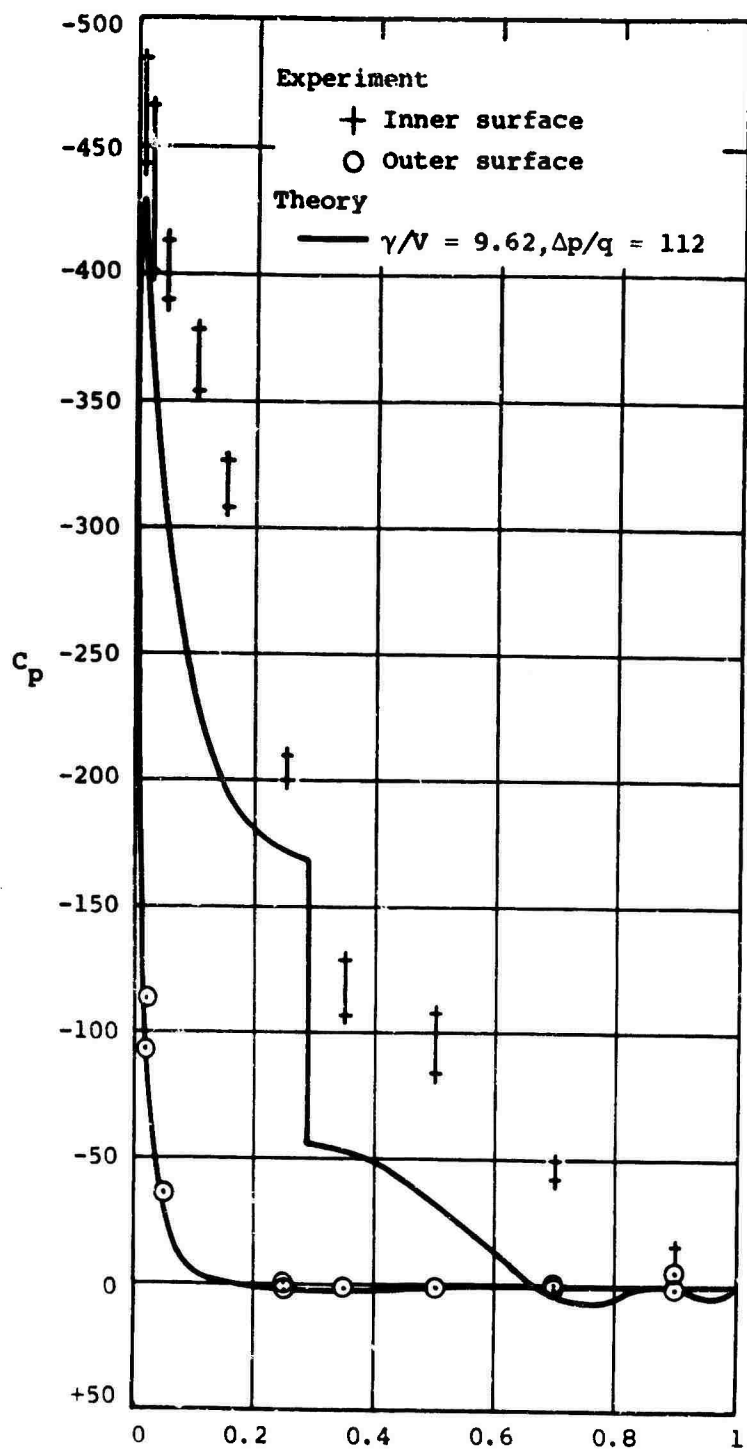
Figure 9.- Concluded.

60
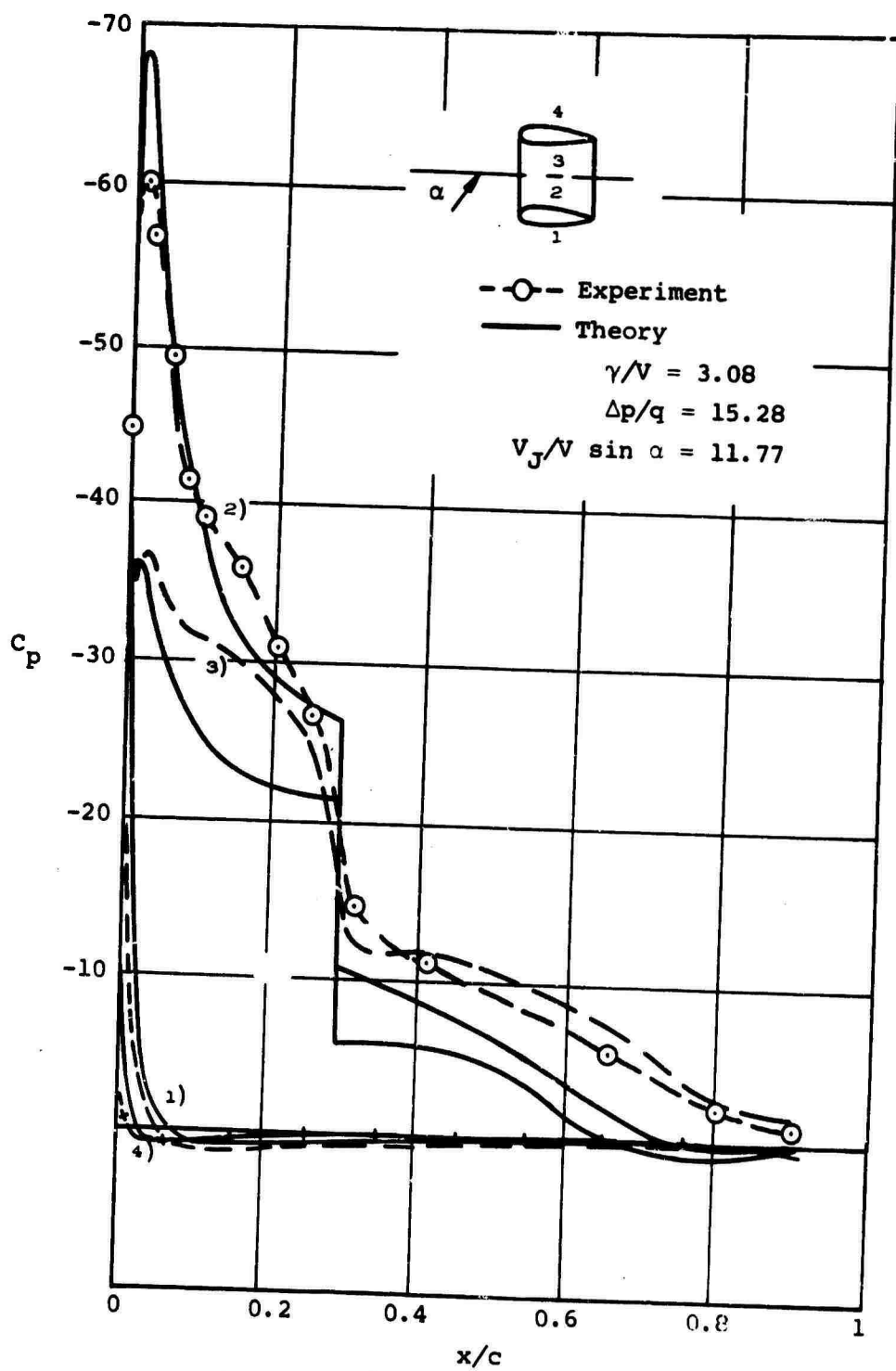
(a) $\alpha = 20^{\circ}$, $J = 0.178$, $C_{T_{DP}} = 19.5$.

Figure 10.- Pressure distributions for the 4-foot model duct at $\alpha > 0$, $J \approx 0.17$.
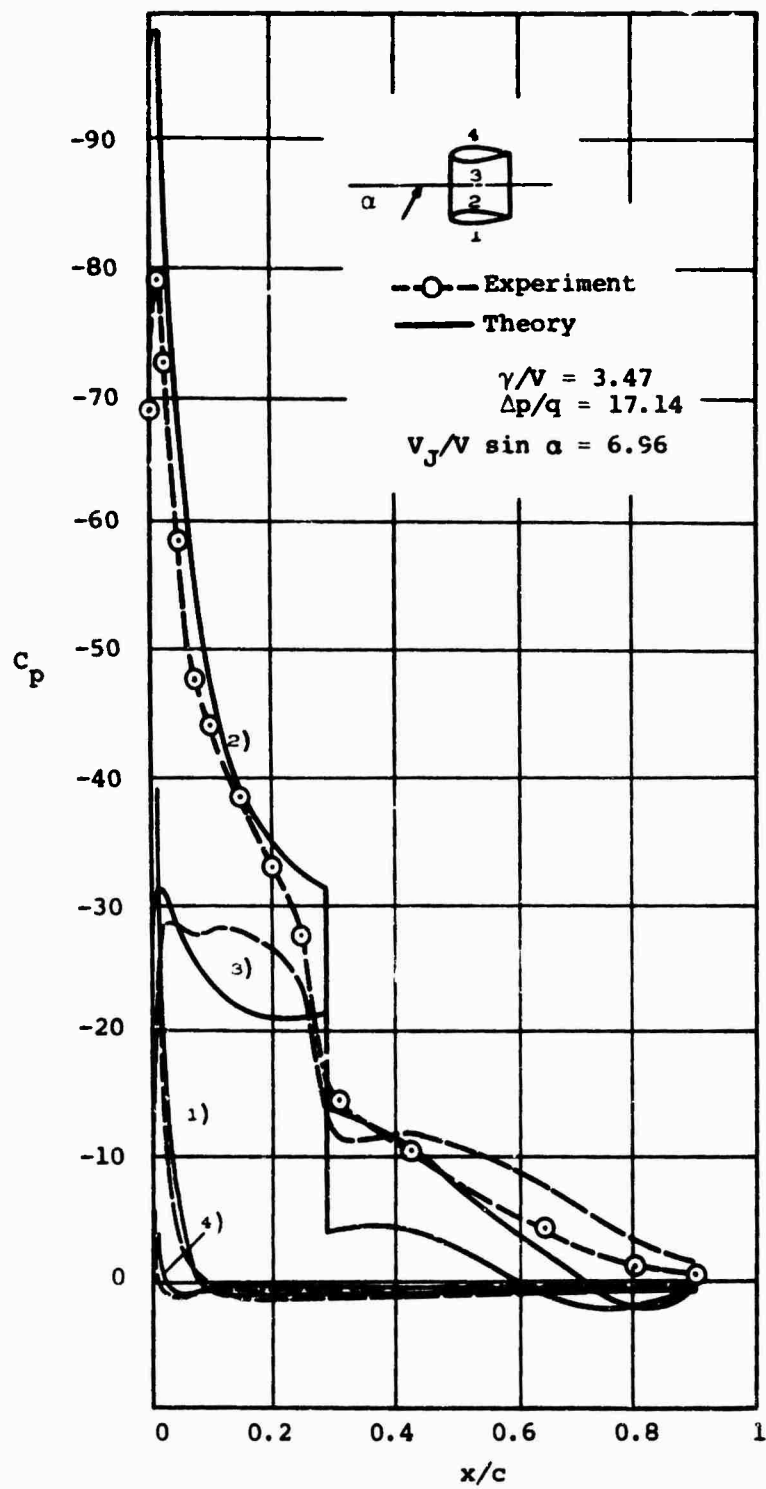
(b) $\alpha = 40^{\circ}$, $J = 0.178$, $C_{T_{DP}} = 21.2$.

Figure 10.- Continued.

(c) $\alpha = 60^o$, $J = 0.176$, $C_{T_{DP}} = 25.5$.
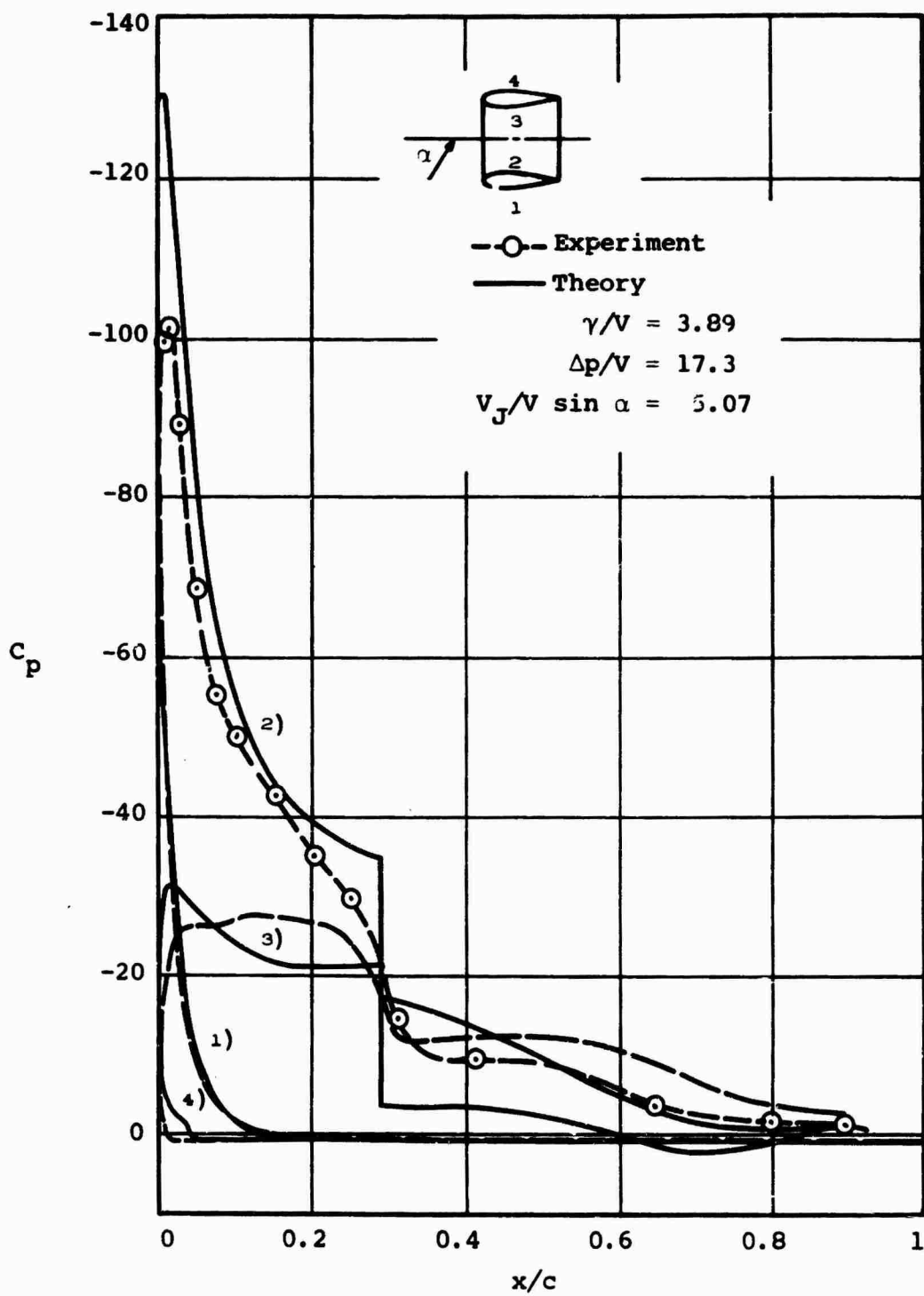
Figure 10.- Continued.
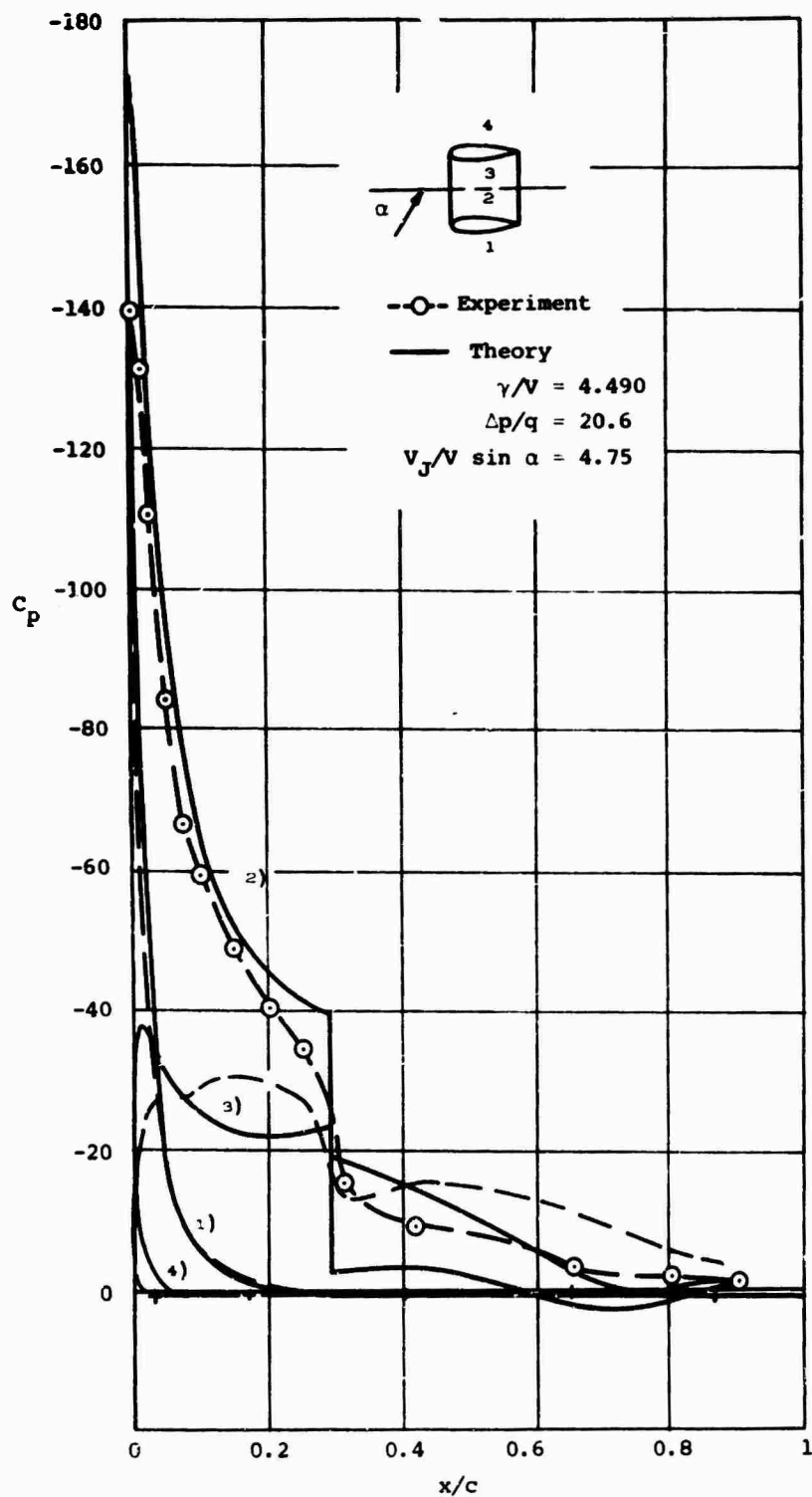
(d) $\alpha = 80^\circ$, $J = 0.166$, $C_{T_{DP}} = 34.1$.

Figure 10.- Concluded.
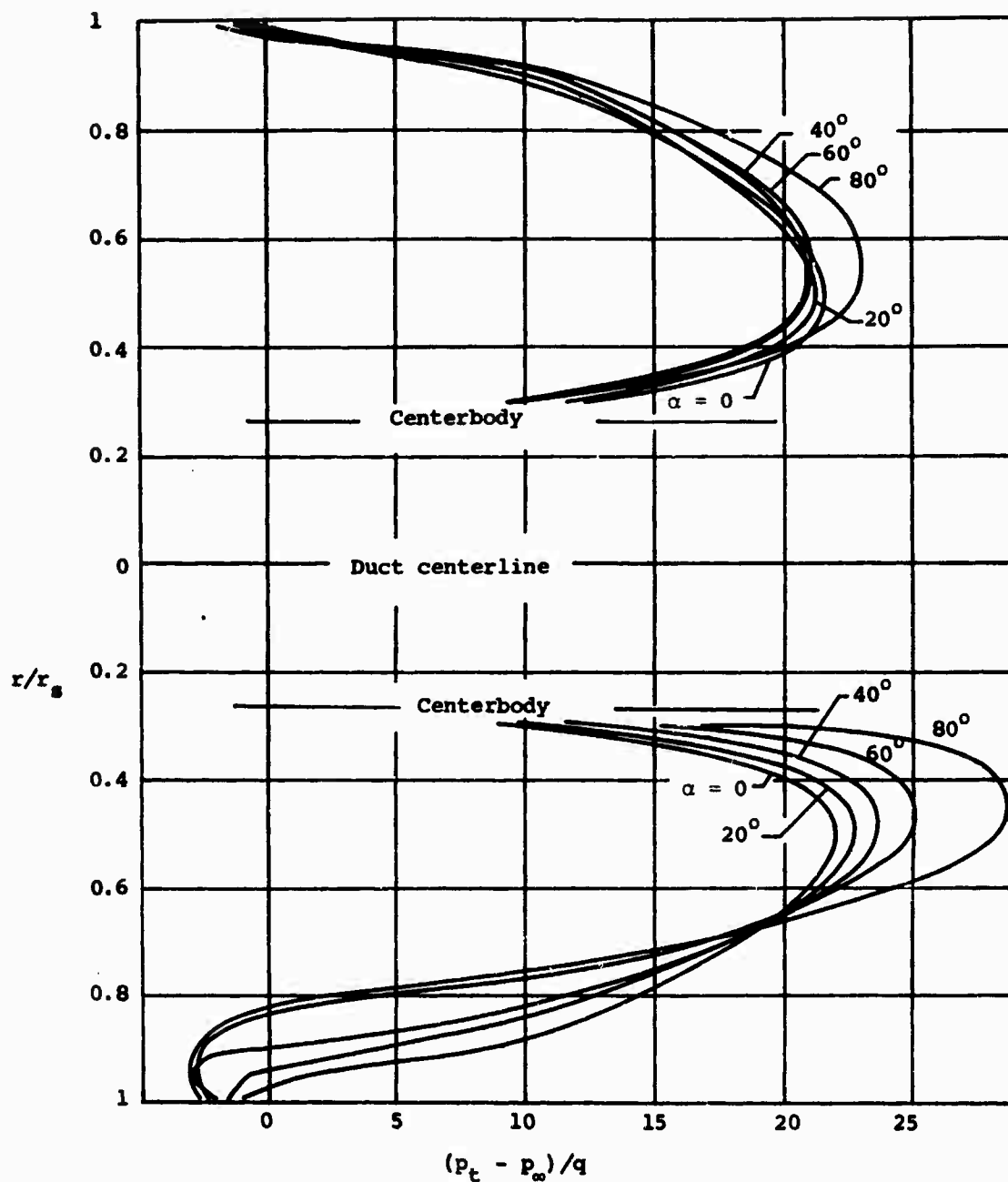
Figure 11.- Total pressure distributions measured across the exit plane of the 4-foot model duct at $\alpha \geq 0$ with $J \approx 0.17$.
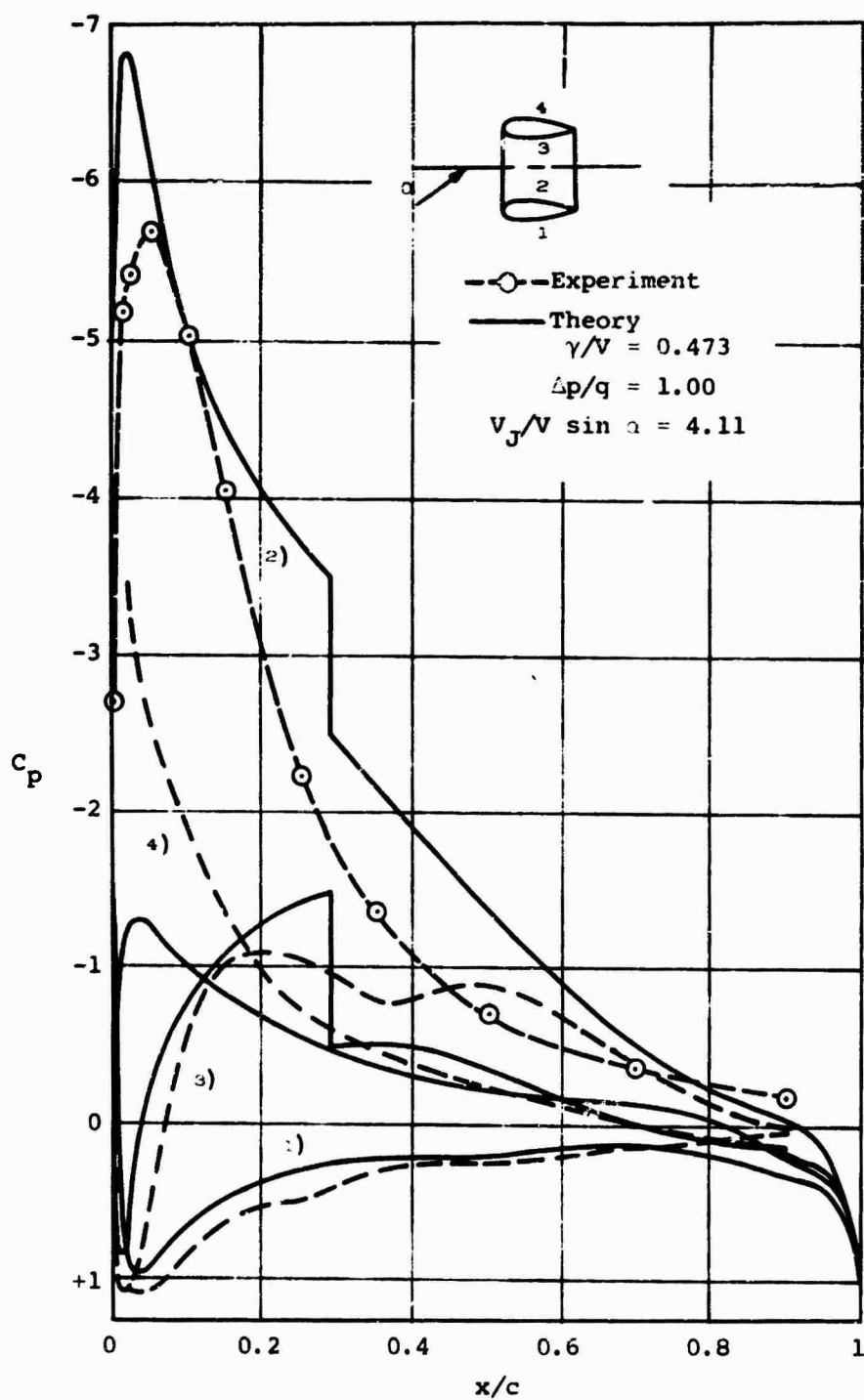
(a) $\alpha = 20°$, $J = 0.521$, $C_{T_{DP}} = 1.24$.

Figure 12.- Pressure distributions for the 7-foot model duct
at $\alpha > 0$ with $\beta = 19°$, $\delta_e = 0$, $J \simeq 0.52$.
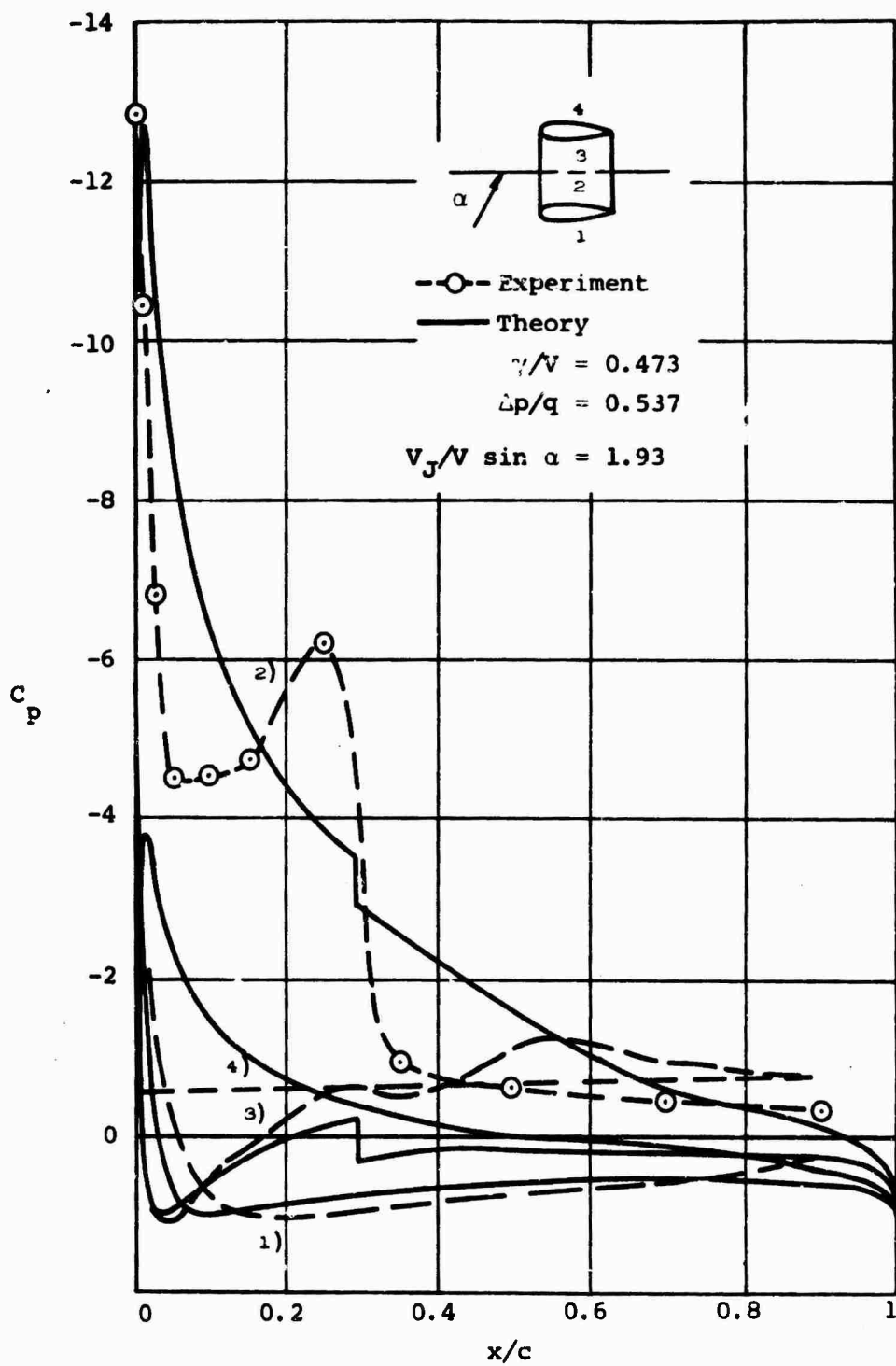
(b) $\alpha = 40^{\circ}$, $J = 0.529$, $C_{T_{DF}} = 1.53$.

Figure 12.- Concluded.
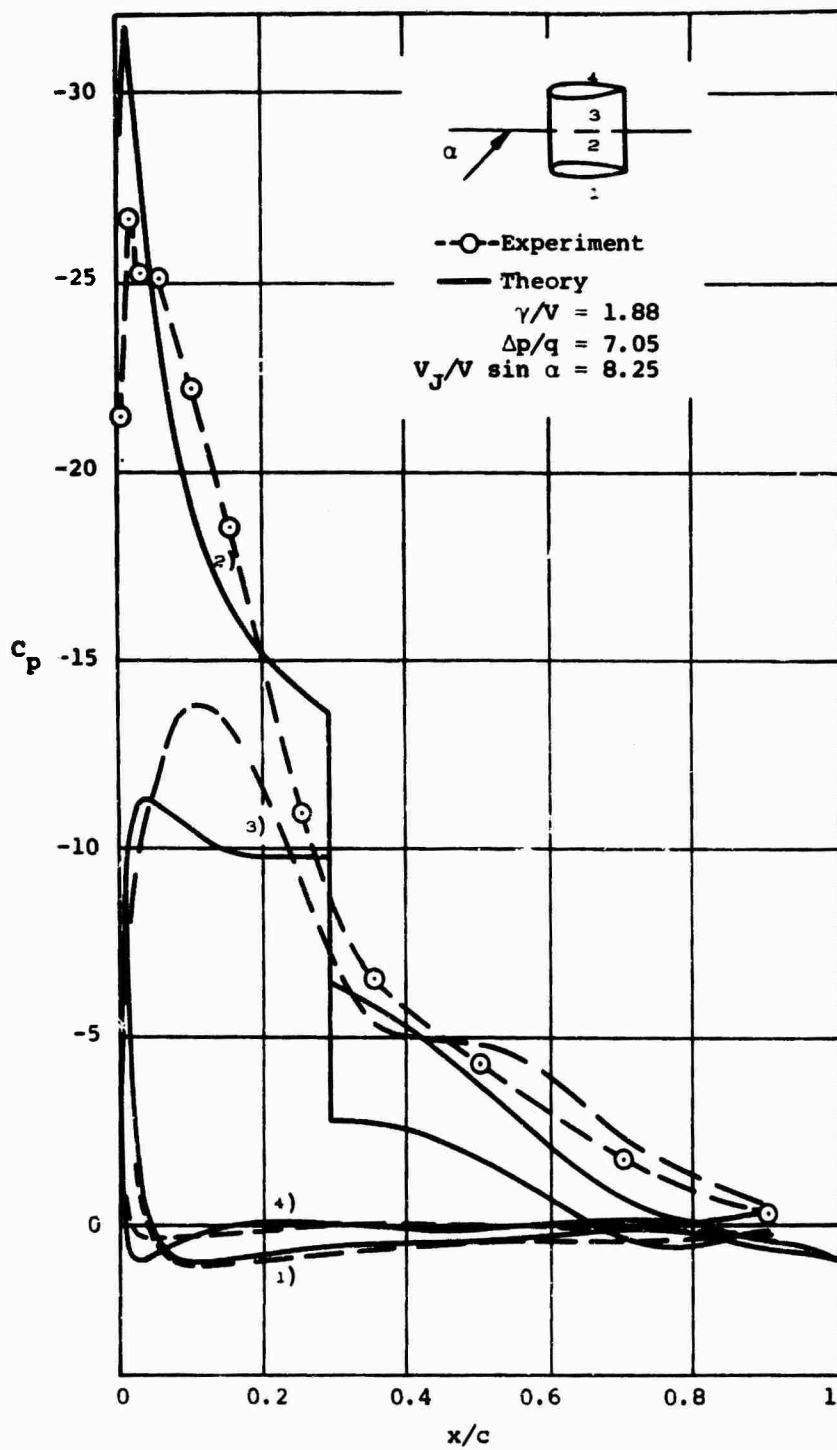
(a) $\alpha = 20^\circ$, $J = 0.213$, $C_{T_{DP}} = 12.0$.

Figure 13.- Pressure distributions for the 7-foot model duct
at $\alpha = 0$ with $\beta = 19^\circ$, $\delta_e = 0$, $J \approx 0.52$.
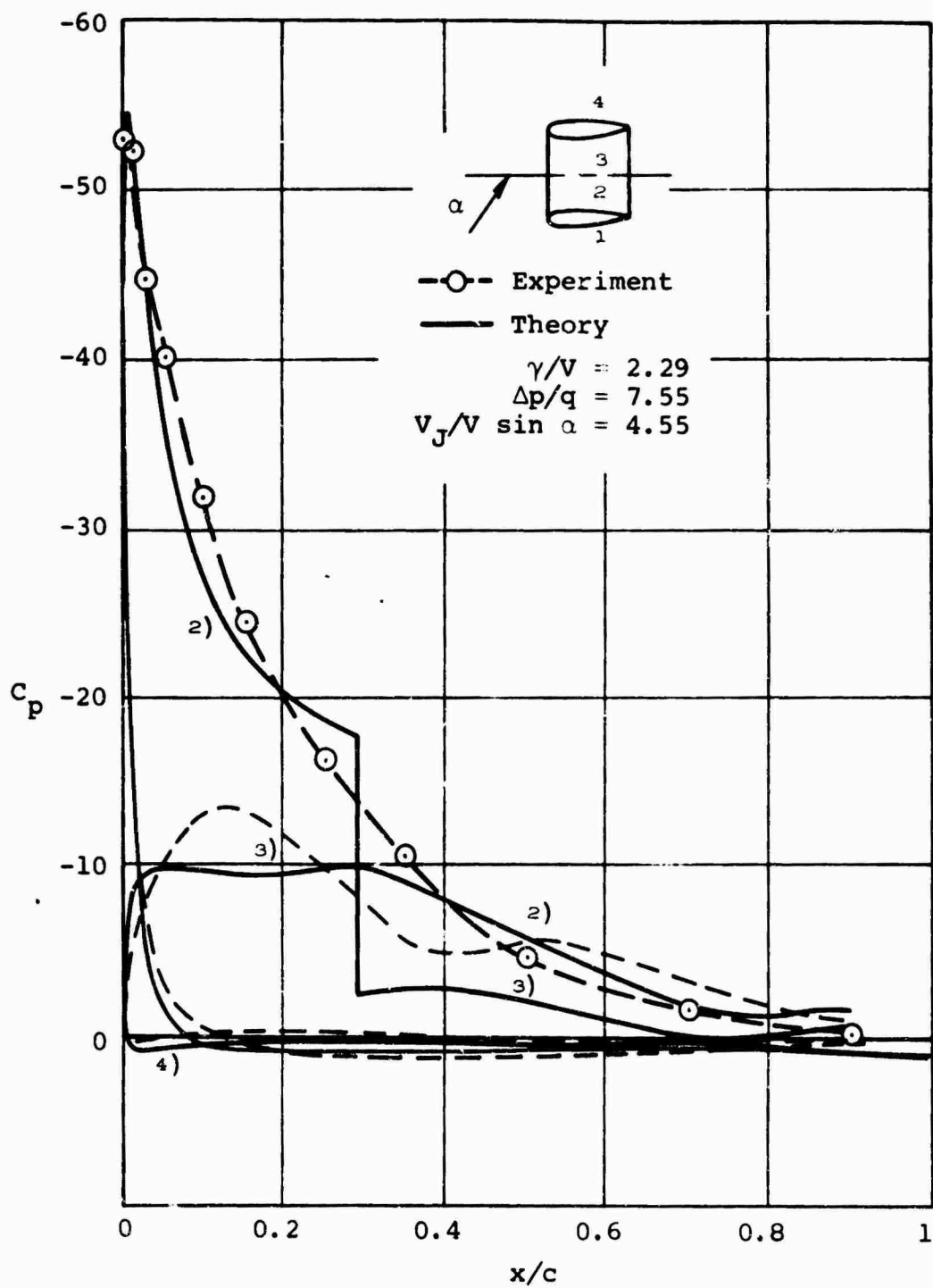
(b) $\alpha = 40°$, $J = 0.199$, $C_{T_{DP}} = 12.0$.

Figure 13.- Concluded.
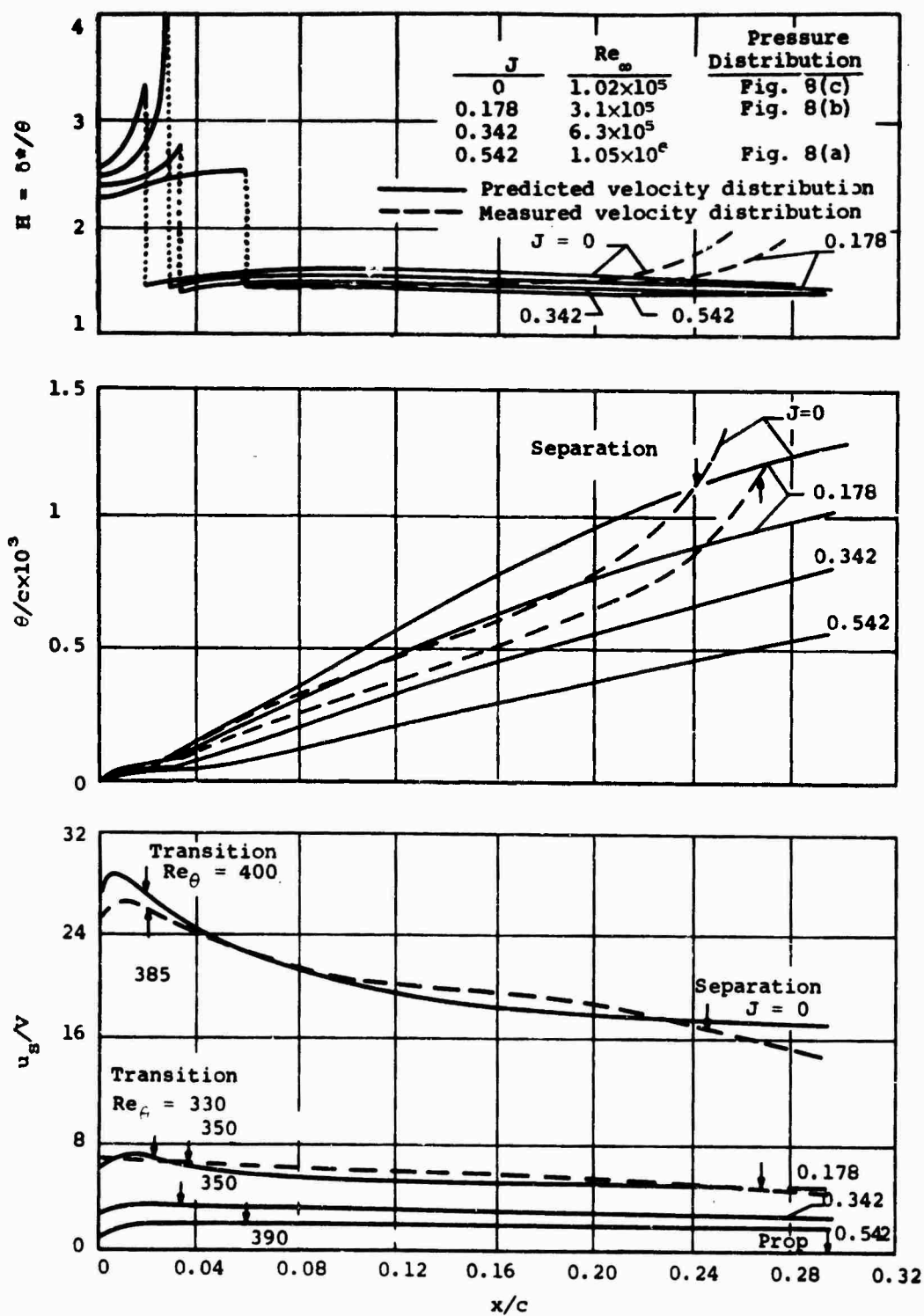
Figure 14.- Computed boundary layers for the 4-foot model duct at $\alpha = 0°$.
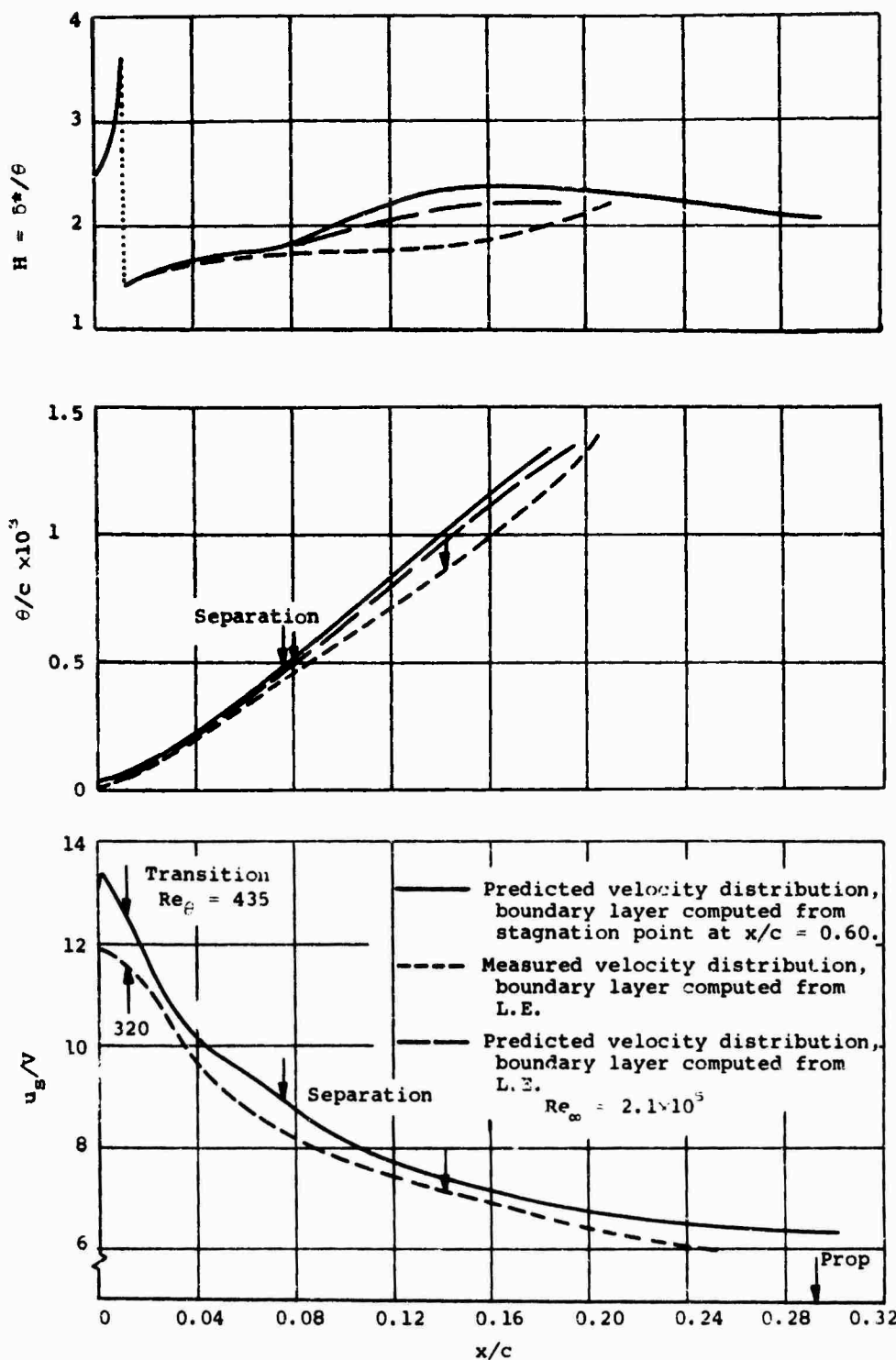
Figure 15.- Computed boundary layers for the 4-foot model duct
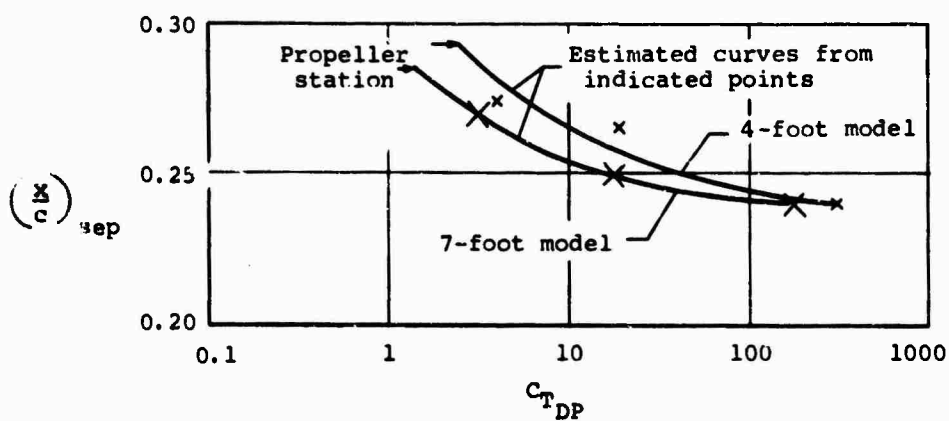at $\alpha = 80^{\circ}$, $J = 0.166$.

71
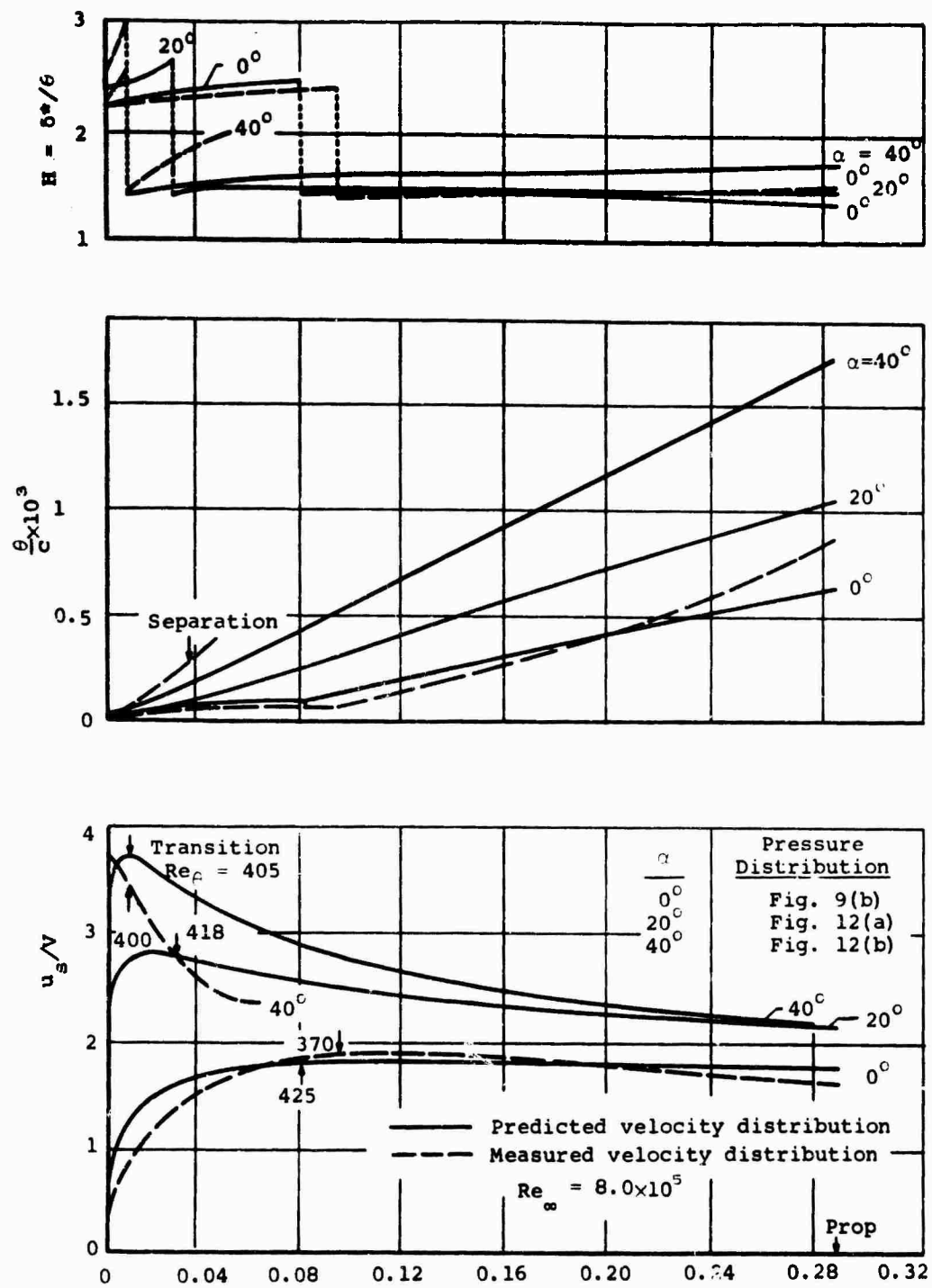
Figure 16.- Computed boundary layers for the 7-foot model duct at $\alpha \gtrsim 0$, $J \approx 0.52$.

72
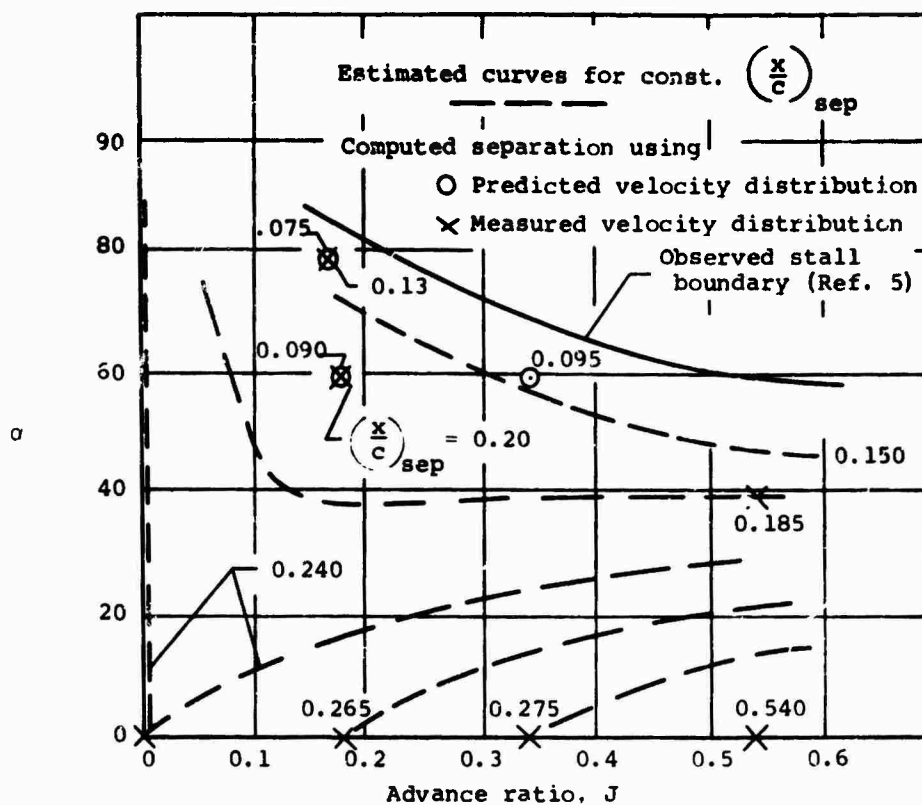
(a) Observed stall boundary and computed separation
points for the 4-foot model duct.

(b) Computed separation points for both ducts at $\alpha = 0$.

Figure 17.- Flow separation from both ducts.
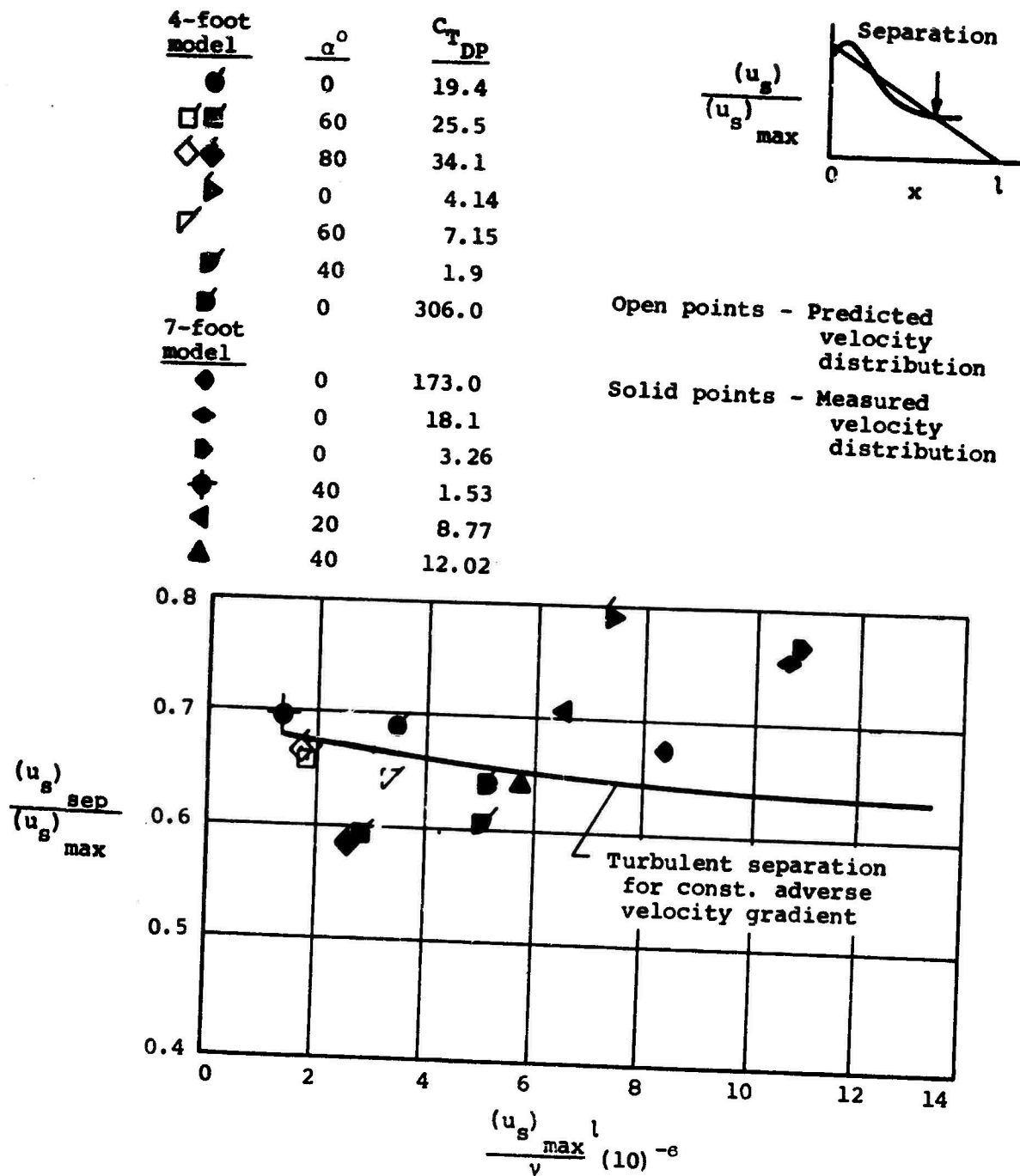
73

Figure 18.- Summary of computed location of separation for both ducts.

74

AEROTHERMODYNAMIC PERFORMANCE OF A HIGH
BYPASS TIP TURBINE CRUISE FAN SYSTEM

by

EUGENE G. SMITH

Lift Fan Systems Operation
Advanced Technology and Demonstrator Programs Department
General Electric Company
Cincinnati 15, Ohio

ABSTRACT

One of the promising propulsion systems for use in V/STOL aircraft systems is the high bypass lift/cruise fan. This system incorporates the turbomachinery of the tip turbine driven lift fan presently powering the XV-5A research aircraft. These high bypass systems require inlet and exhaust system geometry outside the range of most existing test results.

A test program was initiated to provide large scale model aerodynamic and thermodynamic performance characteristics for this lift/cruise system installation. The model incorporated a propulsion system consisting of the X-376 pitch fan from the XV-5A aircraft, with a bypass ratio of ten, and a T58 core engine. Model geometry was obtained by changing the fan inlet and exhaust system. Testing was performed in the NASA-Langley 16 foot wind tunnel covering a range of zero to 0.85 Mach.

This paper presents the results of this test program in terms of:

o Estimated remote fan and axisymmetric nacelle performance

o Performance of fan and close-coupled engine-fan nacelles including interference problem caused by nacelle intersections

o Possible solutions to problems of close-coupled system as applicable
to future test programs and designs of full scale high bypass lift/
cruise fan systems.

NOTATION

A_I -   inlet leading edge area

A_0 -   stream tube area for inlet mass flow

A_π -   nacelle area based on maximum diameter

$C_{D\pi}$ -   nacelle drag coefficient, $\dfrac{D_N}{q_0 A_\pi}$

C_P -   pressure coefficient

D_N -   nacelle external drag

D_I -   nacelle leading edge diameter

D_{TH} -   inlet throat diameter

D_{max} -   nacelle maximum diameter

K -   inlet loss correction factor for mass flow ratio

L_I -   inlet length from maximum diameter to leading edge

L_N -   nacelle length

L_T -   total installation length

M_{CR} -   Mach number for local critical flow

M_0 -   free-stream Mach number

q_0 -   free-stream dynamic pressure

q_{TH} -   average velocity at inlet throat based on total pressure and
flow

2

ϕ — fan flow coefficient, ratio of inlet velocity to fan tip speed

Ψ — fan pressure coefficient, ratio of fan pressure rise to dynamic pressure based on fan tip speed

η_s — fan stage efficiency, ratio of fan horsepower developed to turbine power extracted

$\bar{\omega}$ — inlet loss coefficient based on throat velocity head

INTRODUCTION

Recent increased emphasis on V/STOL aircraft systems has shown the need of several new families of propulsion systems. One of the promising systems in the high bypass category is the lift/cruise fan. This propulsion system incorporates the principle of the tip turbine driven fan. The main propulsion system component is the fan rotor, consisting of a single stage fan with the turbine blades attached around the periphery of the fan blades. This component is an outgrowth of the technology of the fan systems presently used in the XV-5A research aircraft. Figure 1 shows the present wing fan rotor system used in the XV-5A aircraft.

In addition to the rotor, the complete propulsion package consists of the inlet and exhaust systems for the fan, and the manifolds required for ducting the core engine exhaust gases to the fan tip turbine. Figure 2 shows a typical lift/cruise fan system. The fan inlet consists of the bulletnose and nacelle front cowl. The cowl is designed to meet both static takeoff and cruise requirements as well as providing an enclosure for the hot gas ducting. The installation as shown in a close-coupled arrangement where the gas generator or core engine nacelle is close to or part of the fan inlet system. Another typical installation is the remote arrangement that permits locating the core engine in any convenient position and ducting of the hot gas flow to the fan nacelle through a pylon mount.

The exhaust system for the fan forms the nacelle afterbody and provides a means of area control for the fan system. The typical arrangement as shown uses a convergent plug nozzle with an inflatable rubberized fabric

boot on the plug, providing a two position nozzle. Both the hot turbine and cold fan flows are discharged through the common nozzle annulus; the cold flow being adjacent to the nozzle plug system.

Design studies have shown that a typical optimum lift/cruise fan system will have a bypass ratio of between 5 and 8 and a fan pressure ratio of 1.3 to 1.5. At present there is no operating full scale fan hardware in this range of pressure and bypass ratios, one of the closest systems is being the pitch control fan of the XV-5A. This fan system, designated X-376, has a bypass ratio of about 10, a pressure ratio of 1.1, and a fan tip diameter of 36 inches. In order to obtain much needed installation aerodynamics applicable to the lift/cruise fan systems, a test program utilizing the X-376 fan system was initiated. The tests were performed in the NASA-Langley 16 foot transonic wind tunnel under the sponsorship of the U.S. Army Aviation Materials Laboratory.

This paper presents some of the most important performance criteria obtained during conduction of the test program. The results of the test program are reported fully in Reference 1.

THE TEST MODEL

The model (Figure 3) used in the test program consisted of the following major components arranged as a close-coupled lift/cruise fan system:

- o The X-376 fan system
- o A T-58 core engine
- o The engine inlet nacelle
- o Three interchangeable fan inlet cowls
- o Three interchangeable afterbody systems
- o Three interchangeable nozzle plug systems.

The combination of interchangeable components provided for twenty-seven possible test configurations. Eight of the most realistic configurations were tested. Pertinent geometric data for the eight test configurations

4

are given in Figure 4. The test models covered a range of design cruise Mach numbers from 0.55 to 0.8, with variations of both nozzle area and afterbody length.

The test model was sting mounted in the wind tunnel (Figure 5), with the engine inlet located below the fan inlet centerline. This arrangement is inverted from the normal expected installation as an aircraft propulsion system, but was required to facilitate installation in the wind tunnel.

Instrumentation was provided for measurement of pressure distributions on both the internal and external surfaces of the model. In addition, the flow conditions were measured at the inlet and discharge planes of the core engine and fan system. This instrumentation provided data for evaluating propulsion system internal and nacelle external performance. Total model forces were measured by a three component strain gage balance located at the attachment of the model to the sting mount.

The test program included investigation of system performance for a range of Mach numbers up to 0.85 at various power settings of the propulsion system. Performance under conditions of variable angle of attack were investigated on one of the test models, but will not be discussed in this presentation.

PRESENTATION OF RESULTS

Since the model used in this test program included a complete propulsion system in addition to an aerodynamic model, the test results will be presented as two different categories. The first catagory will involve the aerothermodynamic performance of the fan system under conditions for forward speed. Normal propulsion system parameters will be used such as thermodynamic efficiency and fan pressure ratio. The second catagory and the main body of the results will involve the aerodynamic performance of the fan inlet and afterbody systems. The performance in this case will be presented as local surface velocity distributions using pressure coefficient notation. Particular attention will be directed to the levels of the maximum

5

surface velocities and the conditions required for establishment of local velocities greater than critical (Mach number equal to 1). The conditions required for local critical flow will be discussed and compared with similar existing test results.

Test Results - Propulsion System

The X-376 fan system is presently installed as the pitch control fan of the XV-5A aircraft. In this installation, the fan is installed with its axis normal to the free-stream velocity. Fan performance has been investigated for a range of flight speeds up to 100 knots. The Langley installation as tested, provided the first source of test data for the fan installed with its axis aligned with the flow direction at speeds up to a Mach number of 0.85. A second installation difference existed in that the fan exhaust system incorporated a confluent or mixed flow nozzle system. This type of nozzle is characterized by the merging of both the fan turbine and fan discharge streams prior to accelerating the mixed flow in the nozzle throat. In this system, there is an interaction of the two flow streams that is of interest in terms of effects on propulsion system performance.

Figure 6 shows a typical fan operating map obtained while testing one of the eight test models. Fan operation in this case is depicted as the variation of stage efficiency and pressure coefficient with fan flow coefficient. These are conventional parameters presently used in defining performance of a single stage fan system with relatively low pressure ratios. The data shown in the figure represents the complete test range from static to a Mach number of 0.8. The complete range of core engine power settings from "windmill" to "maximum" is also included in the data. Windmill is the condition with the core engine inoperative and fan rotational speed provided by the ram drag forces. The significance of this single performance characteristic is the convergence of all data into a single characteristic, that also agrees quite well with the predicted performance. This effect lends to confidence in predicting cruise fan performance based on static or predicted performance. An almost identical characteristic was obtained for the seven

6

other test models, indicating that reasonable changes in nacelle geometry do not produce significant changes in propulsion system performance.

The second important propulsion system performance parameter that was verified by this program, was the performance of the exhaust nozzle system. In analysis of mixed flow cruise fan system, it has been normal to assume the static pressure of the fan and fan turbine flows to be equal at the plane where mixing is initiated. Measurements of the pressures in this plane of the model, verified this assumption within reasonable accuracy. All eight test models, covering a range of exhaust nozzle geometry showed that these pressure levels were equal.

Utilizing the fan map presented above, the verification of equal static pressure at the discharge plane, and an assumption of an ideal inlet and exhaust system, the performance of the X-376 fan system as a lift/cruise fan can be obtained readily and is shown in Figure 7. Here, fan net thrust, power requirements and optimum nozzle area are presented versus flight Mach number. Two levels of nacelle drag coefficient are shown. As can be seen, nacelle drag has significant effects on system thrust for a low pressure ratio fan system. Effects of nacelle drag are less for a higher pressure ratio system.

Test Results - Inlet System

Some of the most significant results obtained during the test program involved the aerodynamics of the numerous nacelle geometries in a typical close-coupled lift/cruise fan installation. Representative remote lift/cruise fan installation performance, may be assumed to exist on the axisymmetric part of the nacelle opposite the core engine nacelle. The following is a discussion of some of the inlet performance obtained by analysis of the test results.

Fan inlet internal performance may be presented in two ways; first, the effects of inlet geometry on inlet total pressure losses and, second, the relationships of local maximum surface velocities on the inlet loading edge. The three inlet geometries tested are shown in Figure 8 for reference.

7

Figure 9 presents typical inlet loss coefficient variation with mass flow ratio for the three inlet systems. The fairing of the actual test results is shown as a solid line. The dashed curves represent an empirical correlation of the test data using the following equation:

$$\bar{\omega} = 0.017 \frac{L_I}{D_{TH}} (K)$$

The first part of the equation is an empirical factor relating inlet loss with inlet length and diameter at static conditions. The second term is an empirical constant that is a function of mass flow ratio as shown in Figure 10. The agreement of the empirical equation and the actual test data is very good. This correlation can be a useful tool in predicting performance of lift/cruise fan system where inlet losses have significant effects on total installed performance.

The second indicator of inlet performance is the maximum surface velocity near the inlet leading edge. Figure 11 shows a typical family of inlet internal pressure distributions for one of the test inlets covering a range of test Mach numbers and mass flow ratios. Correlation of the peak pressure coefficient with mass flow ratio is shown in Figure 12. The two longer inlet systems, inlet 1 and 2, exhibit similar characteristics. Inlet 3 shows significantly higher velocities at the higher speed condition, high values of A_I/A_0. This difference may be attributed to the extension of the bulletnose foreward of the inlet leading edge. The data shows that an inlet system of the type tested, all having an inlet leading edge diameter of 1.13 times the throat diameter, will have a peak local velocity of about 1.6 times the calculated average velocity. Using local sonic flow as a criteria, this limits the inlet mass flow at static condition to 84 percent of the theoretical choking value.

Tests under conditions of variable angle of attack showed that the nacelle angle of attack must be greater than 12 degrees before the peak inlet internal velocity exceeds the levels as occur at static conditions. This tends to indicate that the design conditions for the inlet throat size is established by the static operating condition.

8

Nacelle external performance may be investigated by observing the levels of maximum velocity on the inlet external surface under conditions of forward speed and varying mass flow. Figure 13 shows a typical set of nacelle pressure distributions taken at low Mach numbers and at different mass flow ratios. The pressure distributions are typical of a low speed inlet of this type and exhibit highest local velocities under conditions of minimum mass flow ratio. It should also be pointed out that the levels of pressure coefficient around the nacelle system vary considerably; minimum pressure coefficients occur in the region of the fairing of the fan inlet to the engine nacelle.

Cross-ploting the numerous pressure distributions for the eight test models for a range of mass flow ratios and free-stream Mach numbers yielded the following conclusions:

o The peak velocities on the fan inlet external surface are independent of afterbody geometry for the range of models tested.

o Peak pressure coefficient levels are generally higher in the region of the fairing and approach critical flow condition at Mach numbers lower than expected based on axisymmetric inlet design criteria.

o Characteristic increases in peak pressure coefficient were observed with conditions of decreasing mass flow ratio and increasing Mach number.

Faired test data, showing effects of free-stream Mach number and inlet circumferential position, are presented in Figure 14, for the three inlet geometries. The rise in pressure coefficient with Mach number agrees quite well with typical theories of compressibility. The variation of critical Mach number with circumferential position is also apparent, showing interaction effects at the fairing section of the inlet.

Effect of mass flow on local peak pressure coefficient are also shown in Figure 15.

9

Low Mach number conditions are shown in these figures because restriction in propulsion system operation did not permit large excursions of mass flow at the higher Mach numbers. This restriction existed because at high speeds fan rotational speed at windmill conditions and maximum power conditions were equal, and consequently mass flow did not vary.

Making use of this data for relatively short inlet systems and the previous correlations performed in Reference 2, a set of design characteristics for selection of inlet geometry based on local critical flow were obtained. These characteristics are shown in Figure 16 and 17. Using the same criteria as in Reference 2, Figure 16 shows the variation of critical Mach number with both inlet length and inlet leading edge diameter. In general, increases in inlet length and increases in inlet diameter result in higher Mach number capability for the inlet. However, mass flow ratio must be greater than that shown in Figure 17 in order for the critical Mach number characteristics to apply. This figure shows that increases in inlet diameter cause additional restrictions in mass flow ratios at which the inlet can operate. An iterative procedure of designing an inlet system, taking into consideration inlet mass flow ratio, design Mach number and geometric limitations, is required.

FAIRING RECONTOUR BASED ON TEST RESULTS

As previously pointed out in the discussion, the region in the vicinity of the fairing exhibits large negative pressure coefficients and consequently low critical Mach numbers. Making use of the test data of Figure 15, 16 and 17, it is possible to develop a criteria for redesign of the fairing region for nearly uniform circumferential velocity distributions. Comparison of conditions for equal pressure coefficients, tends to indicate that the fairing region is operating with a mass flow of about 1.4 times the equivalent axisymmetic condition. This infers that the inlet leading edge in the fairing is spilling not only the normal amount of flow, but an additional 40 percent that is not spilled over the inlet in the vicinity of the engine nacelle. This level seems quite reasonable. Making use of this additional spillage or reduced mass flow ratio, it is possible to determine a set of characteristics

10

applicable to redesign of the inlet contour in the engine to fan nacelle fairing region. Figure 18 shows the proposed design parameters applicable to the fairing design. The factors presented are an increase in inlet length and a reduction in inlet diameter as required for simultaneous critical flow over the complete nacelle system. This set of characteristics were obtained by simply recalculating the design criteria as presented for axisymmetic inlet systems, (Figure 16 and 17) at a 40 percent reduced mass flow ratio. Comparison of required inlet length and inlet leading edge diameter then resulted in the characteristics as presented.

A comparison of a typical cruise fan nacelle system in the original test and the proposed modified configurations is shown in Figure 19. It is apparent from the sketch that the redesign produces an inlet that has both a swept back effect and a general thickening of the inlet lip in the vicinity of the fairing. The sweep back angle would be about 10 degrees for an inlet system designed for a critical Mach number of about 0.8.

An interesting verification of this redesign criteria was obtained while testing one of the models under conditions of variable angle of attack. Tests on inlet 1, showed that general decreases in local pressure coefficient and consequently local Mach numbers occurred in the fairing region under conditions of negative angle of attack. Negative angle of attack exists when the engine inlet moves down in front of the fan inlet. A negative angle of attack of about 6 degrees was required to produce pressure distributions equivalent to design Mach number in the fairing region. This level of 6 degrees compares quite favorably with the 10 degrees discussed above.

NACELLE EXTERNAL DRAG

A region of lift/cruise fan performance lacking either experimental and analytical data is total nacelle external drag. This test program provided a source of this type of experimental test data. Utilizing total model forces, as measured by the balance system, and fan system net thrust, based on measured flow conditions, the nacelle external drag was evaluated. Only one questionable parameter is required in determining the nacelle drag and

11

this is the exhaust nozzle thrust coefficient. For evaluation of the test data, the nozzle thrust coefficient was estimated using the following two assumptions:

o The nozzle velocity coefficient, because of flow angularity, will be 0.99.

o All other nozzle losses will be due to surface skin friction that was calculated based on measured surface velocities and an average skin friction coefficient.

These two assumptions resulted in nozzle thrust coefficients between 0.95 and 0.97. The low levels of thrust coefficient are due to the scrubbing drag on the large areas of the nozzle plug system. It should be noted that the large plug geometries are not typical of the 1.3 to 1.5 pressure ratio fan system but are required because the X-376 is only a 1.1 pressure ratio and was used in a typical higher pressure ratio nacelle system.

Making use of these estimated thrust coefficients and the measured balance forces, the nacelle total low-speed drag as measured is shown in Figure 20. This nacelle drag coefficient included the following:

o Fan inlet external friction drag
o Afterbody friction drag
o Complete nacelle form drag including the fairing region
o Core engine inlet friction and form drag.

Not included in the drag coefficient are:

o Inlet internal losses
o Exhaust nozzle losses including plug friction drag.

Measured system drag coefficients varied between 0.09 and 0.04 depending on mass flow ratio and inlet geometry. Estimated engine nacelle friction drag coefficient was estimated to be 0.016 and is shown on the figure. Since engine nacelle form drag is probably a small fraction of the total drag as shown, the drag numbers as measured and reduced by 0.016, represent a typical total nacelle drag coefficient level. The top band of the data represents the longer nacelle systems and the lower region, the shorter configurations.

12

The drag coefficients as previously discussed represent the low-speed values only in the range of free-stream Mach numbers between 0.2 and 0.4. A premature drag rise was also indicated by the balance measurements, similar in nature to the premature critical flow problems in the fairing region. Using faired data for the eight test models, it was observed that the drag rise with increasing Mach number was a function of the nacelle inlet configuration only. The ratio of drag to low speed drag for the three inlets is shown in Figure 21 as a function of free-stream Mach number. Note that drag rise occurred at Mach numbers of 0.4, 0.5 and 0.6 for inlets 3, 2 and 1, respectively. Design Mach numbers for the inlet were 0.55, 0.7 and 0.8. Although the exact cause of the drag rise is not readily apparent, it is probable that the problems of the fairing design and associated interactions are the cause of these trends. This is a region of performance that will remain unanswered until a test program of the redesign system is accompolished.

CONCLUSIONS

Analysis of high speed tests of a family of typical lift/cruise fan propulsion systems indicated the following:

1. The lift/cruise fan system is not adversely affected by simulated high speed operation.

2. Nacelle low speed drag coefficients, not including core engine nacelle drag ranged between about 0.035 at high mass flow ratios and 0.065 at near design mass flow ratios.

3. The models as tested exhibited high spillage and consequently low critical Mach numbers in the region of the core engine to fan nacelle fairing. A proposed redesign of the fairing was established using the test data.

13

References

1. Smith, Eugene G., <u>High-Speed Wind Tunnel Tests of a High Bypass Lift/ Cruise Fan Propulsion System</u>, USAAVLABS Technical Report No. 66-40, Fort Eustis, Virginia, 1966.

2. Nichols, Mark R., and Keith, Arvid L., Jr., <u>Investigation of a Systematic Group of NACA 1 - Series Cowlings With and Without Spinners</u>, NACA Report No. 950, Langley Research Center, Langley Field, Virginia, 1949.

14
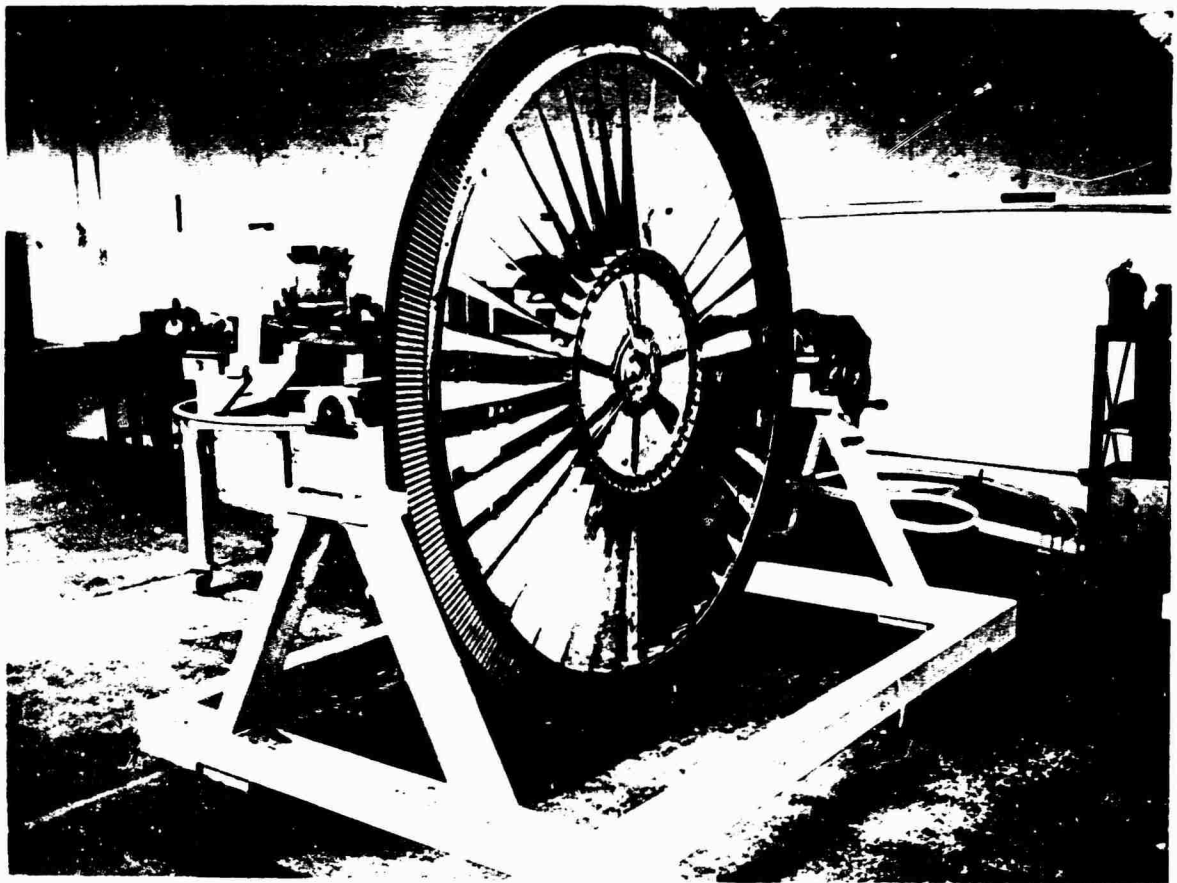
Figure 1.   X-353-5B Fan Rotor.
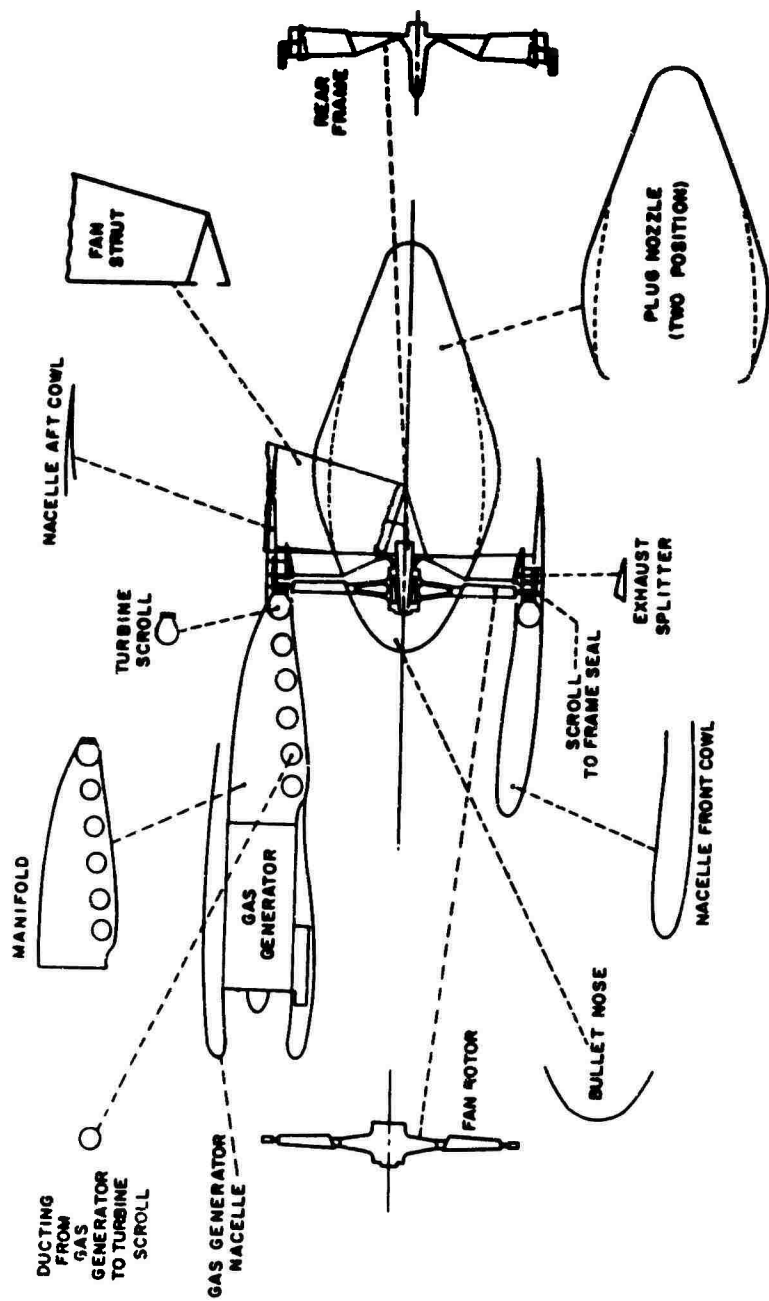
Figure 2. Typical Components of Lift/Cruise Fan System.

REAR FRAME

FAN STRUT

NACELLE AFT COWL

TURBINE SCROLL

PLUG NOZZLE (TWO POSITION)

EXHAUST SPLITTER

SCROLL TO FRAME SEAL

MANIFOLD

GAS GENERATOR

NACELLE FRONT COWL

BULLET NOSE

FAN ROTOR

DUCTING FROM GAS GENERATOR TO TURBINE SCROLL

GAS GENERATOR NACELLE
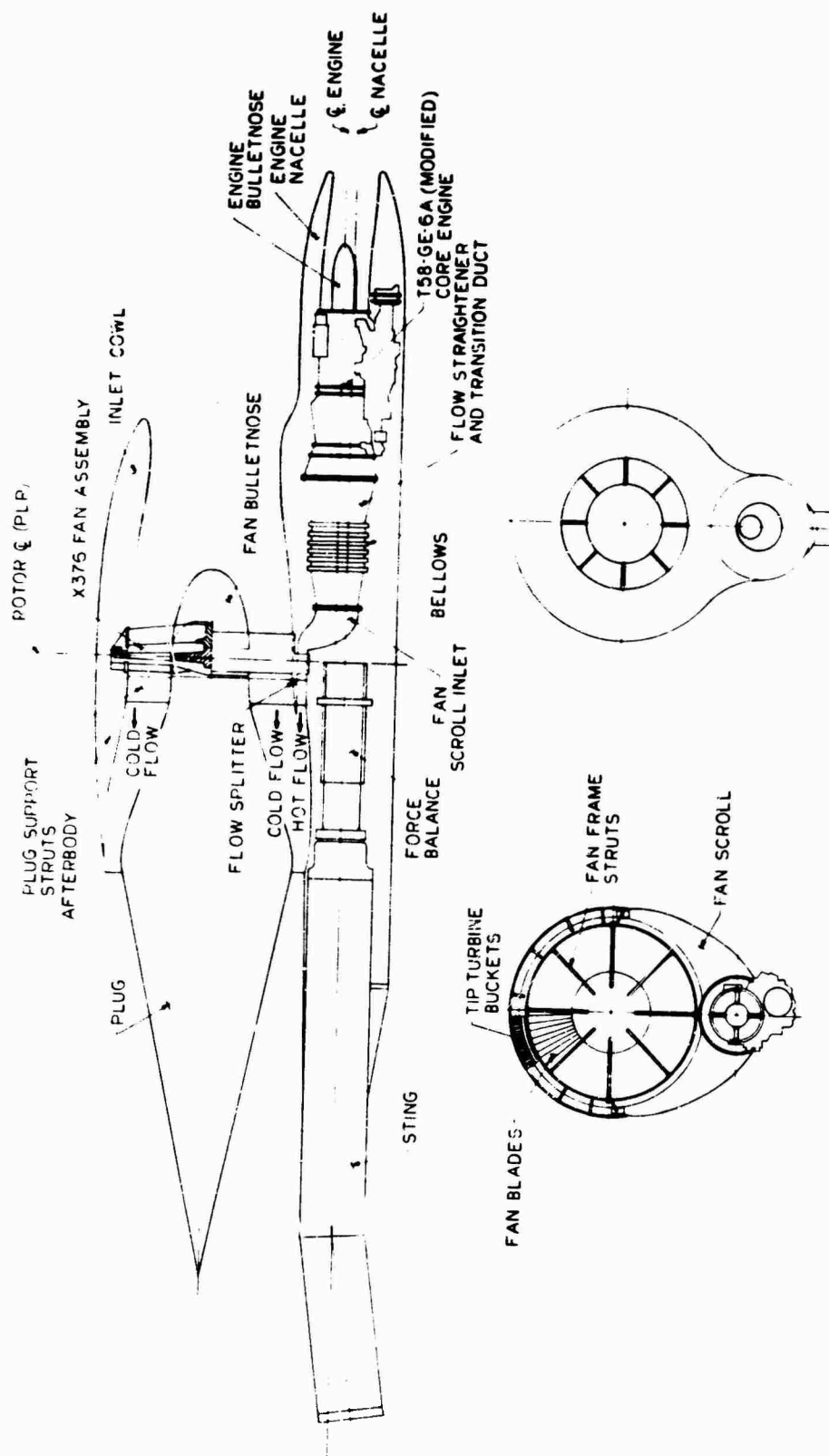
Figure 3. Cross Section of Test Model.

D_{max} = 50 Inches
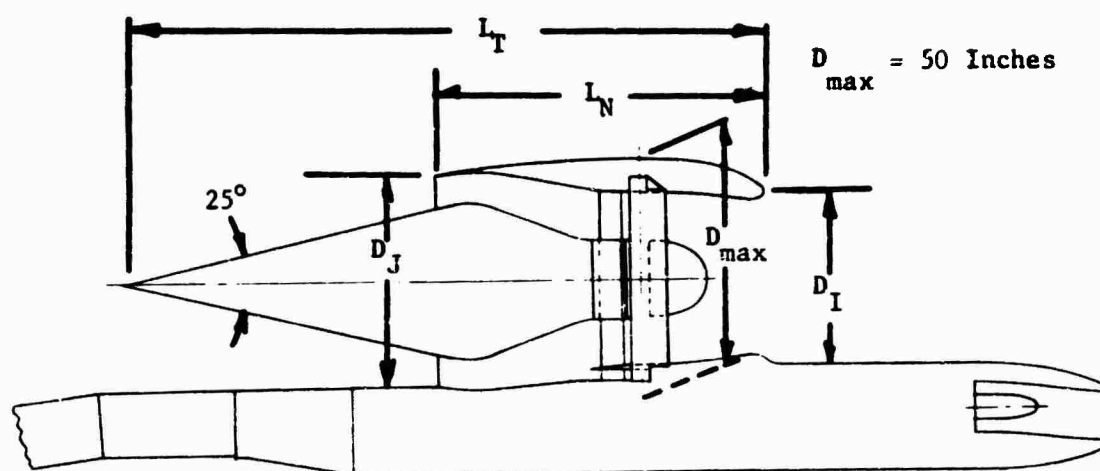
Model	M_{des}	L_N/D_{max}	L_T/D_{max}	D_I/D_{max}	D_J/D_{max}	Aj (sq in)
1	0.8	1.87	3.52	0.65	0.87	430
2	0.8	1.43	3.08	0.65	0.87	430
3	0.7	1.43	2.81	0.73	0.87	770
4	0.55	1.13	2.78	0.82	0.87	430
5	0.55	1.13	2.38	0.82	0.77	570
6	0.8	1.87	3.24	0.65	0.77	430
7	0.8	2.06	3.31	0.65	0.77	570
8	0.8	2.06	3.43	0.65	0.77	430

Figure 4. Geometric Data for Test Models.

18

a. Front View of Model 3

b. Rear View of Model 3

Figure 5. Model Mounted in Test Section.
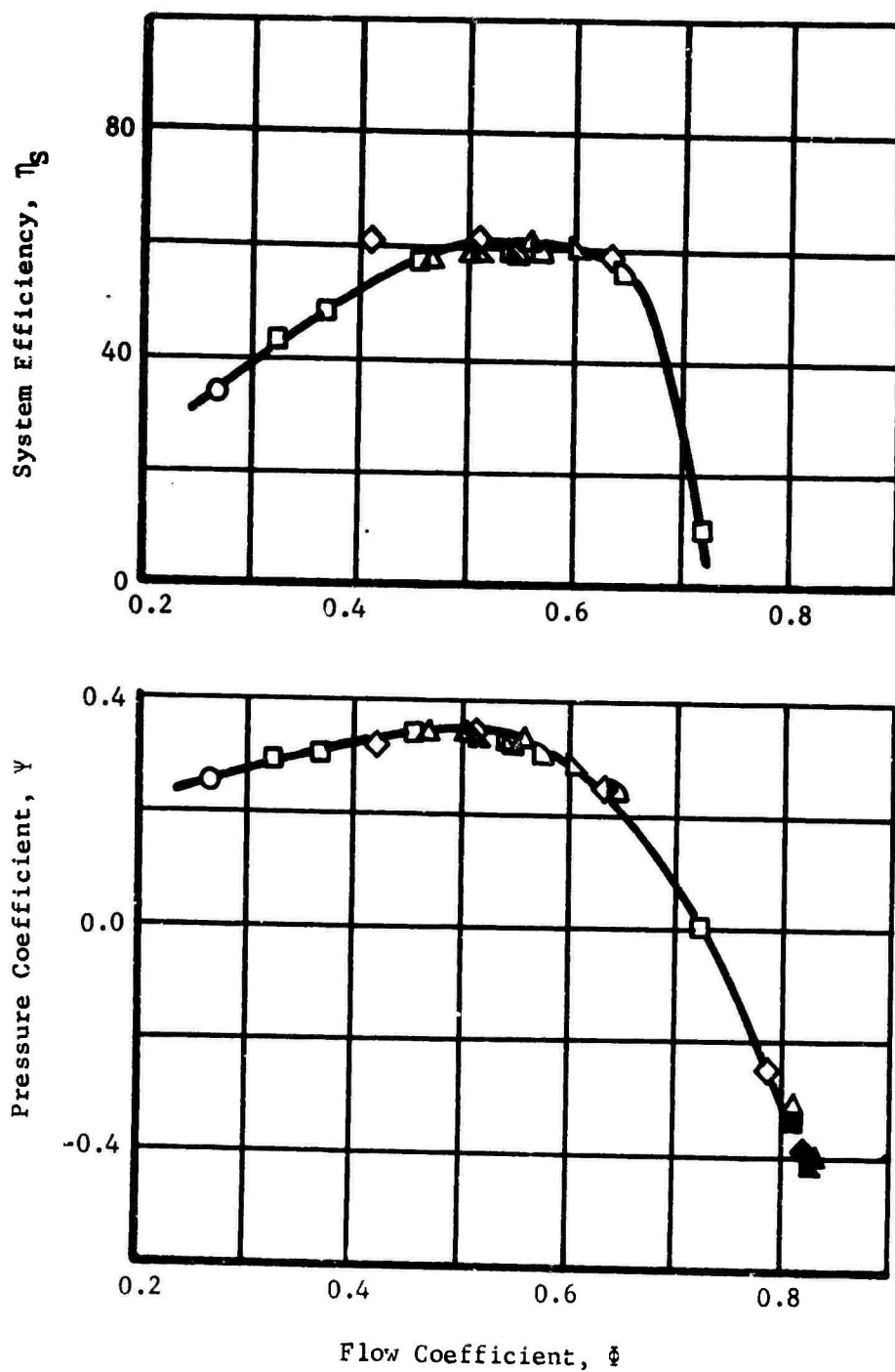
Figure 6. Typical Fan Operating Characteristics.
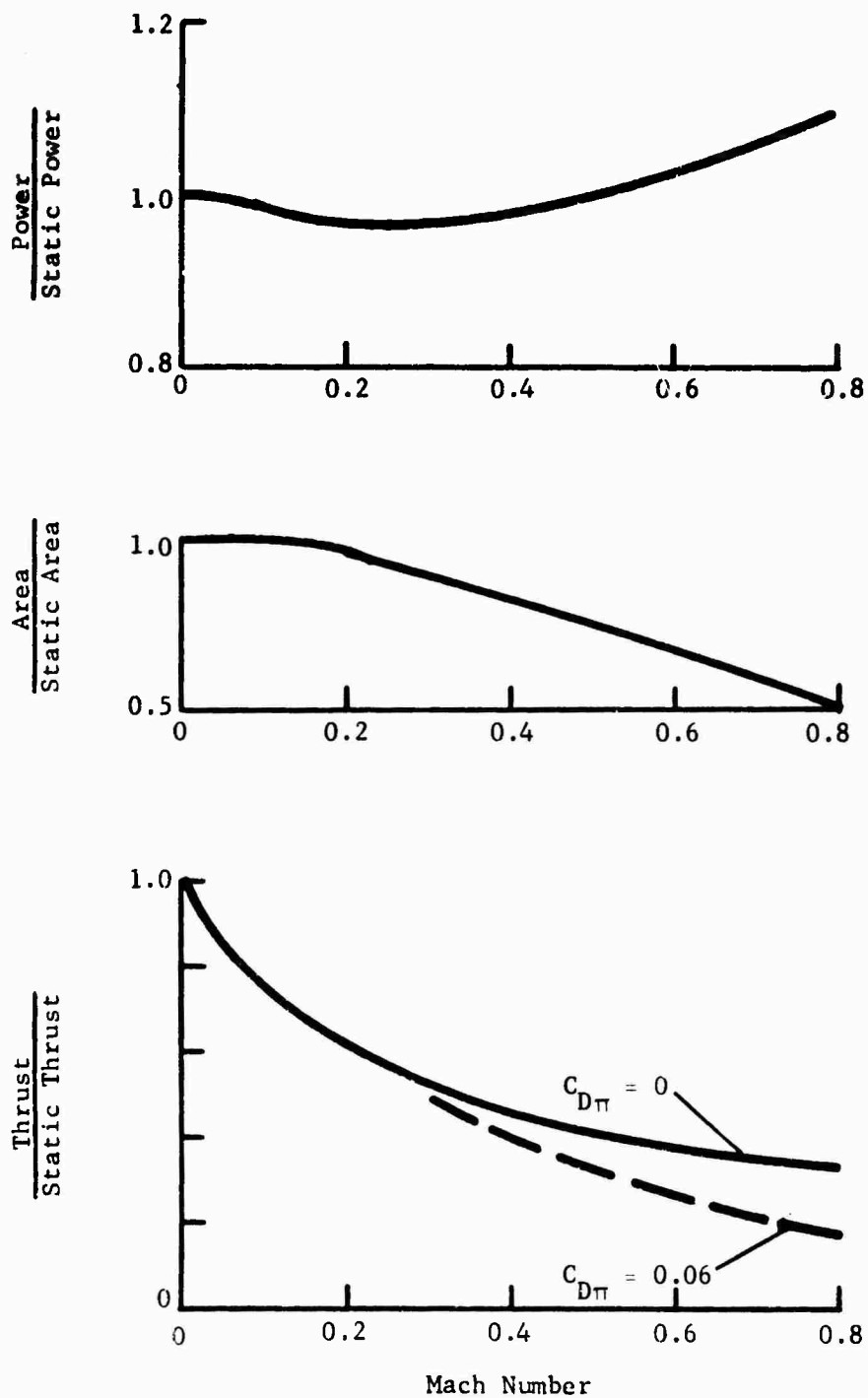
Figure 7. X-376 Lift/Cruise Fan Performance.

21
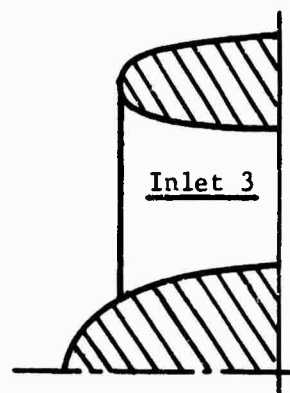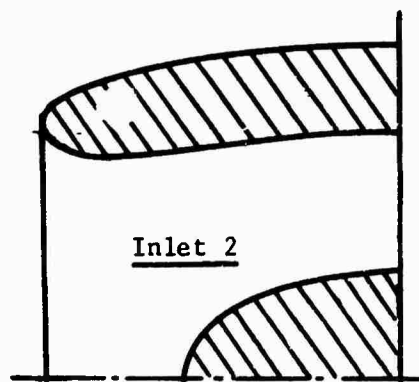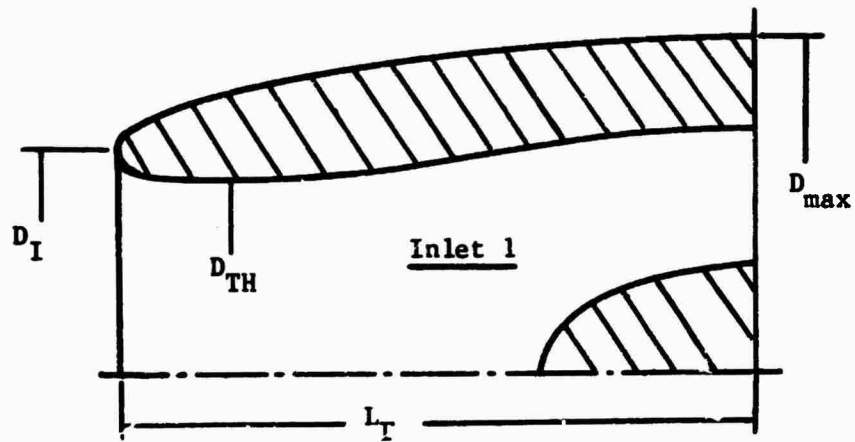
Inlet	$\dfrac{L_I}{D_{max}}$	$\dfrac{D_I}{D_{max}}$	$\dfrac{D_{TH}}{D_{max}}$
1	0.98	0.65	0.57
2	0.54	0.73	0.64
3	0.36	0.82	0.72

Figure 8. Comparison of the Three Inlet Designs.
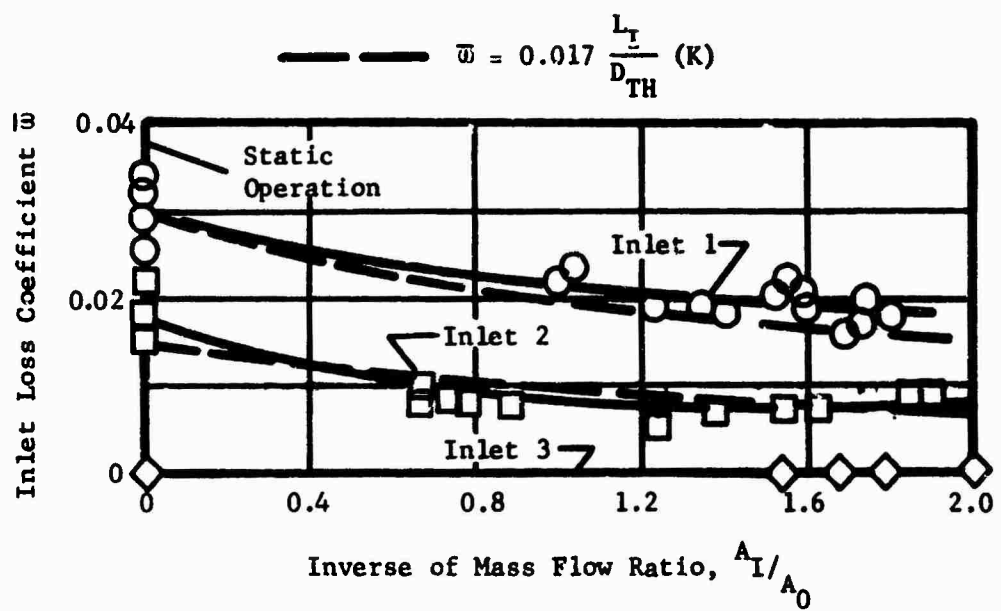
Figure 9.   Inlet Total Pressure Losses.
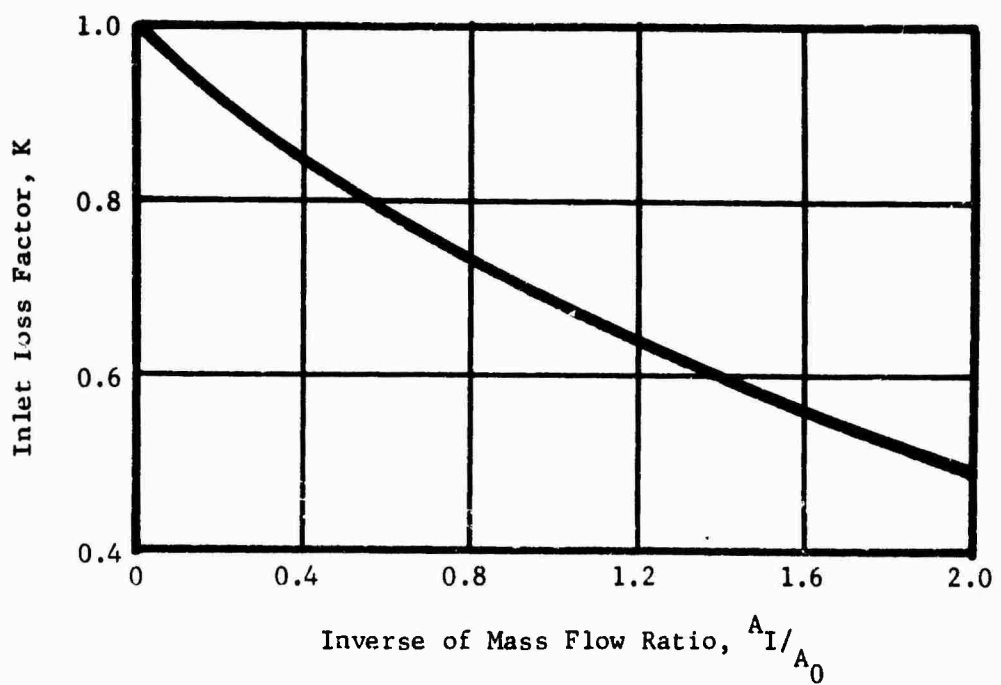
Figure 10.   Inlet Loss Factor.

23
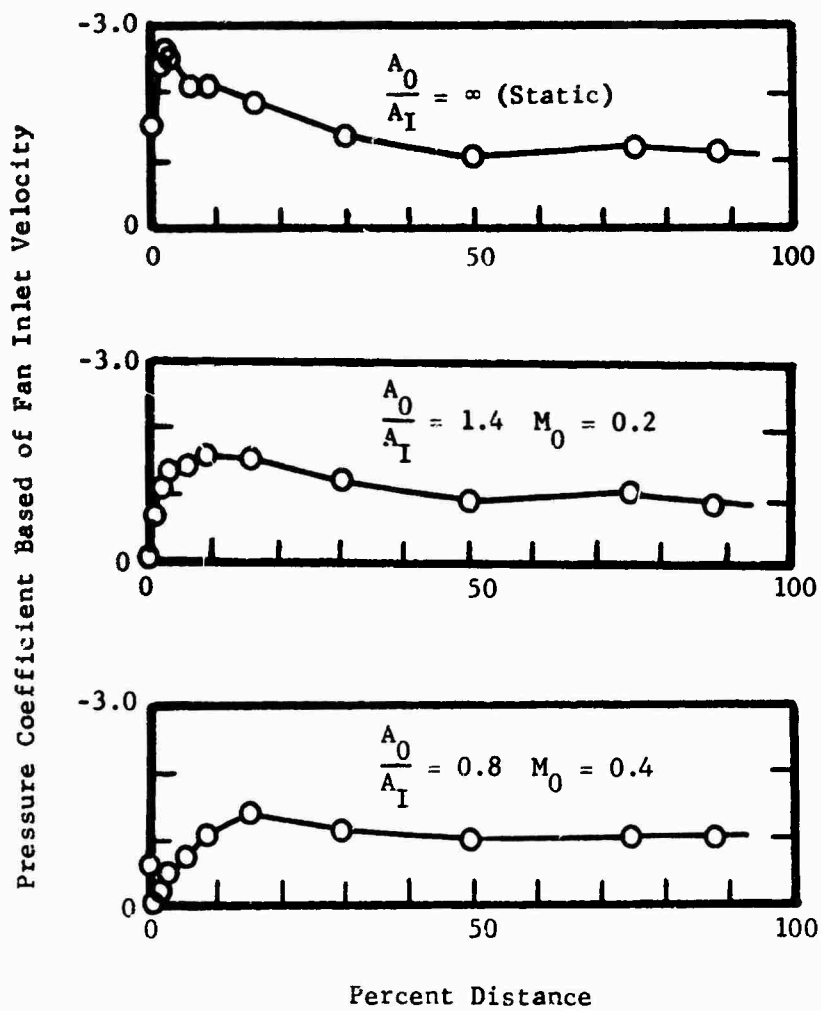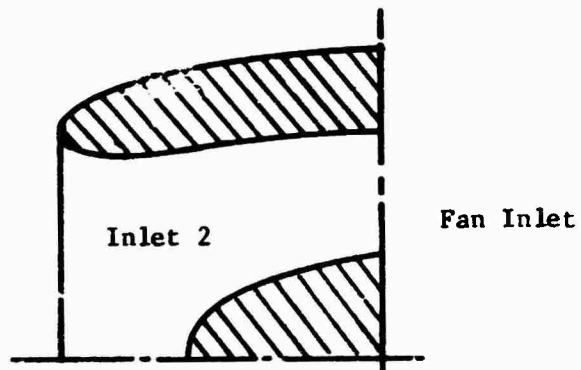
Figure 11. Typical Inlet Internal Pressure Distributions.

24
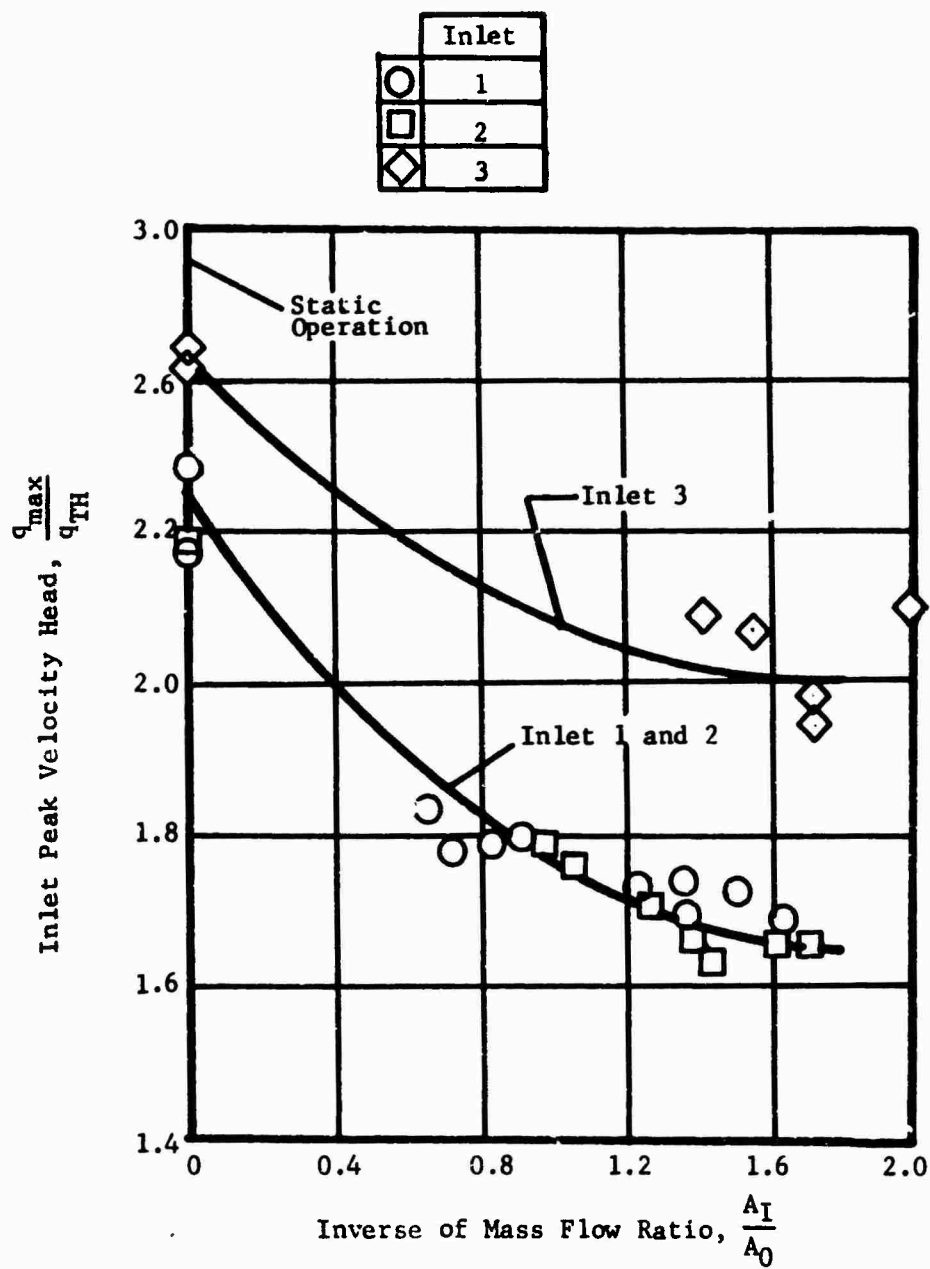
Figure 12. Inlet Peak Velocities.
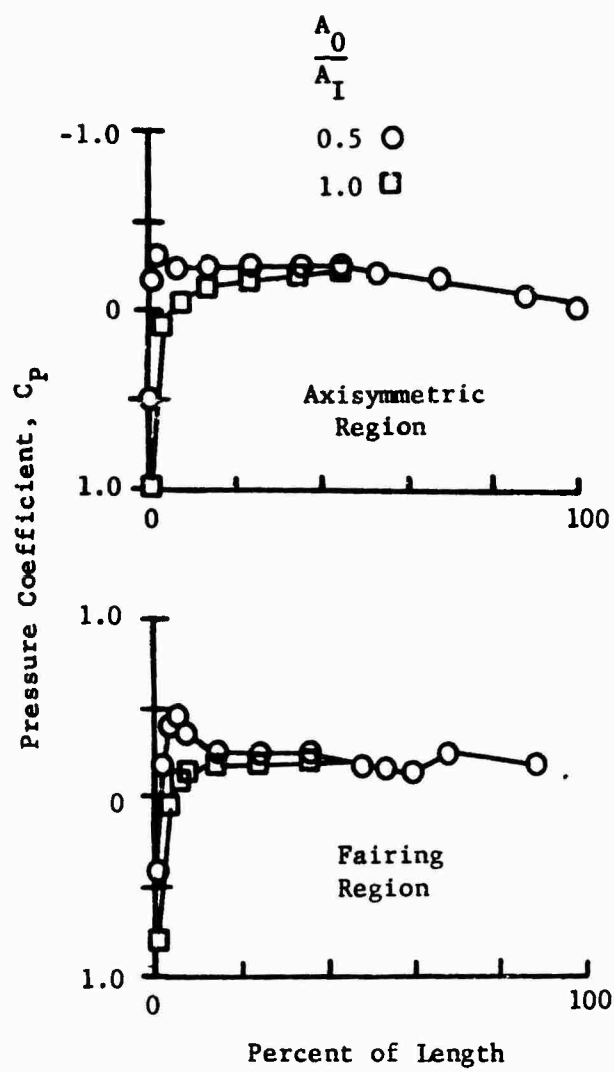
Figure 13.   Typical Nacelle External Pressure
            Distribution.
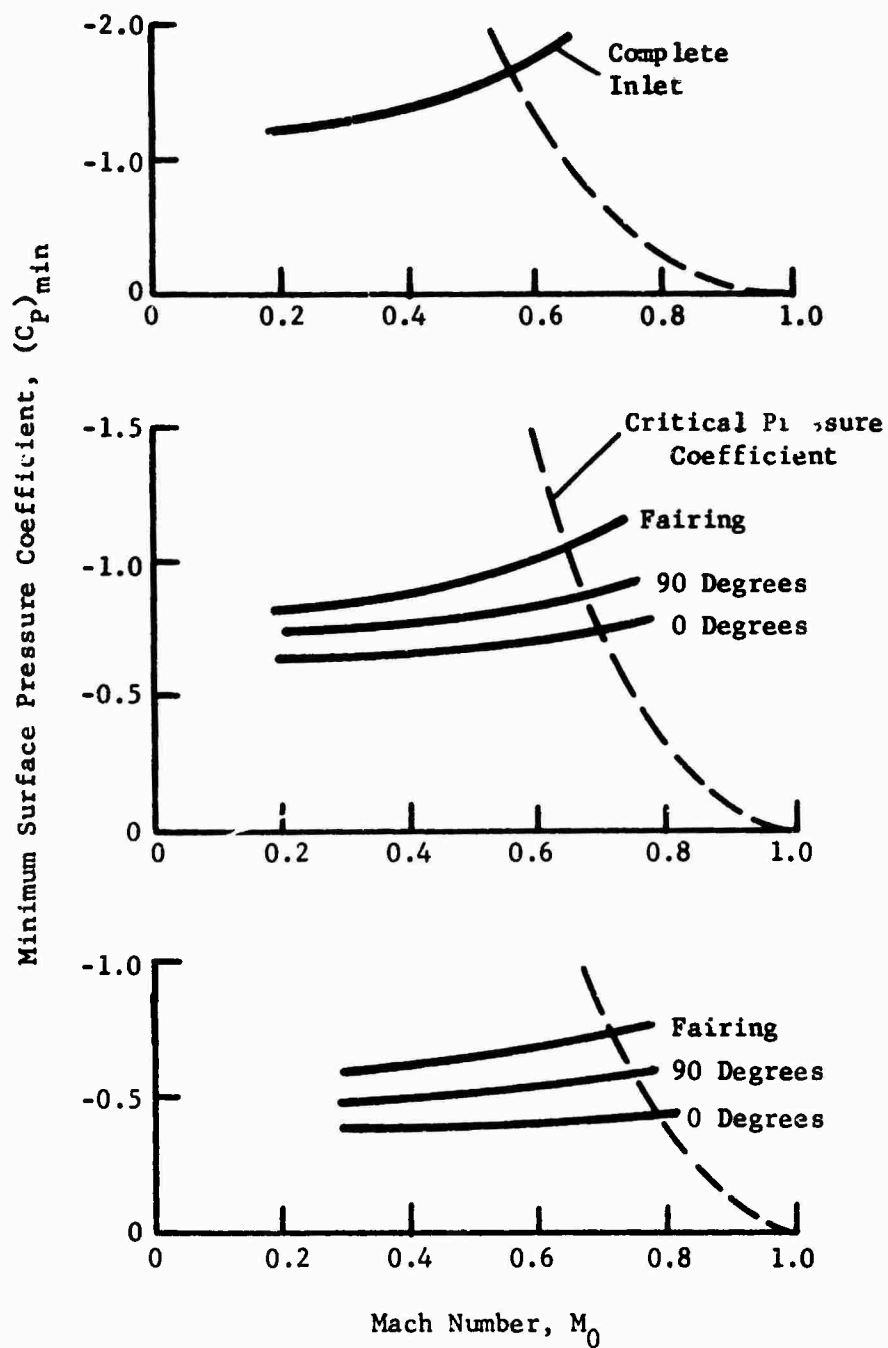
Figure 14. Effects of Mach Number on Inlet External Pressure Coefficient.
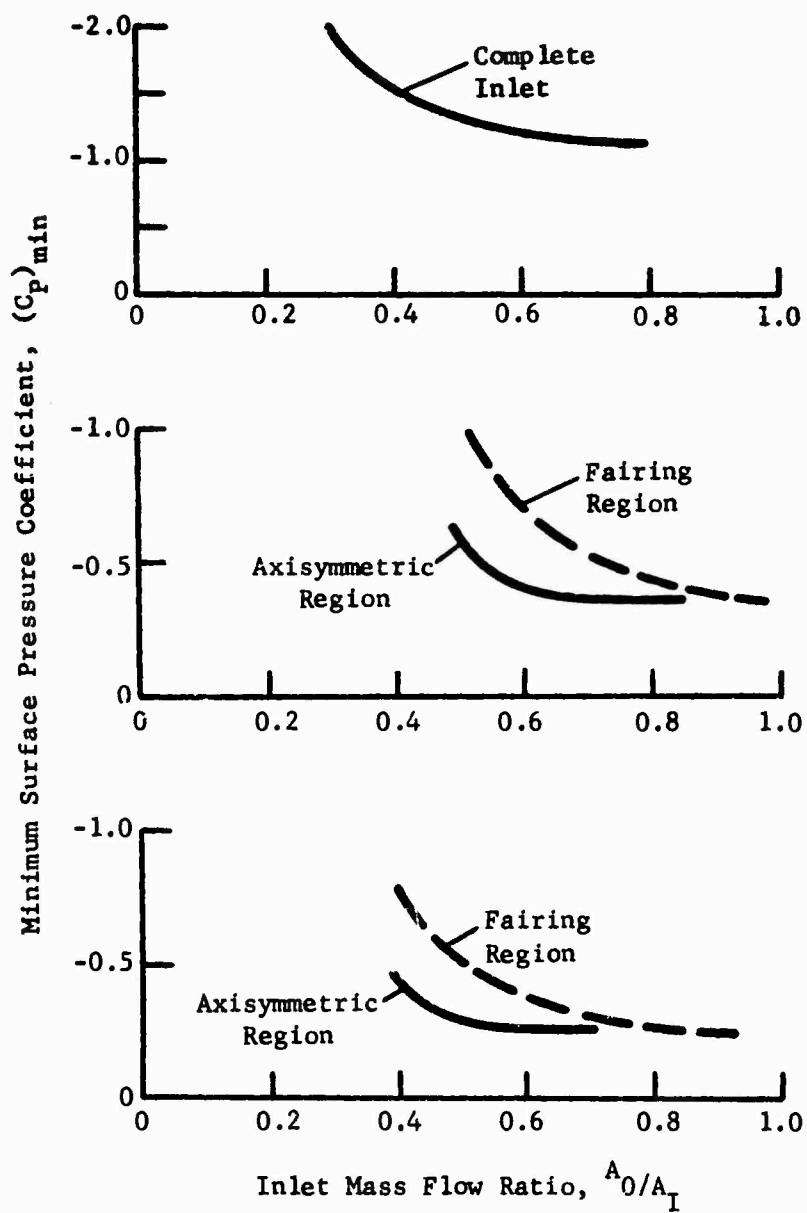
Figure 15. Effects of Mass Flow Ratio on Inlet External Pressure Coefficients.

28
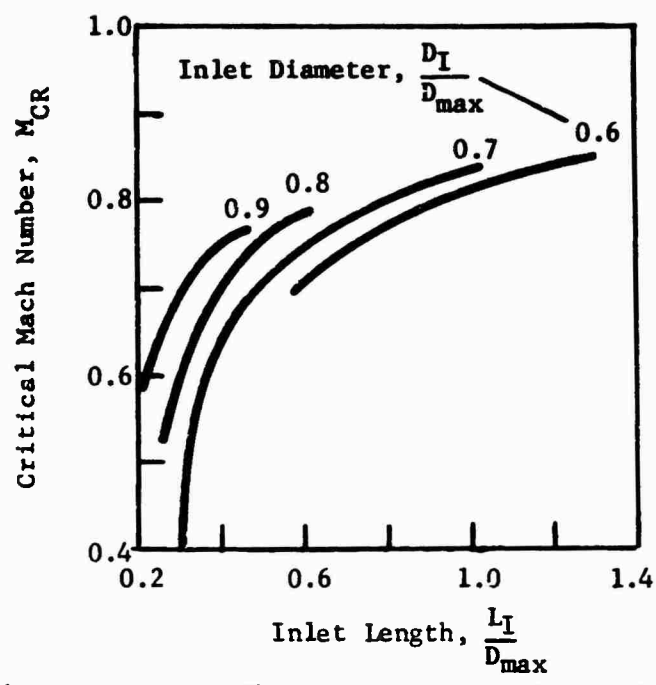
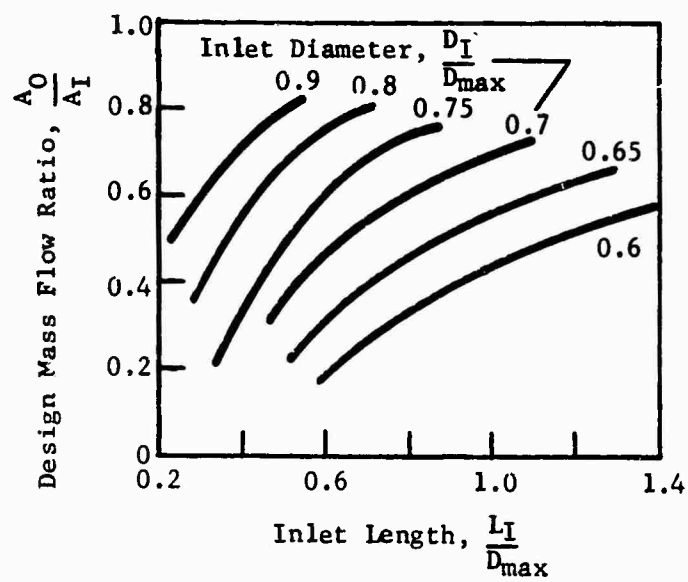Figure 16. Inlet Design Characteristics, Critical Mach Number.

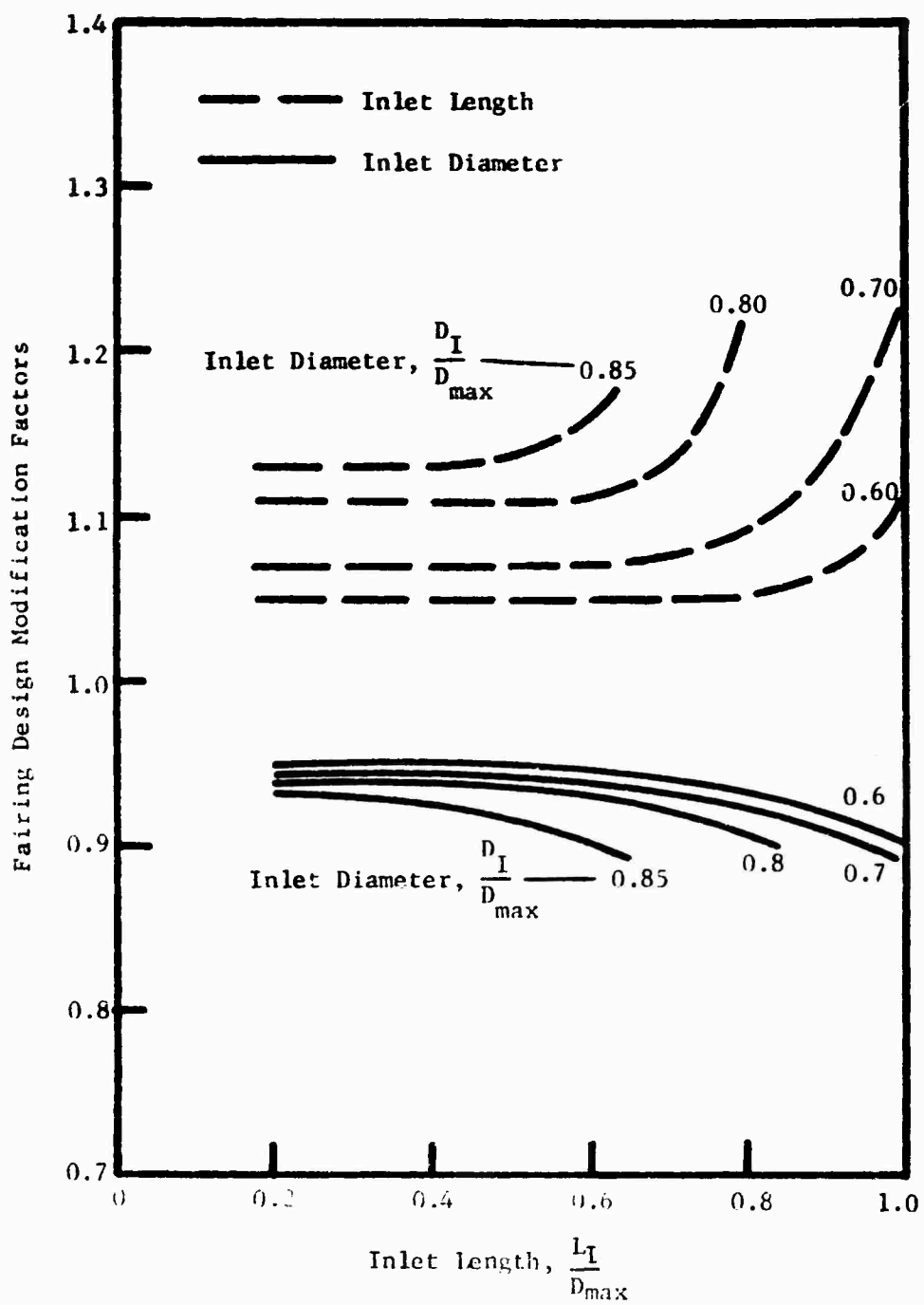Figure 17. Inlet Design Characteristics, Minimum Mass Flow
Ratio.
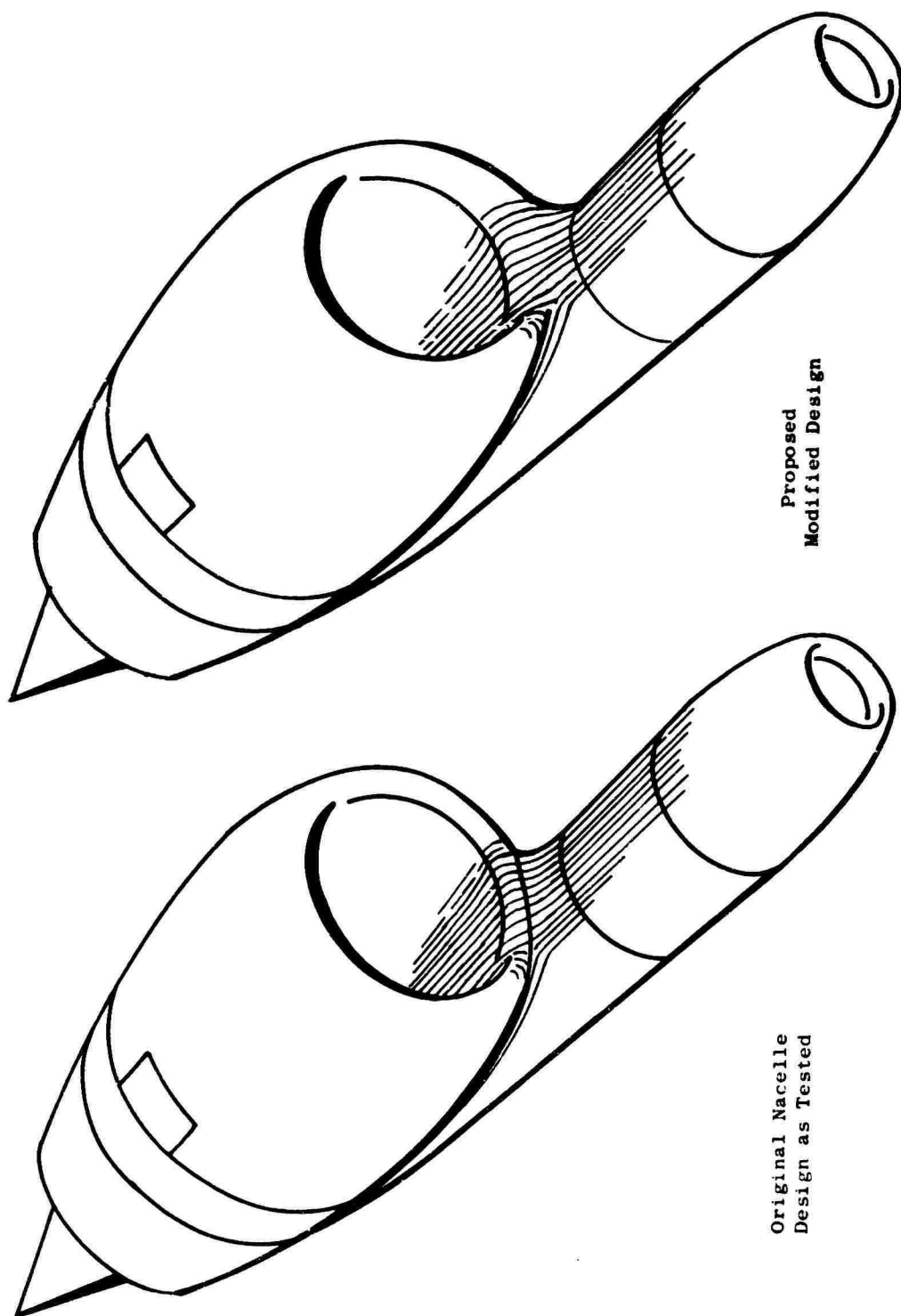
Figure 18. Design Factors for Engine-Inlet Fairings.

30

Original Nacelle
Design as Tested

Proposed
Modified Design

Figure 19. Sketch of Model 8 Showing Original and Modified Nacelle Designs.

31

	Model
◯	1
▢	2
◇	3
△	4

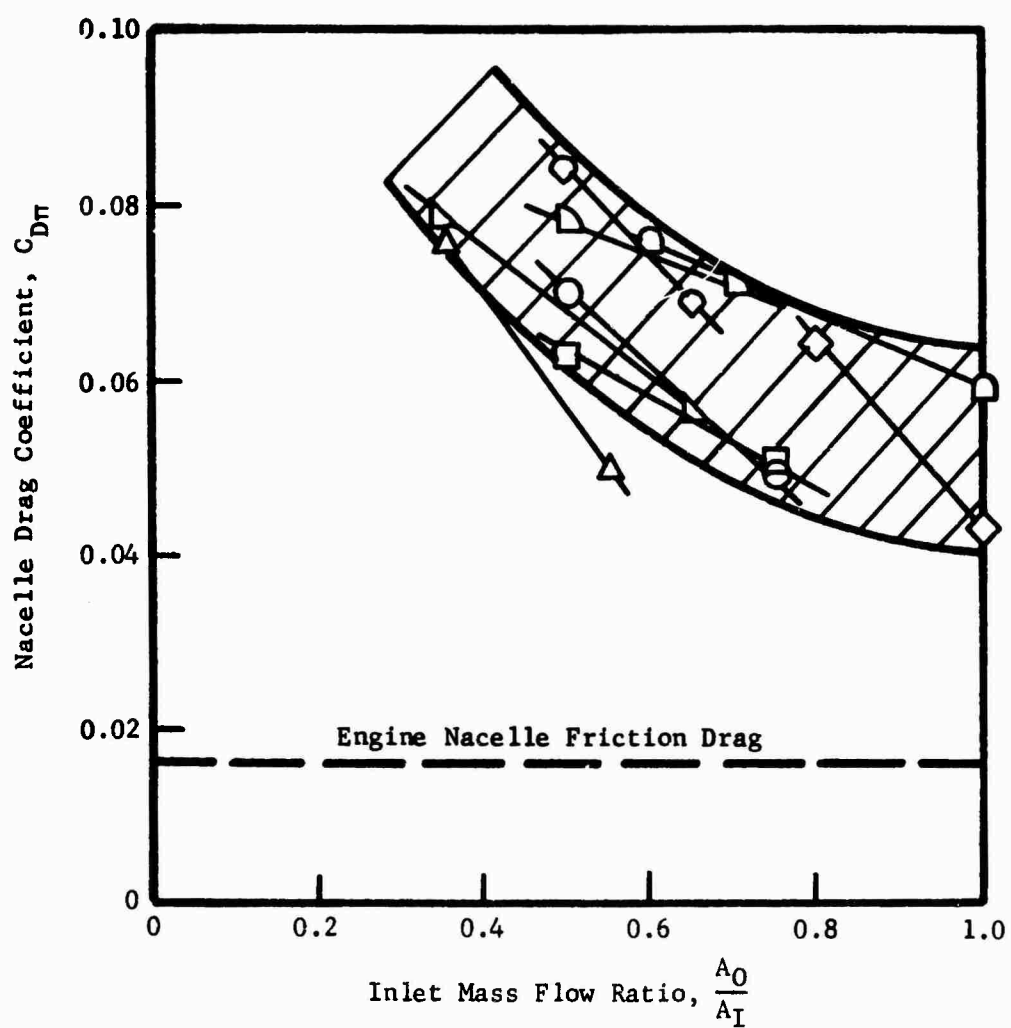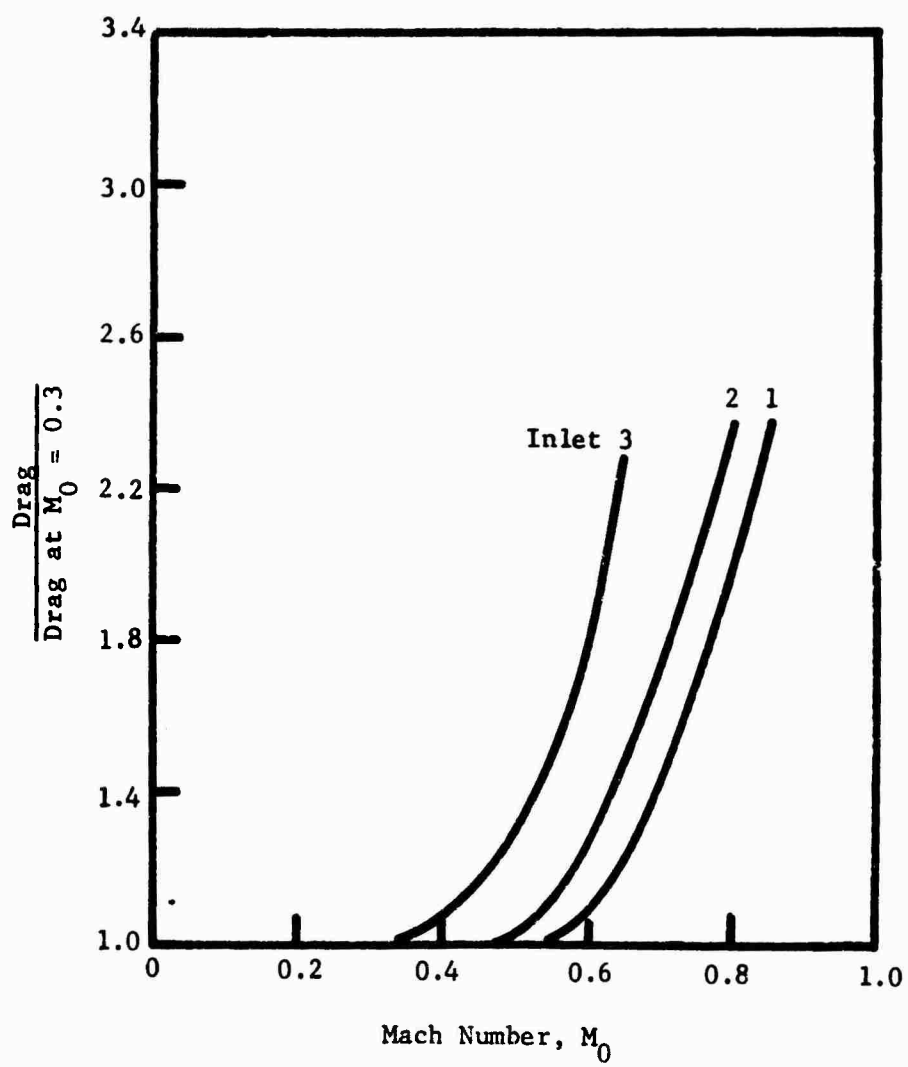|	Model
◺	5
◹	6
◿	7
◔	8

Figure 20. Nacelle Total Drag.

Figure 21. Nacelle Drag Rise.

NOTES

THRUST DEFLECTION NOZZLES FOR VTOL AIRCRAFT

by

VINCENT J. DISABATO

Pratt and Whitney Aircraft

East Hartford, Connecticut, United States

INTRODUCTION

Airplane studies reported in the literature have indicated that an aircraft using both lift cruise engines and lift engines provides a good propulsion system for a VTOL aircraft. The lift cruise engines are sized for horizontal flight. For VTOL thrust from the lift cruise engine is deflected downward, and the resulting thrust is supplemented by separate lift engines to provide the necessary total thrust. This paper discusses various means of deflecting the thrust from lift cruise engines in an efficient manner. The thrust deflector should have a vertical thrust to deflector weight higher than the thrust to weight ratio of the lift engines.

The thrust deflection device should:

1. Be lighter than a corresponding lift engine.
2. Deflect the thrust as efficiently as possible.
3. Provide horizontal performance equal to or nearly equal to an undeflected nozzle.

Data from nozzle model tests and thrust deflection devices conducted in the early 1960's is presented. This data illustrates the performance trends that can be expected from various thrust deflection devices and engine nozzles.

GENERAL THRUST DEFLECTOR NOZZLE DESIGN

The wide range of flight capability required of future VTOL aircraft demands nozzles that will be extremely versatile to meet critical design points efficiently and still maintain a deflection capability. Technology in the area of nozzles for horizontal

subsonic and supersonic flight has been developing steadily with the aid of scale model and flight testing. Thrust deflection, however, is relatively new and adds more complexity.

The function of the thrust deflection system is to turn the engine airflow from an axial direction to a vectored or vertical direction and thus provide lift. The vertical thrust produced by the deflector depends upon the static pressures acting on the walls of the nozzle and the wall static pressure must be higher than the static pressure surrounding the nozzle to produce a desirable thrust force.

Figure 1 shows the regions of pressure change on the inside and outside wall, (from Ref. 3, Figure 73). The static pressure distributions in a curved channel, upstream of a nozzle, differs from that of a straight duct due to the centrifugal force associated with the turning. This radial force produces an increase in pressure on the outside wall. On the inside wall, the pressure decreases around the bend and then increases to the exit.

The regions of adverse pressure gradients can cause the flow to detach or separate with a loss in total energy. The flow separation is most severe on the inner wall where the highest adverse pressure gradient occurs. This is shown graphically in Figure 2, (from Ref. 1, Figure 11). The velocity distribution is shown, at the exit of the bend, as a function of the distance from the inner wall for inlet Mach numbers of 0.32 and 0.66. It can be seen from the figure that the flow is separated, and no flow is encountered for 7 to 12 percent of the duct.

The total pressure loss distribution for an inlet Mach number of 0.2 is shown in Figure 3, (from Ref. 2, Figure 4). The inner wall shows the largest contribution to total pressure loss; this is true for the inlet Mach numbers of interest from 0.10 to 0.60.

Since the centrifugal force is a function of the turning radius, $F = \dfrac{dmv^2}{r}$ the parameter r/d is important, where "r" is the radius of the centerline of the constant area duct and "d" is the diameter. The turning radius ratio, pressure loss variation is shown in Figure 4, (from Ref. 1, Figure 10), for a few inlet Mach

2

numbers   The total pressure loss through the constant area duct is now defined.

It can be assumed that the addition of a nozzle to the duct will not appreciably change the pressure loss through the duct for an engine operating pressure ratio (P_t/P_a) of approximately two. The total pressure loss through the duct results in a loss in gross thrust coefficient. The total pressure loss is converted to gross thrust coefficient loss by the following equation.

$$\Gamma \frac{(F g_t/A_j P_t)}{d(P_t/P_a)} = 1/2 \left\{ \frac{2}{\gamma-1}\gamma^2 \left(\frac{2}{\gamma+1}\right)^{\frac{\gamma+1}{\gamma-1}} \left[1-\left(\frac{P_a}{P_t}\right)^{\frac{\gamma-1}{\gamma}}\right]\right\}^{-1/2} \left\{ \frac{-2\gamma^2}{\gamma-1} \left(\frac{2}{\gamma-1}\right)^{\frac{\gamma+1}{\gamma-1}} \left(\frac{1-\gamma}{\gamma}\right)\left(\frac{P_t}{P_a}\right)^{\frac{1-\gamma}{\gamma}-1} \right\}$$

The gross thrust coefficient loss is shown in Figure 5 as a function of the duct turning radius for a few inlet Mach numbers.

For a constant area duct turn, the following compromises are evident from a study of Figure 5:

1. Low inlet Mach number is necessary for a high gross thrust coefficient.

2. A turning radius of approximately 2.5 duct diameters is optimum for high gross thrust coefficient.

GENERAL THRUST DEFLECTOR REQUIREMENTS

The cycle used in the lift-cruise engine has a strong influence on the design of the thrust deflector. The number of deflectors for each engine can vary from one or two for a simple jet engine to as many as four for a fan engine (two for the fan and two for the primary stream). The burner length requirements for the augmenting system can affect the location of the deflectors. Augmentation may also cause rejection of otherwise attractive deflection schemes because of:

1. Excessive cooling requirements.

2. Variable area nozzle requirements.

The engine installation in the aircraft affects the design of the deflector system in the following ways:

3

<u>VTOL mode</u>

The basic stability of the aircraft during take-off and landing requires that the sum of the moments produced by the thrust of the engines around the aircraft c.g. be in static balance. Using lift engines in addition to the deflected lift cruise engine allows greater freedom in the choice of engine and/or engine deflection locations, i.e. the engines need not be concentrated at the aircraft c.g.

<u>Transition mode</u>

The deflection device must be continuously controllable during transition to provide an axial component to accelerate the aircraft while maintaining enough lift. No unwanted roll components should exist. The deflector should respond quickly and accurately during transition.

<u>Forward flight mode</u>

The nozzle must have high performance in the horizontal mode where all of the usual nozzle thrust and drag problems with external flow will be present.

DISCUSSION OF DEFLECTOR TYPES

Deflection devices which have been studied in the past few years include:

1. Swivel nozzle
2. Ventral nozzle
3. Ventral nozzle with rotating cascade
4. Aft-hood deflector

Swivel Nozzle

The swivel nozzle uses the same duct for the horizontal and vertical flight modes. The nozzle is rotated on a bearing to change the thrust vector from horizontal to vertical and is shown in Figure 6. The gas path for the horizontal mode requires a degree of flow turning. This inherently causes a slight performance loss in the horizontal mode. As the nozzle is rotated for transition, the flow turning is increased by a small amount and, therefore, the transition performance and the vertical performance can be good. During transition, however, the swivel nozzle develops a

4

side force as it rotates around the bearing. This side force must be counterbalanced if only one lift cruise engine is planned for the aircraft, usually requiring the use of two swivel nozzles.

The swivel nozzle is simple and can have a simple and reliable actuation system. The thrust to weight of this type of system is in the range of 35 to 50 according to our studies. The swivel nozzle, however, is not flexible enough to be used or modified effectively for efficient supersonic horizontal flight. The swivel nozzle causes an increase in cross sectional area of the aircraft. Minimizing this increase of frontal area results in a much increased weight of the swivel nozzle, hence a poorer thrust to weight ratio.

Ventral Nozzle

The ventral nozzle is located in the afterburner section of the engine. A flow blocker, possibly a clamshell, is used to make the transition from the horizontal to vertical mode. The ventral nozzle device shown in Figure 7 has a clamshell to close off part of the horizontal flow and open up part of the ventral nozzle so a constant total amount of flow comes from the engine at any clamshell position. The clamshell is closed until all of the flow is coming out the ventral nozzle to obtain vertical thrust.

During horizontal flight, the gas path is unhampered by the deflection device. This allows the maximum augmentation for horizontal operation and any type of supersonic nozzle can be used with the ventral nozzle deflector.

The thrust to weight of the ventral nozzle would be in the range of 18 to 25. This is somewhat heavier than the swivel nozzle, but produces no increase in aircraft frontal area due to the deflector.

Ventral Nozzle with Rotating Cascade

The ventral nozzle with cascades is very similar to that without cascades. The flow blocker, however, in the nozzle with cascades completely blocks the horizontal flow at the same time uncovering the ventral opening. The transition from the

5

horizontal to vertical mode is then made by the rotation of the cascade. This scheme is shown in Figure 8.

The thrust to weight of this deflector system would also be in the range of 18 to 25.

Aft-Hood Deflector

The aft-hood deflector deflects the flow by a curved blocker located in a supersonic nozzle downstream of the afterburner. Augmentation is available for deflected thrust operation. The aft-hood deflector is shown in Figure 9.

The transition from the horizontal to vertical mode is made by opening doors in the bottom of the ejector shroud and rotating the hood to the desired position for the vertical mode. The primary or afterburner nozzle is then opened to the max-afterburning position, thus transferring the minimum jet area or control area to the deflector exit. This is done so that the flow can be turned at a low Mach number reducing the turning losses through the system.

The transition from the vertical to horizontal mode is made by rotating the hood to the stowed position. When a thrust vector of approximately 45 degrees is obtained, the control area is switched back to the primary nozzle by closing down the primary nozzle. The hood is quickly rotated into the stowed position, and the ejector shroud is closed.

The gas path is unhampered by the deflection system and max-augmentation is possible when the hood is stowed. This system has very good thrust vectoring capability and supersonic performance.

The thrust to weight of this system is in the range of 20 to 30, or somewhere between the ventral nozzle and the swivel nozzle.

EXPERIMENTAL TEST FACILITY

Thrust deflector nozzle performance data presented in this paper was obtained from scale model tests in the United Aircraft Research Laboratory static cold flow facility. The facility was originally designed to conduct static tests on airbreathing

6

engine exhaust models. It has been adapted for thrust deflector testing by the addition of a rotating plenum. The balance and rotating plenum are shown in Figure 1C.

The rotating plenum is used to rotate the force vector produced by the thrust deflector to a horizontal position. The angle of the rotating plenum or the angle cf the thrust vector is recorded while the force magnitude is measured by the balance. Forces are measured with a thoroughly developed null type balance. A hollow tube, supported by a pair of flexures to the balance housing, is constrained to move only in the thrust or drag direction. Balance displacements are indicated by a Schaevitz coil. Nulling is achieved by adjustment of the balance base pressure. Once the balance is nulled, the pressures are recorded; these measurements are transformed into nozzle thrust coefficients. Airflow measurements are made in accordance with standard ASME techniques using a bellmouth flow meter.

TYPICAL DEFLECTED JET PERFORMANCE

Swivel Nozzle

A swivel nozzle scale model of a nonaugmented engine system is shown in Figure 11. The Mach number at the inlet to the model is 0.35 and the model is approximately one tenth full size. The performance of this nozzle at various nozzle pressure ratios and rotation angles is shown in Figure 12. The horizontal performance is 2 to 3 percent lower than a convergent nozzle would obtain due to a bend in the duct upstream of the swivel bearing. The performance falls smoothly during transition by another 2 to 3 percent as the nozzle is rotated due to worsening of the internal geometry.

The flow coefficient is nearly constant during the transition. The thrust angle lags the nozzle geometric angle for 60 and 90 degrees, but this can be compensated for by overturning the nozzle to obtain the desired thrust angle.

Ventral Nozzle

A ventral nozzle is shown in Figure 13. The model simulates a possible full scale installation having a ventral nozzle located downstream of the turbine exit plane

7

in the afterburner. Afterburning while in the deflected mode with the ventral nozzle in this position would be difficult; therefore, the model jet area simulated a nonafterburning full scale engine condition for the vertical mode. The inlet Mach number to the ventral nozzle tested was 0.20.

The performance of the ventral nozzle is shown in Figure 14. The thrust coefficient is 4 to 6 percent lower than a convergent nozzle. The results were obtained for a simple design and it is possible to improve the performance with a more refined design.

The flow coefficient at a pressure ratio of 2.0 is about 10 percent below a conventional convergent nozzle. The hole can be sized on this basis to pass the engine flow, or the design can be modified to improve the flow coefficient. The transition from the horizontal mode of this deflection system is made by closing down the horizontal nozzle and opening the ventral nozzle. This type of transition is shown in Figure 15. The transition performance is compromised with this type of operation because the flow is divided between the horizontal and ventral nozzle.

Ventral Nozzle with Rotating Cascade

A ventral rotating cascade nozzle model is shown in Figure 16. This device is similar to the ventral nozzle previously described. Performance for the transition from the horizontal to vertical mode is shown for the case of blocking completely the horizontal passage and opening the ventral opening while the cascade is rotated for thrust vectoring the model simulated nonafterburning engine operation. The inlet Mach number to the ventral nozzle was 0.20. This model is identical to the ventral nozzle shown above except for the rotating cascade.

The performance of the ventral nozzle with cascade is shown in Figure 17 for 90 degrees thrust deflection. The addition of the cascade to the ventral nozzle decreased the thrust by another 4 percent for a total loss of almost 10 percent from a convergent nozzle. Further work on the design of the rotating cascade and the approach to the cascade could improve the performance; however, we have found that cascades do have

an inherent loss associated with their design.

The transition performance is shown in Figure 18. The performance decreases rapidly as the cascade is rotated due to the vector angle of the flow from the cascade which is not measured. This side force would be canceled with a two engine installation. Two nozzles would be necessary to cancel the side force in a single engine installation. It is obvious that this deflector is not desirable below 75 degrees or 80 degrees deflection.

Aft-Hood Deflector

An aft-hood deflector model is shown in Figure 19. Since this deflection device is capable of partial augmentation, a partial augmentation engine condition was simulated by the model. The inlet Mach number to the nozzle was 0.315. The performance is shown in Figure 20. The thrust coefficient of this system is good, within 2 or 3 percent of a convergent nozzle at full deflection. The flow coefficient is lower than what is expected from a convergent nozzle; however, the effective area, AjQ, is sufficient for the engine condition. If an unaugmented engine condition were simulated the turning losses would further decrease. The transition performance is shown in Figure 21 for a pressure ratio of two. It can be seen from the figure that the aft-hood transition performance is also good, losing only 2 to 3 percent additional thrust at the worst condition.

GROUND EFFECTS

The use of deflected jet exhaust for vertical thrust raises the problem of ground proximity effects on the engine exhaust nozzle performance. The deflected nozzle, when in the vertical mode, would be close to the ground causing large changes in nozzle performance. A series of tests have been performed to determine the effect of ground proximity on nozzle performance.

The performance characteristics presented are for an uninstalled circular convergent nozzle. There are no surfaces except the nozzle itself and the ground upon which the flow acts. The performance is shown in Figure 22. It is seen that the

nozzle performance decreases rapidly with decreasing distance to the ground. This means that serious engine flow suppression as well as a loss in thrust will occur if the nozzle exit is positioned too close to the ground.

TRANSITION TIME

A simple study was made to illustrate that the transition time from hovering to axial flight of a given VTOL aircraft can be affected by deflector characteristics. Two lift cruise engine deflection systems are compared, the ventral nozzle and the ventral nozzle with rotating cascades. These two systems were used because they would require no changes in the lift drag relationships of the aircraft.

A typical lift cruise airplane having 60,000 pounds gross weight was assumed for this analysis, powered by two lift cruise engines and four lift engines. The lift cruise engines have a take-off thrust of 24,000 pounds each and the lift engine 6,000 pounds each. The total available vertical thrust is 72,000 pounds.

The transition time is shown in Figure 23. The results show that the greater horizontal thrust of the cascade initially increases the velocity of the airplane at a faster rate than the ventral nozzle without the cascade. After about ten seconds, the opening of the axial nozzle results in a faster rate of acceleration for the ventral nozzle without the cascade. The ventral nozzle with the rotating cascade completes the transition more slowly than the ventral nozzle without the cascade but is at a higher altitude.

This comparison reaches no conclusions other than the fact that the choice of deflector has a significant effect on transition time. Obviously, a short transition time is desirable, but the time must be evaluated against the flight path (altitude vs distance) and stability.

CONCLUSIONS

It was found that the inner wall of a bend shows the largest contribution to the total pressure loss of the bend. Good thrust performance will be obtained when the inlet Mach number to the bend is low and the turning radius ratio is approximately 2.5

10

duct diameters.

The conclusions reached in the paper for each of the deflection devices are shown in the following comparison.

	90° Deflection Thrust Coef. Cvr	Vectoring Capability	Supersonic Capability	Effect on Horizontal Performance	Deflector Thrust/Weight*
Swivel Nozzle	0.94	Good	Limited	1 to 3% Decrease	35 to 50
Ventral Nozzle	0.93	Limited	Good	No Effect	18 to 25
Ventral with Rotating Cascade	0.89	Limited	Good	No Effect	18 to 25
Aft-Hood Deflector	0.96	Good	Good	No Effect	20 to 30

*Vertical Thrust Divided by Weight added by Deflection Device

The performance levels shown are for rather crude test models. In each case one can expect to refine these models and airflow characteristics and reach higher performance levels. Improvements in thrust to weight ratios are also possible.

On the other hand, approximately the same degree of effort went into each of these designs and it is possible that the deflector that best satisfies the requirements of a good thrust deflector is the Aft-Hood Deflector.

REFERENCES

1)   Higginbotham, Wood, Valentine: "A Study of the High-Speed Performance Characteristics of 90 Degree Bends in Circular Ducts", NACA TN 3696, June 1956.

2)   Wilbur, Stafford W.: "An Investigation of Flow in Circular and Annular 90 Degree Bends with a Transition of Cross Section", NACA TN 3995, June 1957.

11

3)   Kaufmann, Walter: "Fluid Mechanics", McGraw Hill 1963.

4)   Horgan, Migdal: "Thrust Nozzles for Supersonic Transport Aircraft", ASME
        63-AHGT-73, January 1963.

NOMENCLATURE

P_T -   Total pressure

P   -   Static pressure

D   -   Diameter

r/D   -   Turning radius ratio

M   -   Mach number

Fg_1 -   Ideal gross thrust = $A_j Q P_t \sqrt{\dfrac{2\gamma^2}{\gamma-1} \left(\dfrac{2}{\gamma+1}\right)^{\frac{\gamma+1}{\gamma-1}} \left[1 - \left(\dfrac{Pa}{Pt}\right)^{\frac{\gamma-1}{\gamma}}\right]}$

Q   -   Flow coefficient equal to the measured-to-ideal weight flow

A   -   Physical area

Θ   -   Angle between the engine centerline and the deflected gross thrust
            vector in the vertical plane

Cvr   -   Deflected gross thrust/ideal gross thrust

q   -   Dynamic pressure

SUBSCRIPTS

1   -   Region before flow turn

2   -   Region after flow turn

J   -   Nozzle exit

a   -   ambient

REGIONS OF INCREASING STATIC PRESSURE

AIRFLOW

CENTRIFUGAL FORCE

dm

r

$$\text{CENTRIFUGAL FORCE} = \frac{dm\,v^2}{r}$$
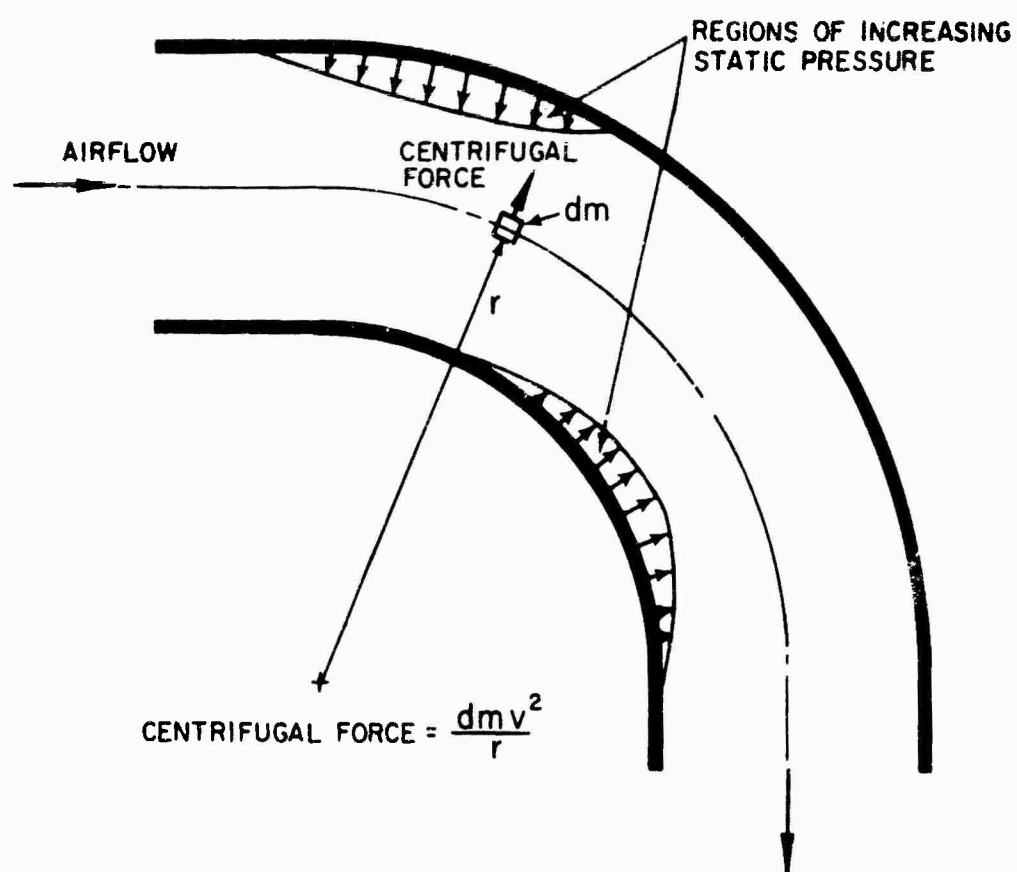
Figure 1   Flow Through a Bend

13
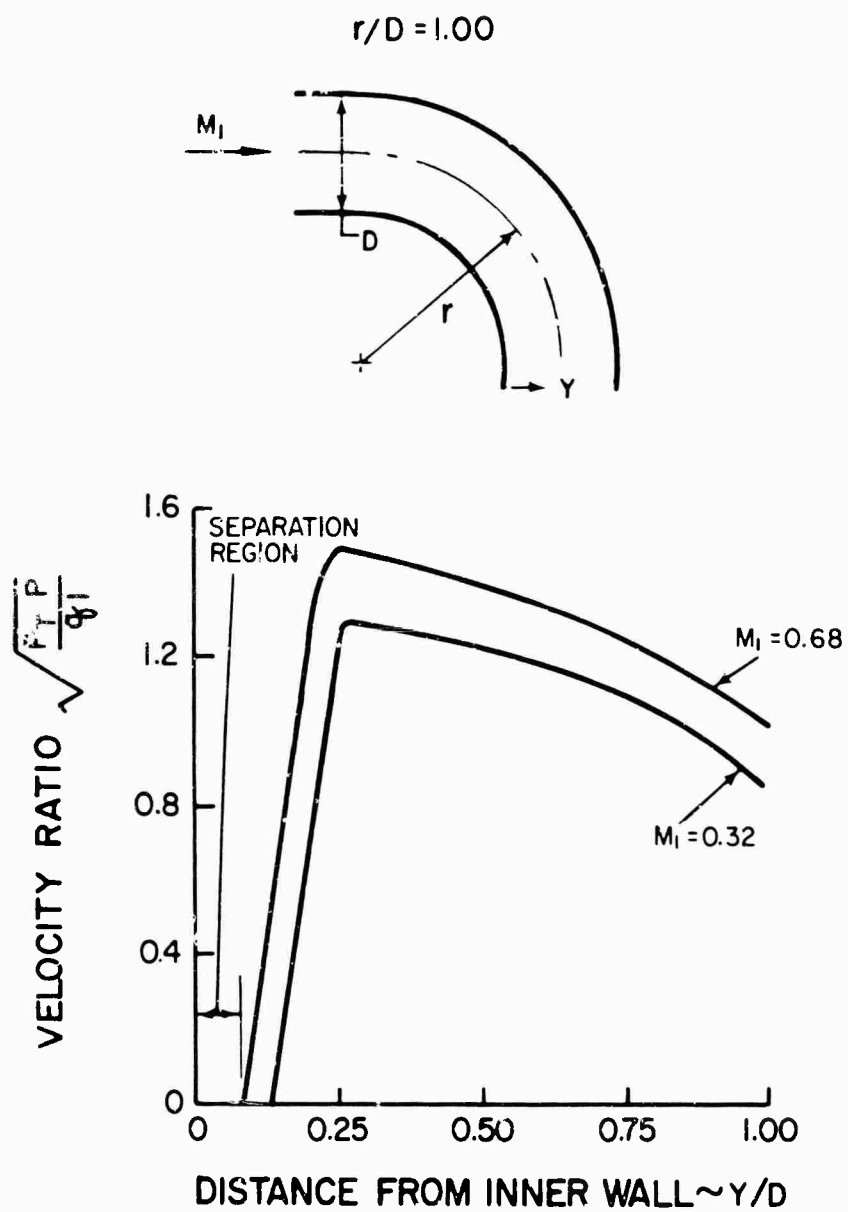
Figure 2   Local Velocity Variation at the Exit of a Bend
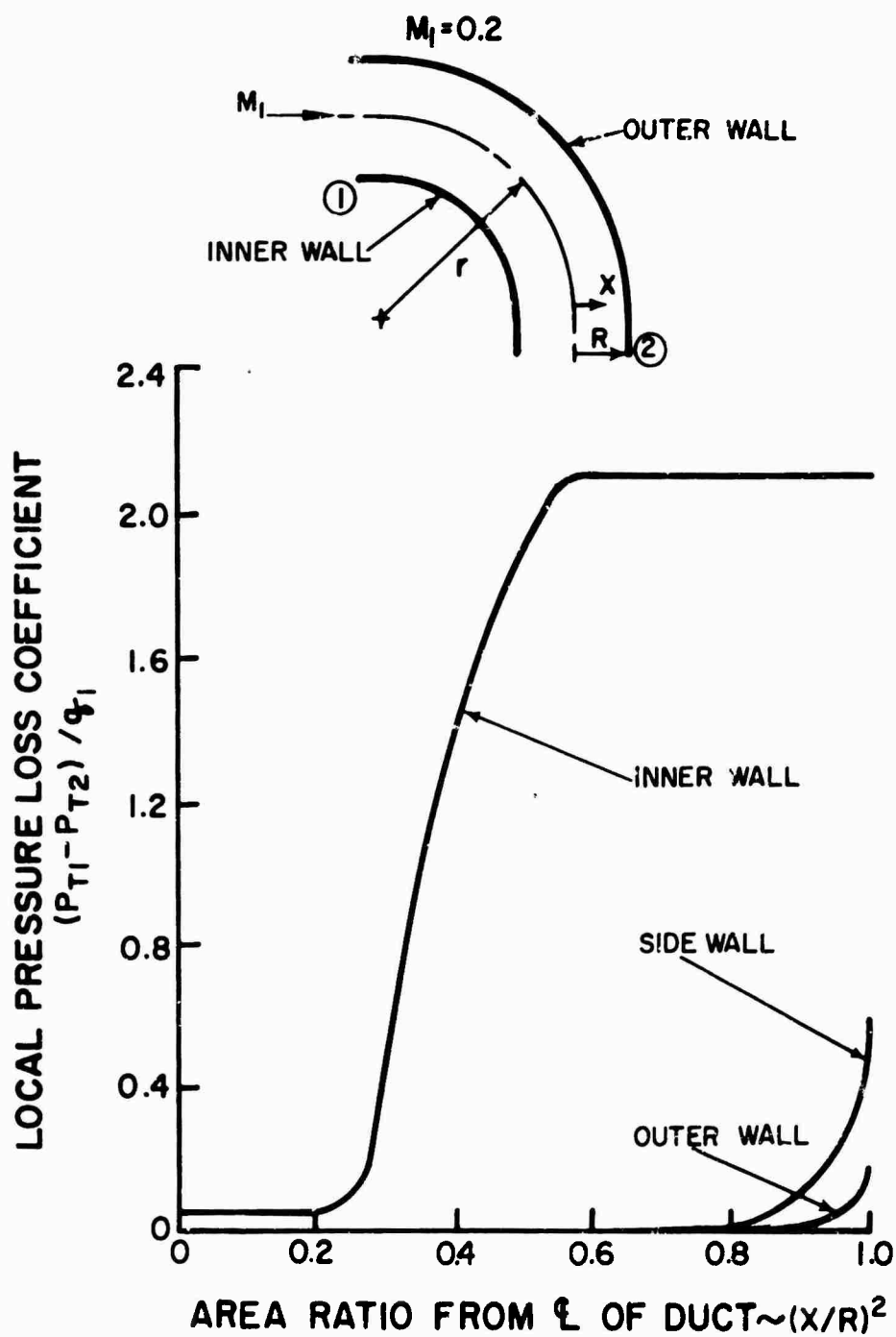
Figure 3   Total Pressure Loss Distribution

15
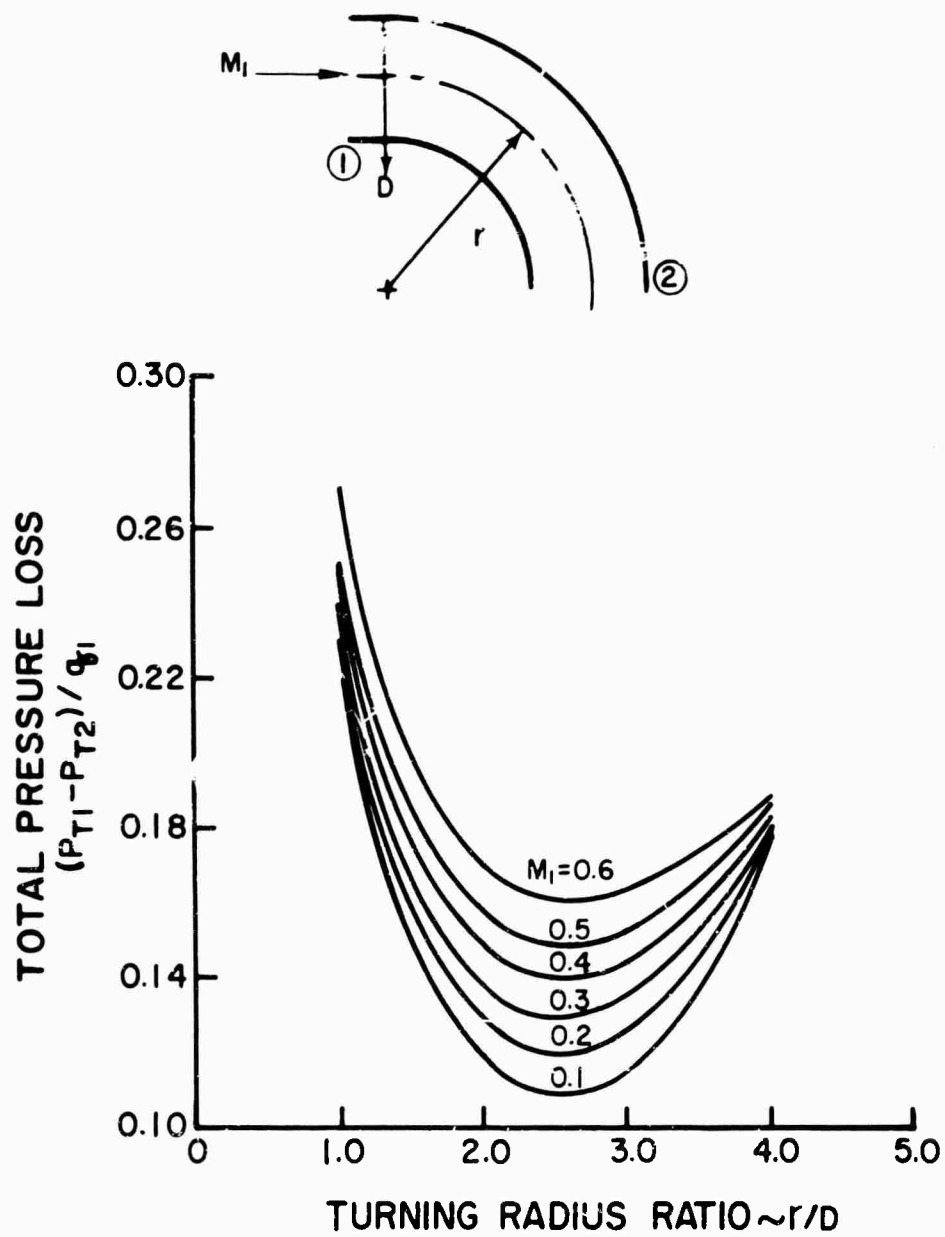
Figure 4   Total Pressure Loss Variation with Turning Radius

16
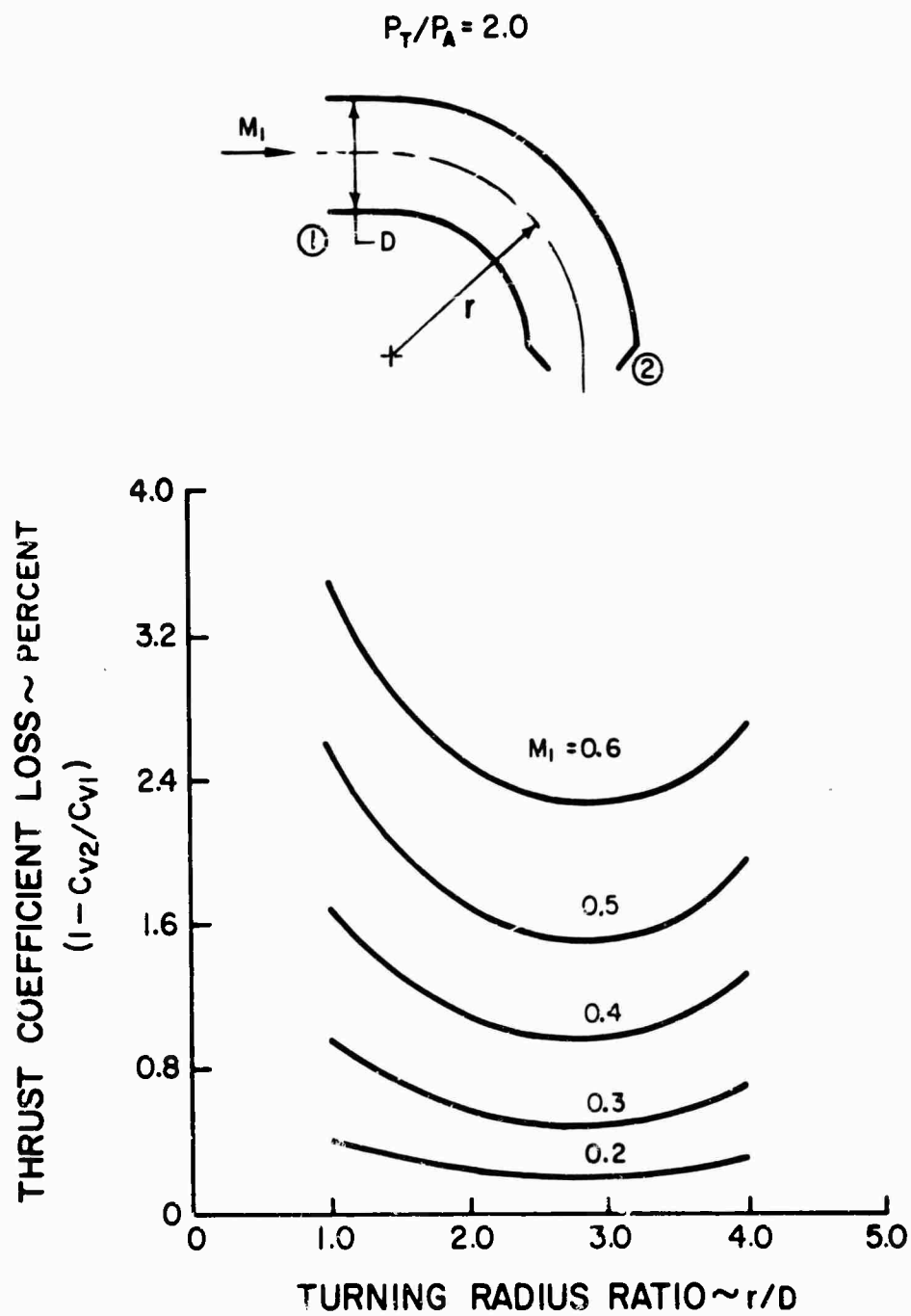
Figure 5   Thrust Coefficient Loss Variation with Turning Radius

17

SWIVEL
BEARING
HOUSING

NOZZLE ROTATION AXIS
NOZZLE AND THRUST VECTOR
ROTATE ABOUT THIS AXIS

THRUST VECTOR
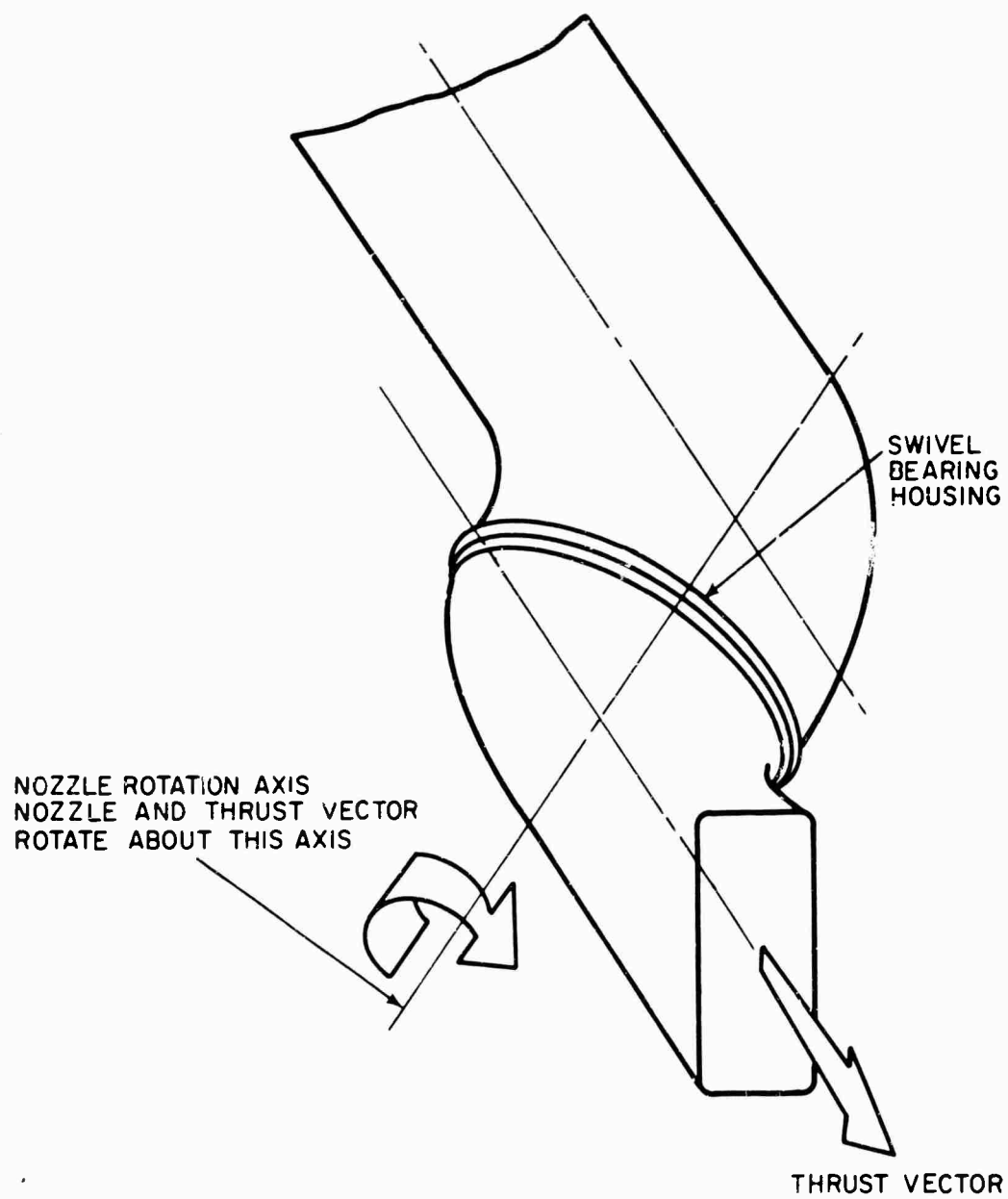
Figure 6   Swivel Nozzle Operation Axial Thrust Position

18
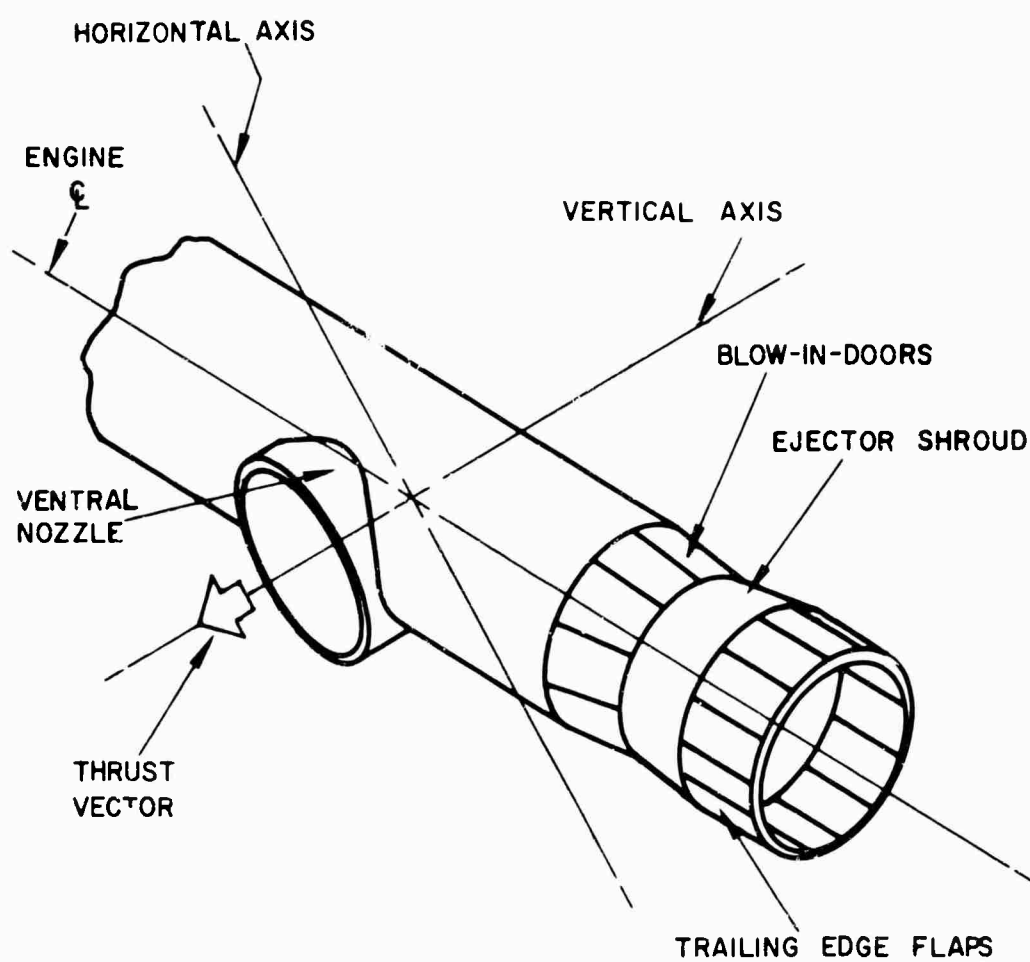
Figure 7   Ventral Nozzle Installation VTOL Position

19

HORIZONTAL AXIS

VERTICAL AXIS

AXIS OF ROTATION
(CASCADE AND THRUST VECTOR
ROTATE ABOUT THIS AXIS)

ANGLE BETWEEN AXIS
OF CASCADE ROTATION
AND HORIZONTAL AXIS

EJECTOR SHROUD

VENTRAL
NOZZLE

CASCADE

THRUST
VECTOR

ROTATIONAL
BEARING HOUSING

BLOW-IN-DOORS

TRAILING EDGE FLAPS
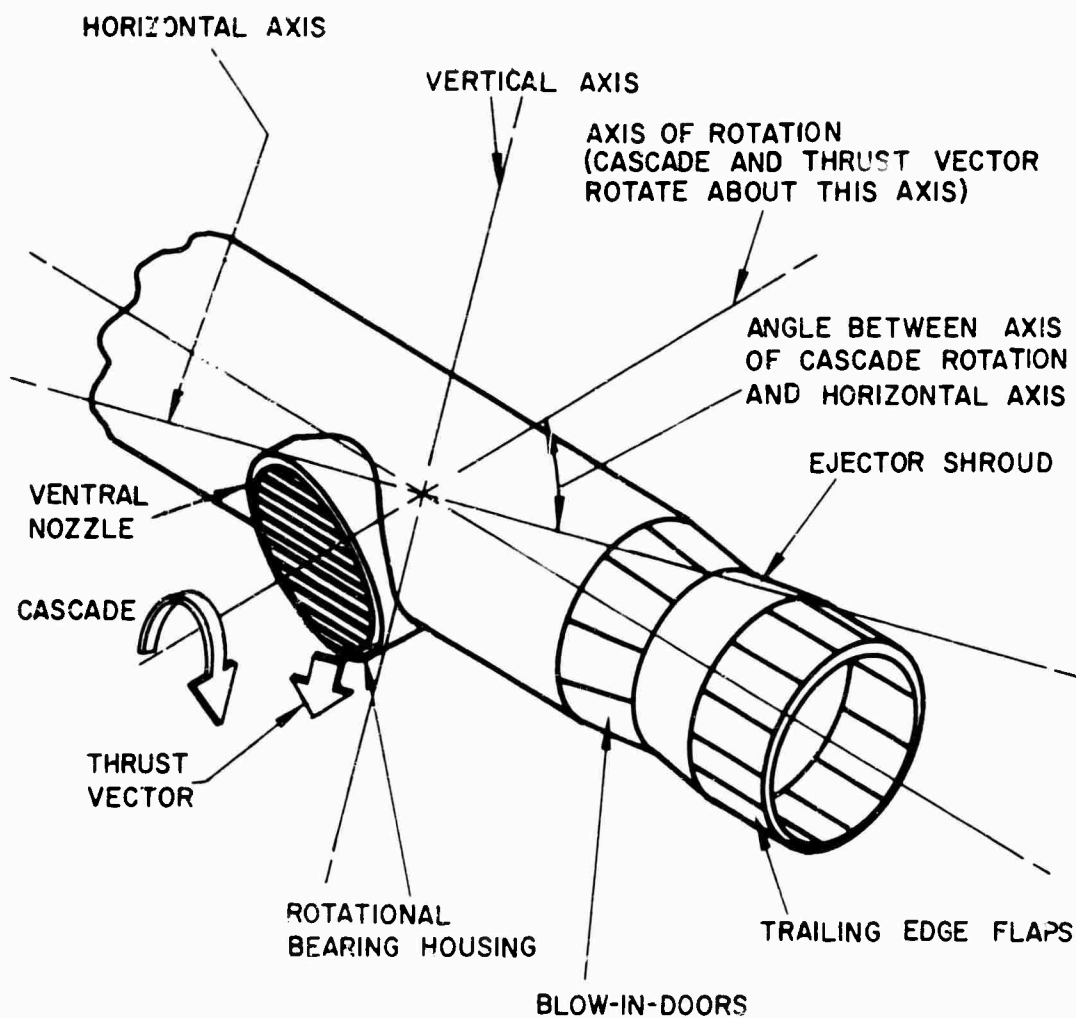
Figure 8   Ventral Nozzle Operation VTOL Position

BLOW-IN-DOORS

AFT-HOOD

PRIMARY
NOZZLE

TRAILING EDGE
FLAPS
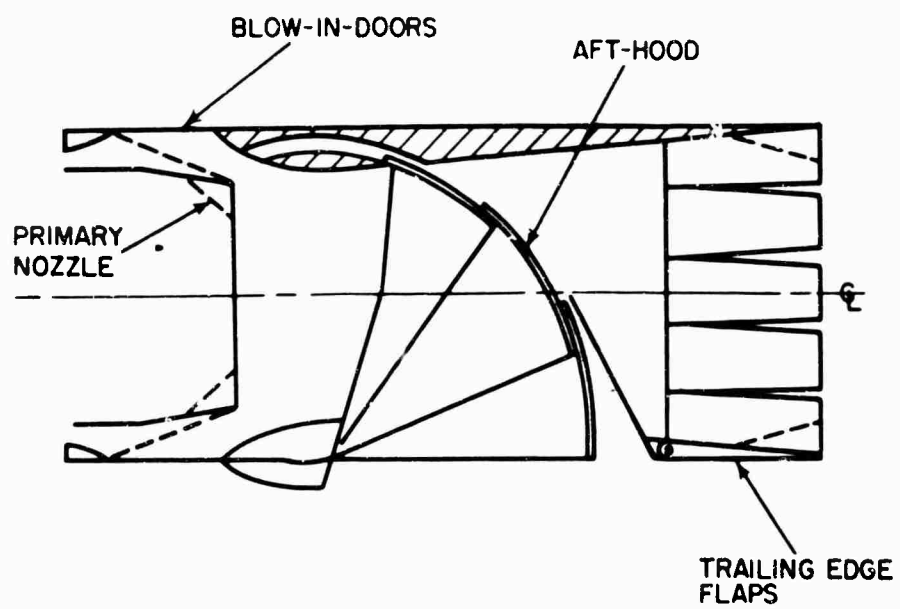
Figure 9   Aft-Hood Deflector Installed in Blow-In-Door Ejector

21

DEFLECTION NOZZLE

PLENUM ROTATING MOTOR

AXIAL THRUST BALANCE

PLENUM

AIR SUPPLY
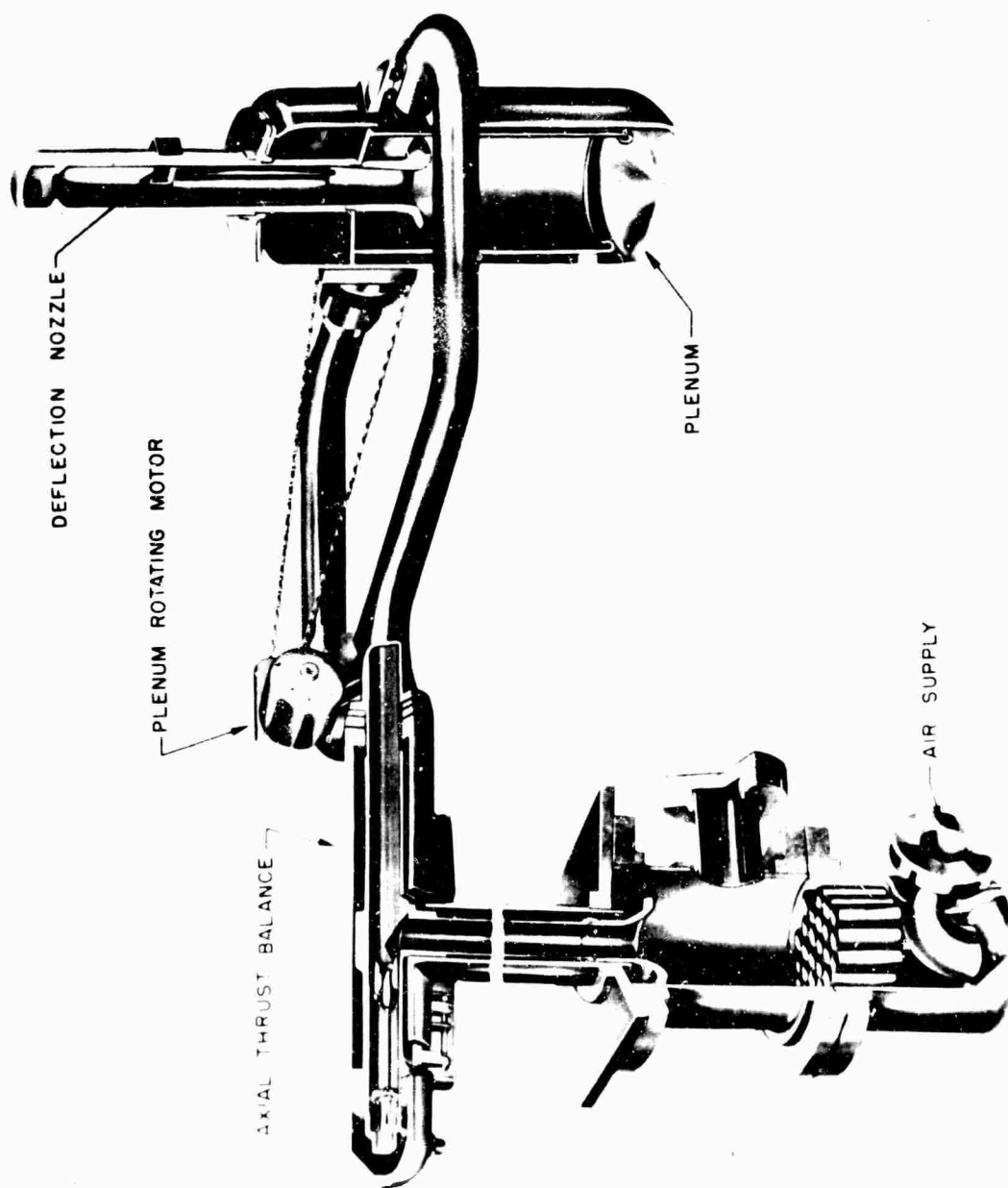
Figure 10   Rotating Plenum Thrust Balance

Figure 11   Swivel Nozzle Model 90 Degree Deflected Position
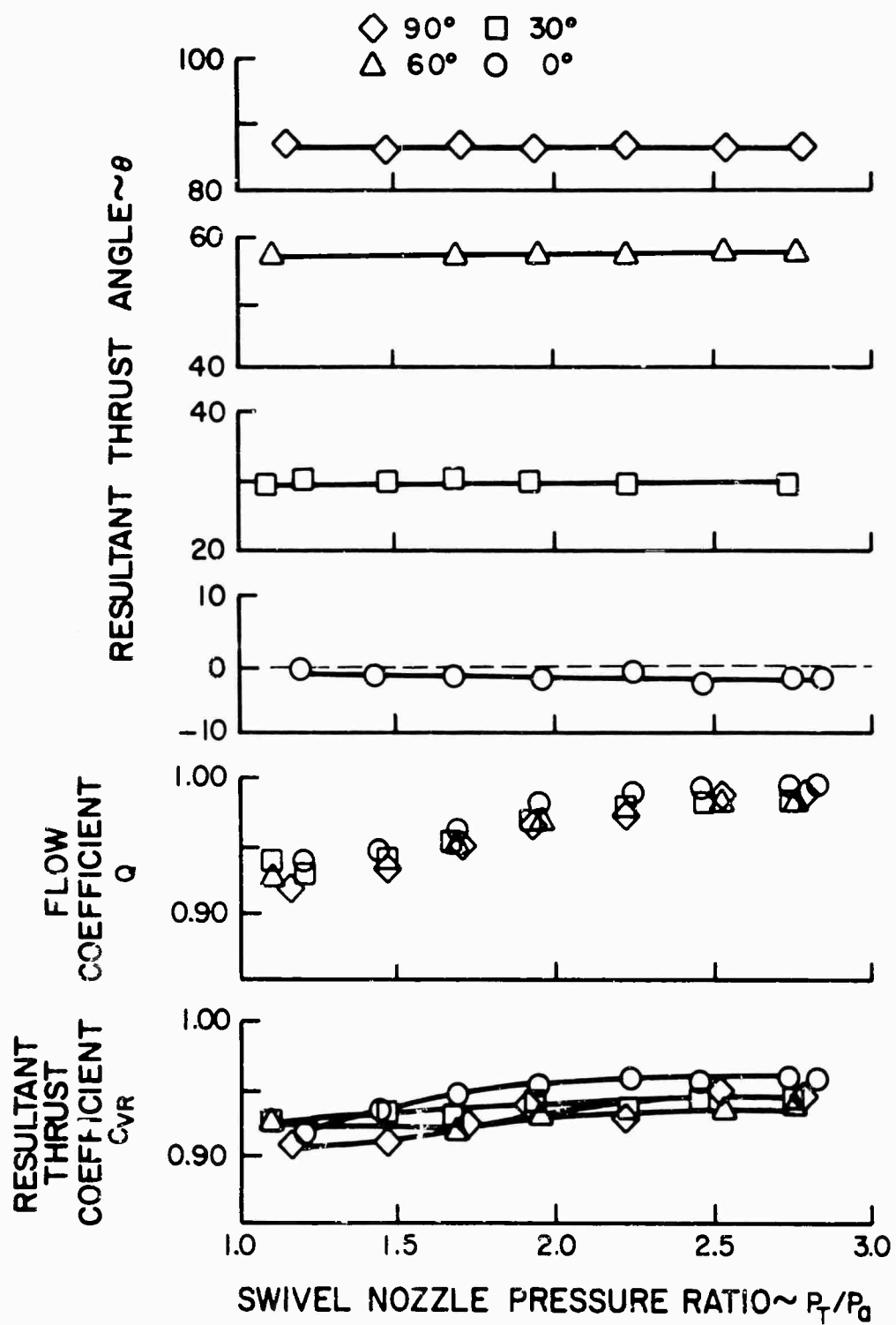
Figure 12   Swivel Nozzle Performance

24

Figure 13   Ventral Nozzle Model
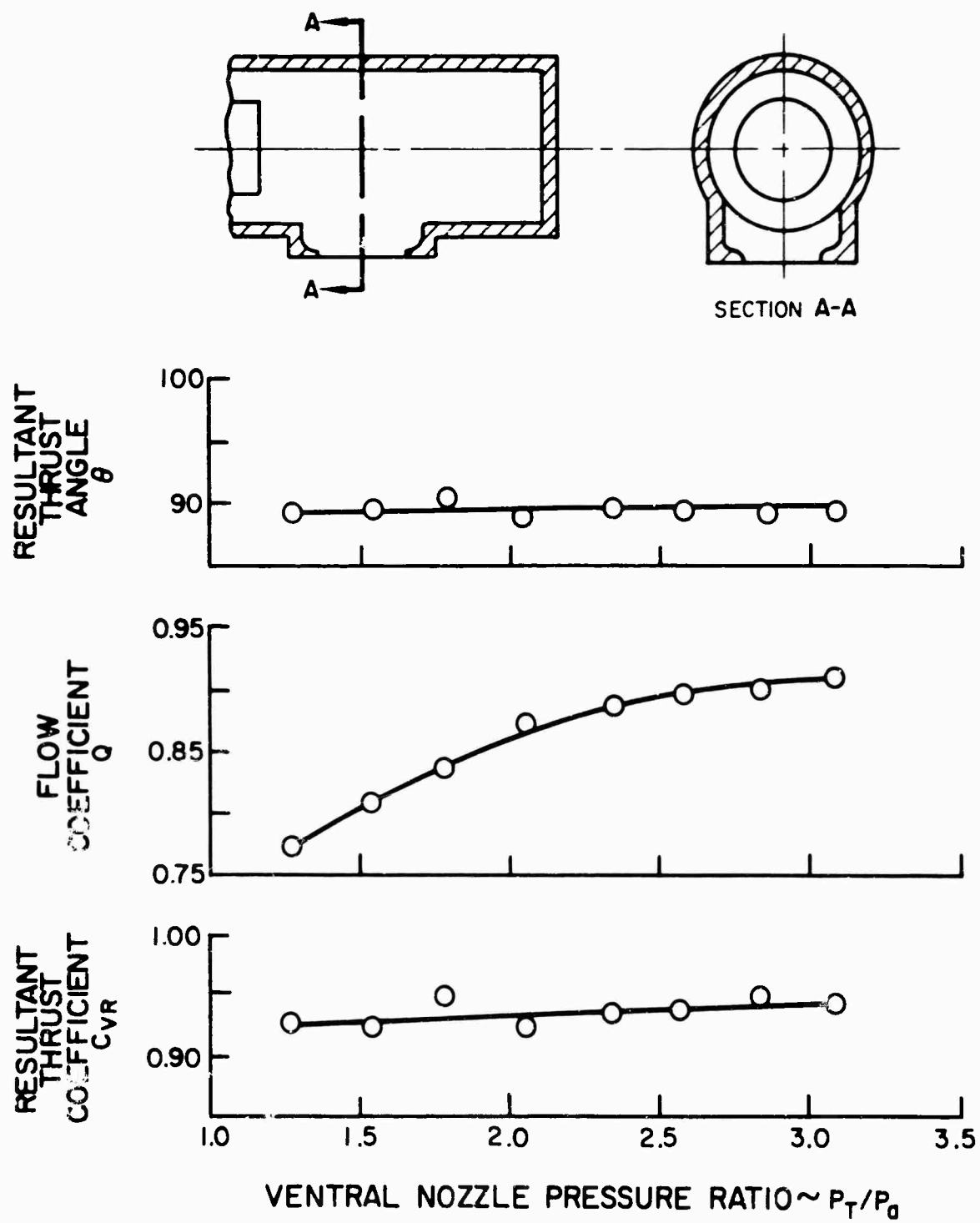
Figure 14   Ventral Nozzle Performance

$P_T/P_a = 2.0$

SECTION A-A

RESULTANT THRUST COEFFICIENT ~ C_{VR}

ESTIMATED

RESULTANT THRUST ANGLE ~ θ ~ DEGREES
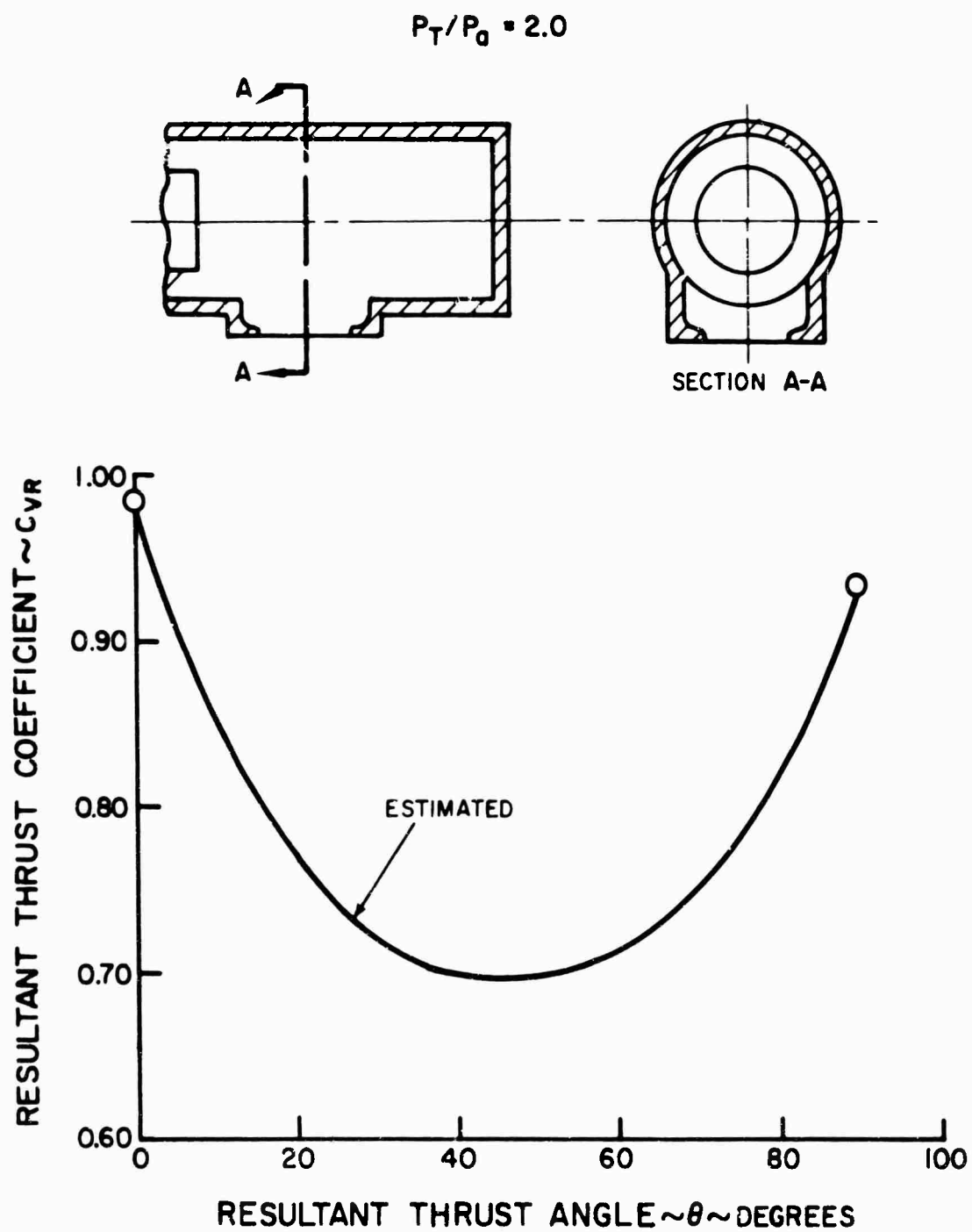
Figure 15   Ventral Nozzle Transition Performance

27

Figure 16   Ventral Nozzle with Rotating Cascade Model
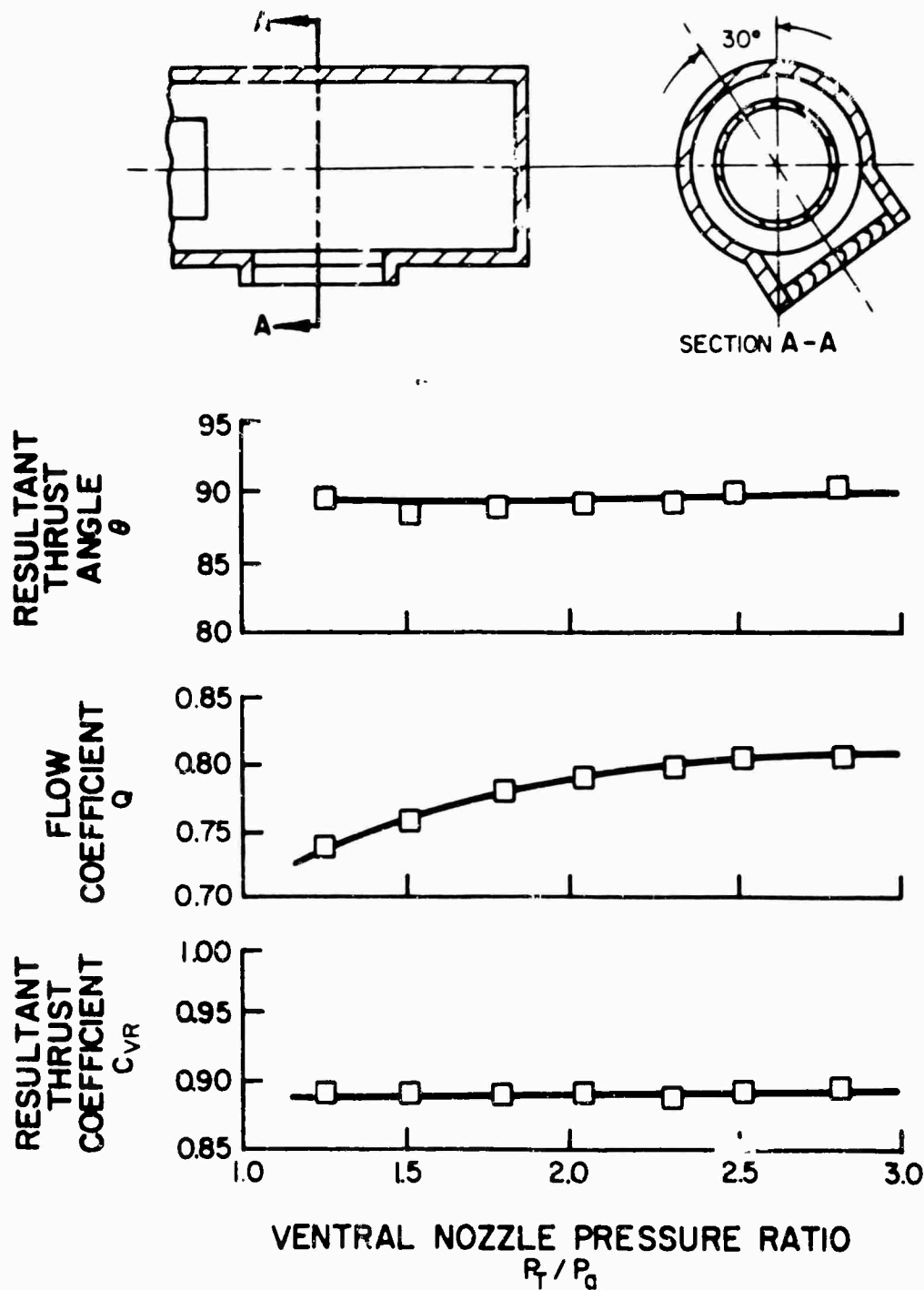
Figure 17   Ventral Nozzle with Rotating Cascade Performance

$P_T /P_a = 2.0$
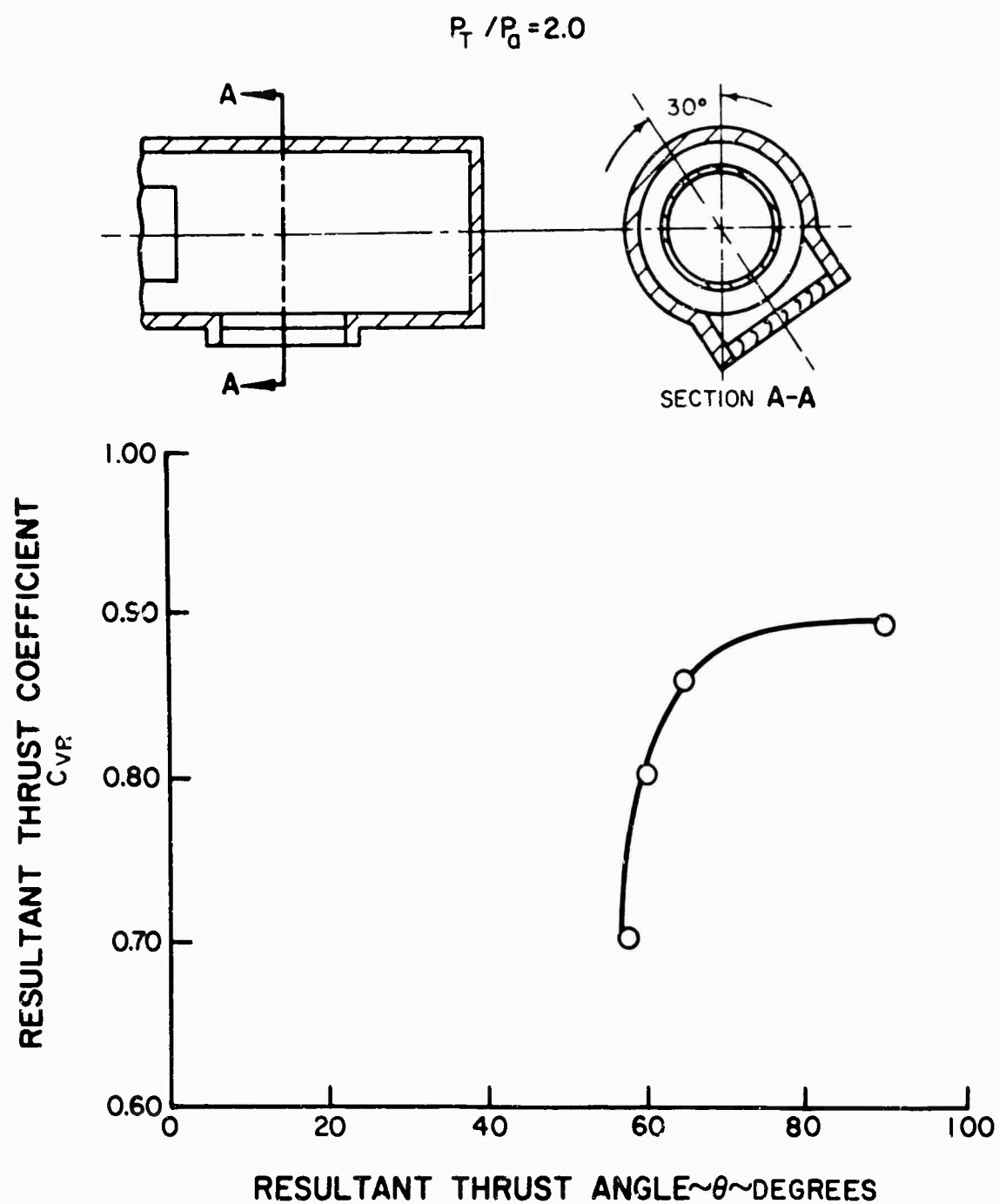
Figure 18   Ventral Nozzle with Rotating Cascade Transition Performance

30

Figure 19   Aft-Hood Deflector Model
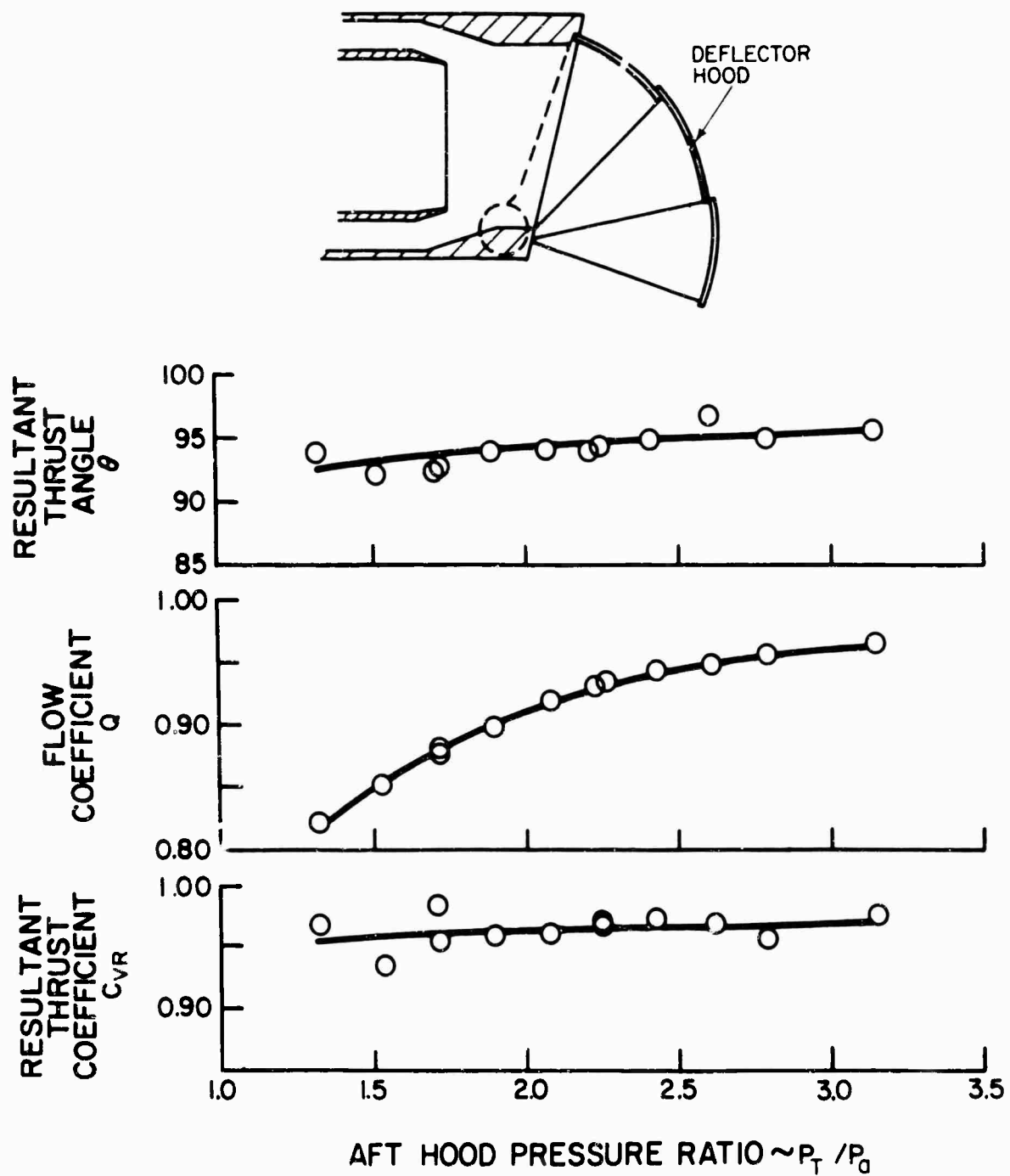
Figure 20   Aft-Hood Deflector Performance
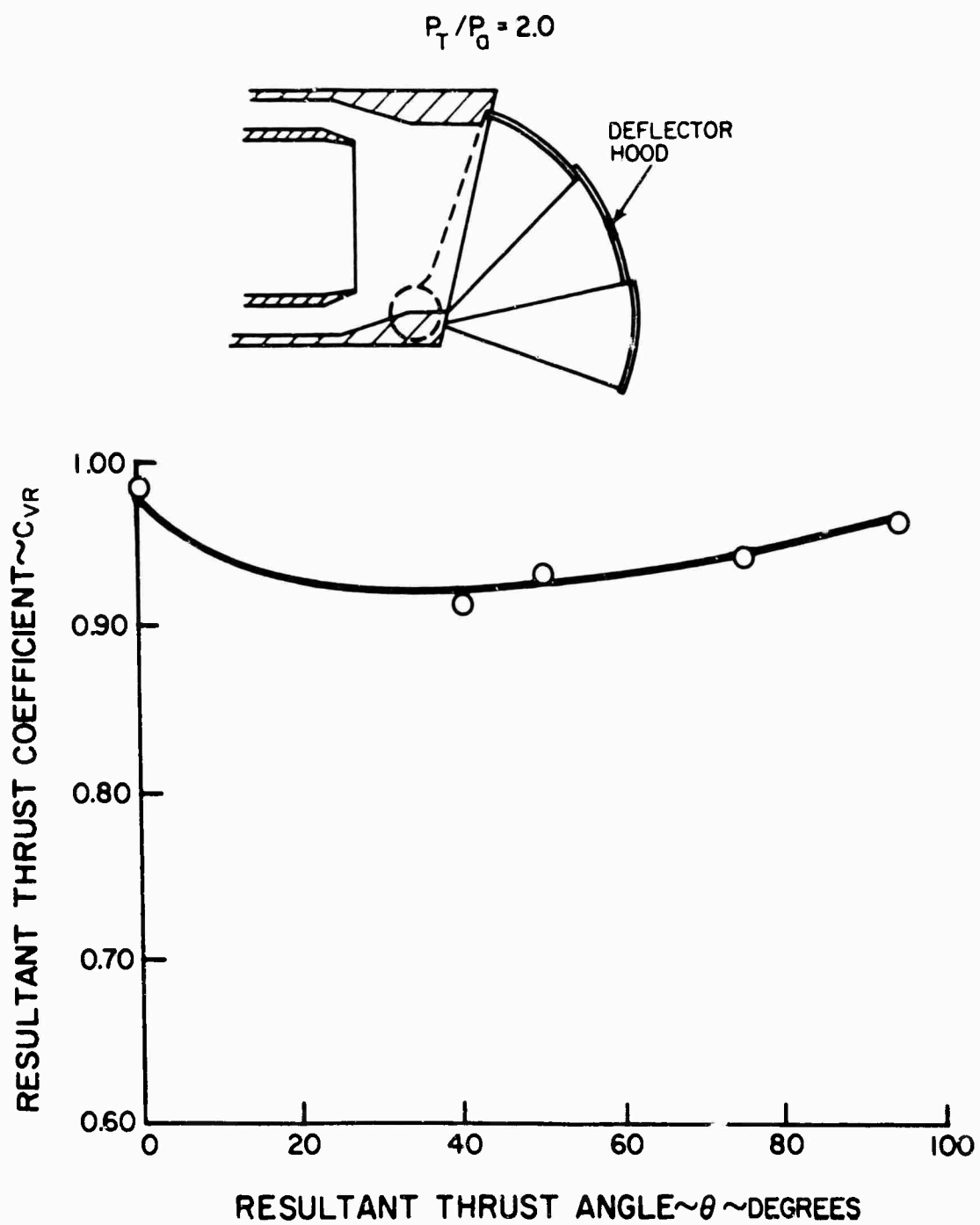
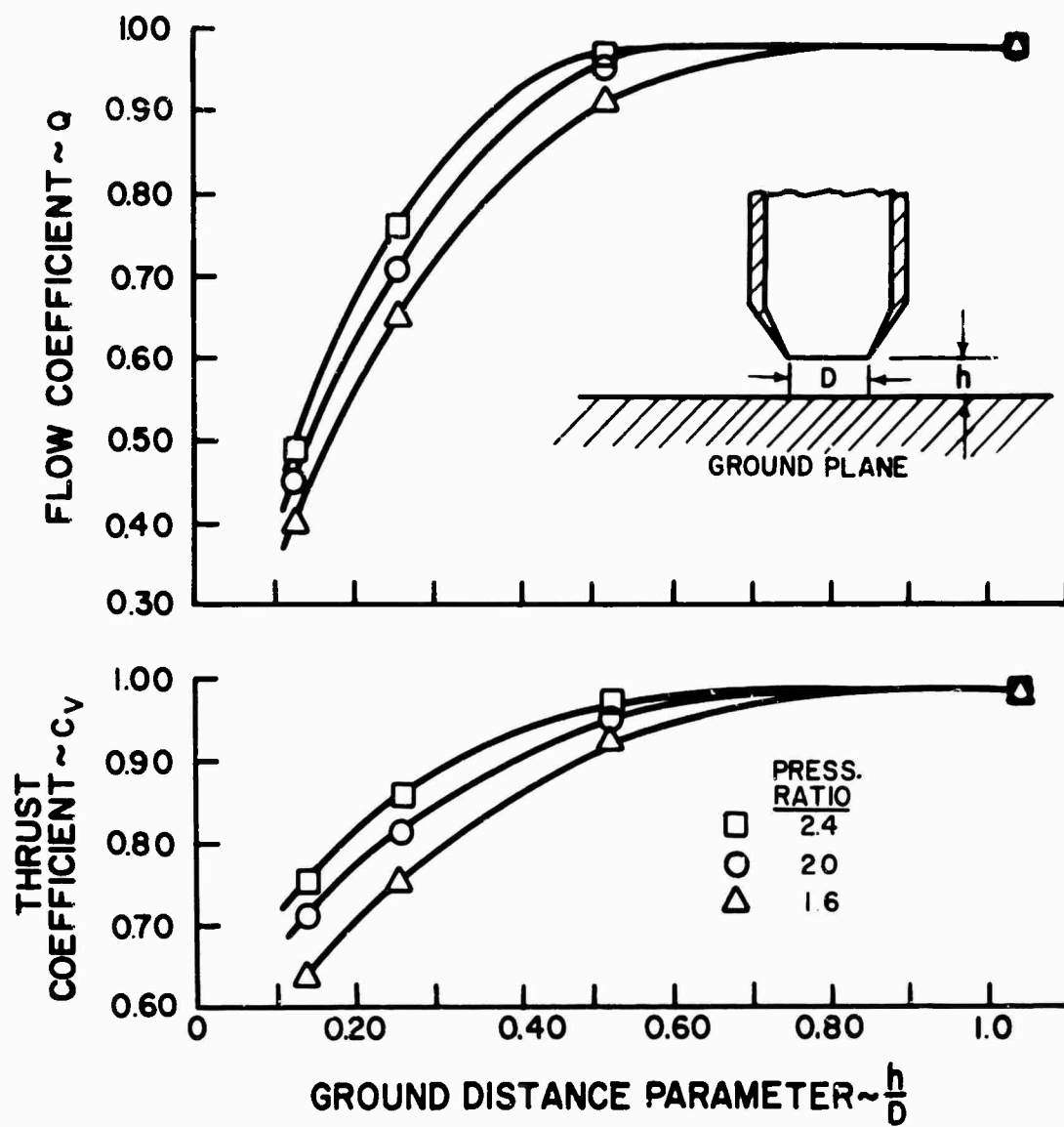Figure 21   Aft-Hood Deflector Transition Performance

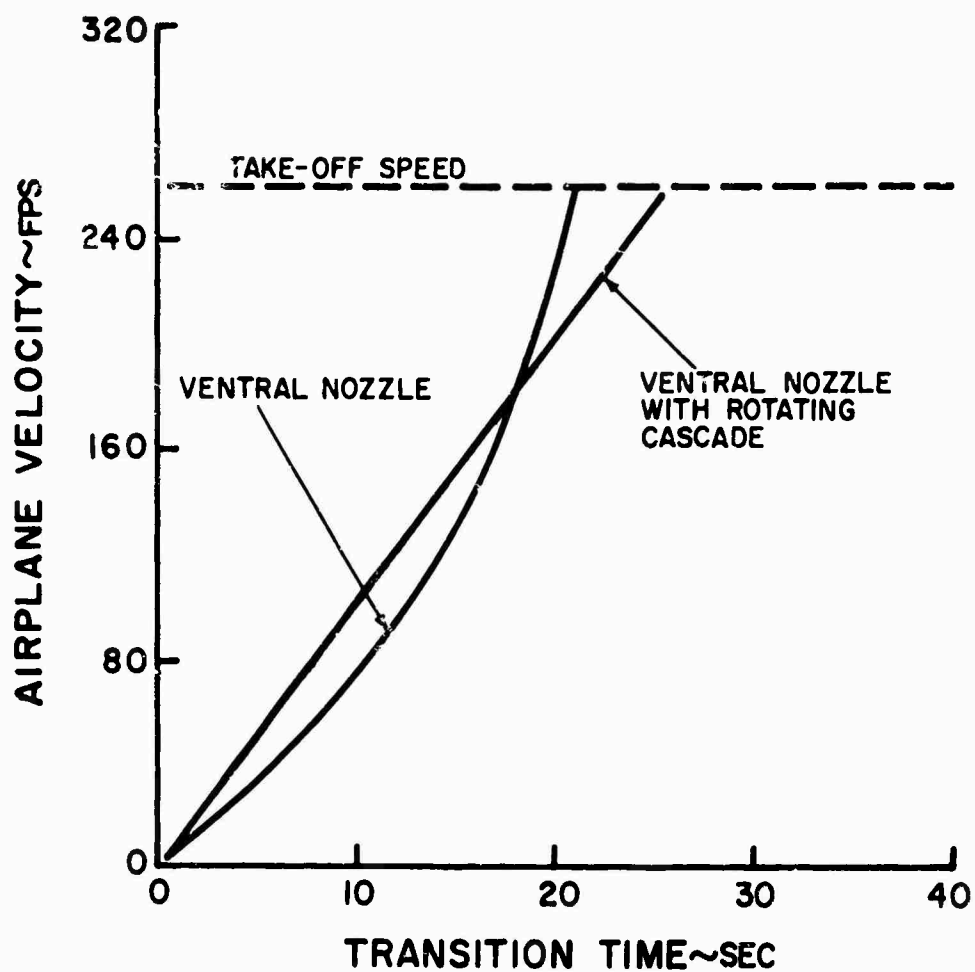Figure 22   Ground Proximity Effects on Nozzle Performance

34

Figure 23   Transition Time

NOTES

SHROUDED PROPELLER RESEARCH AT
MISSISSIPPI STATE UNIVERSITY LEADING TO
APPLICATION ON THE UNITED STATES ARMY XV-11A

by

JOE F. THOMPSON and S. C. ROBERTS

Aerophysics Department, Mississippi State University
State College, Mississippi, U.S.A.

INTRODUCTION

The failure of the conventional propeller to provide power for climb
at speeds below 36 m.p.h. on an Army L-21 Cub with suction boundary layer
control provided the impulse for shrouded propeller research at Mississippi
State University some ten years ago. As is well known, the static perfor-
mance of an open propeller designed for maximum efficiency at cruising speed
leaves much to be desired. However, high static and low speed thrust is just
as much a requirement as is high lift for the achievement of STOL operation.
Although shrouded propellers have been used for some time to increase the
static thrust of tug boats, only recently has the interest in STOL operation
prompted their employment on aircraft.

The circulation about the airfoil section of the shroud induces a
velocity increment at the propeller plane, especially near the propeller
tips. This induced velocity compensates, to some degree, for the wide change
of angle of attack near the tips with flight speed, and thereby allows the
propeller to operate at near optimum conditions over a wider range of flight
speeds. With a properly designed shroud a higher efficiency can be obtained
for the same thrust, or the thrust can be increased without a loss in effi-
ciency.

This circulation about the shroud also produces a "lift" vector on the shroud, which when angled forward results in a thrust component on the shroud which can be in excess of the propeller thrust. Finally, when the clearance between the propeller and the shroud is made small, the shroud effectively end-plates the propeller, reducing the losses due to vortex shedding.

The combination of these effects results in a considerable increase in thrust, especially in the static condition and in low speed flight. On the minus side, the shroud is an additional drag producing element. However, with careful design the break-even velocity (flight velocity at which shroud drag equals shroud thrust) can be made quite large.

SHROUD LEADING EDGE SEPARATION

Early Model Studies

Early studies on model shrouded propellers at Mississippi State
University revealed the necessity of preventing leading edge separation on
the shroud if its full potential for thrust augmentation is to be realized.
This separation occurs in precisely the case when the increased thrust from
the shroud is most important - the static and low speed conditions. At zero
or low flight speed the flow must turn around the shroud leading edge from
behind, and is apt to separate just downstream of the leading edge on the
inside of the shroud (Figure 1). The possibility of this separation is
heightened by the fact that a constant pitch propeller operates inefficiently
at the tips due to the angle of attack change with radius. Once separation
occurs, the portion of the propeller within the separated region is ineffec-
tive or even detrimental.

Full-Scale Studies

Full-scale tests were conducted on a shroud mounted around the
pusher propeller of an Anderson-Greenwood AG-14 aircraft (Figure 2). Leading
edge separation occurred on the shroud with an untwisted propeller (Figure 3).
However, when the inflow velocity profile across the propeller plane was
measured and the propeller was twisted to match this angle of attack distri-
bution, separation was suppressed (Figure 3), and thrust increased signifi-
cantly. With this configuration, shroud thrusts even greater than propeller
thrusts were achieved.

Separation Suppression by Boundary Layer Control

3

The possibility of suppressing shroud leading edge separation by suction boundary layer control in the shroud was investigated, again on the shroud on the AG-14. The severity and extent of the separation was considerably reduced from the case of no boundary layer control. In this particular case the application of boundary layer control resulted in an increase in thrust from 350 pounds to 490 pounds with an expenditure of 5 horsepower of suction power. As a point of interest, the original thrust of this aircraft with the open propeller was 280 pounds. This investigation also showed that headwinds can cause separated flow to attach, and tailwinds can lead to separation. The flow is also very sensitive to crosswinds, with separation occurring on the windward side and attachment on the leeward.

THE SHROUDED PROPELLER OF THE XAZ-1 MARVELETTE[4]

Design

The shrouded propeller on the AG-14 was subjected to extensive testing, both in the static condition and in flight (Figure 4). This full-scale testing provided the experience and design principles necessary for the design of the shrouded propeller to be used on the XAZ-1 MARVELETTE research aircraft. The XAZ-1 MARVELETTE (Figure 5) was built as a test bed for the high lift, high thrust, low drag concepts to be employed in the design of the U. S. Army XV-11A STOL research aircraft.

There are several reasons that dictate the use of a shrouded propeller in a pusher configuration, rather than a tractor configuration. The shroud is a major stability component and must be located aft of the center of gravity of the aircraft, or else a tremendous fin area will be required

4

to overcome the adverse yaw effect of the shroud. Also, it had been found in research on a high-lift L-19 that the annular region of low dynamic pressure surrounding an open propeller caused early separation upon impingement on the wings, thus negating the boundary layer control system on the wings and limiting the maximum lift attainable. Therefore, the shroud should be located behind the wings on an STOL aircraft in order to assure smooth, undisturbed flow over the wings. A third reason for an aft location of the shroud is, of course, visibility.

The low-drag airfoil section used for the shroud was mounted at zero angle of attack. The leading edge radius was increased to suppress possible leading edge separation. The shroud diffusion angle was approximately 5.3 degrees, which is small enough to prevent possible diffuser separation problems. The three-bladed MARVELETTE propeller was of variable pitch, with blades of constant chord, and in the original configuration the blades were untwisted. This allowed twist modification to be easily incorporated from inflow measurements from ground running and flight tests for optimum propeller performance. The propeller was driven by a fiber glass shaft attached to a Continental C-90 engine which developed 90 horsepower at 2,500 r.p.m.

The shroud was made of fiber glass. The longitudinal and directional control surfaces were incorporated in the shroud in order to eliminate the conventional tail sections and reduce the drag at higher speeds (Figure 6). These controls were constructed so that very little gap existed between the control surfaces at the trailing edge of the shroud, irrespective of the control surface position. Two segments on either side of the shroud acted as

5

rudders, and four segments, top and bottom, served as elevators. Massive
fiber glass strucs maintained the close alignment of the shroud and carried
the shroud thrust loads.

Ground Test Results

Since it was necessary to determine whether any serious separation
or irregularities occurred in the flow around the shrouded propeller, a
considerable number of flow visualization studies were performed using tuft
and napthalene sublimation techniques. Intermittent leading edge separation
on the shroud is evident in the tuft pictures in Figure 7. However, the
separation region is small and the flow is generally quite smooth. Sublima-
tion studies revealed considerable separation from the spinner and the blade
root cuffs. This was reduced by modification of the cuffs. Sublimation also
showed the flow over the propeller blades to be laminar to a large extent,
and the tip clearance to be sufficiently small to reduce or to nearly elimi-
nate tip vortex effects.

The inflow velocity was examined at several angular positions and was
quite symmetrical, with only slight deviations occurring at the bottom near
the fuselage (Figure 8). There was considerable variation in inflow velocity
with radius. Changes in camber of the variable camber wing, or equivalent
flap angle, up to 30 degrees had very little effect on the flow into the
shrouded propeller.

Changes in aircraft airspeed had a very detrimental effect on propel-
ler blade effectiveness, as can be clearly seen in Figure 9, where the propel-
ler blade was in the original untwisted condition. At an airspeed of 70 m.p.h.,
the outer two-thirds of the blade was operating with only a small radial

6

portion at an optimum angle of attack. At 110 m.p.h., only the outer one-third was operating, and the remainder of the propeller was windmilling. This was probably the reason for the nonuniform inflow velocity distributions, and was undoubtably the reason for the poor climb-out performance of the aircraft experienced at 90 m.p.h. Twisting the propeller blade to match the inflow velocity distribution helped to relieve this problem, as can be seen from the results using the twisted blade in Figure 10. At 110 m.p.h., over half of the blade was operating at a reasonably constant angle of attack. This modification considerably improved the climb-out characteristics of the MARVELETTF aircraft.

The static thrust generated by the shrouded propeller of the MARVELETTE was found from tethered tests. Although the tests were performed early in the morning when the wind was generally calm, the aircraft was located inside the hanger to eliminate any crosswinds which could possibly promote flow separation on the shroud. Readings were also taken with the moveable control surfaces in various positions, but it was found that control positions had little or no effect on static thrust. The static thrust of the shrouded propeller was approximately 100 percent greater than the static thrust of the equivalent open propeller driven by the same horsepower engine.

Some dynamic thrust measurements were taken by towing a ground vehicle, but this method was dangerous and impractical at speeds greater than 30 m.p.h. In order to obtain thrust measurements at higher speeds, an instrument was developed which would give an accurate and repeatable plot of aircraft displacement from a fixed point as a function of time. This technique of measuring the variations of thrust with forward velocity was very effective

7

up to speeds below the takeoff airspeed of the aircraft. With careful pilot-ing technique, it could be used at ground speeds in excess of the minimum flying speed of the aircraft.

From **Figure 11**, the theoretical break-even velocity was 152 f.p.s., assuming that the ring tail is additional to the conventional tailplane; however, in the MARVELETTE case, where the conventional tailplane was elimi-nated, the break-even velocity was 162 f.p.s. The experimental curve of total thrust is considerably below the theoretical curve from simple momentum theory (**Figure 12**). This is to be expected because in the theoretical case it was assumed that the complete propeller was operating at an optimum blade angle of attack which, of course, was not the case. Both curves have essen-tially the same shape, and the experimental curve is approximately 75 percent of the theoretical curve. The differences between theoretical and experimental results are due primarily to interference effects and to insufficient or improper blade twist, especially around the blade root. Shroud leading edge laminar separation bubbles and flow separation around the spinner also contrib-ute to the difference in results.

The simple momentum theory[4] involves a number of simplifying assump-tions such as no rotation of flow leaving the shroud, constant inflow velocity, wake area equal to shroud exit area, and static pressure at shroud exit equal to ambient pressure. The method of singularities, as has recently been very elegantly developed by Therm Advanced Research, Inc.[1,2,3], is far superior, provided that its requirements are met. However, due to the fact that shrouded propellers usually operate on the rear of the vehicles where the inflow veloc-ity consists of a combination of free-stream velocity and body wake velocity,

8

it is difficult to design an optimum shrouded propeller without knowing the influence of the vehicle on the inflow velocity field of the propeller.

Flight Test Results

As a result of flight testing of the MARVELETTE (Figure 13), it was necessary to install additional jury struts on the shroud to maintain the close propeller tip clearance. Early in these flights it became clear that the large moment of inertia about the lateral and vertical axes resulted in a tendency toward an oscillation, particularly in pitch. The aircraft was completely manageable, but increased damping in pitch appeared desirable. Consequently, small fins were added to the four spaces between the rudders and elevators. These fins were expected to increase the tail volume, make the outside of the duct more effective, and end-plate the movable surfaces to improve their effectiveness.

The added fins apparently succeeded in improving both steadiness and controllability, although some pitching oscillation was still present. It is probable that most of the oscillation resulted from lost motion in the elevator control linkage. The pitch oscillation and a slight tendency to wallow was most pronounced with reduced power settings used for landing approach. This unsteadiness was probably the result of reduced flow through the duct at low power settings. Stability was generally good, however, and there was no difficulty in making coordinated turns. So much directional stability was present that little use of the rudder was required. The need for pitch control appears to be considerably greater with a ducted propeller than with an open one.

The most important conclusion which can be drawn from the results

9

of the flight testing program is that, although the MARVELETTE was an unconventional aircraft, the general handling characteristics were very similar to those of a conventional airplane. The ducted propeller performed satisfactorily, with sufficient thrust available to accelerate the airplane from 0 to 70 m.p.h. in 17 seconds, even though the blade twist angles were not yet optimized for maximum thrust at low forward velocities.

The major effect of the shroud was thrust augmentation, although the directional stability contribution was sufficient to overshadow the rudder effect in normal flying. The flight results showed that the assumptions used in designing the shroud and control surfaces were adequate to insure adequate control of the airplane.

THE SHROUDED PROPELLER OF THE XV-11A

Design

The results of static and flight tests on the shrouded propeller of the MARVELETTE directed the design of the U. S. Army XV-11A (Figure 14), an aerodynamic research aircraft specifically designed to explore the problem areas inherent in wide speed range, fixed-wing airplanes of interest in Army operations. These problem areas include high lift, low drag, high thrust, and the compatibility of these characteristics with the requirements for good visibility, large usable volume, and rough field or pantabase operation.

The shroud is fiber glass and of the same airfoil section (NACA 4416) used on the MARVELETTE, with the leading edge radius again increased to suppress separation. The shroud inside diameter is 66½ inches, and the chord is 30 inches. The propeller is of 7 inch chord and is a standard Aero Products

10

propeller which was designed for the T-63 engine, except that it had the outer eleven (11) inches removed to fit into the shroud. The clearance between propeller and shroud is 3/32 inch when the propeller is still. The clearance decreases somewhat when the propeller is operating, because of blade expansion under centrifugal force. The propeller is powered by an Allison T-63 gas turbine engine, developing 250 horsepower at 2,000 r.p.m. Conventional tail control surfaces are used (Figure 15) rather than those incorporated in the shroud as on the MARVELETTE. The previously mentioned pitch control problems encountered with the MARVELETTE, plus the fact that the heavy control linkage system inside the MARVELETTE shroud caused some deformation resulting in some hits by the propeller, prompted this change.

Tests Results

The XV-11A began its flight testing (Figure 16) in December 1965, and no difficulties have yet been encountered with the propulsion system. The shrouded propeller develops 1,400 pounds of thrust, giving a thrust per horsepower of 5.6 lb/HP. Since the aircraft gross weight is only 2,400 pounds, it is well capable of STOL operation. In fact, the thrust at the engine flight idling position is so great that the propeller must be put in reverse pitch for landing in short distances. Flight speeds of 150 m.p.h. have been attained at 43 percent power levels, and the break-even speed, where shroud drag exceeds shroud thrust, is estimated to be 160 m.p.h.

SHROUD FLOW PATTERNS IN REARWARD AND FORWARD MOTION

Although many investigations have been directed toward determining the thrust and overall performance characteristics of shrouded propellers,

11

only little consideration has been given to determining the flow pattern about the shroud.

Shroud thrust calculations are performed by the method of distributed singularities[1-3] which assumes a stagnation line at the trailing edge, satisfying the Kutta condition. In reality viscous interaction of the propeller slipstream with the external flow alters this simple flow pattern so that, in addition to the stagnation line at the trailing edge, a stagnation line exists on the outer surface of the shroud. For instance, in the static condition the inviscid flow pattern shown in Figure 17 is altered by slipstream interaction so that the actual flow pattern is that shown in Figure 18. Inviscid flow theory would have the two stagnation lines coinciding at the trailing edge. This forward movement of one stagnation line reduces the circulation below that which would be calculated by the distributed singularities methods. Thus the shroud thrust will be less than the theoretical value, the reduction being a function of the distance between the outer surface stagnation line and the trailing edge.

Therefore, an extensive investigation was undertaken to determine the flow pattern and pressure distribution about the shroud of a shrouded propeller in the static condition, in rearward motion, and in forward motion. The inclusion of the case of rearward motion was prompted by the recent application of shrouded propellers on VTOL aircraft. For static testing the propeller was mounted on a propeller test stand as shown in Figure 19. The entire propeller test stand used in the static testing was mounted on an automobile chassis, facing aft as shown in Figure 20, for rearward motion studies and facing forward (Figure 21) for forward motion studies.

12

Static

Typical stagnation lines are shown in the shroud tuft pictures in
Figure 22. Since fluctuations in the flow made the stagnation lines some-
what irregular in some cases, the locations used in data correlation were
averages over all tufts on the four pictures taken in each case. Figure
23 shows the stagnation line location as a function of the shroud thrust
coefficient. At 5° pitch angle the stagnation line is located fairly
far forward, around the three-quarter chord position. As the shroud circu-
lation increases, either because of pitch angle or rotational speed increase,
the stagnation line moves toward the trailing edge, rapidly at first and
then more slowly, approaching a chord fraction between 0.90 and 0.92.
Although there is some irregularity due to the flow fluctuations, the curves
are of the same general shape for all rotational speeds.

Rearward Motion

In rearward motion essentially three types of shroud pressure dis-
tribution were observed as sketched in Figure 24. Type A, occurring at the
higher circulations and lower speeds, is the same type of pressure distribu-
tion as observed in the static case. Type B, occurring at intermediate
circulations and speeds, is characterized by the occurrence of positive
values of the pressure coefficient on the inner shroud surface and one
intersection in the curve. Type C, at lower circulations and higher speeds,
exhibits two intersections with lower pressure on the outer surface over
most of the shroud. The transition from Type A to Type B is much more
sudden than that from B to C. In some cases two types of pressure distribu-
tion were observed at the same pitch angle, rotational speed, and linear

13

speed. Thus the occurrence of a particular type of pressure distribution seems to be a question of stability.

Typical stagnation lines and conditions of the wire tufts above, in front of, and behind the shroud are shown in Figure 25. The flow patterns about the shroud as indicated by the wire tufts are drawn in Figure 26. At all speeds the shroud is surrounded by a ring vortex which encloses another ring vortex on the outer surface of the shroud. For the sake of brevity the 0.0 chord position will be referred to as the leading edge and the 1.0 chord position as the trailing edge in both rearward and forward motion, even though in the rearward case these terms are misnomers. The transition of flow patterns proceeds as follows:

(1) (Figure 26a) At low speed the enclosed vortex on the outer surface is located near the trailing edge and is very small. This condition results in a stagnation line located at high chord position. The flow turns sharply around the leading edge of the shroud causing a low pressure peak near the leading edge and resulting in a pressure distribution of Type A, similar to that of the static condition.

(2) (Figure 26a) As speed increases, the enclosed vortex grows and the stagnation line moves toward lower chord positions. The pressure distribution remains of Type A, but the low pressure peak decreases since the turn about the leading edge is more gradual.

(3) (Figure 26b) When the stagnation line nears the leading edge, the enclosed vortex has become quite large. The turn around the leading edge is very gradual so that the low pressure peak has disappeared. The increase in pressure across the propeller now results in positive pressure

14

coefficients on the inner surface near the trailing edge, since the pressure upstream of the propeller has increased. This results in a pressure distribution of Type B.

(4) (Figure 26b) Further increase in speed causes the enclosed vortex to be inclined rearward with a small stagnation line movement toward larger chord positions. The increased velocity on the outer surface causes the pressure on the outer surface to decrease. However, the lowest pressures still occur near the leading edge on the inner surface so that the pressure distribution is still of Type B.

(5) (Figure 26c) Still further speed increase causes the inclination of the enclosed vortex to increase so that it becomes pressed down on the outer surface of the shroud. This increased velocity on the outer surface of the shroud results in lower pressures on the outer surface than on the inner. The stagnation line reverses directions again and moves toward the leading edge as the vortex is pressed down on the surface.

In Figure 27 the shroud thrust coefficient is plotted against the advance ratio, with the pressure distribution type given for each point. The points are well correlated by one curve for each pitch angle. Although some several points fall off these curves, most of these points represent pressure distributions of types not consistent with those of neighboring points on the curves. This results from the above mentioned temporary occurrence of pressure distributions of a type not the most stable at the particular values of pitch angle, rotational speed, and linear speed. The shape of the lines at high advance ratio is questionable because of the scarcity of points in that region.

15

The stagnation line location is plotted in Figure 28 as a function of advance ratio. As mentioned above, the trend is for the stagnation line to move toward the leading edge as J increases. Upon reaching the vicinity of the leading edge, the motion of the stagnation line is reversed, and it moves toward higher chord positions as J increases. Still further increase in J causes another reversal and movement toward the leading edge again.

Figure 29 shows a correlation of shroud thrust coefficient against stagnation line location. Again it is possible to draw one line for each pitch angle. However, in this case, errors in measurement compound each other to produce more scatter.

Forward Motion

Typical stagnation lines and conditions of the wire tufts in forward motion are shown in Figure 30. Flow patterns are drawn in Figure 31. Even at low speeds the stagnation line is located forward of the quarter chord point, yielding a flow pattern as shown in Figure 31a.

Large increases in speed cause the stagnation line to move to the leading edge, with a flow pattern as in Figure 31b. As speed is further increased, leading edge separation and reattachment occurs on the outer surface. The speed at which separation occurs is lower at the lower circulations.

The stagnation line location is plotted in Figure 32 as a function of advance ratio. It should be noted that here the initial forward movement of the stagnation line is the same for all propeller rotational speeds, while in the case of rearward motion this initial forward movement decreased as rotational speed increased. The stagnation line moves rapidly forward

16

toward the leading edge with the initial increase in advance ratio. It then continues to approach the leading edge, but more slowly. After the stagnation line reaches the leading edge, leading edge separation occurs with further increase in advance ratio. Thus the low points at high advance ratio and low circulation do not represent the location of the above-mentioned stagnation line, which is still at the leading edge, but rather the location of the reattachment after the separation bubble.

CONCLUSION

In conclusion, a shrouded propeller has been successfully employed on the XAZ-1 research aircraft and on the U. S. Army XV-11A STOL research aircraft. Significant increases in static and low speed thrust have been obtained by using the shrouded propeller on these aircraft, with little degradation of high speed performance. Adaptation of the propeller to the shroud by twisting the propeller to match the inflow velocity profile significantly reduces shroud leading edge separation and improves performance. The shroud introduces no significant control and handling problems.

Viscous interaction of the propeller slipstream with the external flow does indeed cause a stagnation line to be located on the outer surface of the shroud of a shrouded propeller, as well as at the trailing edge. The forward movement of this stagnation line causes a reduction in circulation about the shroud and, consequently, in shroud thrust. Furthermore, the existence of this stagnation line on the outer surface of the shroud means that the actual thrust will be less than that calculated by the distributed singularities methods.

17

The thrust reduction in the static condition and in rearward motion can be correlated with the distance between the stagnation line and the trailing edge. In forward motion the suddenness of the forward movement of the stagnation line precludes such a correlation, although the shroud thrust does decrease as the stagnation line moves forward.

BIBLIOGRAPHY

1. Kaskel, A. L., Ordway, D. E., Hough, G. R., and Ritter, A., A Detailed Numerical Evaluation of Shroud Performance for Finite-Bladed Ducted Propellers, TAR-TR 635, Therm Advanced Research, Inc., Ithaca, New York, December 1963.

2. Ordway, D. E. and Greenberg, M. D., General Harmonic Solutions for the Ducted Propeller, TAR-TR 613, Therm Advanced Research, Inc., Ithaca, New York, August 1961.

3. Ordway, D. E., Sluyter, M. M., and Sonnerup, B. O. U., Three-Dimensional Theory of Ducted Propellers, TAR-TR 602, Therm Advanced Research, Inc., Ithaca, New York, August 1960.

4. Roberts, Seán C., The MARVEL Project, Part C: An Investigation of the Shrouded Propeller Propulsive System on the MARVELETTE Aircraft, Research Report No. 48, Aerophysics Department, Mississippi State University, State College, Mississippi, January 1964.

5. Thompson, Joe F., Jr., An Experimental Investigation of the Effect of Forward and Rearward Motion on the Thrust of a Shrouded Propeller, Research Report No. 65, Aerophysics Department, Mississippi State University, State College, Mississippi.

FLOW AROUND SHROUD
STATIC CONDITION
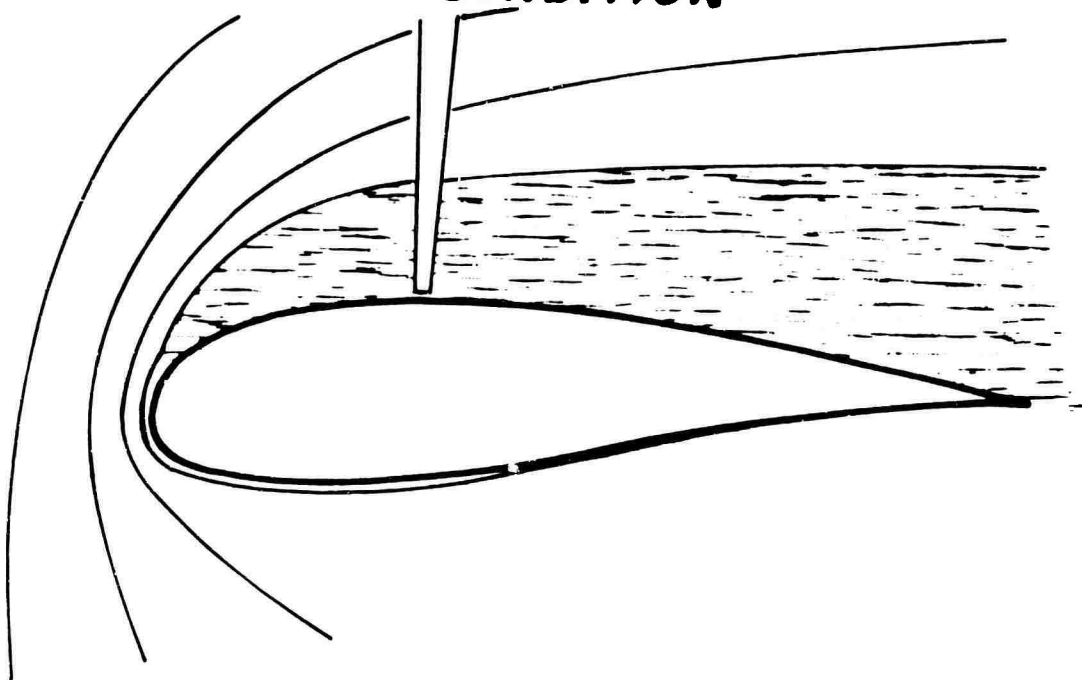
STANDARD PROPELLER

Figure 1. Shroud Leading Edge Separation.

20
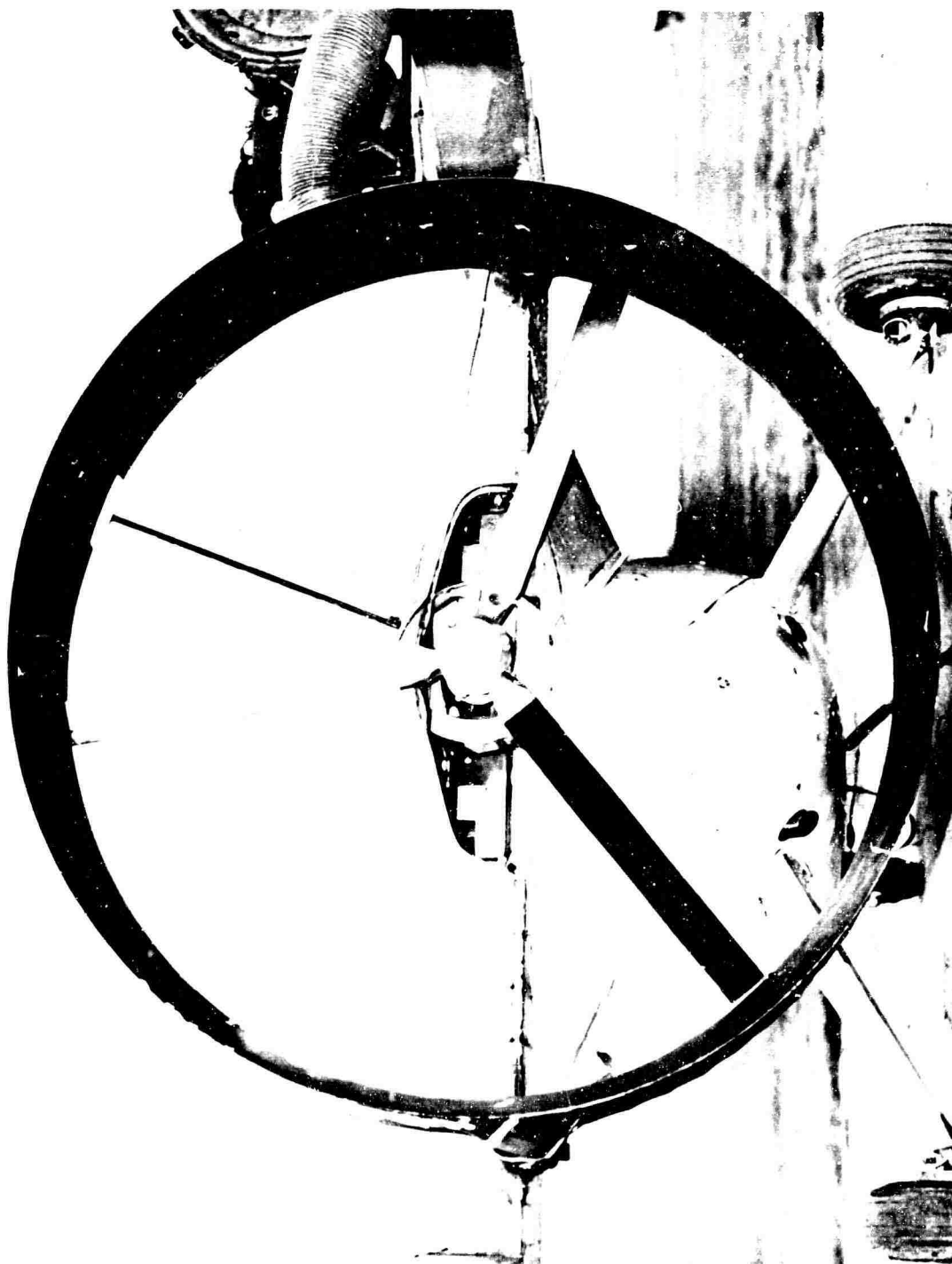
Figure 2. Experimental Shrouded Propeller on AG-14.

STANDARD PROPELLE. IN SHROUD
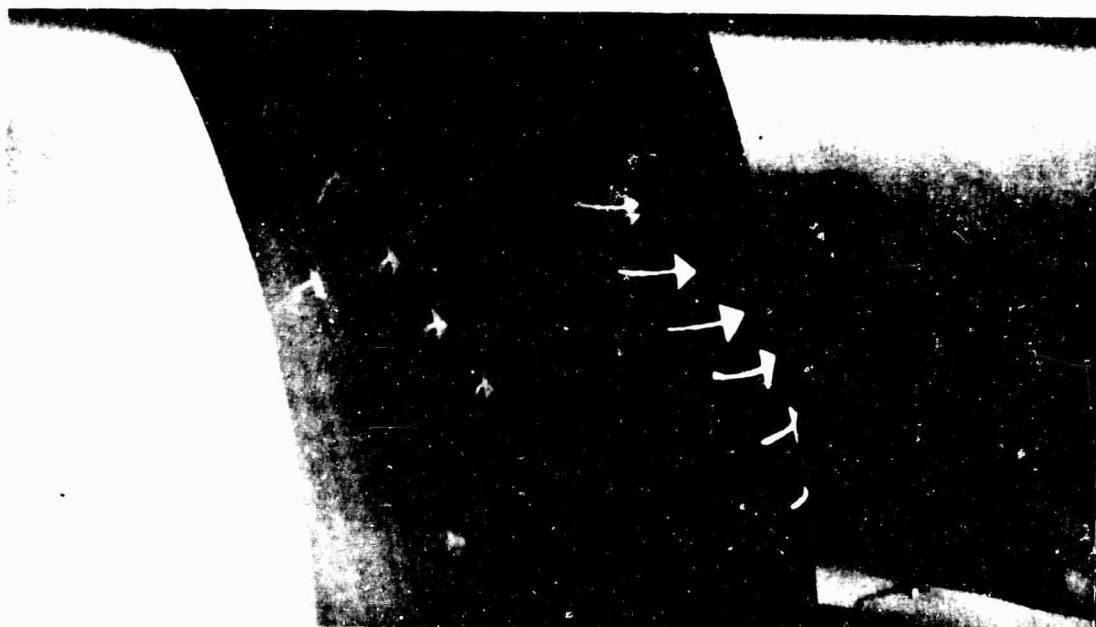
MODIFIED TWIST PROPELLER IN SHROUD

Figure 3. Shroud Leading Edge Separation on AG-14 Shroud.

Figure 4.   AG-14 with Shrouded Propeller in Flight.

Figure 5. XAZ-1 MARVELETTE Research Aircraft.

24
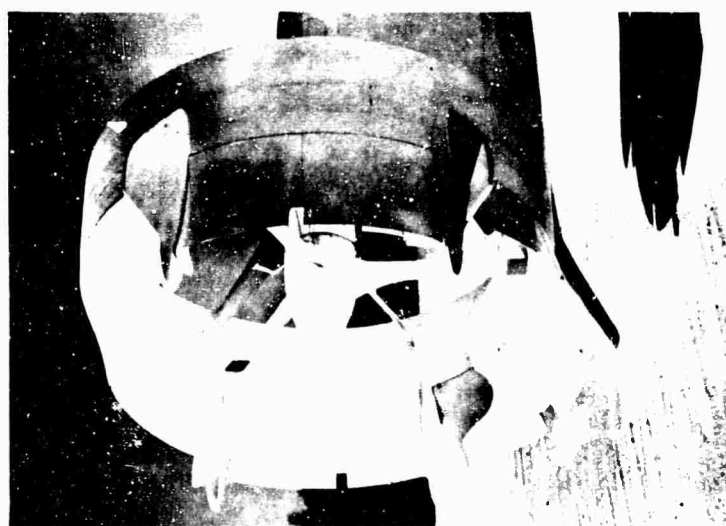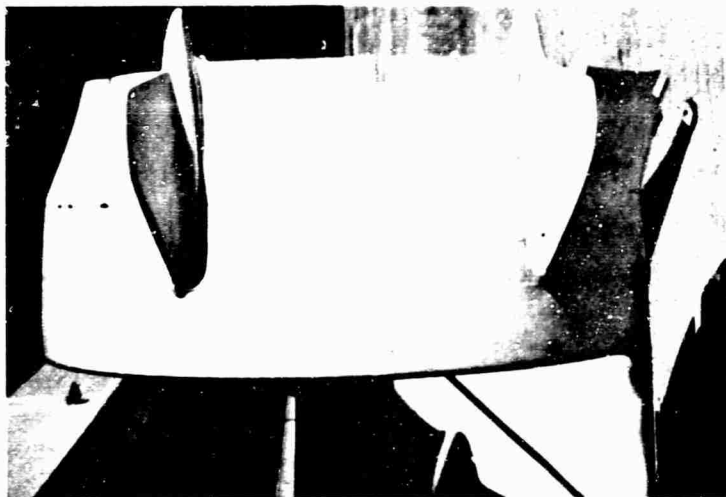
Figure 6. Shroud and Control Surfaces of XAZ-1.

25

Figure 7. Leading Edge Separation on XAZ-1 Shroud, Untwisted Propeller.
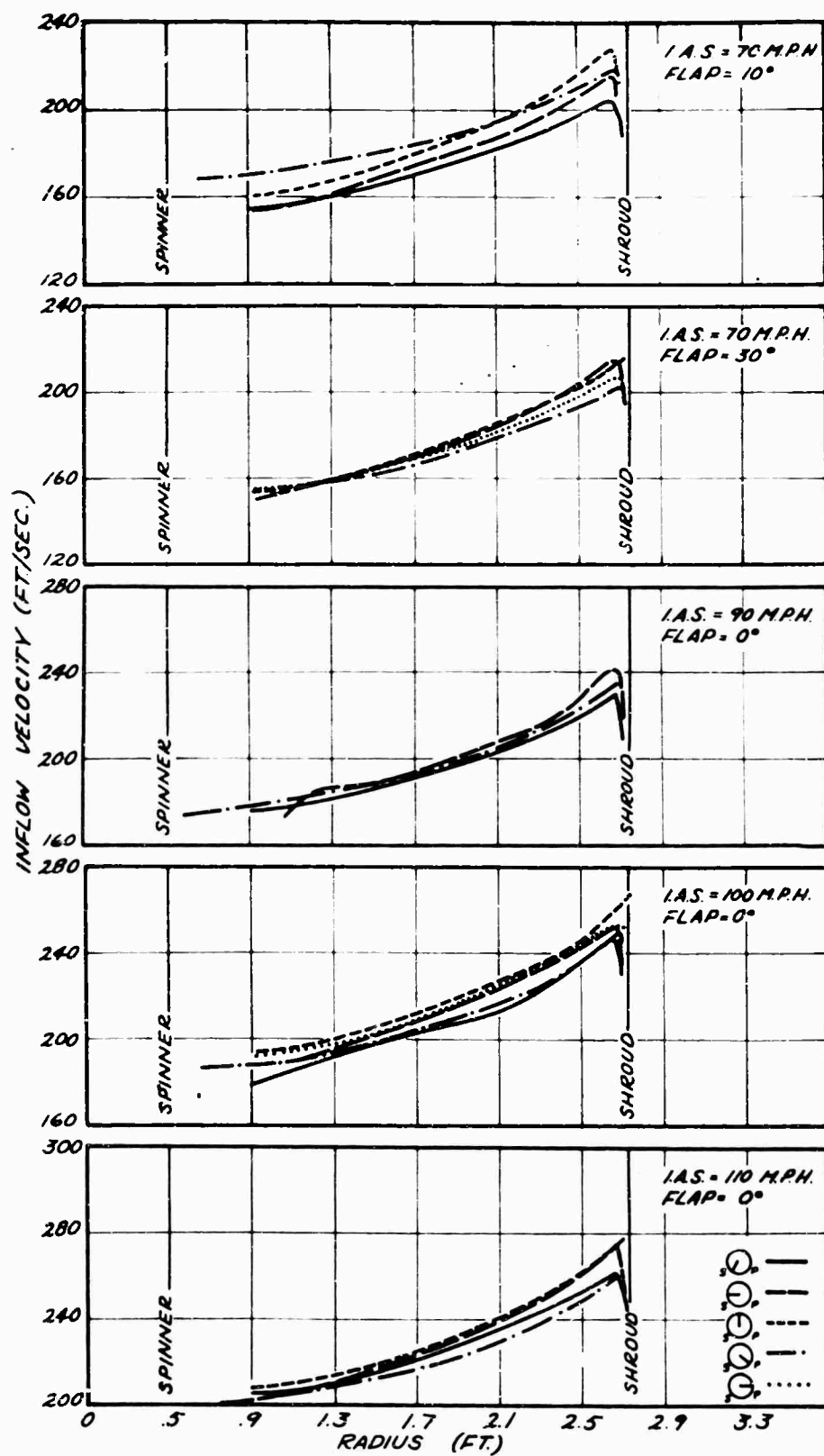
Figure 8. Inflow Velocity Distribution, XAZ-1 Shroud, Untwisted Propeller.

27
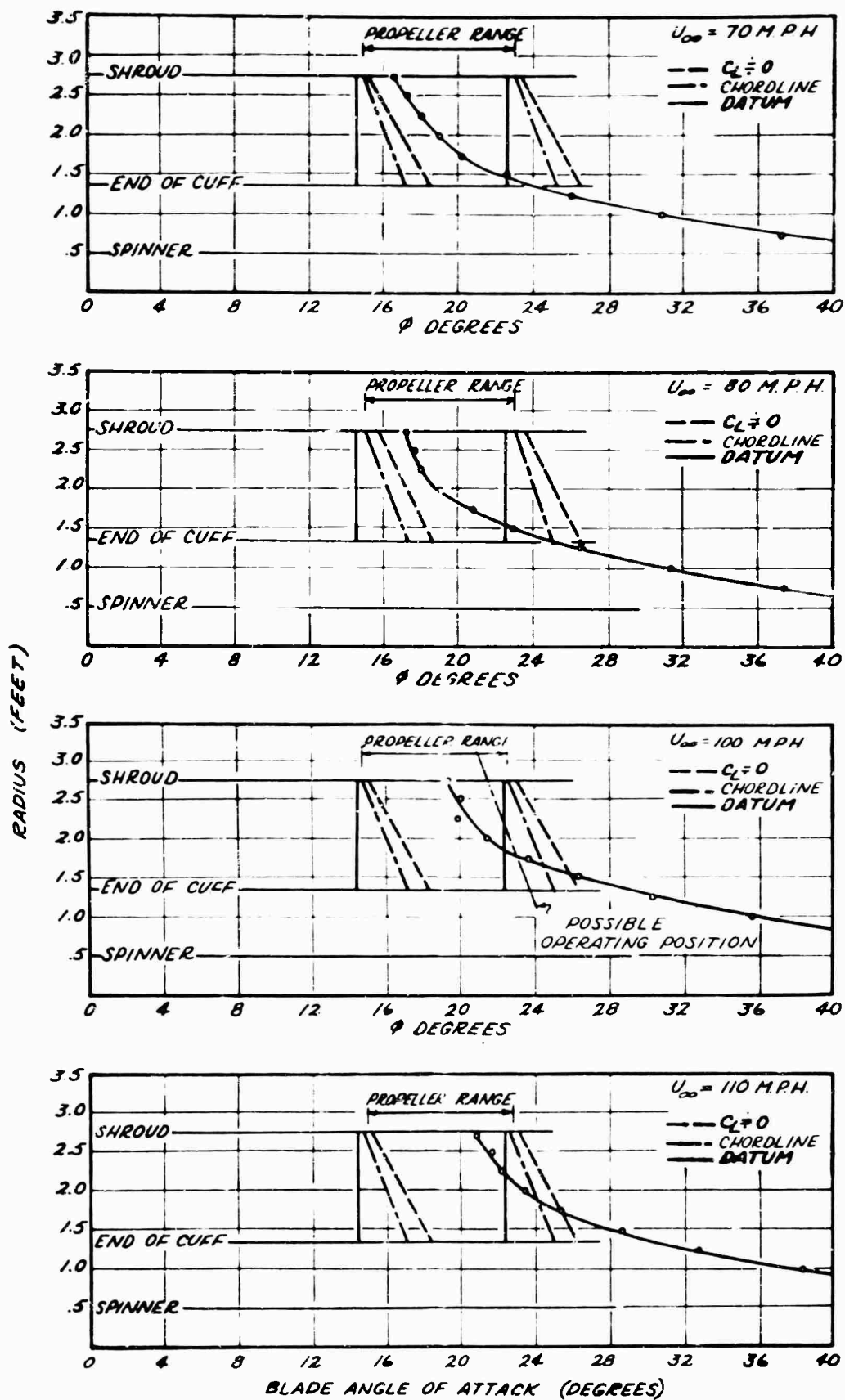
Figure 9. Propeller Angle of Attack Distribution, XAZ-1 Shroud, Untwisted Propeller.
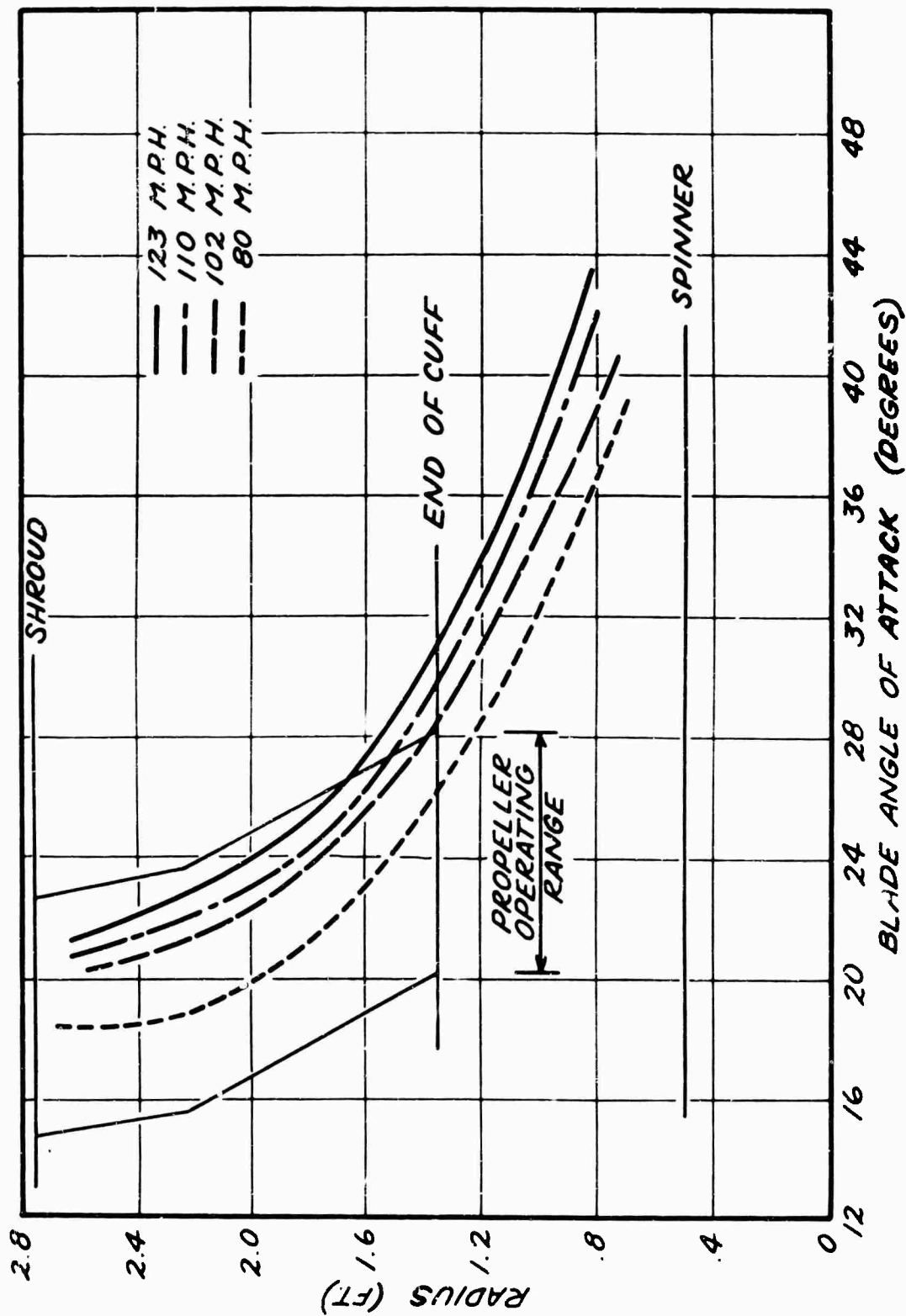
Figure 10. Propeller Angle of Attack Distribution, XAZ-1 Shroud, Twisted Propeller.

29
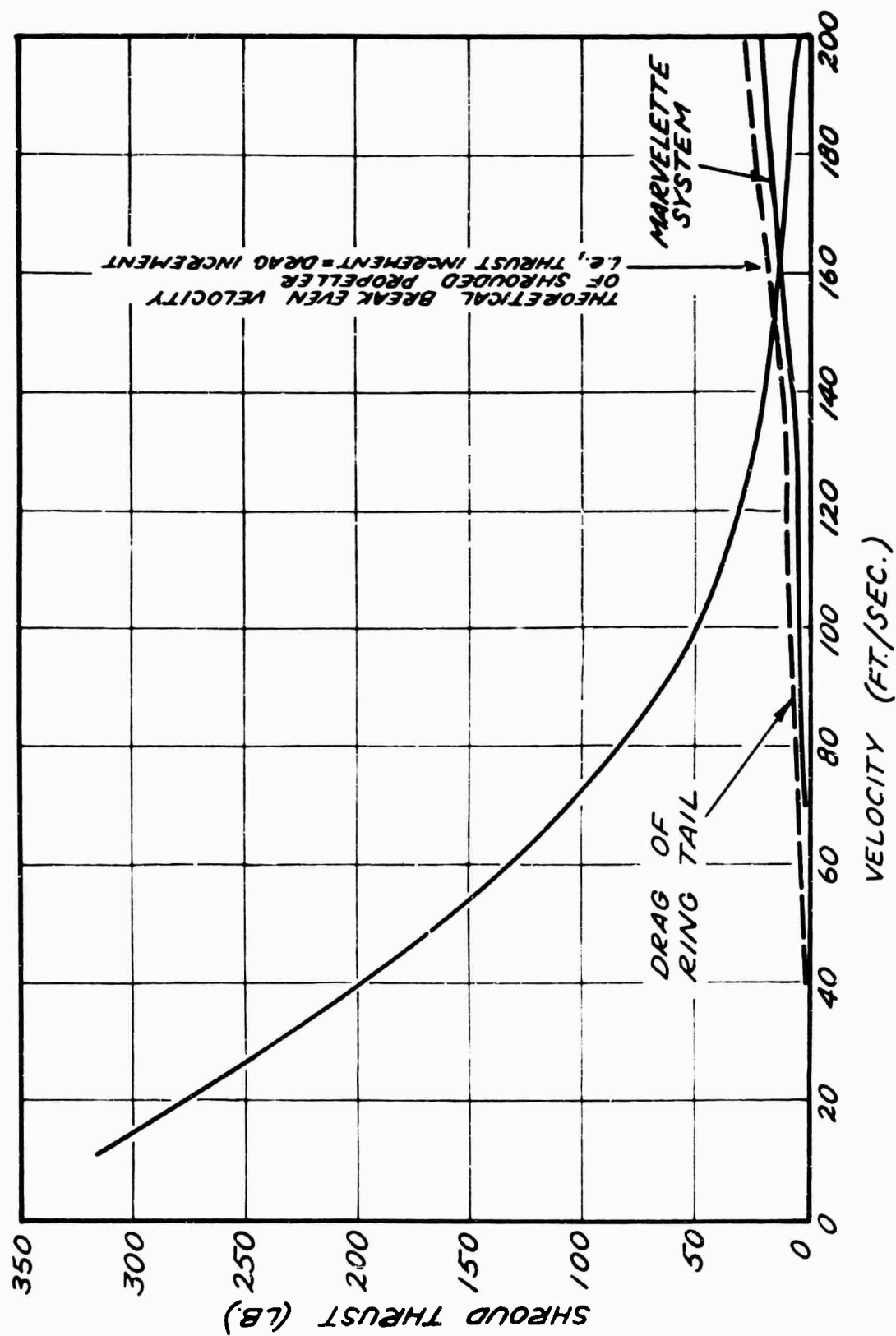
Figure 11. Determination of Break-Even Velocity of XAZ-1.
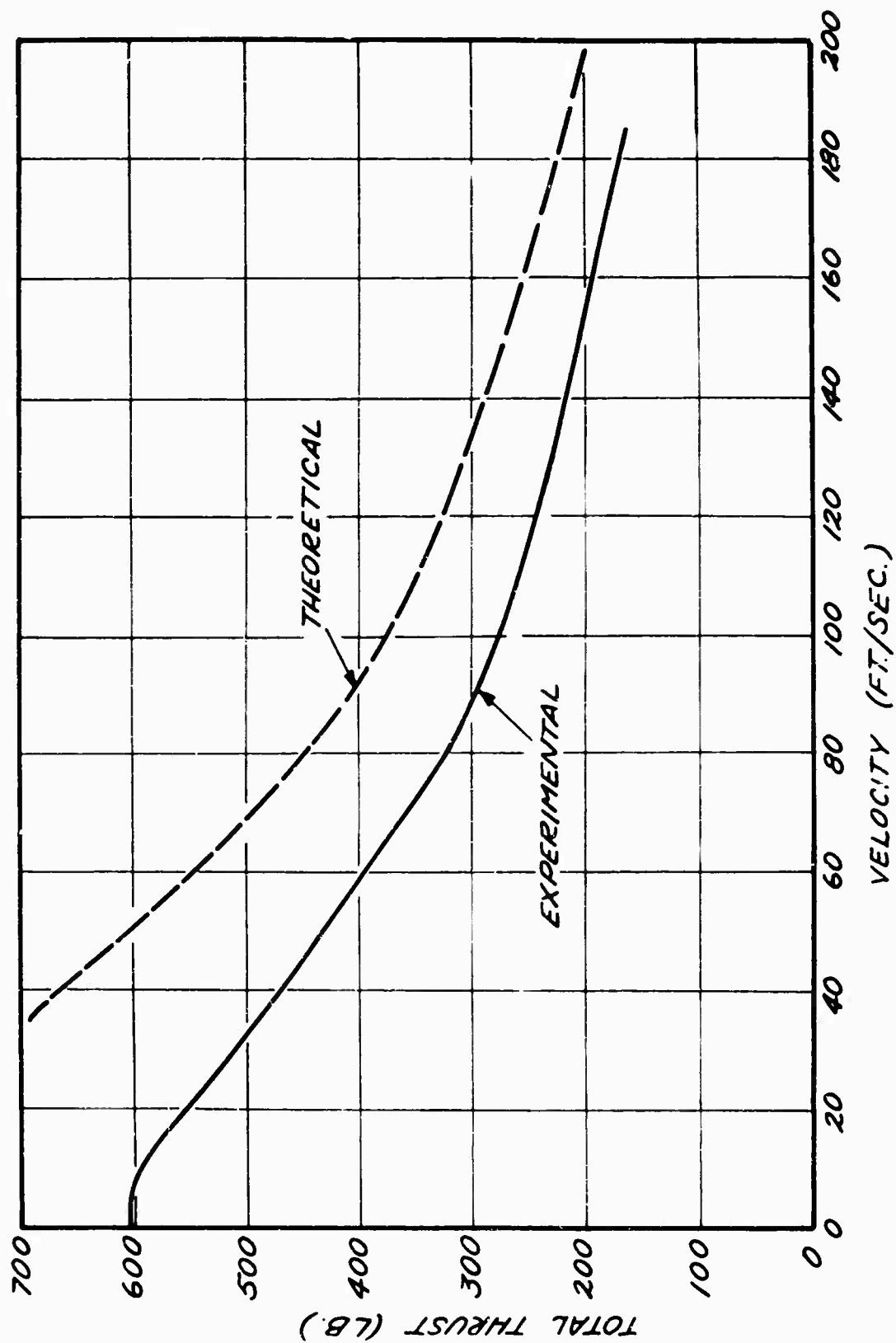
Figure 12. Comparison of Experimental Total Thrust of XAZ-1 with Prediction of Simple Momentum Theory.

31
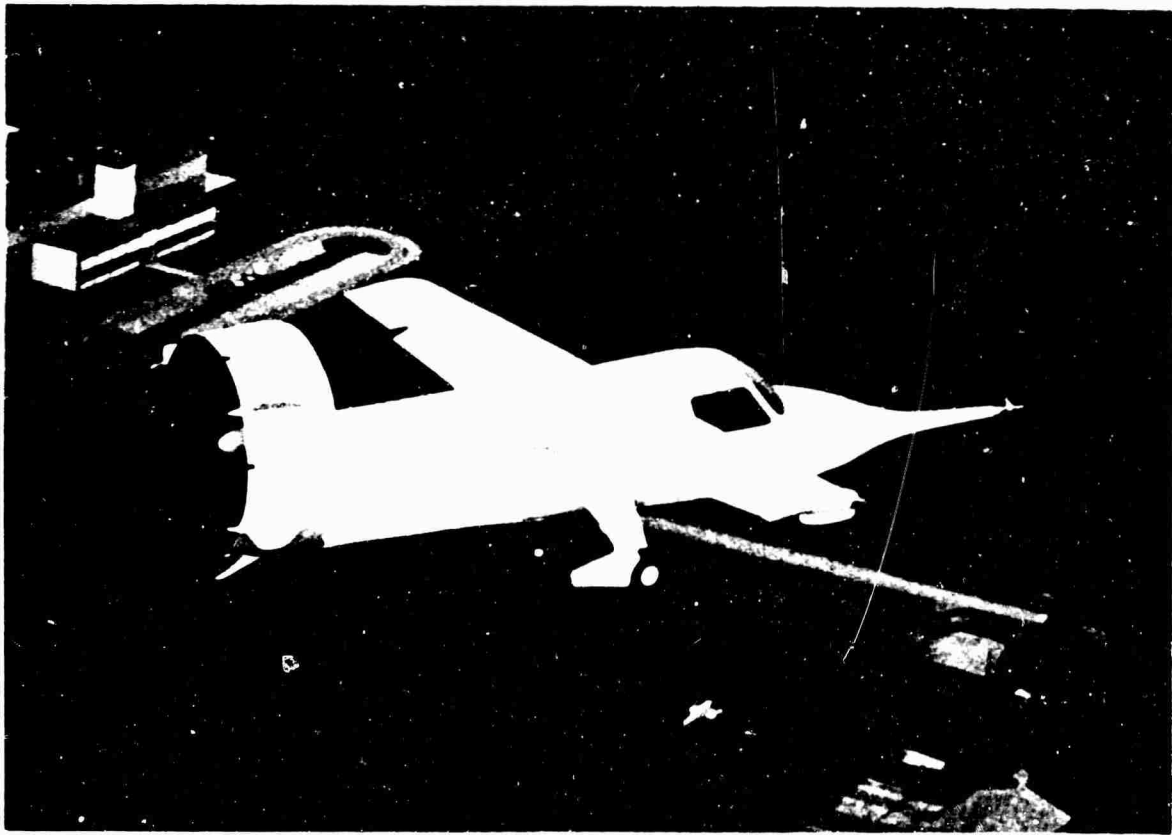
Figure 13.   XAZ-1 in Flight
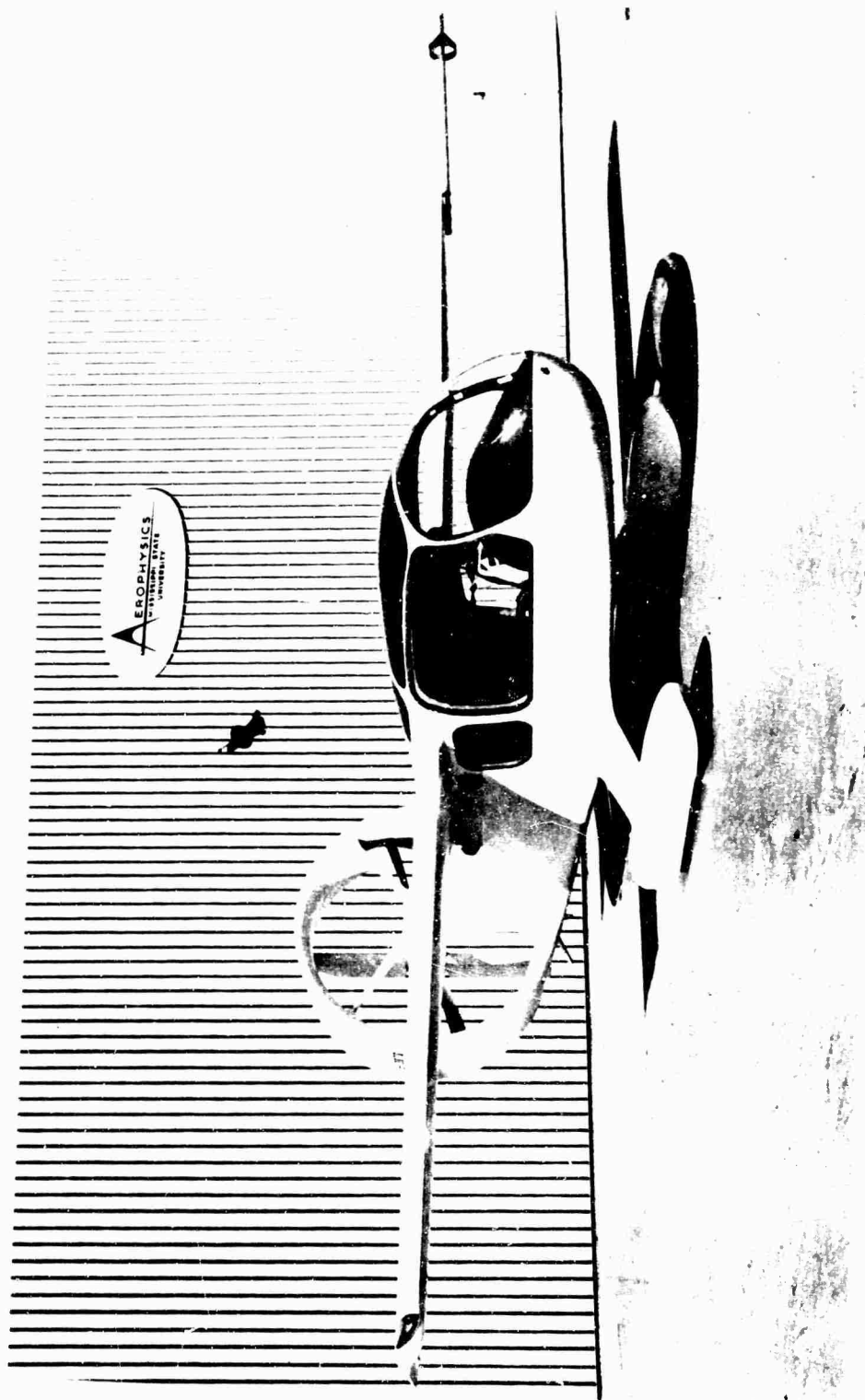
Figure 14. U. S. Army XV-11A STOL Research Aircraft.
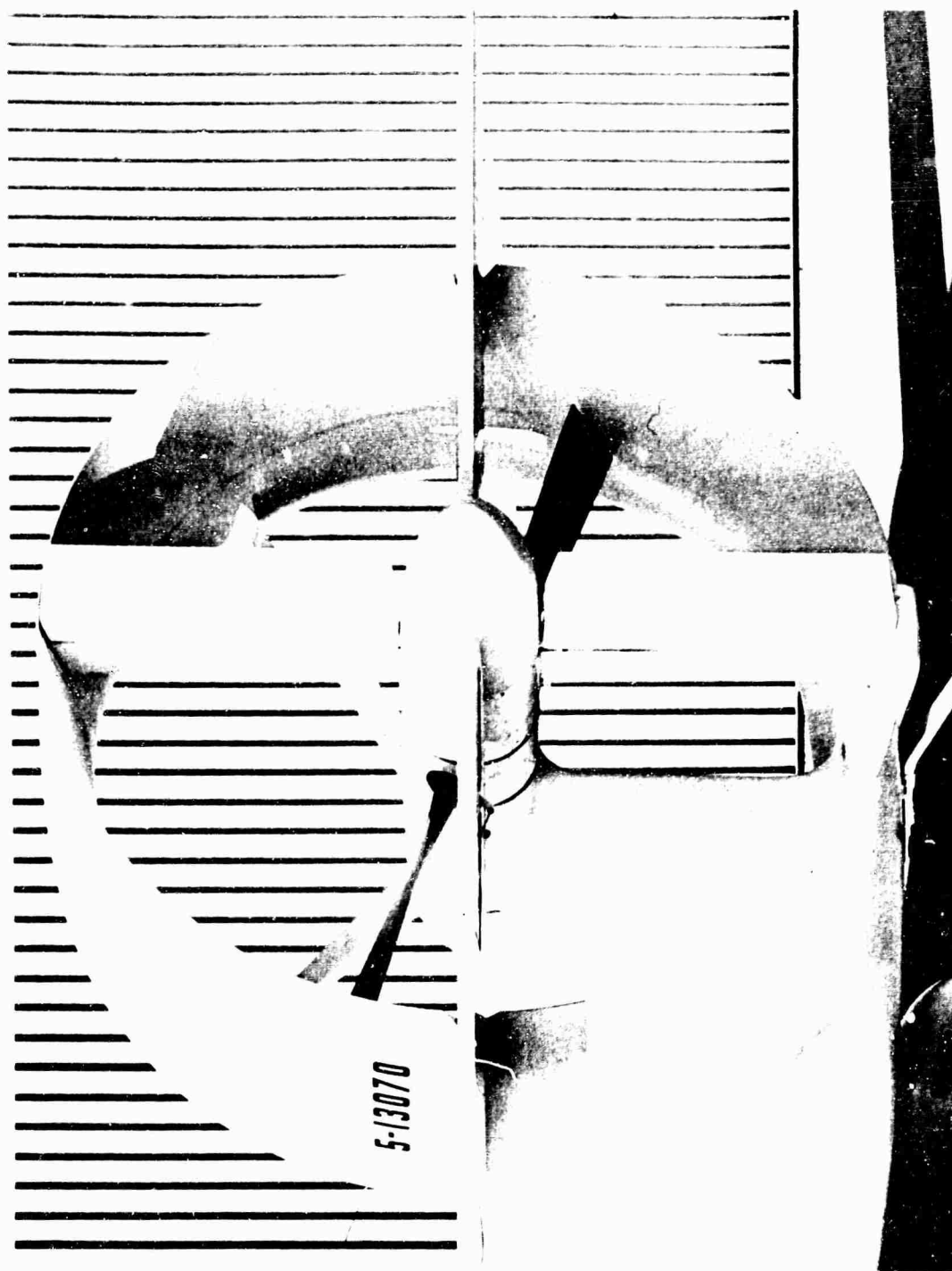
Figure 15. Shroud and Control Surfaces of XV-11A.

5-13070

34
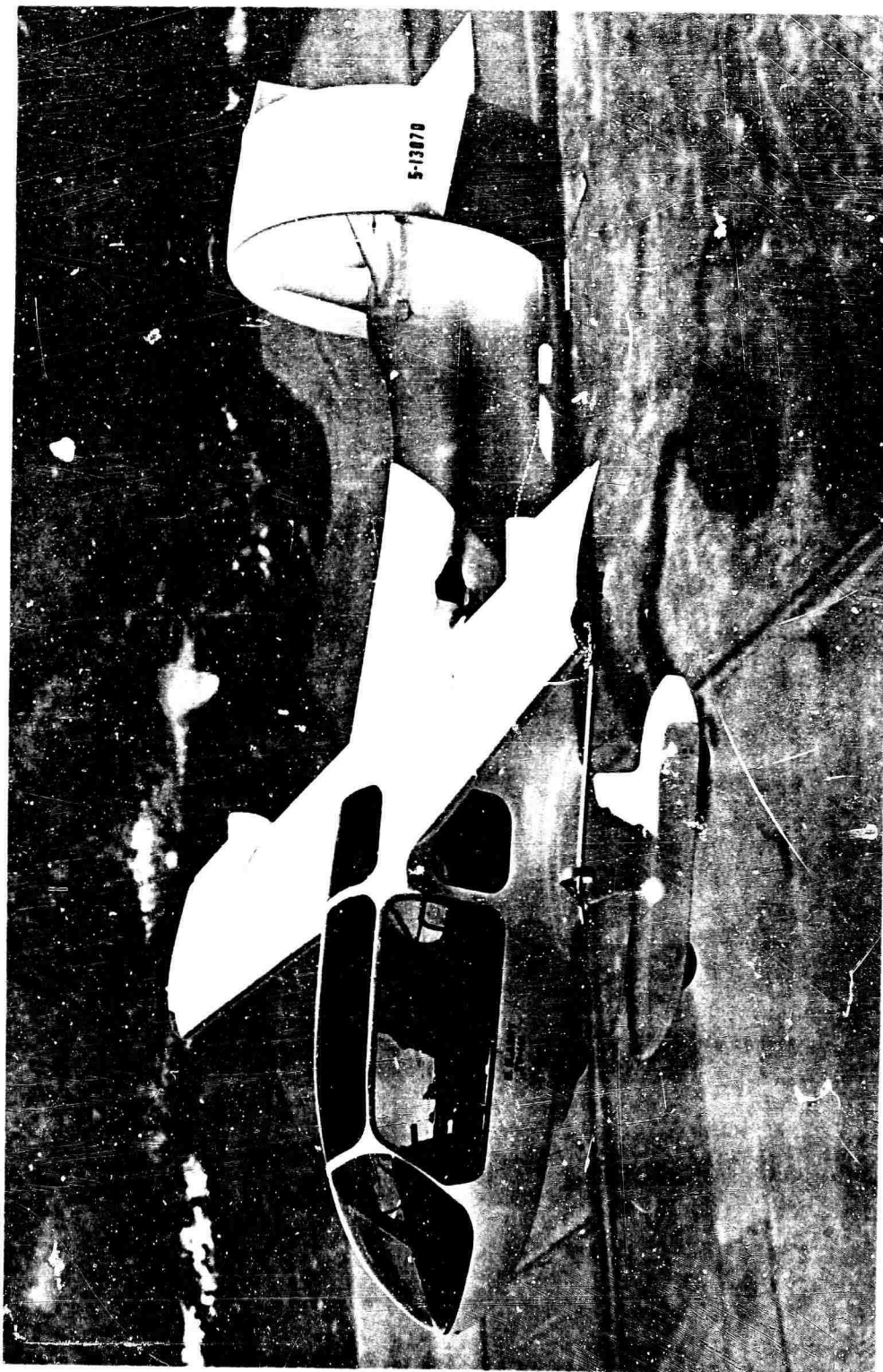
Figure 16. XV-11A in Flight.

S-13070

35
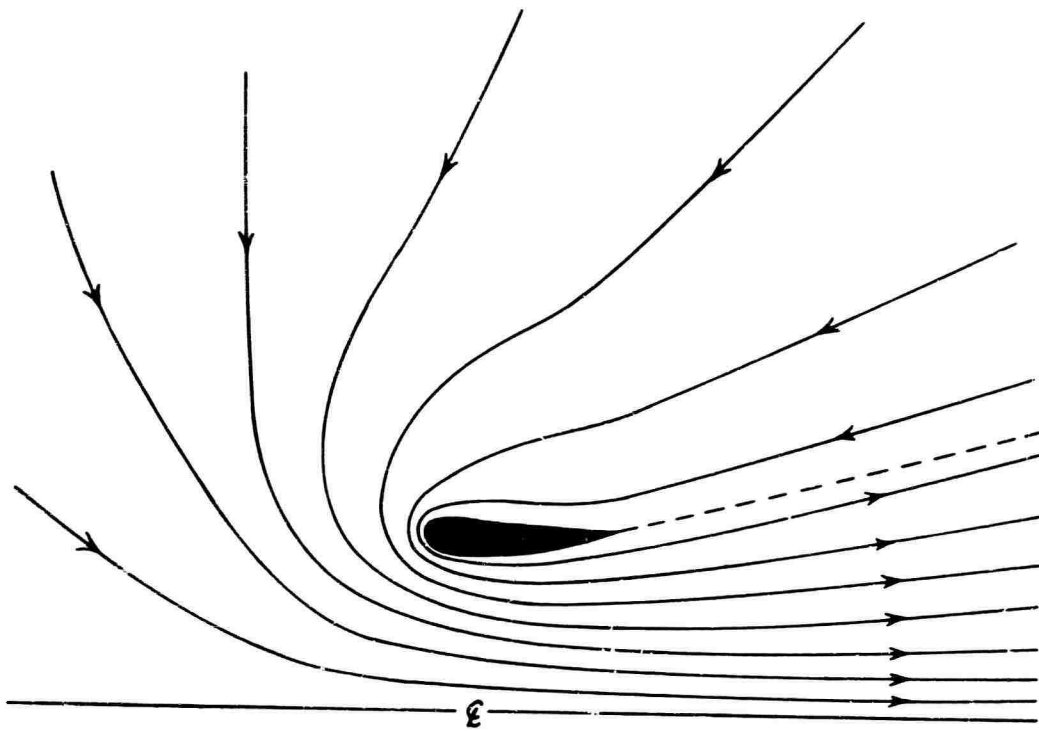
Figure 17.   Inviscid Flow Pattern - Static Condition.
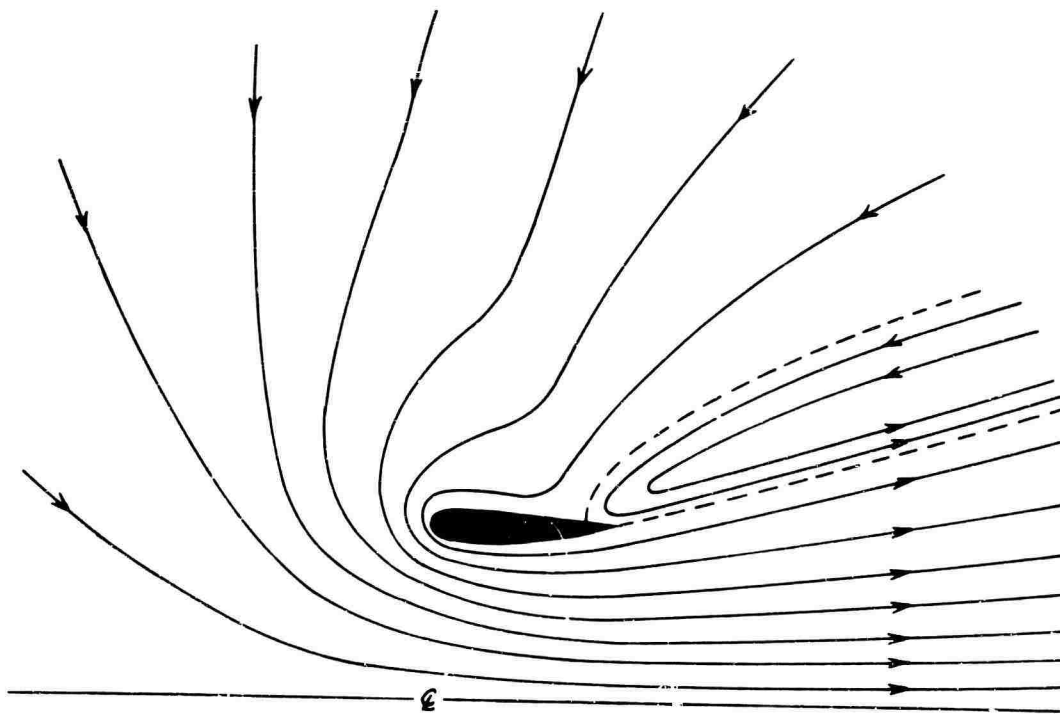
Figure 18.   Actual Flow Pattern - Static Condition.
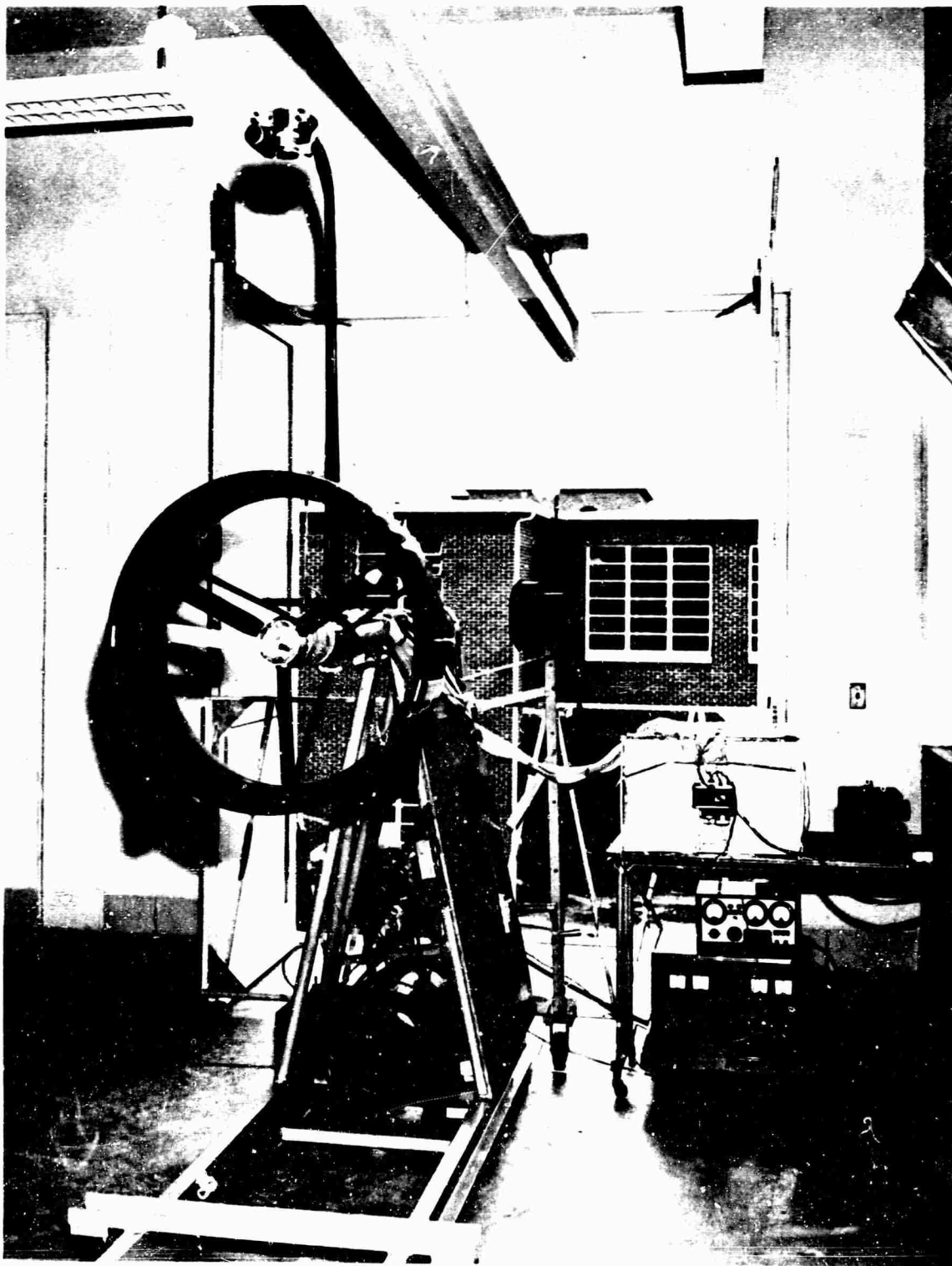
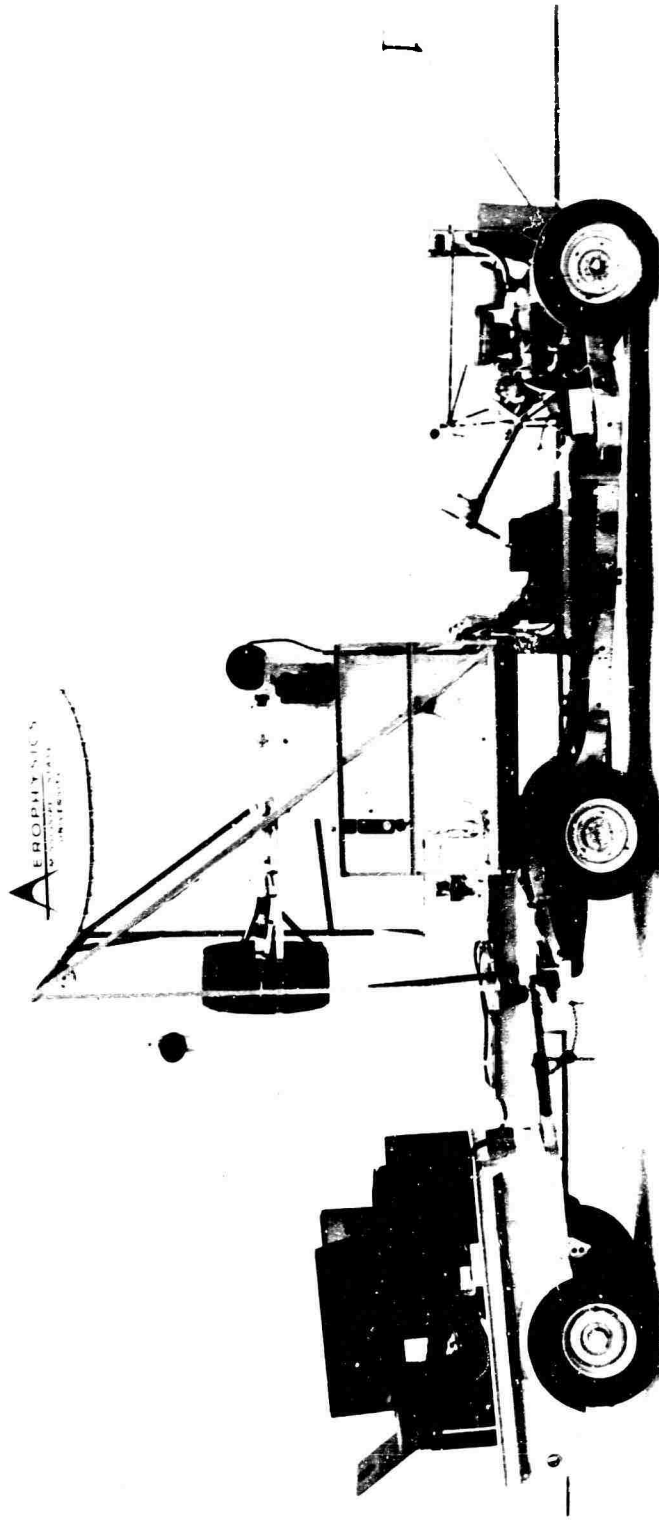Figure 19. Static Test Apparatus.

37

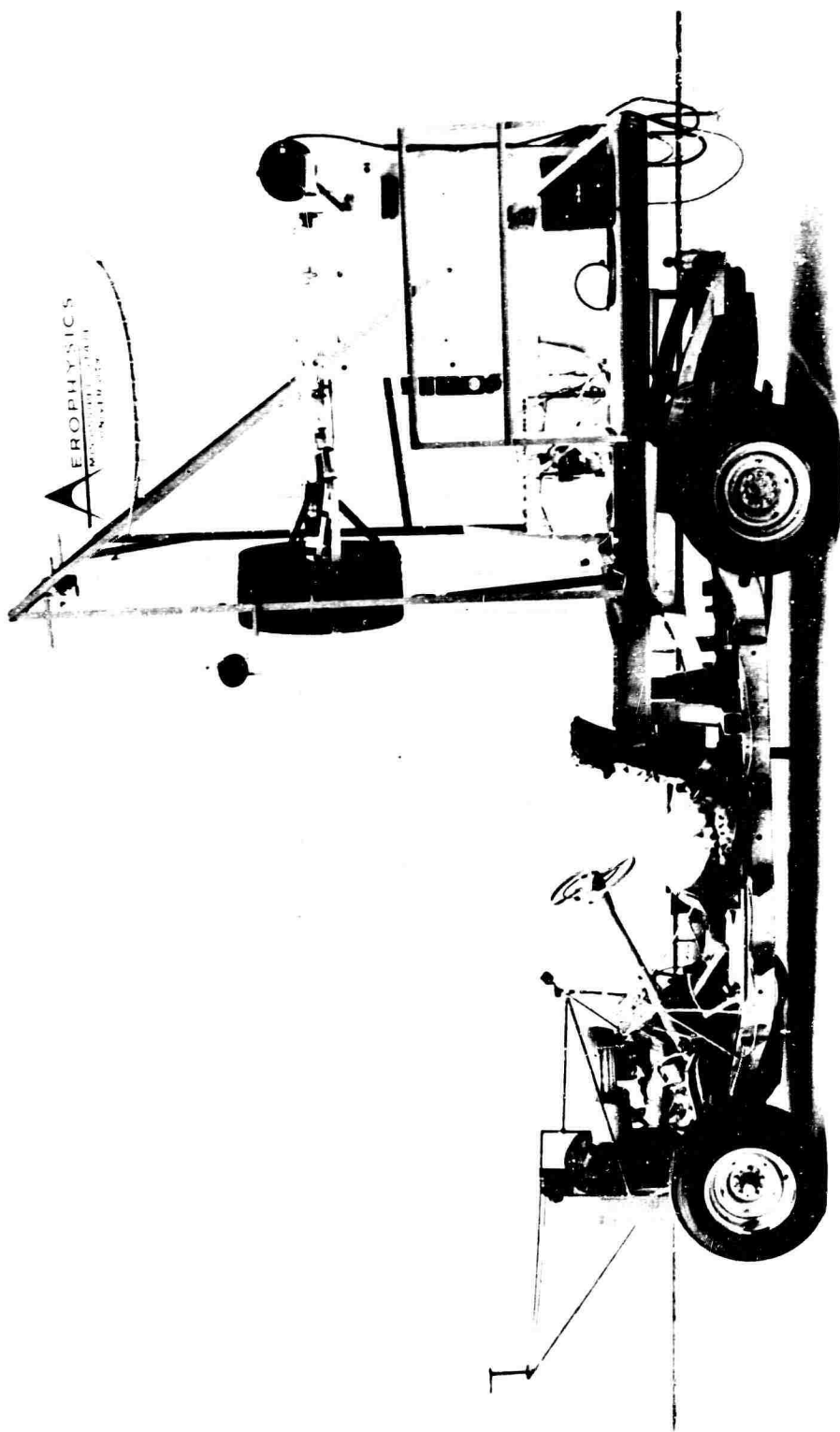Figure 20. Rearward Motion Test Apparatus.
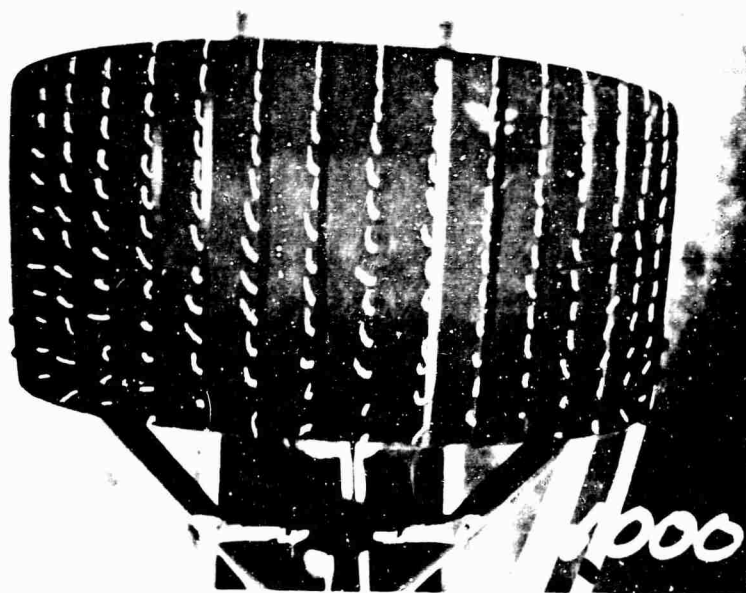
38

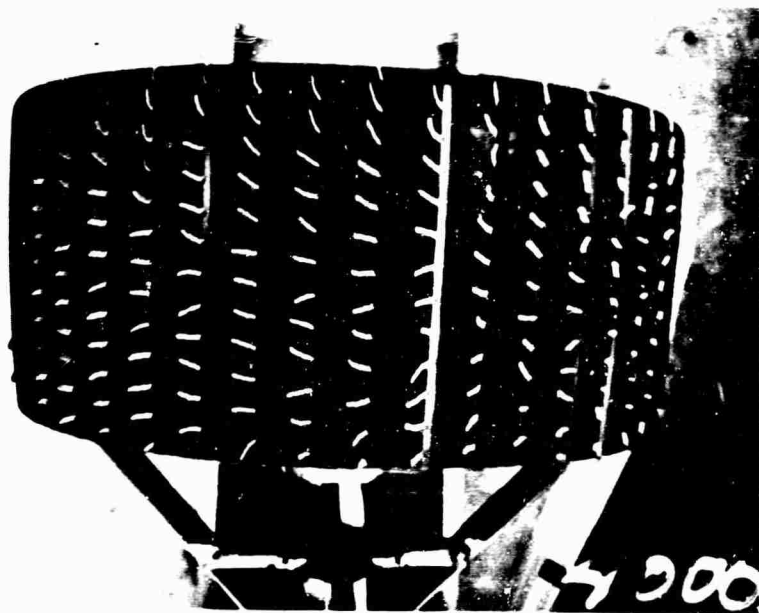Figure 21. Forward Motion Test Apparatus.

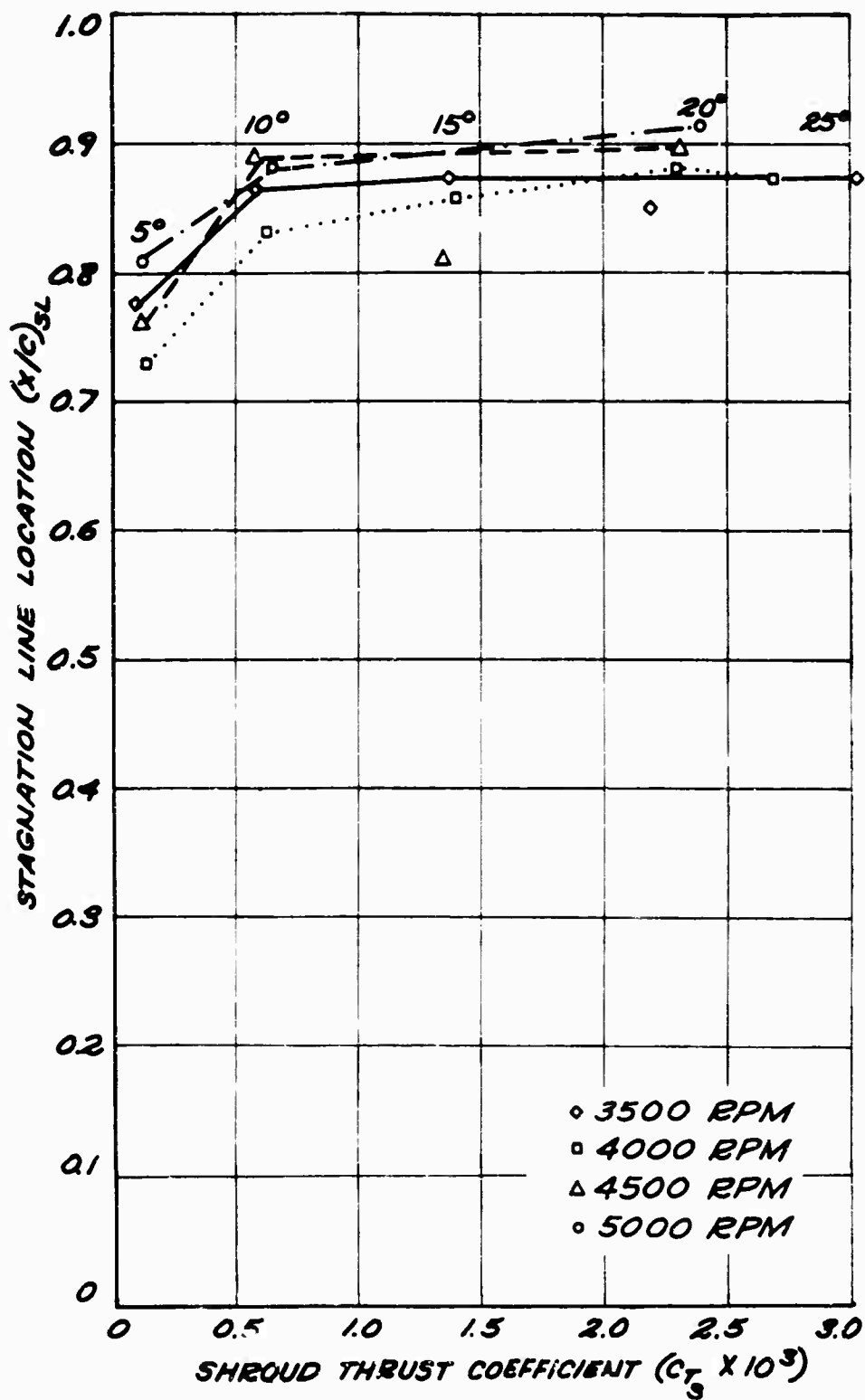Figure 22. Tuft Patterns - Static Condition.
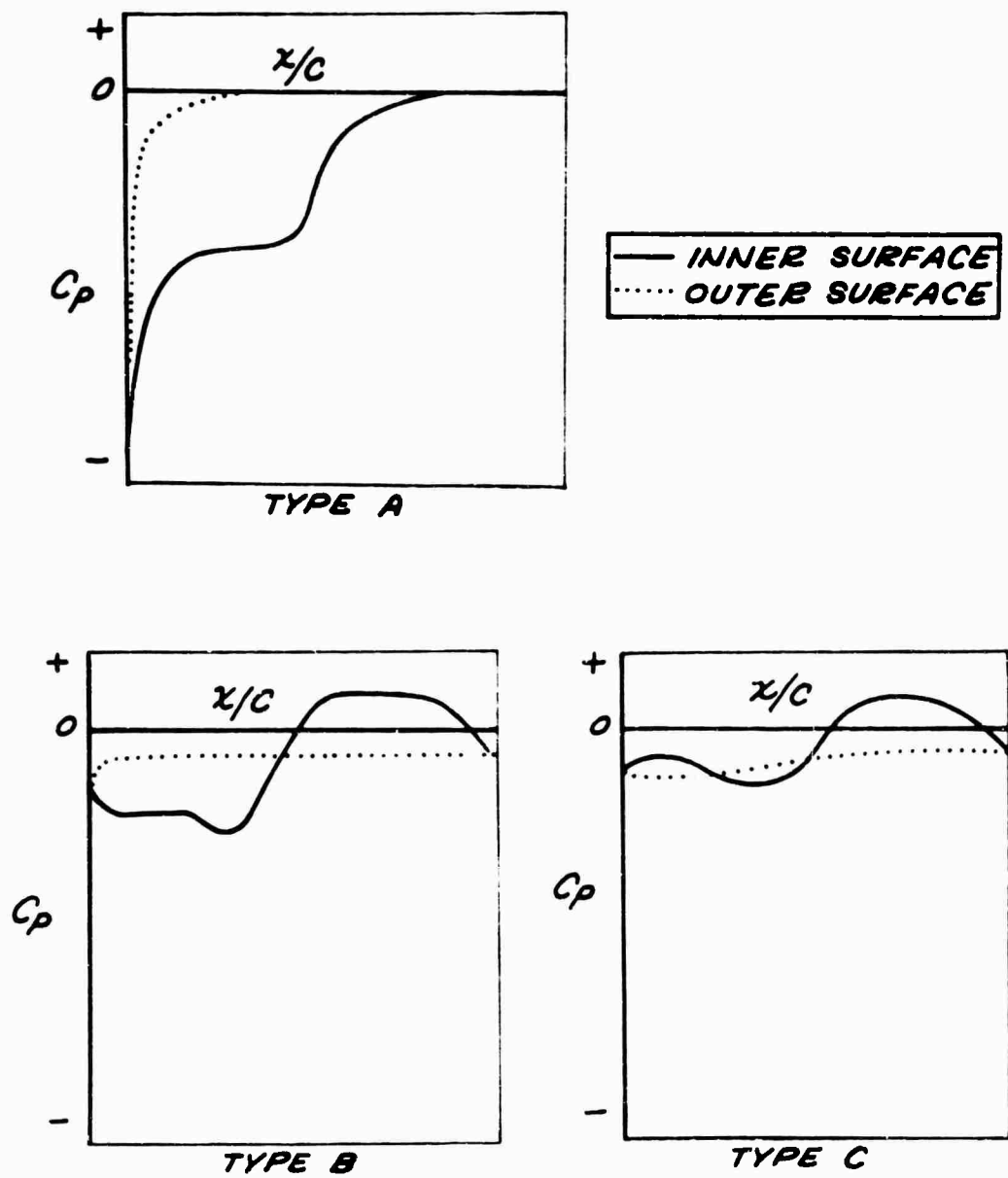
Figure 23.   Stagnation Line Location - Static Condition.

41

Figure 24. Pressure Distribution Types - Rearward Motion.
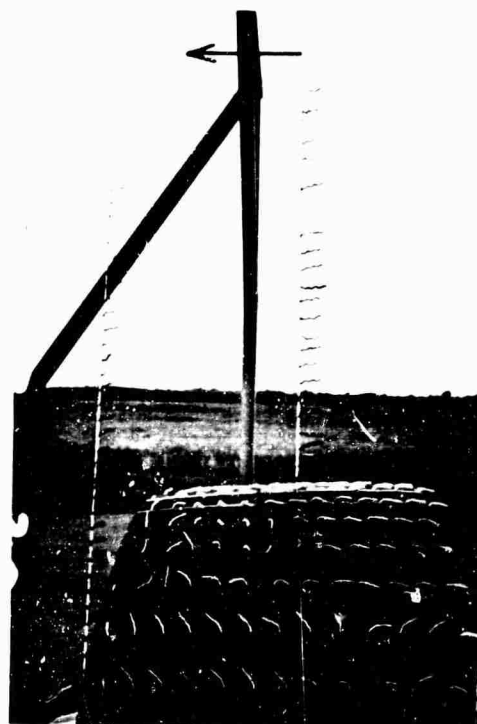
42

Figure 25.   Tuft Patterns - Rearward Motion.

43
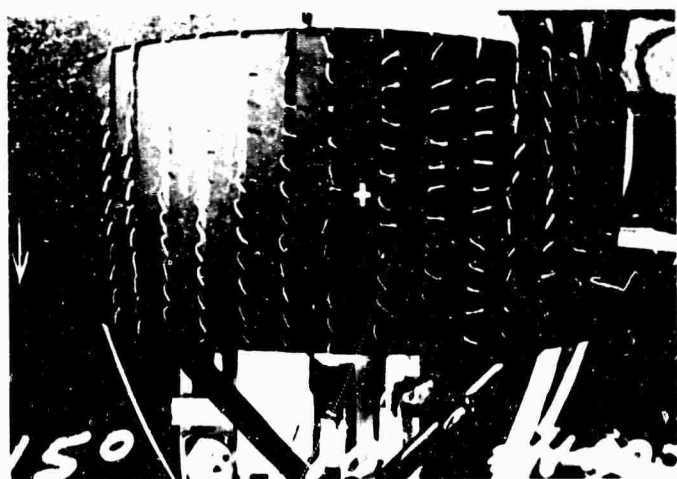
Figure 25. (Continued)

44
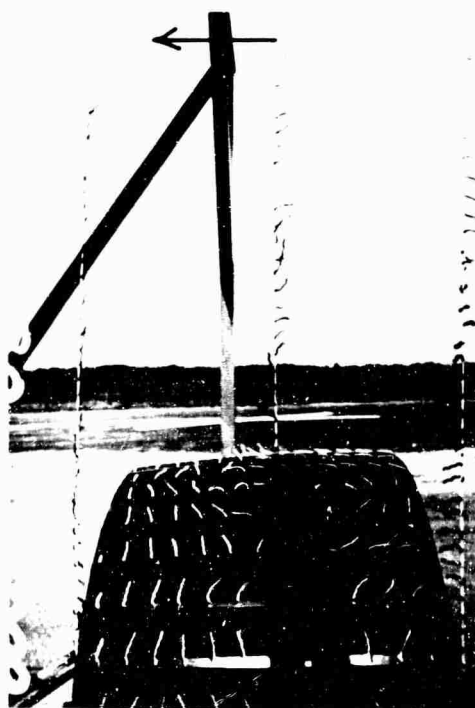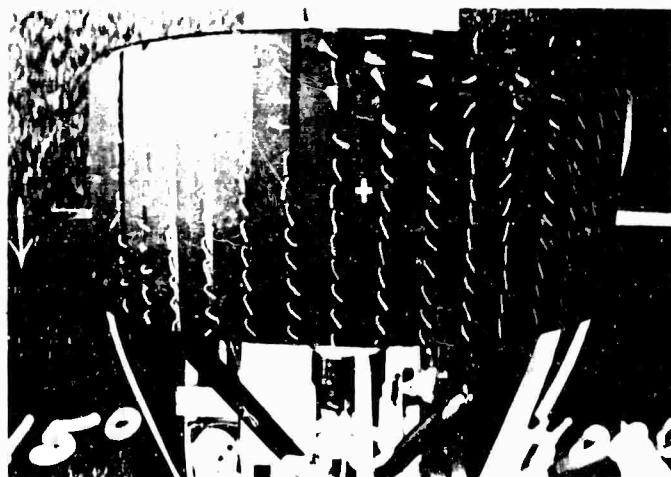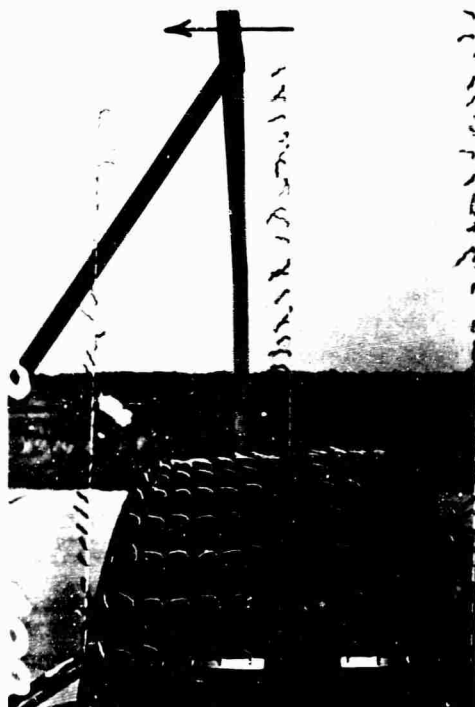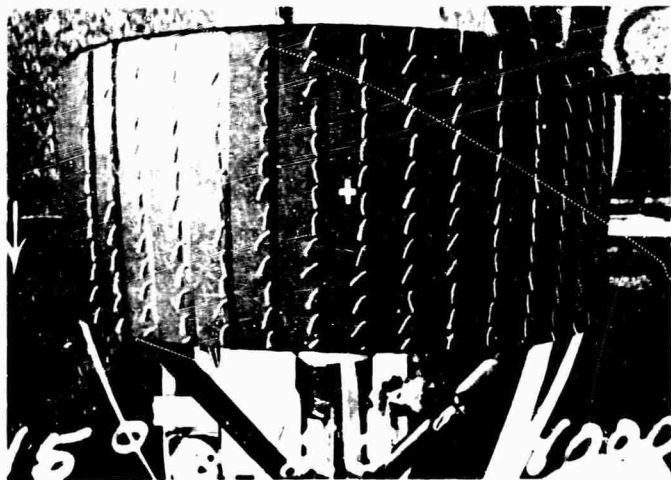
Figure 25.   (Concluded)

45

V_1

TYPE A

$V_2 > V_1$

TYPE A
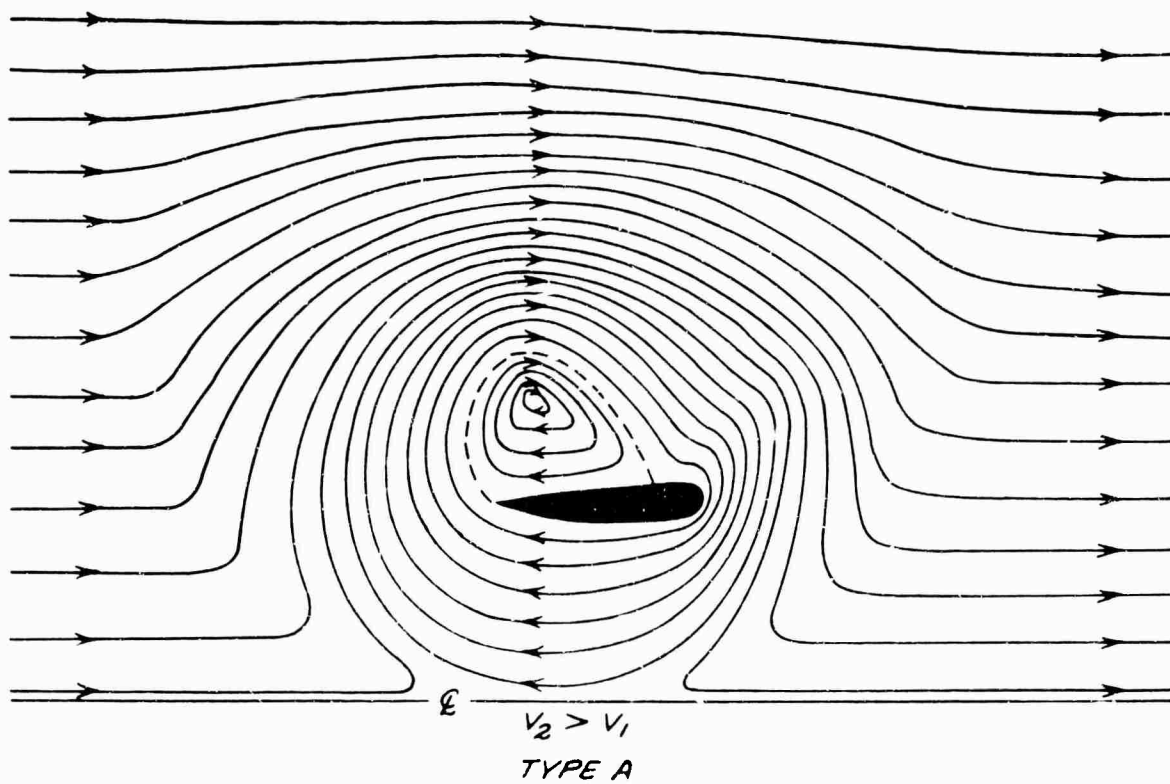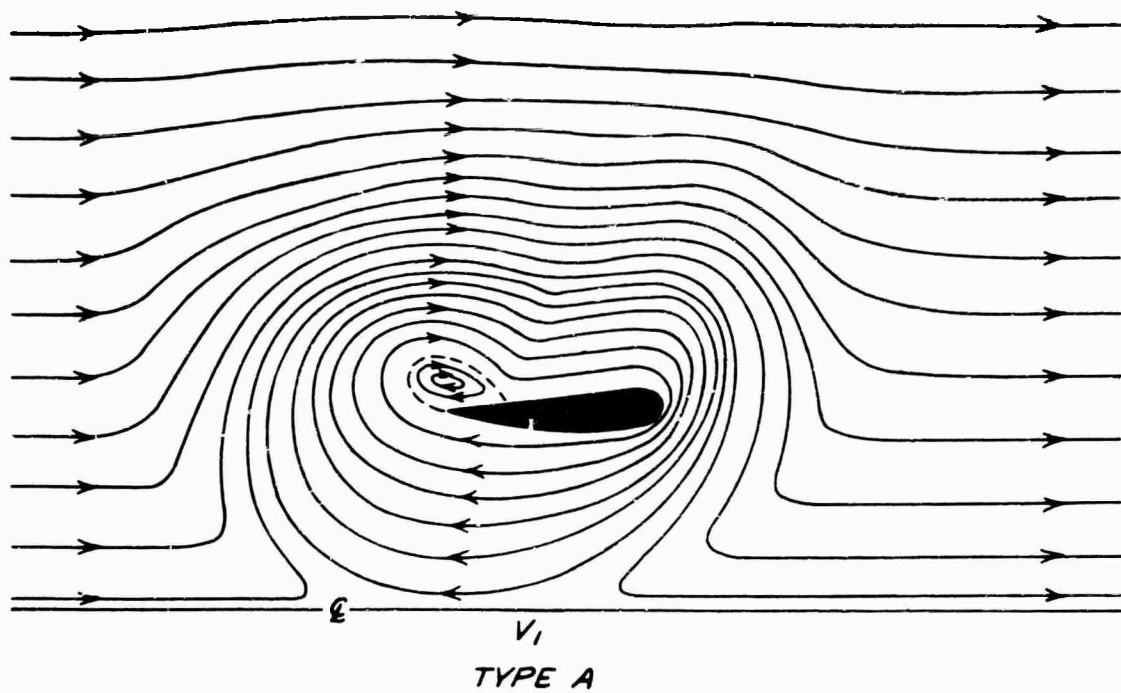
Figure 26a. Flow Pattern - Rearward Motion.
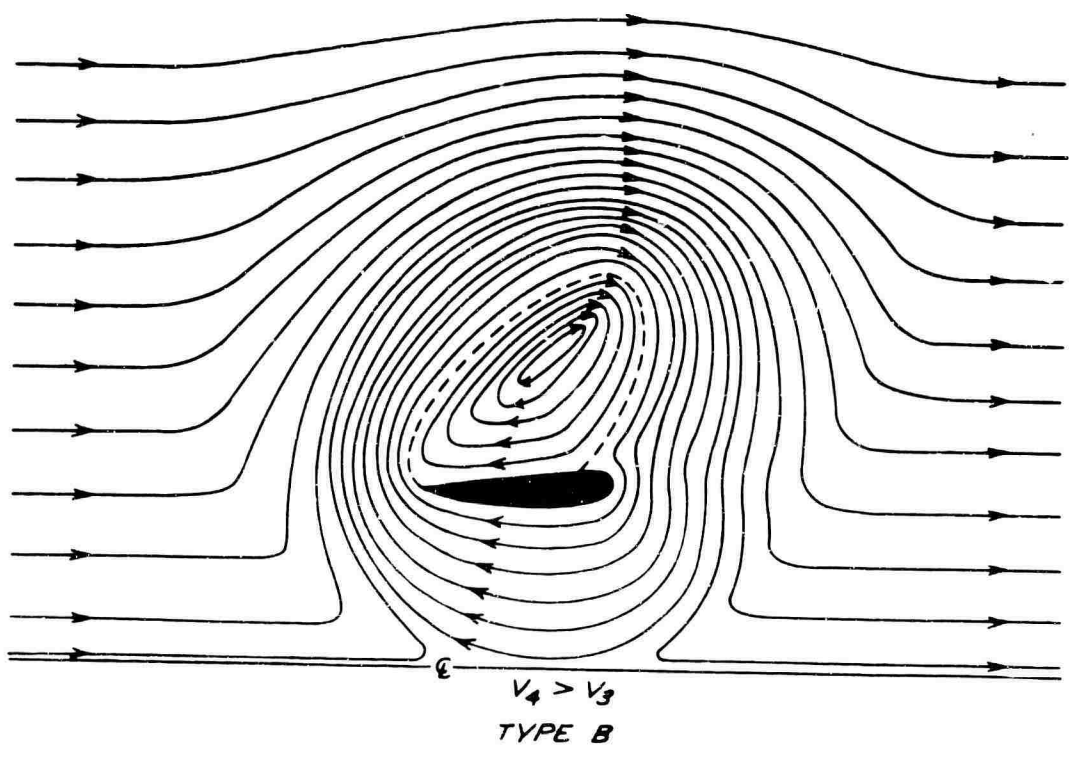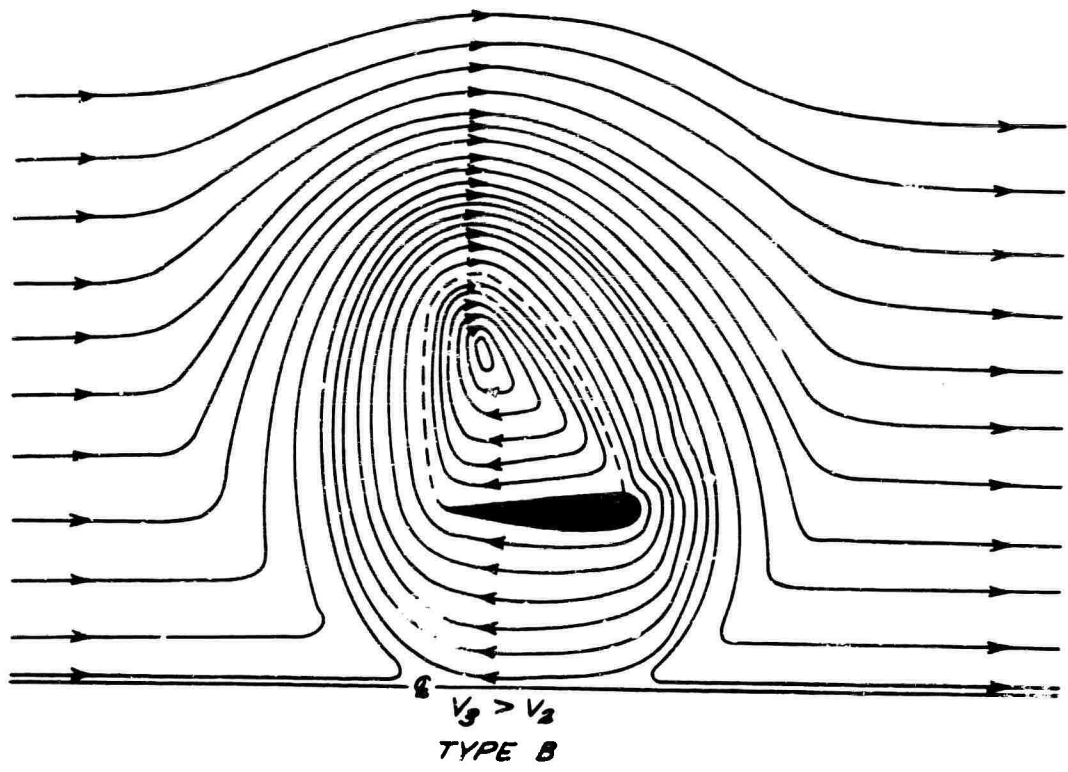
Figure 26b. Flow Pattern - Rearward Motion.

47

$\mathscr{E}$ $V_5 > V_4$
TYPE C
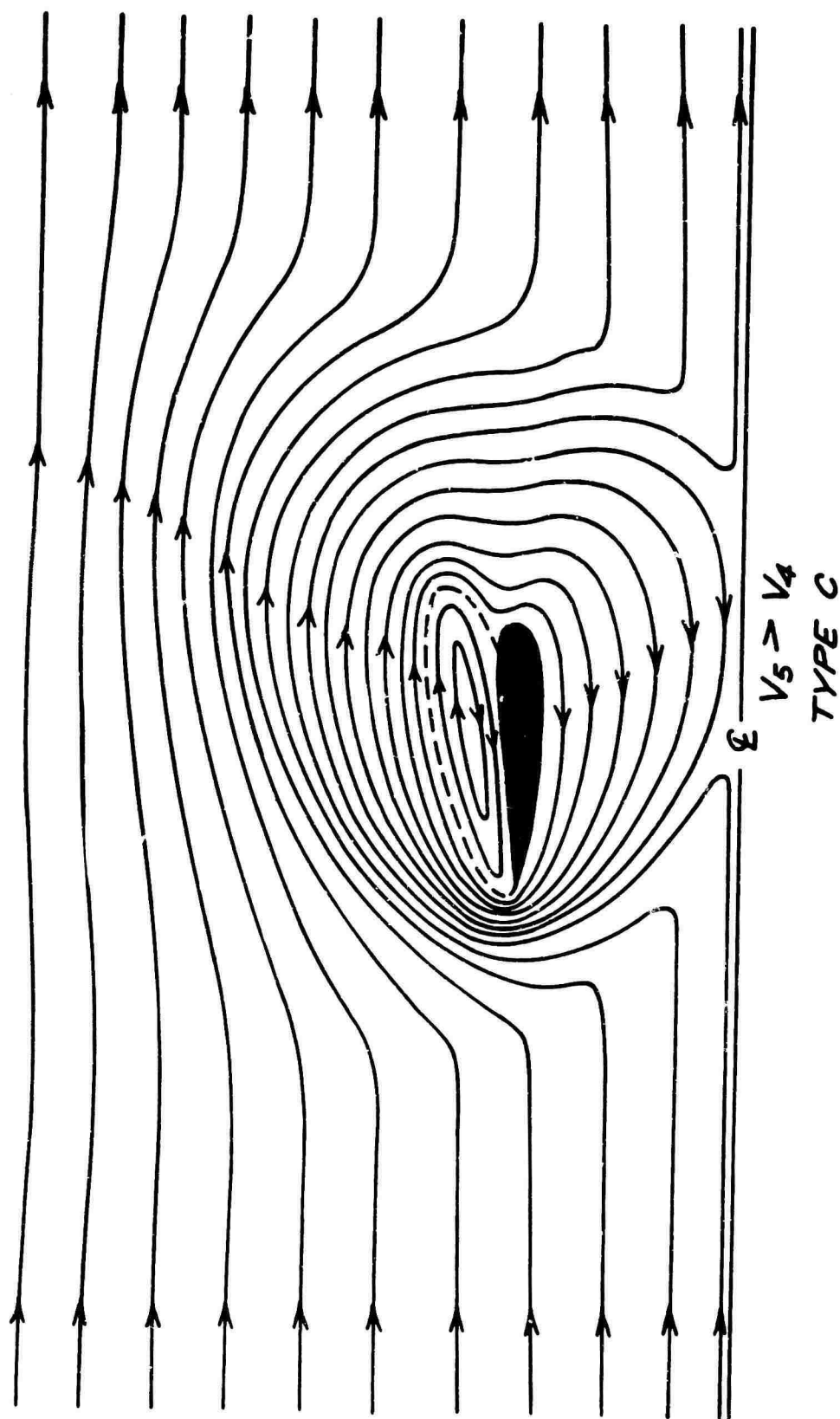
Figure 26c. Flow Pattern - Rearward Motion.
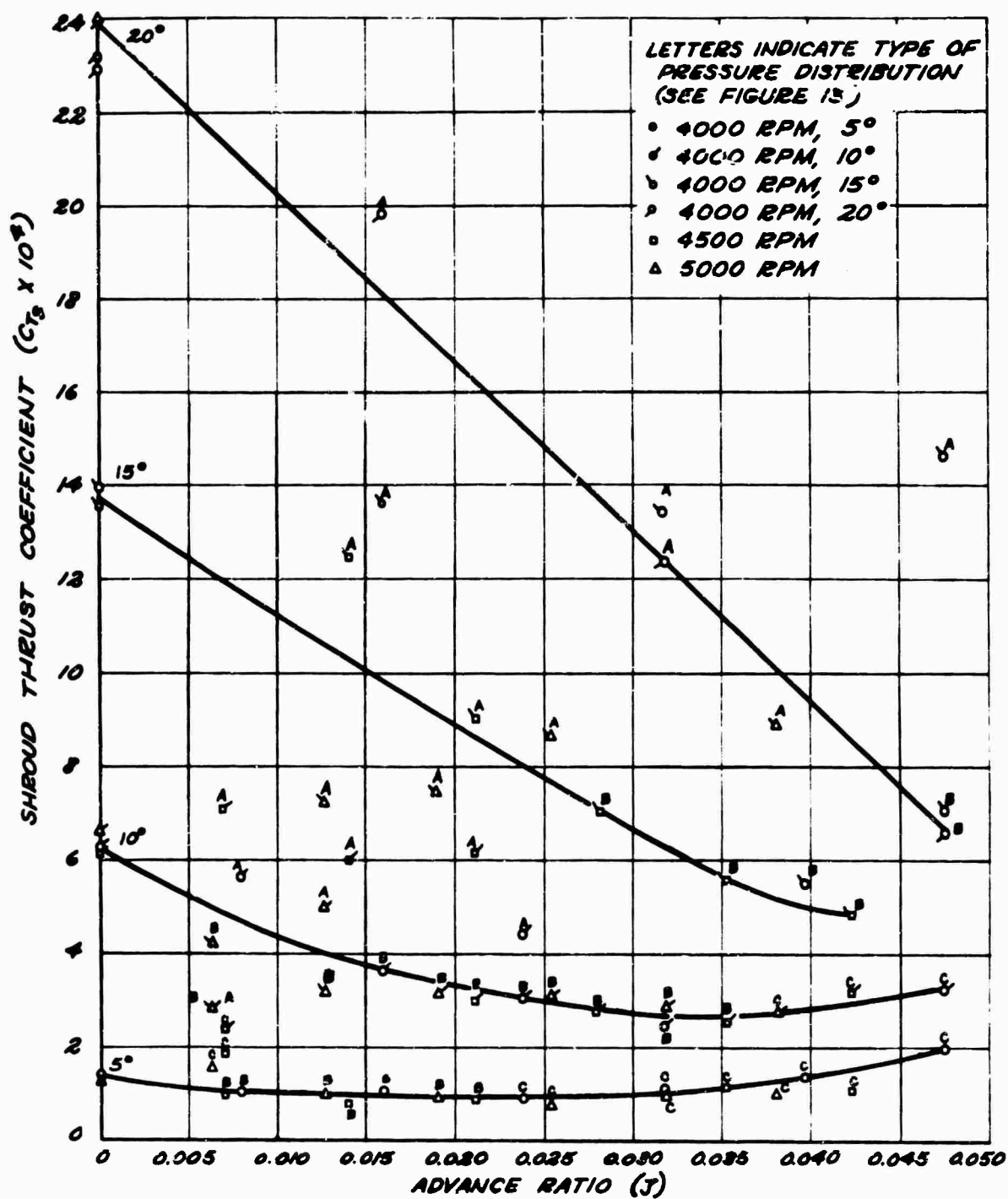
Figure 27.   Shroud Thrust - Rearward Motion.

49
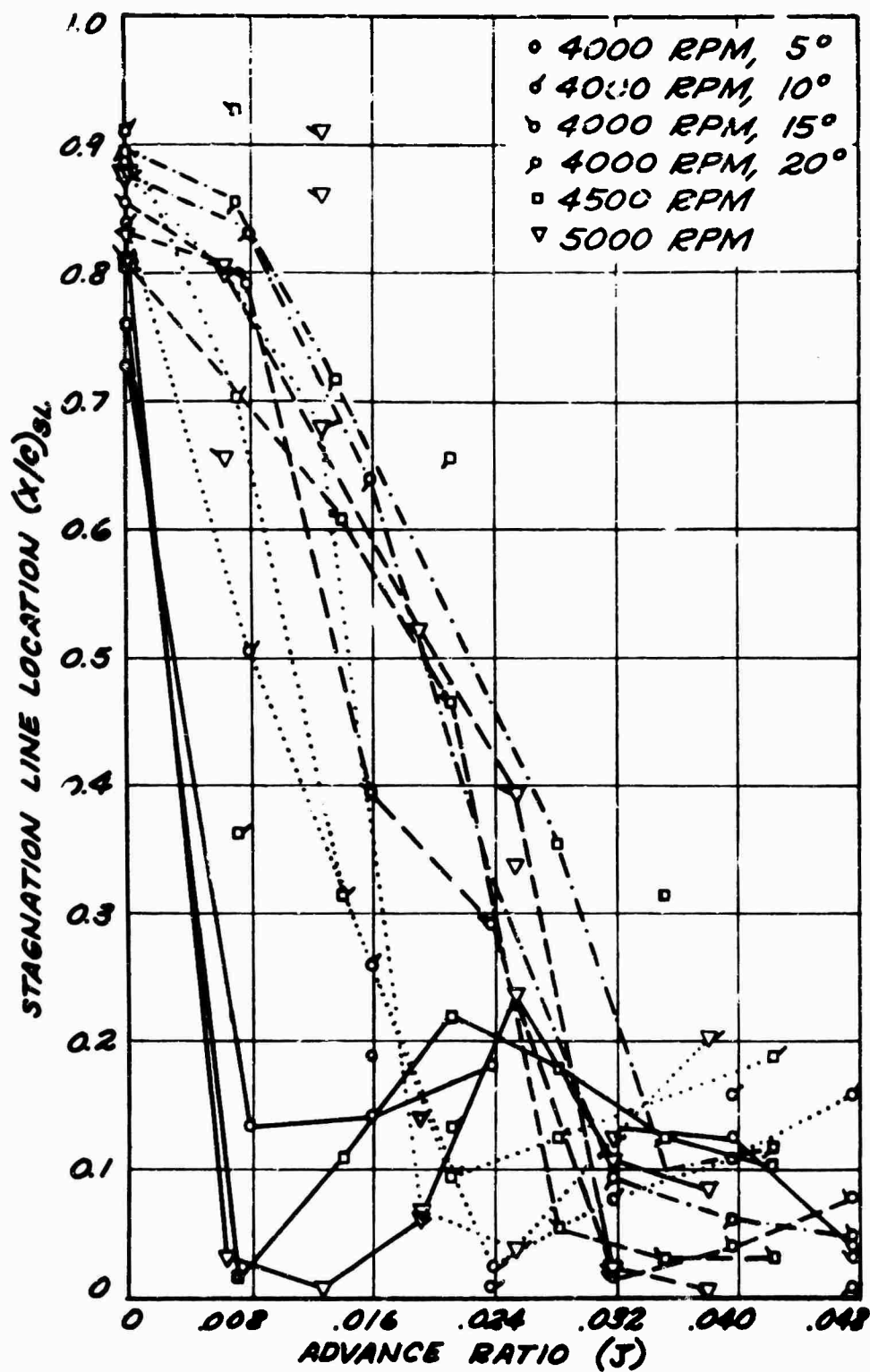
Figure 28. Stagnation Line Location - Rearward Motion.

50
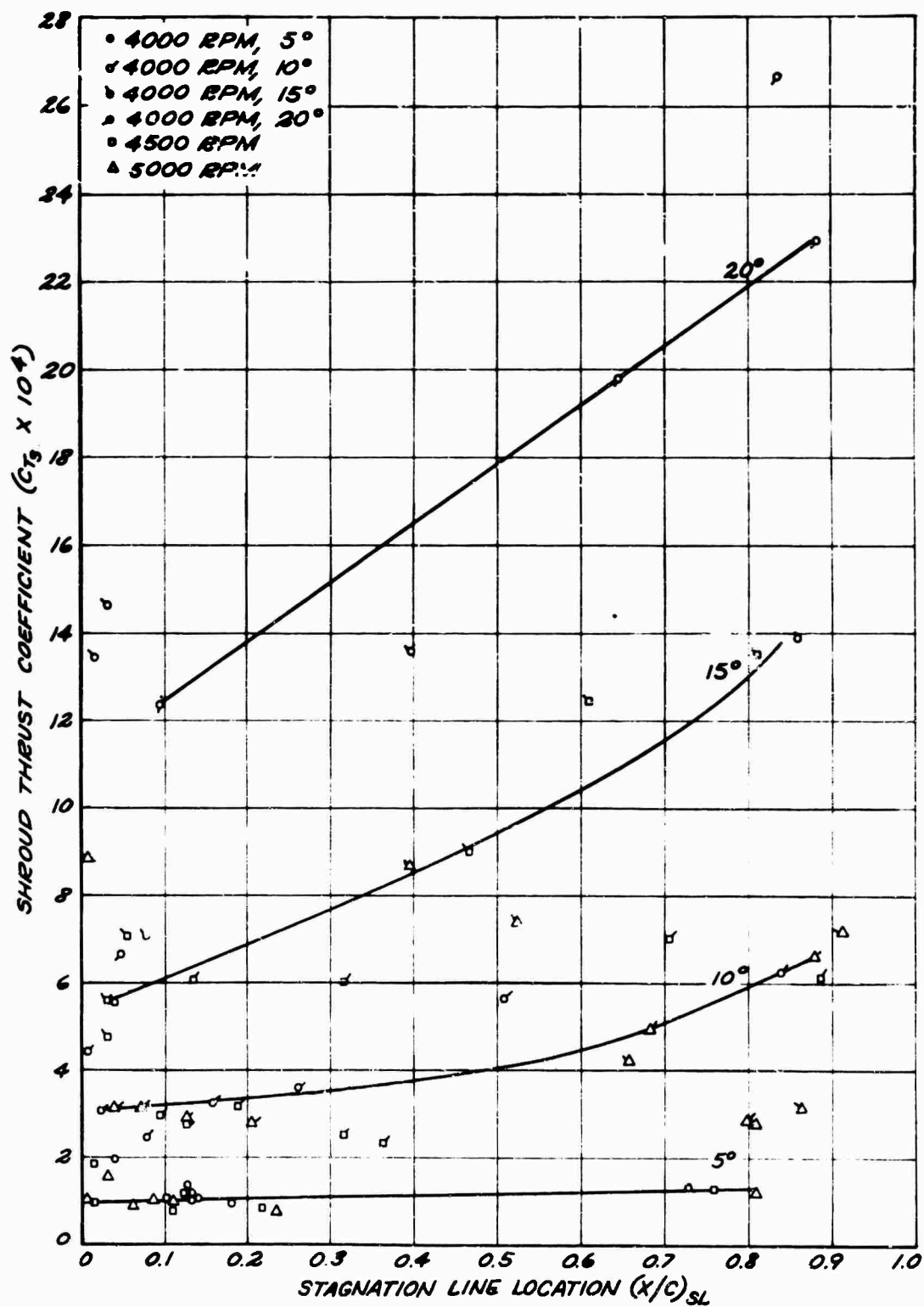
Figure 29. Relation of Shroud Thrust to Stagnation Line Location.

51

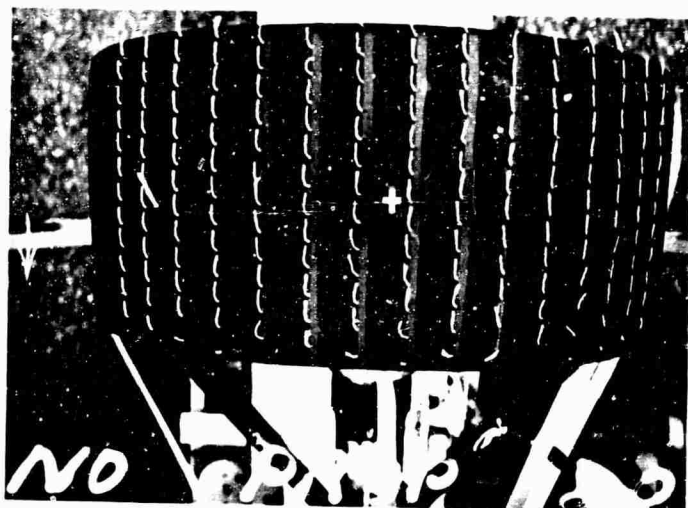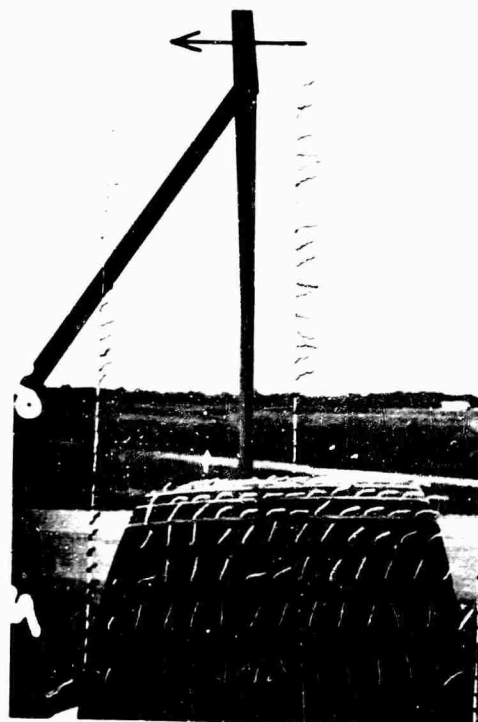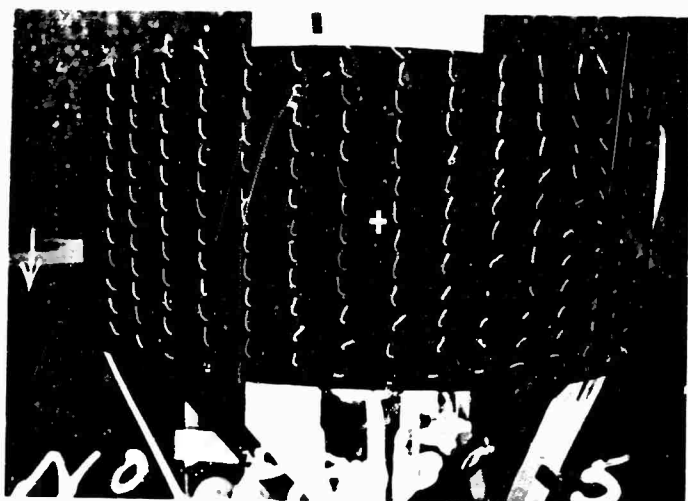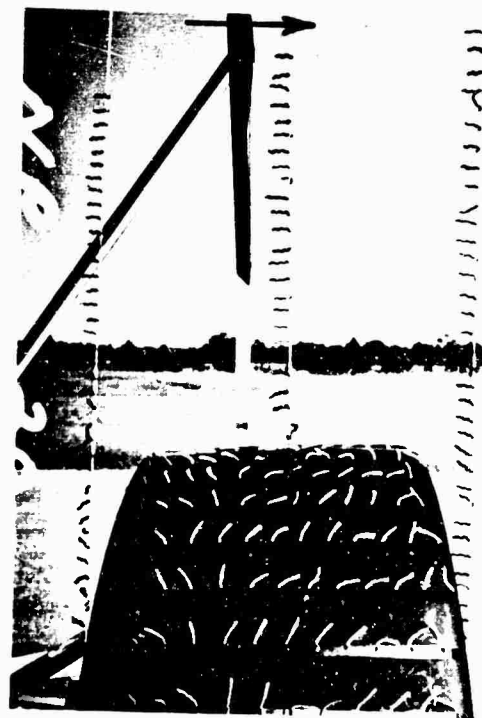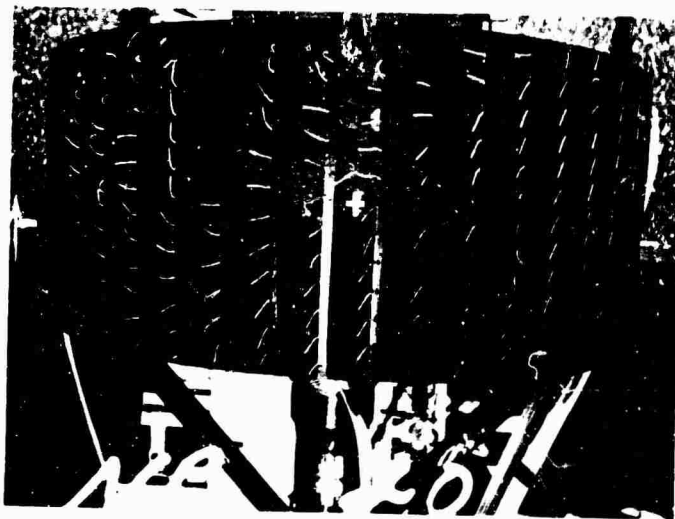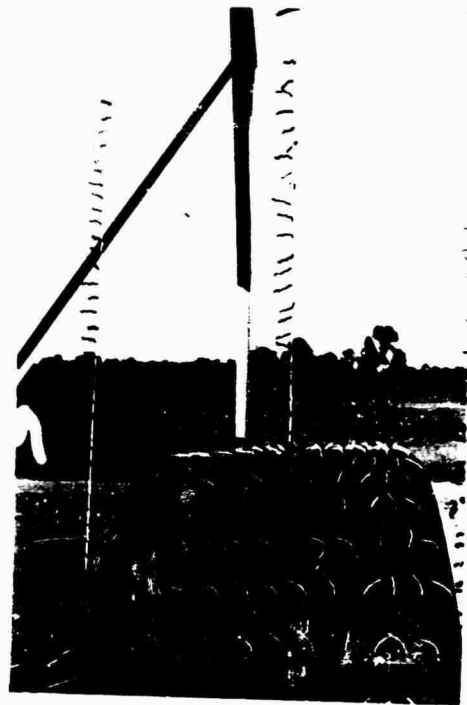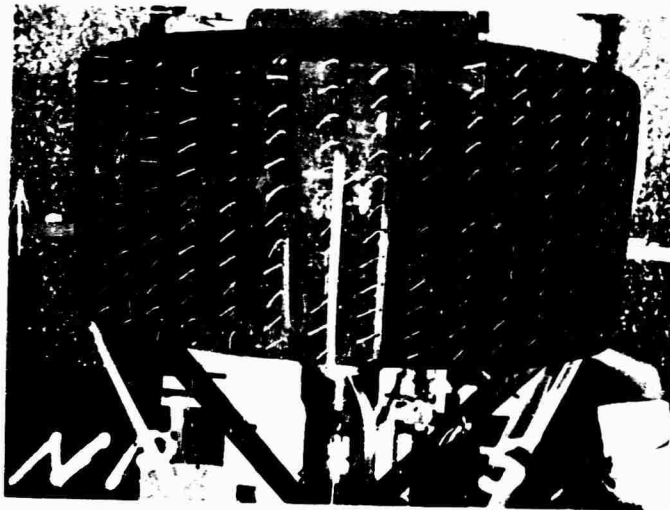Figure 30. Tuft Patterns - Forward Motion.
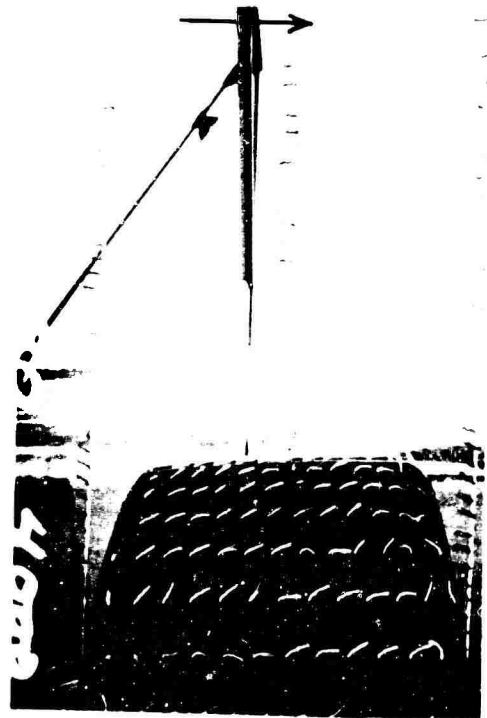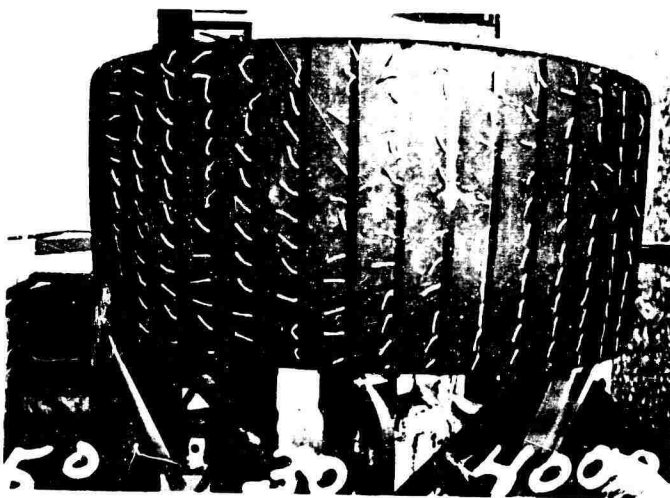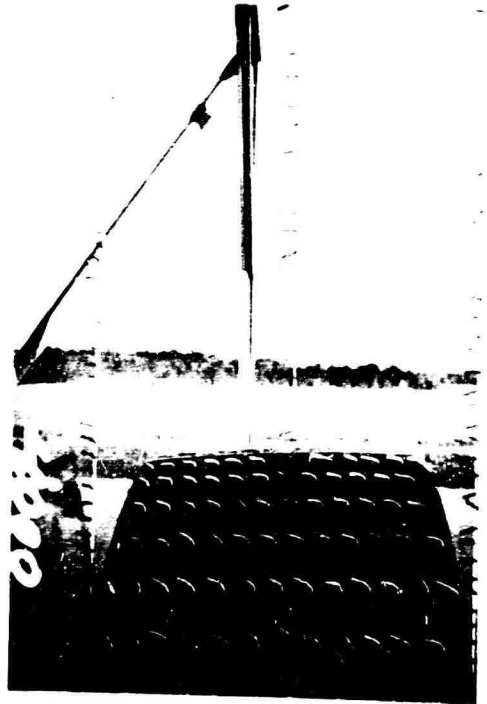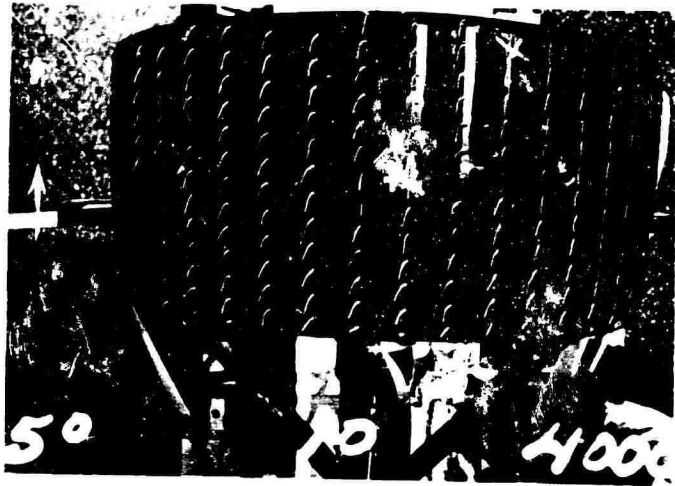
Figure 30. (Continued)
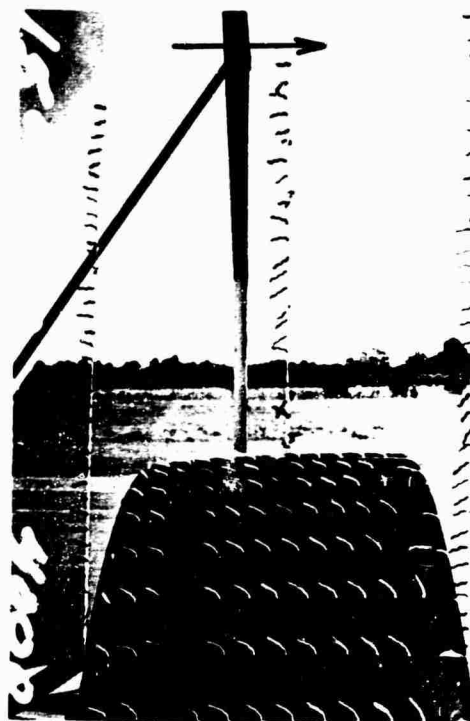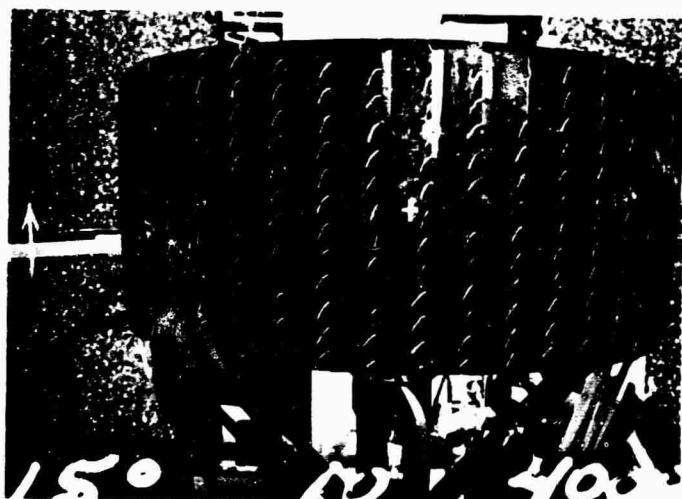
Figure 30.   (Concluded)

54

TYPE A

TYPE B
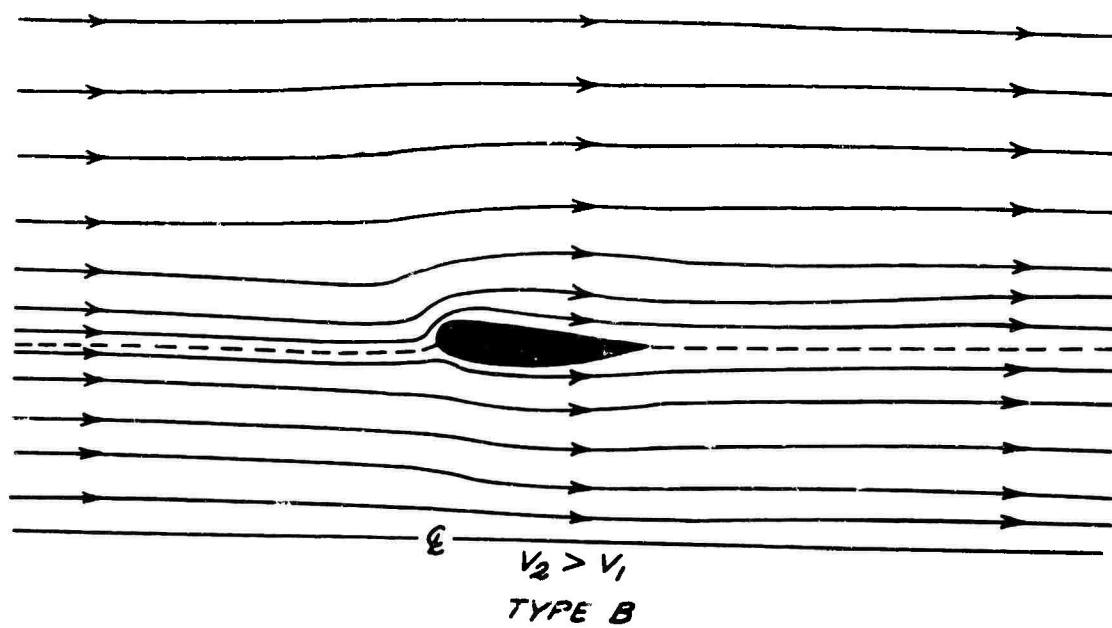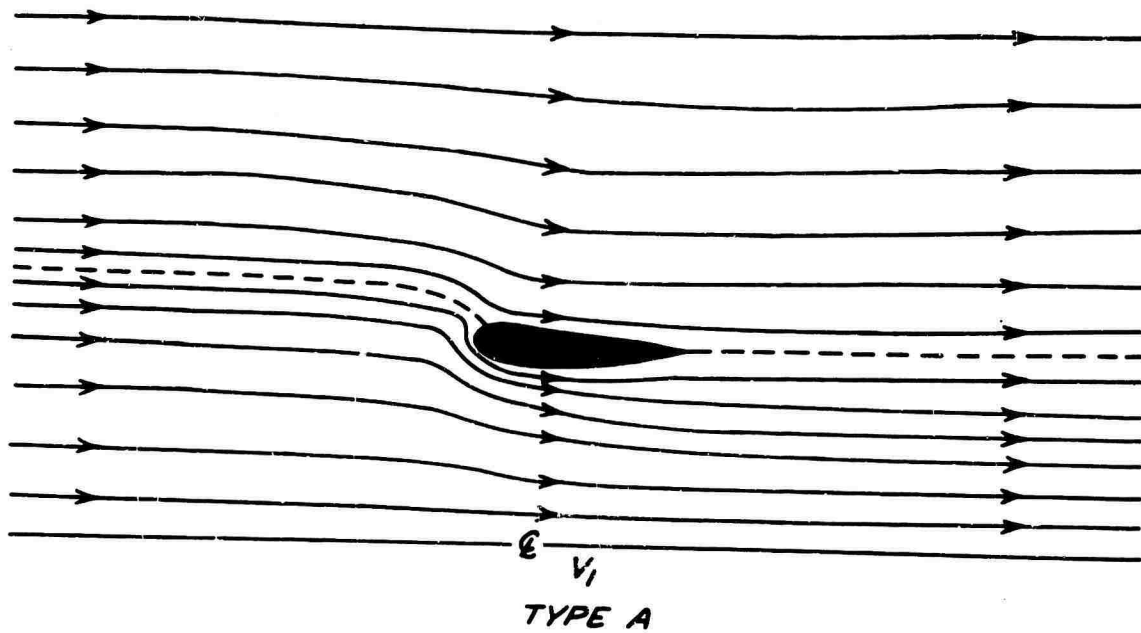
Figure 31.   Flow Pattern - Forward Motion.
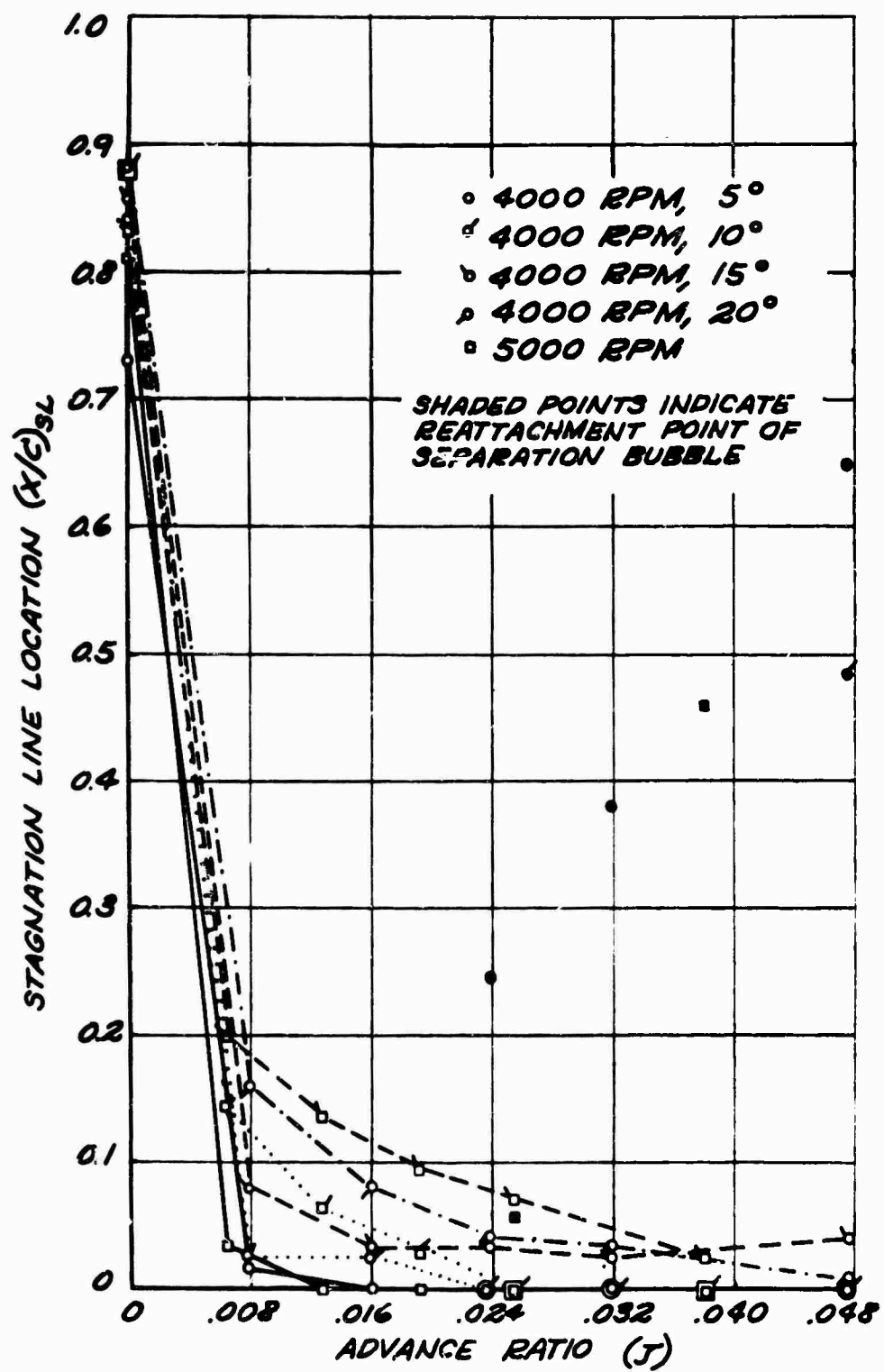
Figure 32.   Stagnation Line Location - Forward Motion.

56

TECHNICAL SESSION IV

INTERFERENCE AERODYNAMICS

Thursday Afternoon
23 June 1966

SESSION CHAIRMAN

I.H. Culver
Lockheed-California Company

NOTES

THE LIFT, DRAG AND STABILITY
OF WINGS IMMERSED
IN PROPELLER SLIPSTREAM

by

K.P. HUANG AND N. MILLER
Dynasciences Corporation
Blue Bell, Pennsylvania

ABSTRACT

An analytical method is developed to determine the effect of propeller slipstream on wing lift, drag and stability. The method is used to predict the onset of stall of slipstream-immersed wings. The use of propeller slipstream to augment the stability characteristics of a tilt-wing VTOL aircraft during transition is also investigated. Finally, a simplified analysis is made of the effect of a nonuniform jet velocity.

INTRODUCTION

The problem of the effect of propeller slipstream on wing lift was first investigated by Koning some thirty years ago (Reference 1). His analysis utilizes the assumption that the slipstream velocity is only slightly higher than the free stream velocity Other investigators have extended Koning's work for applications to more practical operating conditions. In general, the methods are relatively complex and solutions to specific problems often require the aid of automatic computing equipment.

In Reference 2 a simple analysis is presented for the lift of a wing spanning a slipstream of uniform velocity. In this paper the analysis is extended and applied to practical V/STOL aircraft wing-propeller configurations. Correlation with available test data is found to be satisfactory.

The method is then used to predict the onset of stall of wings immersed in slipstreams. Also, the use of propeller slipstream to augment the stability characteristics of a tilt-wing VTOL aircraft during transition is investigated.

Finally, an analysis is made of the effect on the wing lift of the nonuniform velocity of the slipstream.

PREDICTION OF LIFT AND DRAG COEFFICIENTS

An expression for the lift of a wing spanning a slipstream of uniform velocity is derived in Reference 2. For a rectangular wing the total lift coefficient is

$$C_L = \frac{8}{\pi}\left[1 + \frac{1}{2\mu^2}\left(\frac{\pi^2}{4} - 1\right)\right]\frac{r_s}{c}\alpha_s \tag{1}$$

The incremental lift coefficient due to the propeller slipstream is

$$\Delta C_L = \frac{\pi^2 - 4}{\pi}\left(\frac{1-\mu^2}{\mu^2}\right)\frac{r_s}{c}\alpha_s \tag{2}$$

The spanwise incremental lift distribution assumes the shape of the symmetrical curve

2

$$\left(\frac{1}{\overline{Y}_s} - \overline{Y}_s\right) \ln\left(\frac{1-\overline{\overline{Y}}_s}{1-\overline{\overline{Y}}_s}\right)$$

For a wing extended through one or more slipstreams the total lift coefficient is obtained as the sum of the basic lift coefficient of the wing, which is generated by the wing when no slipstream exists, and the incremental lift coefficient due to the effect of the slipstream. Thus,

$$C_L = C_{Lw} + \Delta C_L\left(\frac{S_s}{S}\right) \tag{3}$$

In this equation C_{Lw} can be determined by conventional methods (e.g., Reference 3). The incremental part $\Delta C_L\left(\frac{S_s}{S}\right)$ can be rewritten from Equation (2) in terms of thrust coefficient as follows:

$$\Delta C_L\left(\frac{S_s}{S}\right) = 0.468\left[\frac{1}{(1-C_{T,s})\cos(\alpha_T-\phi)} - \cos(\alpha_T-\phi)\right]\left[\frac{\cos\alpha_T}{\sqrt{\cos^2\alpha_T + \frac{C_{LL}}{1-C_{T,s}}}} + 1\right]\frac{ND^2}{S}\alpha_s \tag{4}$$

where the effective angle of attack of the slipstream α_s is

$$\alpha_s = i_w + \phi - \alpha_{Lo} + \lambda\,\delta_f \tag{5}$$

In Equation (5) the slipstream deflection angle ϕ, as shown in Figure 1, is

$$\phi = \tan^{-1}\left[\frac{\sin\alpha_T}{\sqrt{\cos^2\alpha_T + \frac{C_{T,s}}{1-C_{T,s}}}}\right] \tag{6}$$

3

and the empirical factor λ for the flap deflection angle is dependent on the flap type and flap chord.

The total drag coefficient consists of the following:

(a) Induced drag coefficient of the basic wing

(b) Induced drag coefficient from the incremental lift coefficient due to the slipstreams

(c) Profile drag coefficient of the wing areas immersed in the slipstreams

(d) Profile drag coefficient of the wing areas not immersed in the slipstreams

Thus, the total drag coefficient is

$$C_D = C_{D_i} + \Delta C_{D_i} + C_{Dos} + C_{Dow} \tag{7}$$

The induced drag coefficients C_{D_i} and ΔC_{D_i} can be determined from the respective lift coefficients C_{Lw} and ΔC_L by usual methods. The profile drag coefficients C_{Dos} and C_{Dow} are based on available section airfoil data. In obtaining these data the angle $i_w + \phi$ represents the angle of attack within the slipstream-immersed area, and the angle $i_w + \alpha_r = \alpha_w$ is used for the other portions of the wing.

CORRELATION WITH EXPERIMENTAL DATA

As indicated in Reference 2, lift and drag coefficients determined by the analytical method presented above are in good agreement with available experimental data (Reference

4

4, 5 and 6). Additional correlation with the test data from Reference 7 is made in this section.

In Reference 7 test data are presented of the lift coefficient of a propeller-wing configuration with single-slotted flaps. By subtracting the corresponding zero thrust values, the incremental lift coefficients due to the effect of slipstreams plus the contribution from the propeller thrust, $\Delta C_{L,s(p)}$, are obtained. These are shown in Figures 2 and 3 for flap deflection angles of $0°$ and $40°$, respectively. The solid lines on Figures 2 and 3 represent the calculated values, and are seen to correlate well with the test data.

In Reference 7 longitudinal force coefficient data are presented instead of drag coefficient. Correlation is thus only possible for the longitudinal force coefficients. The results, as shown in Figures 4 and 5, are seen to be satisfactory.

PREDICTION OF STALL

The usual method of predicting the onset of wing stall is to find the geometric angle of attack at which the spanwise lift coefficient distribution curve first reaches the maximum airfoil section lift coefficient curve (Reference 8).

The same method is utilized here for a wing immersed in propeller slipstreams. The wing areas immersed in the

5

slipstreams and those which are not are treated separately. In this context it should be noted that the velocity of the slipstream is higher than that of the free stream. Hence, the Reynolds number of the slipstream, and consequently the maximum airfoil section lift coefficient $C_{l_{max}}$ of the wing area inside the slipstream are higher. Data on this subject can be obtained from Reference 9. Furthermore, in the slipstream-immersed areas, the local lift coefficient C_l should be based on the slipstream dynamic pressure, which is higher than the free stream dynamic pressure. The combined effect of the increase of $C_{l_{max}}$ and the decrease of C_l results in a delay of wing stall in the slipstream-immersed areas.

In determining the onset of stall in the wing areas immersed in the slipstreams, the direction of propeller rotation has to be taken into consideration. As pointed out before, for a nonrotating slipstream the incremental lift coefficient distribution curve is symmetrical with respect to the slipstream centerline. However, as a result of the slipstream rotation, the local angle of attack is increased on that portion of the wing in the propeller upwash and vice versa, thereby shifting the peak of the incremental lift coefficient distribution curve away from the centerline. This phenomenon is noticed in the experiments as reported in Reference 10.

A numerical analysis was performed on the lift coefficient distribution of the wing model used in Reference 5. Shown in Figure 7 is the lift coefficient distribution curve

6

with the propeller rotating up at wing tip. In Figure 7 the corresponding result is shown for the propeller rotating down at wing tip. In both cases, due to a comparatively low angle of attack no stall occurs within the slipstream-immersed areas.

When the wing geometric angle of attack is higher, the situation becomes somewhat different. In Figure 8, where the propeller blades rotate up at the ving tip, stall still does not occur within the slipstreams. On the other hand, with the propeller blades rotating down at the wing tip, the peak of the C_l curve, which is now inboard of the propeller centerline, exceeds the local $C_{l_{max}}$. As a result the slip-stream-immersed areas are partially stalled, as shown in Figure 9.

Test data of Reference 6 are used to verify the above mentioned method of predicting the onset of wing stall. The results are presented in Figure 10. The experimental data shown correspond to the wing angles of attack where the lift curve slope begins to change noticeably. It is seen that for constant values of $C_{T,s}$, up to $C_{T,s} = 0.5$ the calculated values of the wing angle of attack at initial stall within the slip-streams correlate well with test data.

EFFECT ON V/STOL AIRCRAFT STABILITY

The feasibility of utilizing the slipstream for stability augmentation was investigated for a 4-propeller

7

tilt-wing VTOL aircraft having a variable-angle flap.

An analog computer analysis was conducted of the
longitudinal stability characteristics for transition flight
speeds of 30 and 70 knots. The results are as follows:

Computer Solution At 30 Knots

The response of the unstabilized aircraft to a flap
pulse input is shown in Figure 11. It is noted that the
response consists of an unstable aperiodic mode with a time
to double of 0.9 seconds.

The variable-angle flap stabilizer system investigated
is described by the following equation:

$$\delta + k_1 \theta + k_3 w = 0 \qquad (8)$$

where
δ is flap stabilizer deflection

θ is fuselage attitude

w is normal perturbation velocity

k_1 is stabilizer attitude gain

k_3 is stabilizer normal velocity gain

The effect of the constants k_1 and k_3 were investiga-
ted and it was found that the aircraft becomes very stable with
the stabilizer setting as described by

$$\delta - 15\theta - 0.32 w = 0 \qquad (9)$$

8

The transient response of the aircraft with this stabilizer setting is shown in Figure 12.

Computer Solution At 70 Knots

The basic unstabilized aircraft's response to a flap pulse input is shown in Figure 13. As expected, the response for this flight condition is similar to that of a typical fixed-wing aircraft. The aircraft response consists of a long period oscillation (phugoid mode) with a period of 10 seconds and a time to half amplitude of 9 seconds.

The use of a flap stabilizer corresponding to

$$\delta - 15\theta - 0.169 w = 0 \qquad (10)$$

results in the response shown in Figure 14. As noted from this figure, the response is very rapid and stable.

EFFECT OF NONUNIFORM VELOCITY PROFILE

In the analysis presented in Reference 2, the slip-stream is assumed to be of uniform velocity. This theory is now extended in order to determine the gross effect of the nonuniform velocity profile on the wing lift characteristics. For this purpose a slipstream with two concentric velocity zones is considered. The velocity pattern is either as in case (a) or case (b) of Figure 15. In the outer ring there is a perturbation velocity potential Φ_1 , and in the central region the potential is Φ_2 . The potential in the free stream is defined as Φ_0 . These potentials are solutions of the two-

9

dimensional Laplace's Equation with the following boundary conditions:

$$\frac{\partial \Phi_1}{\partial z} = -V_1 \alpha_s \quad \text{at} \quad z=0 \quad \text{and} \quad r_s' \leqq r \leqq r_s$$

$$\frac{\partial \Phi_2}{\partial z} = -V_2 \alpha_s \quad \text{at} \quad z=0 \quad \text{and} \quad 0 \leqq r \leqq r'$$

$$V_1 \frac{\partial \Phi_0}{\partial r} = V_0 \frac{\partial \Phi_1}{\partial r} \quad \text{at} \quad r=r_s$$

$$V_0 \Phi_0 = V_1 \Phi_1 \quad \text{at} \quad r=r_s$$

$$V_2' \frac{\partial \Phi_1}{\partial r} = V_1 \frac{\partial \Phi_2}{\partial r} \quad \text{at} \quad r=r_s'$$

$$V_1 \Phi_1 = V_2 \Phi_2 \quad \text{at} \quad r=r_s'$$

$$\Phi_0 = 0 \quad \text{as} \quad r \to \infty$$

$$\Phi_2 \quad \text{is finite at} \quad r=0$$

The potentials at the wing trailing edge are found to be

$$\Phi_{s1} = \frac{2(1+\mu_1^4) V_0 \alpha_s r_s}{\pi \mu_1}$$

$$+ \frac{2(1-\mu_1^2)(\mu_2^2-\mu_1^2) V_0 \alpha_s r_s'}{\pi \mu_1 (1+\mu_1^2)(\mu_1^4+\mu_2^2)} \left\{ 1 + \frac{1}{2} \left[\left(\frac{r_s'}{r_s}\right) \bar{y}_s - \frac{1}{\left(\frac{r_s'}{r_s}\right) \bar{y}_s} \right] \ln \left[\frac{1 + \left(\frac{r_s'}{r_s}\right) \bar{y}_s}{1 - \left(\frac{r_s'}{r_s}\right) \bar{y}_s} \right] \right\}$$

$$- \frac{2 V_0 \alpha_s r_s}{\pi \mu_1} \left\{ 1 + \frac{1}{2} \left[\bar{y}_s - \frac{1}{\bar{y}_s} \right] \ln \left[\frac{1+\bar{y}_s}{1-\bar{y}_s} \right] \right\}$$

$$+ \frac{2(\mu_1^2-\mu_2^2) V_0 \alpha_s r_s'}{\pi \mu_1 (\mu_1^2+\mu_2^2)} \left\{ 1 + \frac{1}{2} \left[\frac{\left(\frac{r_s'}{r_s}\right)}{\bar{y}_s} - \frac{\bar{y}_s}{\left(\frac{r_s'}{r_s}\right)} \right] \ln \left[\frac{1 + \left(\frac{r_s'}{r_s}\right) \frac{1}{\bar{y}_s}}{1 - \left(\frac{r_s'}{r_s}\right) \frac{1}{\bar{y}_s}} \right] \right\}$$

$$+ \frac{2(\mu_2^2-\mu_1^2) V_0 \alpha_s r_s}{\pi \mu_1 (\mu_1^2+\mu_2^2)} \left\{ 1 + \frac{1}{2} \left[\left(\frac{r_s'}{r_s}\right)^2 \frac{1}{\bar{y}_s} - \frac{\bar{y}_s}{\left(\frac{r_s'}{r_s}\right)^2} \right] \ln \left[\frac{1 + \left(\frac{r_s'}{r_s}\right)^2 \frac{1}{\bar{y}_s}}{1 - \left(\frac{r_s'}{r_s}\right)^2 \frac{1}{\bar{y}_s}} \right] \right\} \qquad (11)$$

10

for $\quad \dfrac{r_s'}{r_s} \leqq \bar{\gamma}_s \leqq 1$

and

$$\Phi_{s2} = \frac{2V_0\alpha_s}{\pi\mu_1}\left[\frac{\mu_1}{\mu_1}(1-\mu_1^2)r_s + \frac{1}{\mu_1\mu_2}(\mu_1^2-\mu_2^2)r_s'\right]$$
$$+ \frac{2(\mu_2^2-\mu_1^2)V_0\alpha_s r_s'}{\pi\mu_2(\mu_1^2+\mu_2^2)}\left\{1+\frac{1}{2}\left[\left(\frac{r_s}{r_s'}\right)\bar{\gamma}_s - \frac{1}{\left(\frac{r_s}{r_s'}\right)\bar{\gamma}_s}\right]\ln\left[\frac{1+\left(\frac{r_s}{r_s'}\right)\bar{\gamma}_s}{1-\left(\frac{r_s}{r_s'}\right)\bar{\gamma}_s}\right]\right\}$$
$$+ \frac{2(1-\mu_1^2)(\mu_2^2-\mu_1^2)V_0\alpha_s r_s'}{\pi\mu_2(1+\mu_1^2)(\mu_1^2+\mu_2^2)}\left\{1+\frac{1}{2}\left[\left(\frac{r_s'}{r_s}\right)\bar{\gamma}_s - \frac{1}{\left(\frac{r_s'}{r_s}\right)\bar{\gamma}_s}\right]\ln\left[\frac{1-\left(\frac{r_s'}{r_s}\right)\bar{\gamma}_s}{1-\left(\frac{r_s'}{r_s}\right)\bar{\gamma}_s}\right]\right\}$$
$$- \frac{4\mu_2 V_0\alpha_s r_s}{\pi(\mu_1^2+\mu_2^2)}\left\{1+\frac{1}{2}\left[\bar{\gamma}_s - \frac{1}{\bar{\gamma}_s}\right]\ln\left[\frac{1+\bar{\gamma}_s}{1-\bar{\gamma}_s}\right]\right\} \tag{12}$$

for $\quad 0 \leqq \bar{\gamma}_s \leqq \dfrac{r_s'}{r_s}$

The derivation of these expressions is presented in full detail in Reference 11.

The lift coefficient of the wing spanning a slipstream with two velocity zones based on a free stream dynamic pressure becomes

$$C_L = \frac{4}{\mu_1 V_0 c}\int_{\frac{r_s'}{r_s}}^{1}\Phi_{s_1}d\bar{\gamma}_s + \frac{4}{\mu_2 V_0 c}\int_{0}^{\frac{r_s'}{r_s}}\Phi_{s_2}d\bar{\gamma}_s \tag{13}$$

A numerical investigation was made to compare the total lift coefficient produced by slipstreams of the same thrust but with different velocity profiles as follows:

(a) Velocity in the outer ring is lower than that in the central region

(b) Velocity in the outer ring is higher than that in the central region

11

(c) Uniform velocity

It was found that the total lift coefficient in case (a) is
the highest. The result of this simplified analysis is quali-
tatively substantiated by the test data of Reference 12.
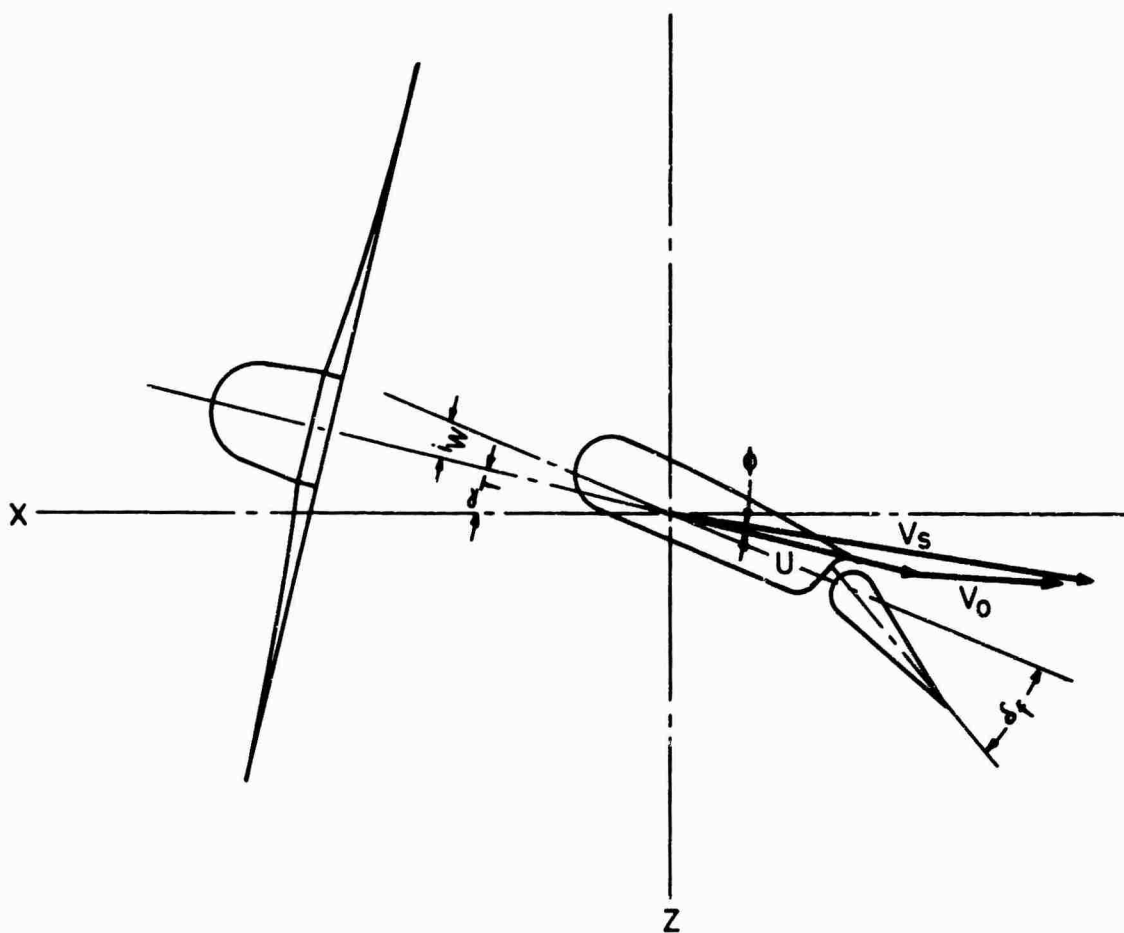
FIGURE I: DEFLECTION OF PROPELLER SLIPSTREAM DUE TO FLIGHT
SPEED

13
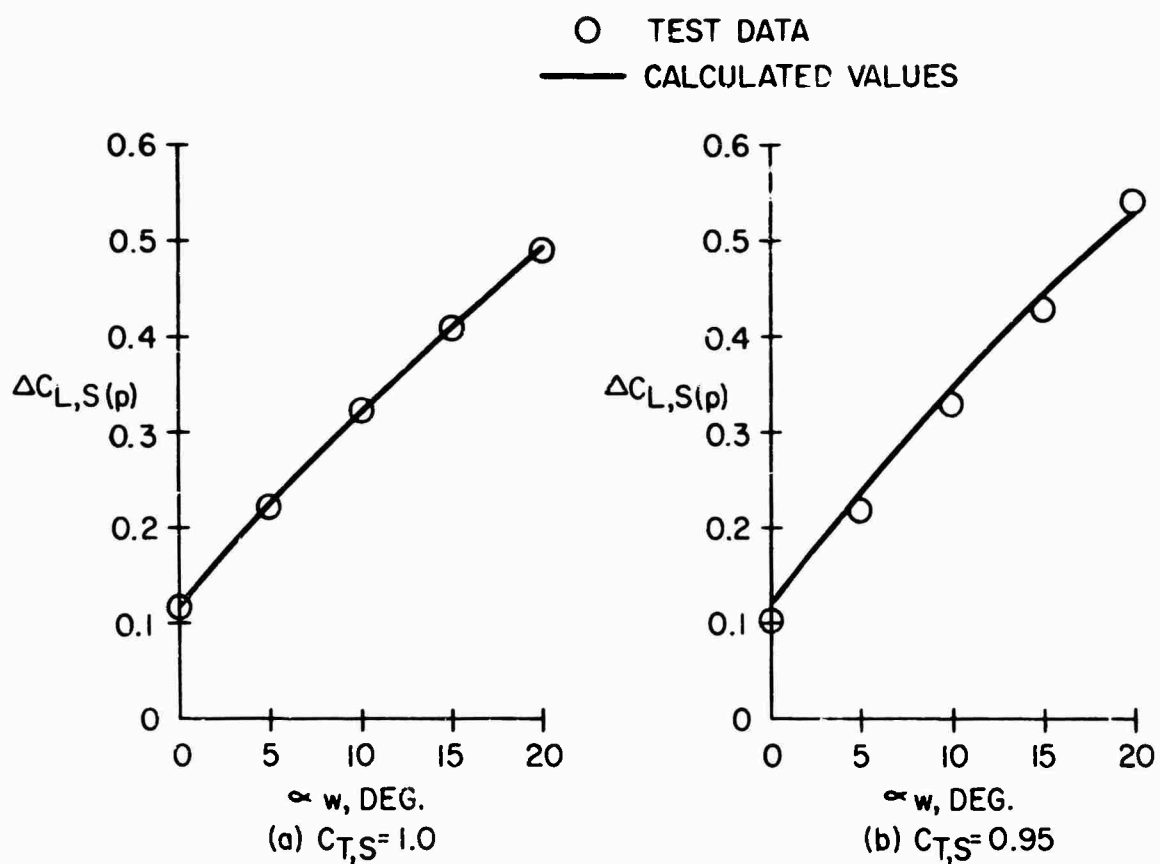
FIGURE 2: CORRELATION OF PREDICTED INCREASE OF LIFT COEFFICIENT DUE TO PROPELLER THRUST AND SLIPSTREAM WITH TEST DATA $(\delta_f = 0°)$
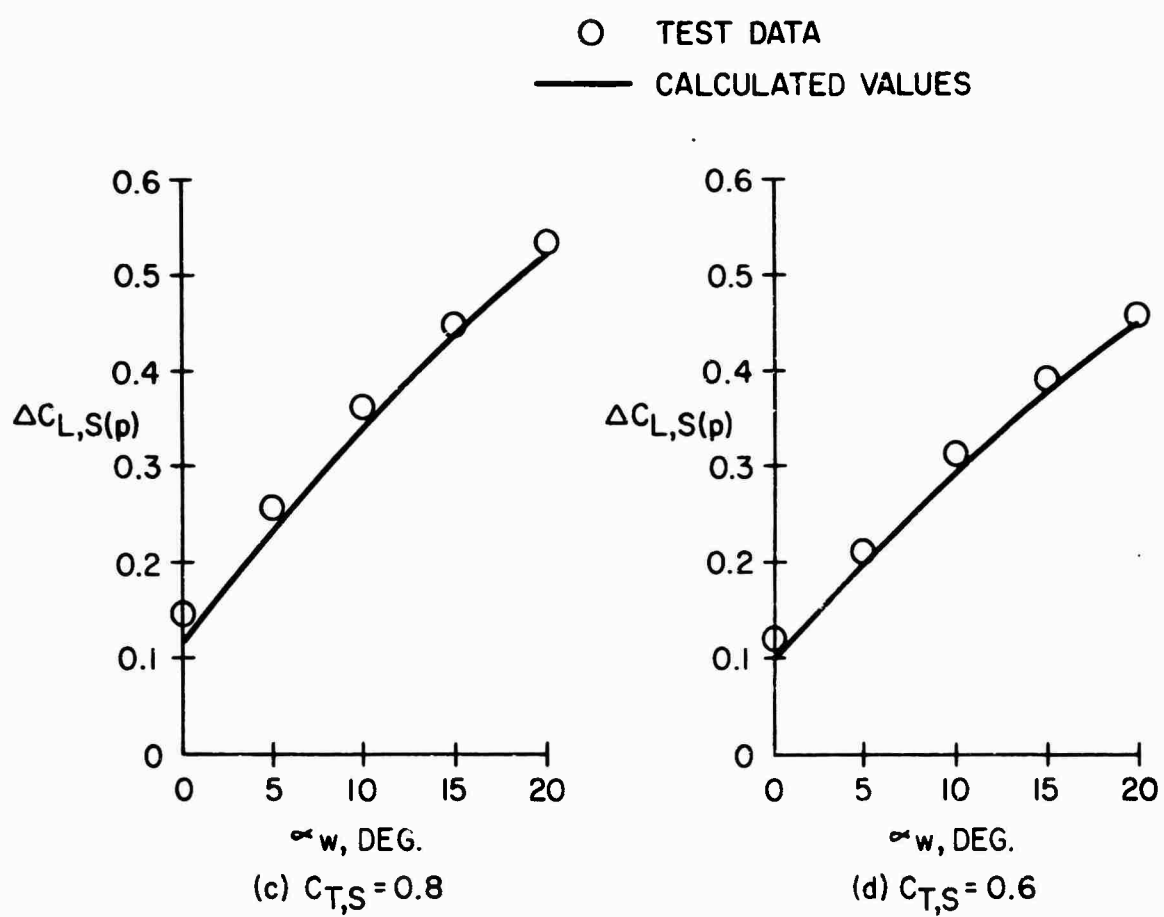
FIGURE 2: CONTINUED
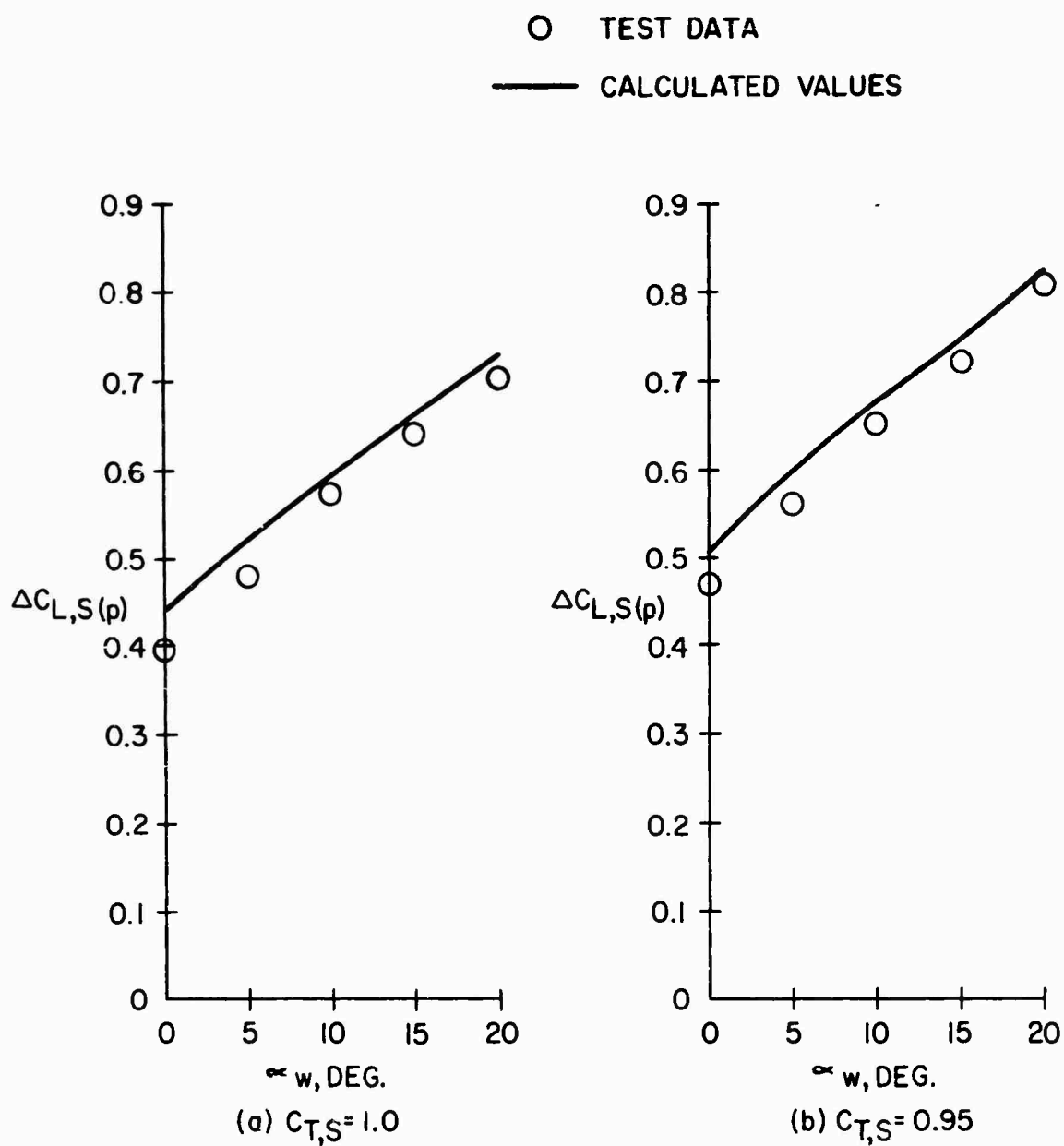
FIGURE 3: CORRELATION OF PREDICTED INCREASE OF LIFT COEFFICIENT
DUE TO PROPELLER THRUST AND SLIPSTREAM WITH TEST
DATA ($\delta_f = 40°$)

16
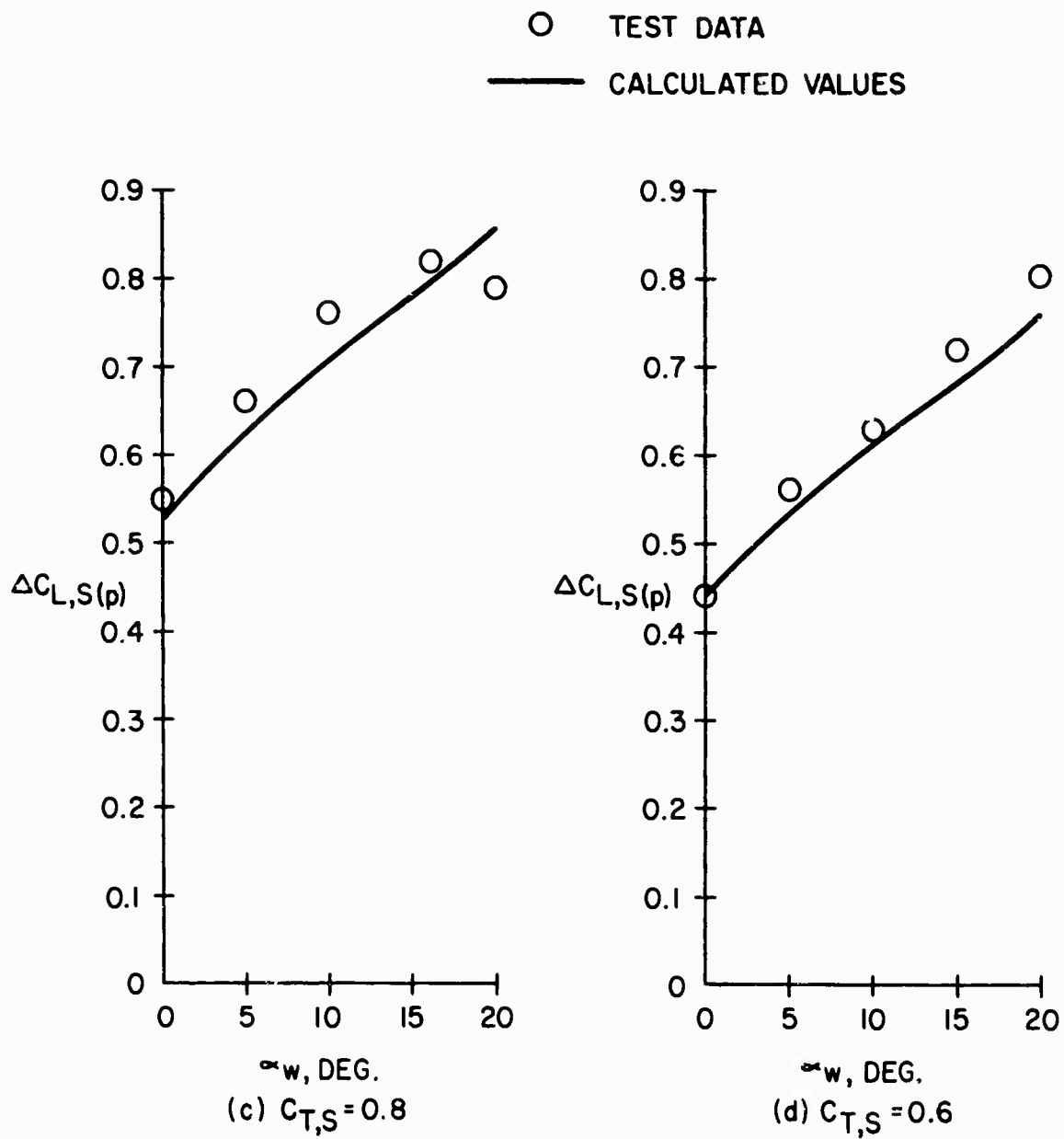
FIGURE 3: CONTINUED
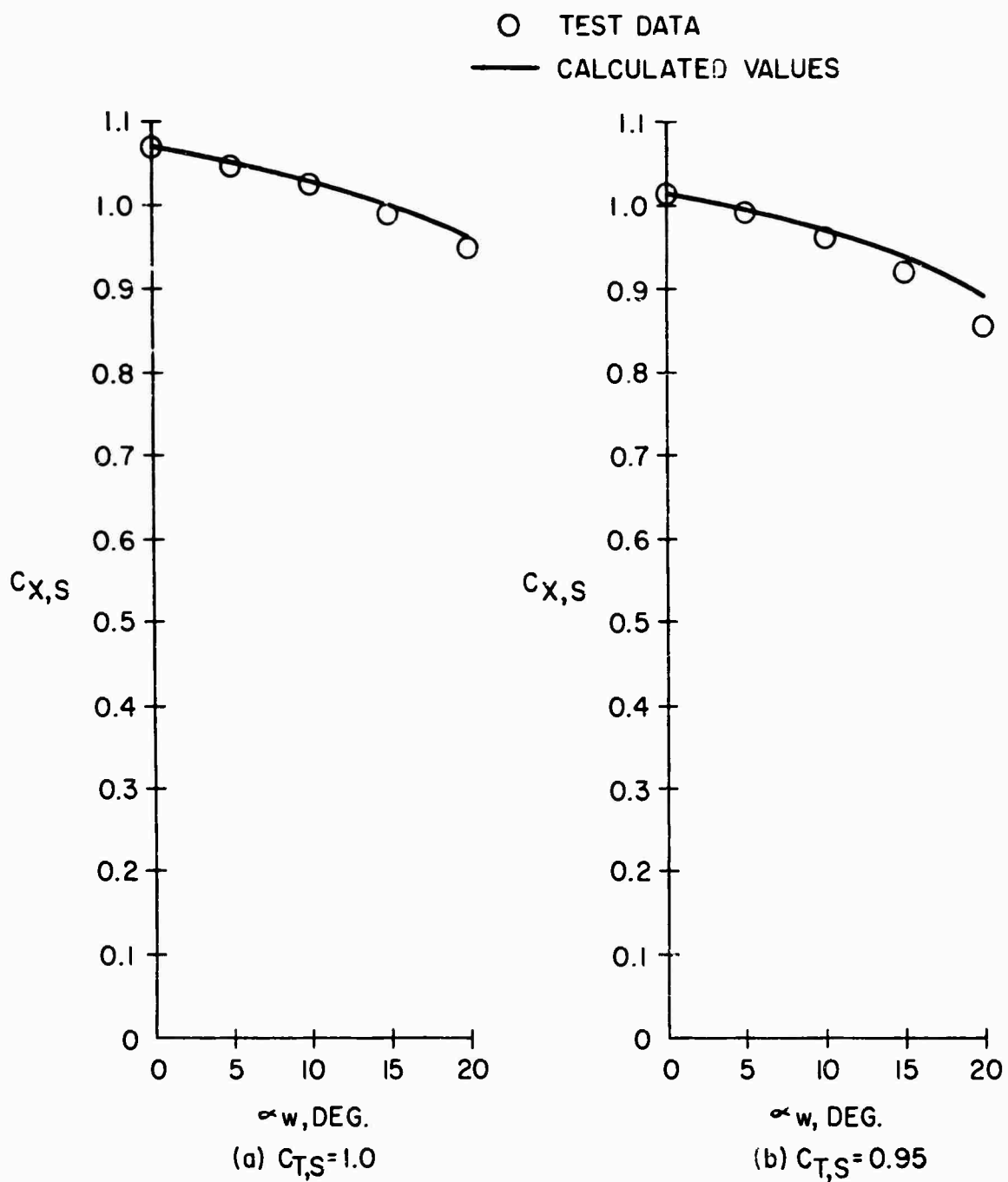
FIGURE 4: CORRELATION OF PREDICTED LONGITUDINAL FORCE
COEFFICIENT WITH TEST DATA ($\delta_f = 0°$)
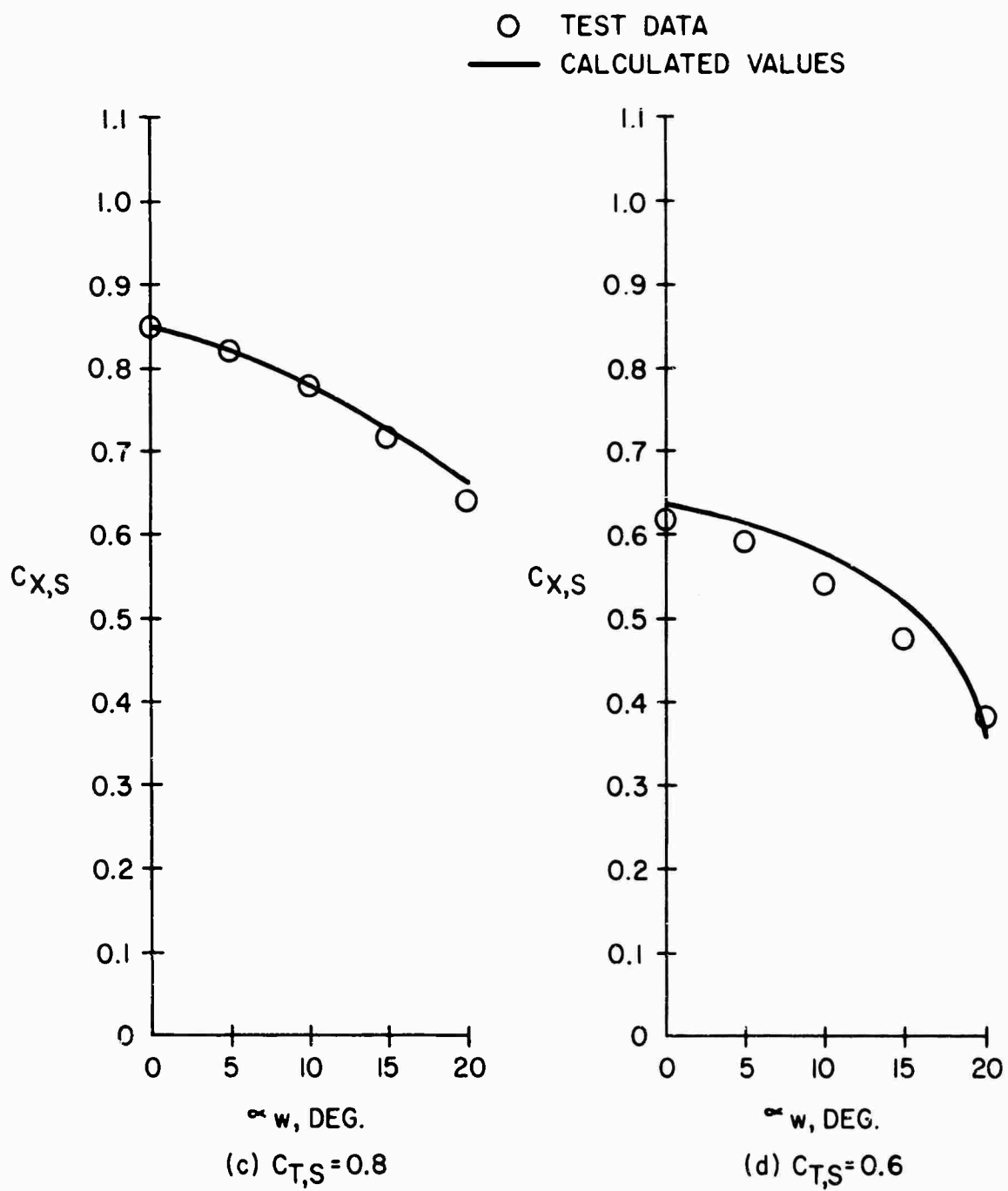
FIGURE 4: CONTINUED

19
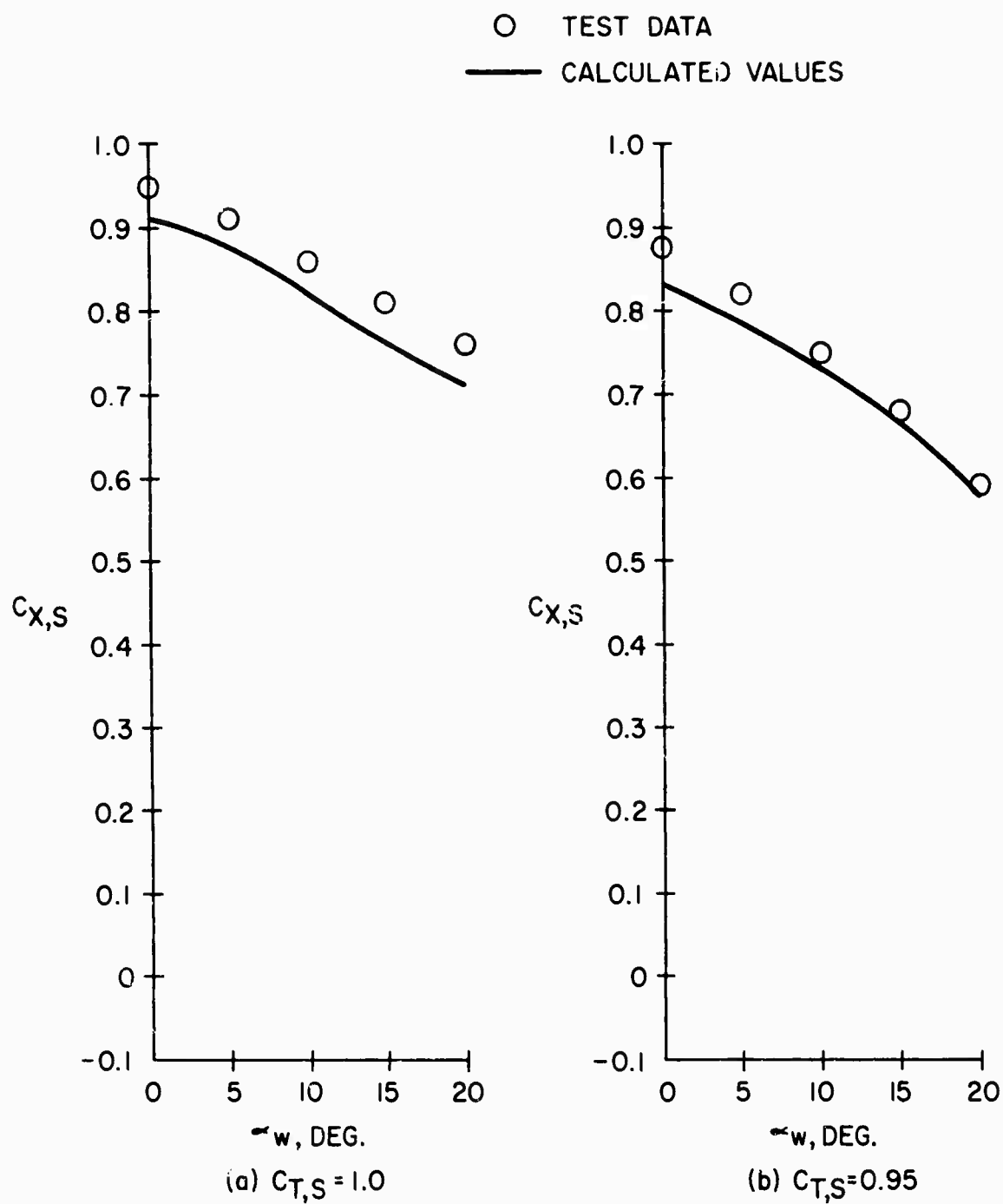
FIGURE 5: CORRELATION OF PREDICTED LONGITUDINAL FORCE
COEFFICIENT WITH TEST DATA OF ($\delta_f = 40°$)
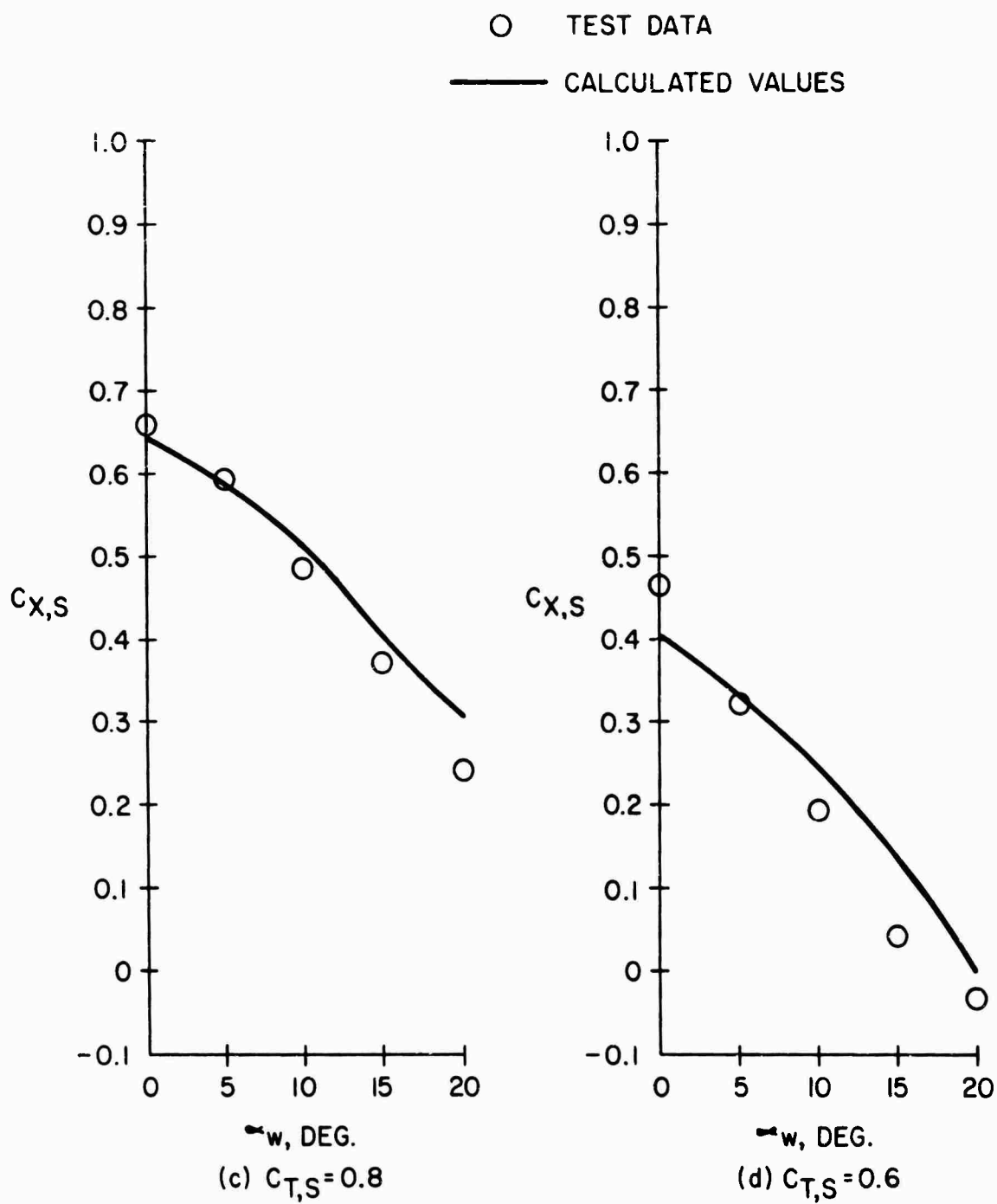
FIGURE 5: CONTINUED
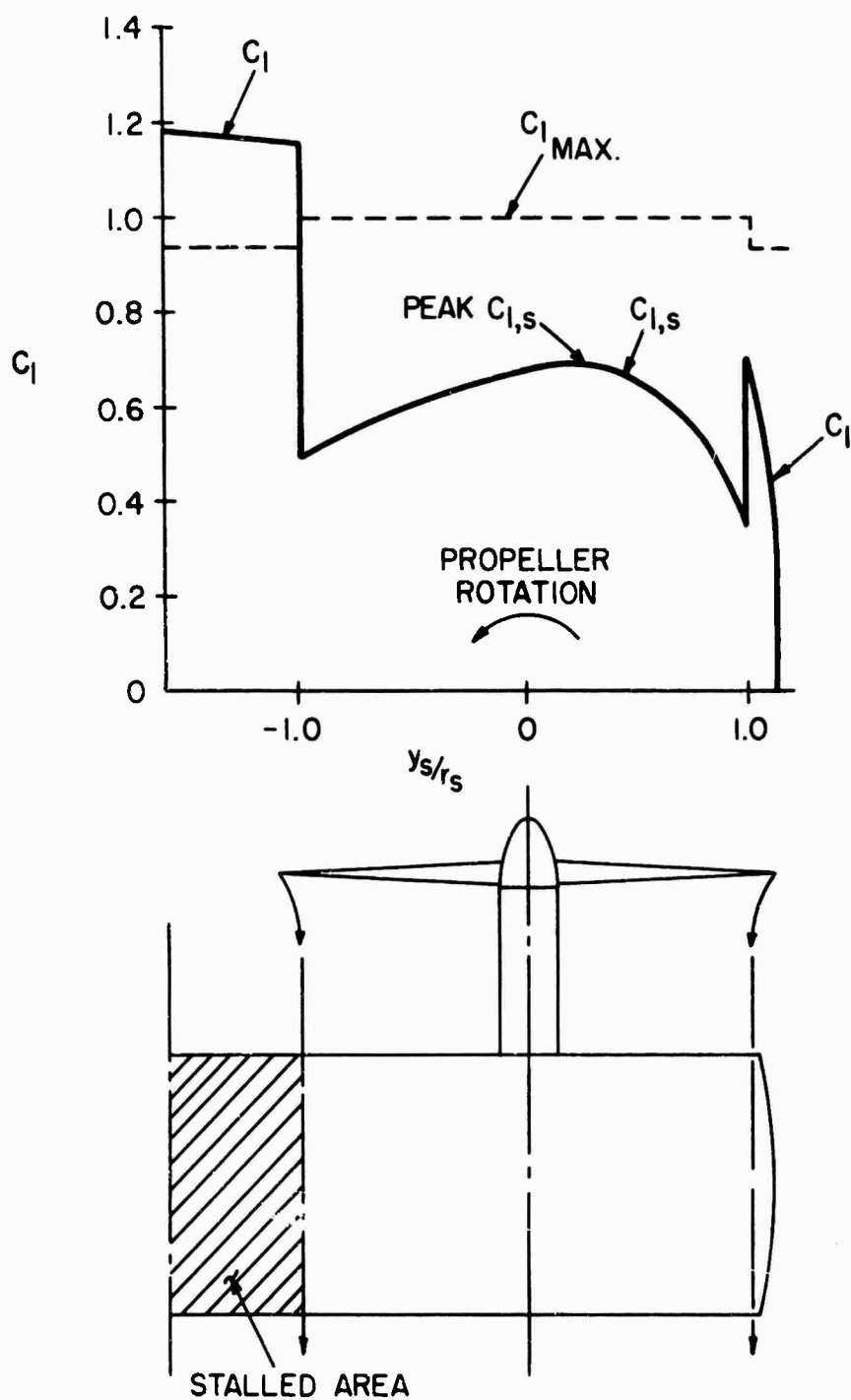
FIGURE 6: PREDICTED SPANWISE LIFT COEFFICIENT DISTRIBUTION AND EXTENT OF WING STALL (PROPELLER ROTATING UP AT WING TIP, α_w = 15 DEGREES, $C_{T,S}$= 0.58, R= 5.00, NACA 0015 AIRFOIL SECTION).

22
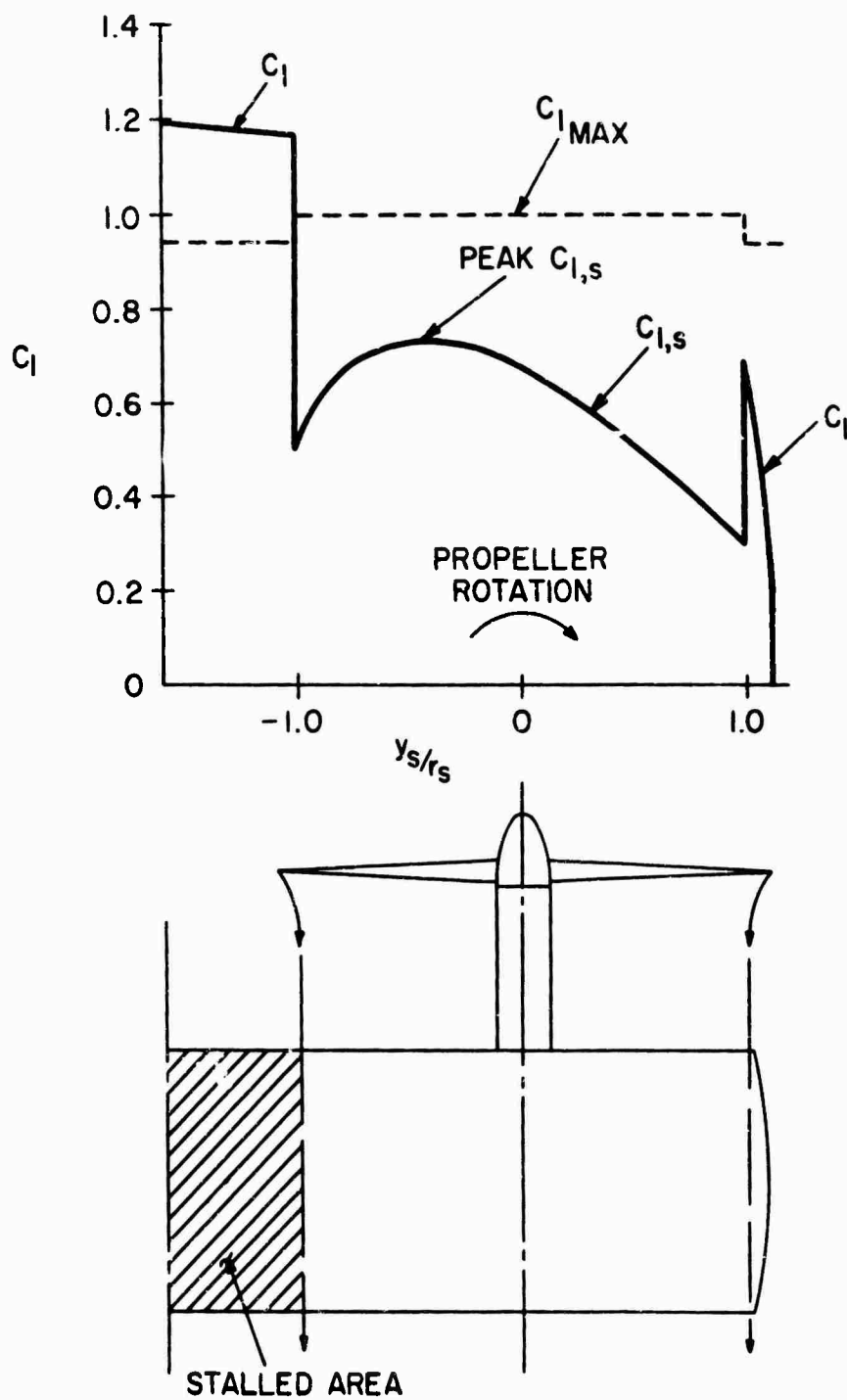
FIGURE 7: PREDICTED SPANWISE LIFT COEFFICIENT DISTRIBUTION AND EXTENT OF WING STALL (PROPELLER ROTATING DOWN AT WING TIP, α_w = 15 DEGREES, $C_{T,S}$= 0.58, R= 5.00, NACA 0015 AIRFOIL SECTION).

23
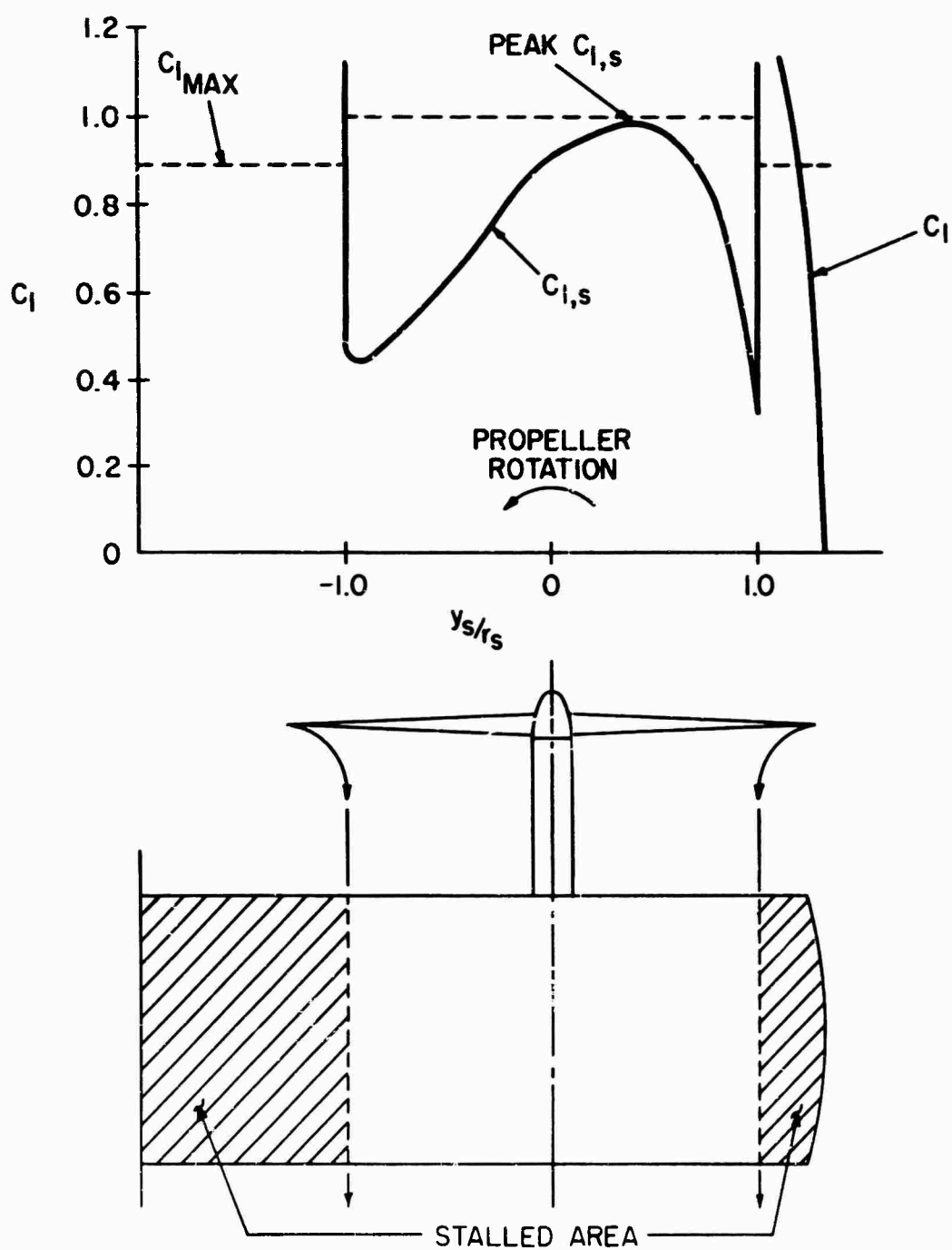
FIGURE 8: PREDICTED SPANWISE LIFT COEFFICIENT DISTRIBUTION AND
EXTENT OF WING STALL (PROPELLER ROTATING UP AT WING
TIP, α_w = 50 DEGREES, $C_{T,S}$ = 0.88, R = 5.0, NACA 0015
AIRFOIL SECTION).
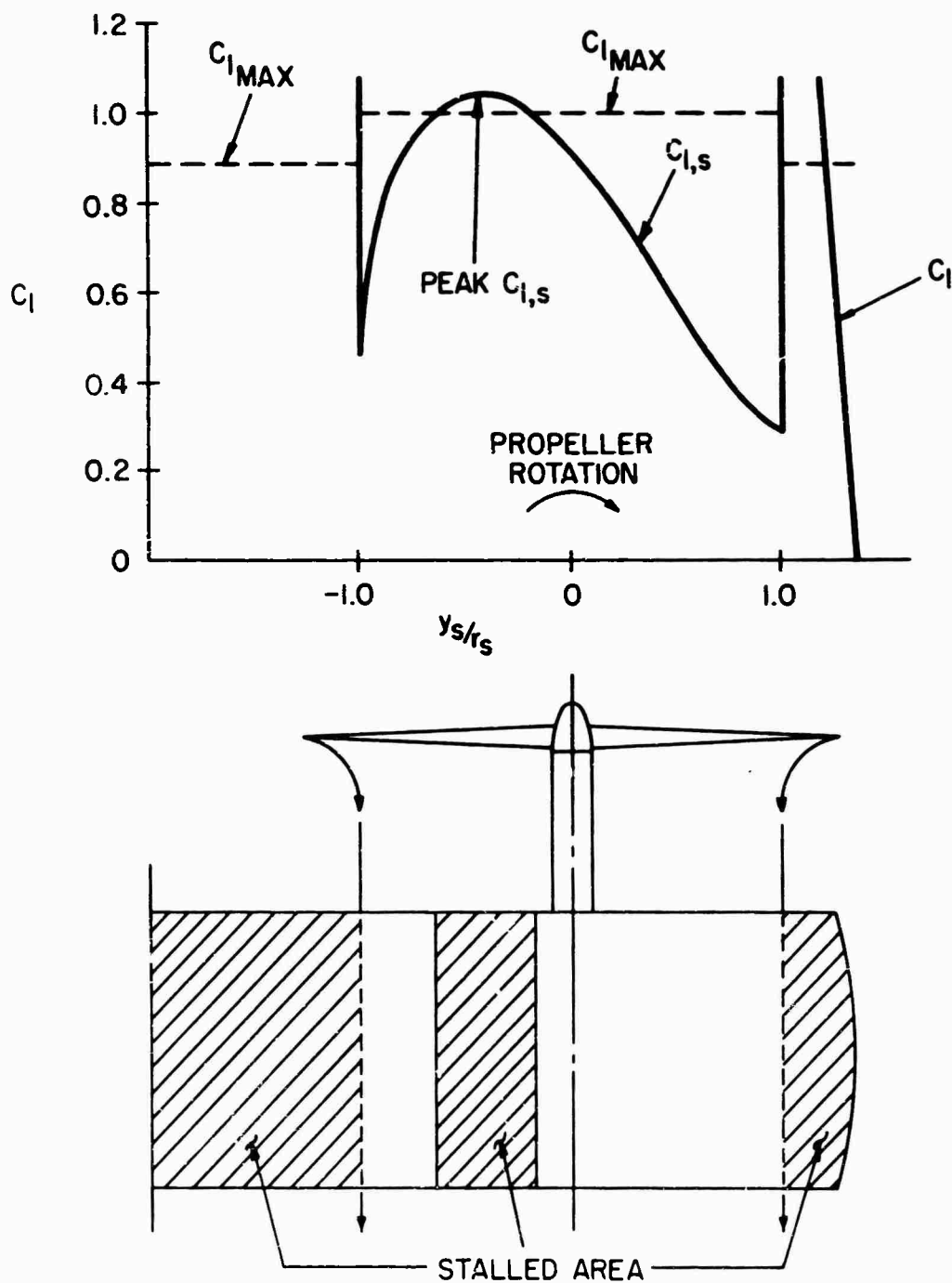
FIGURE 9: PREDICTED SPANWISE LIFT COEFFICIENT DISTRIBUTION AND
EXTENT OF WING STALL (PROPELLER ROTATING DOWN AT
WING TIP, α_w = 50 DEGREES, C_{T_S}= 0.88, R= 5.0, NACA 0015
AIRFOIL SECTION).

25
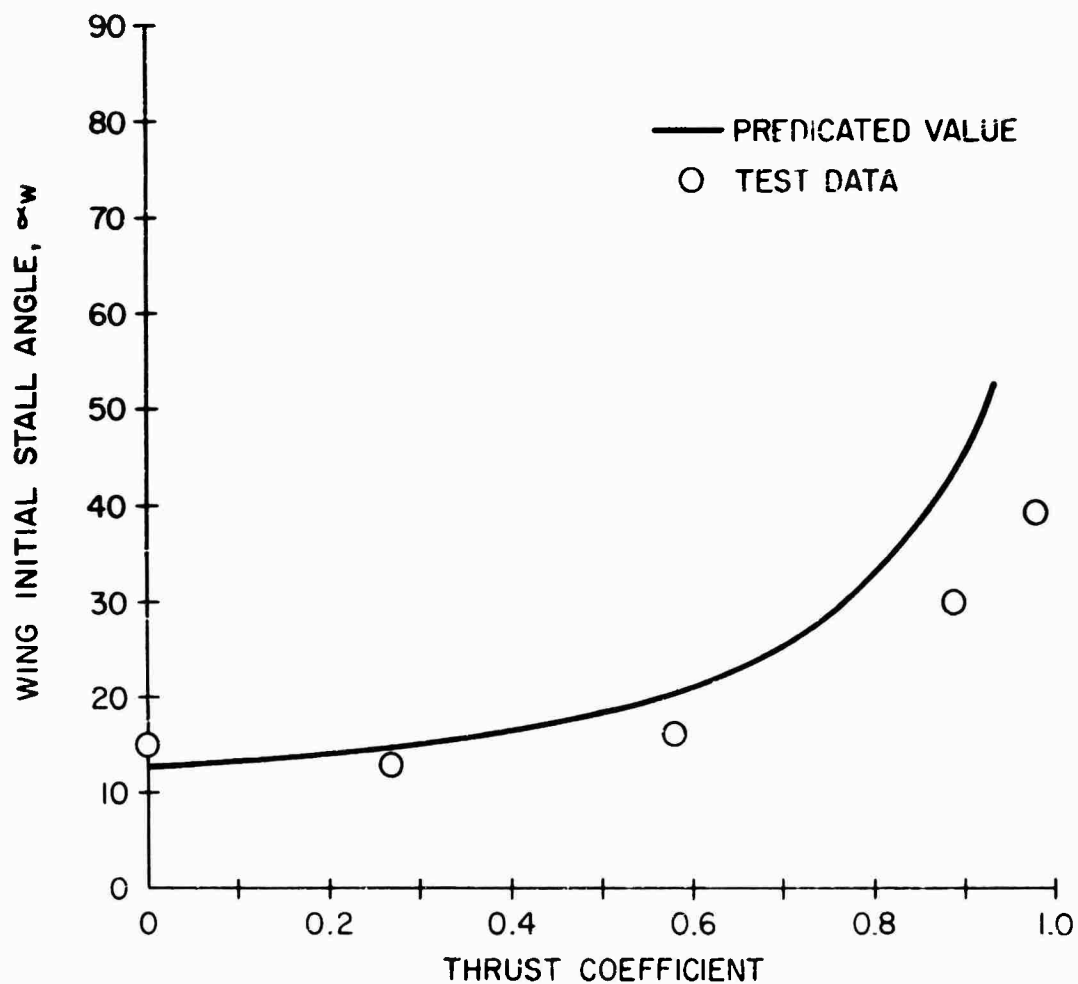
FIGURE IO: CORRELATION OF PREDICTED WING INITIAL STALL WITHIN
SLIPSTREAM WITH TEST DATA (PROPELLER ROTATING
DOWN AT WING TIP, R=5.0, NACA OOI5 AIRFOIL SECTION).
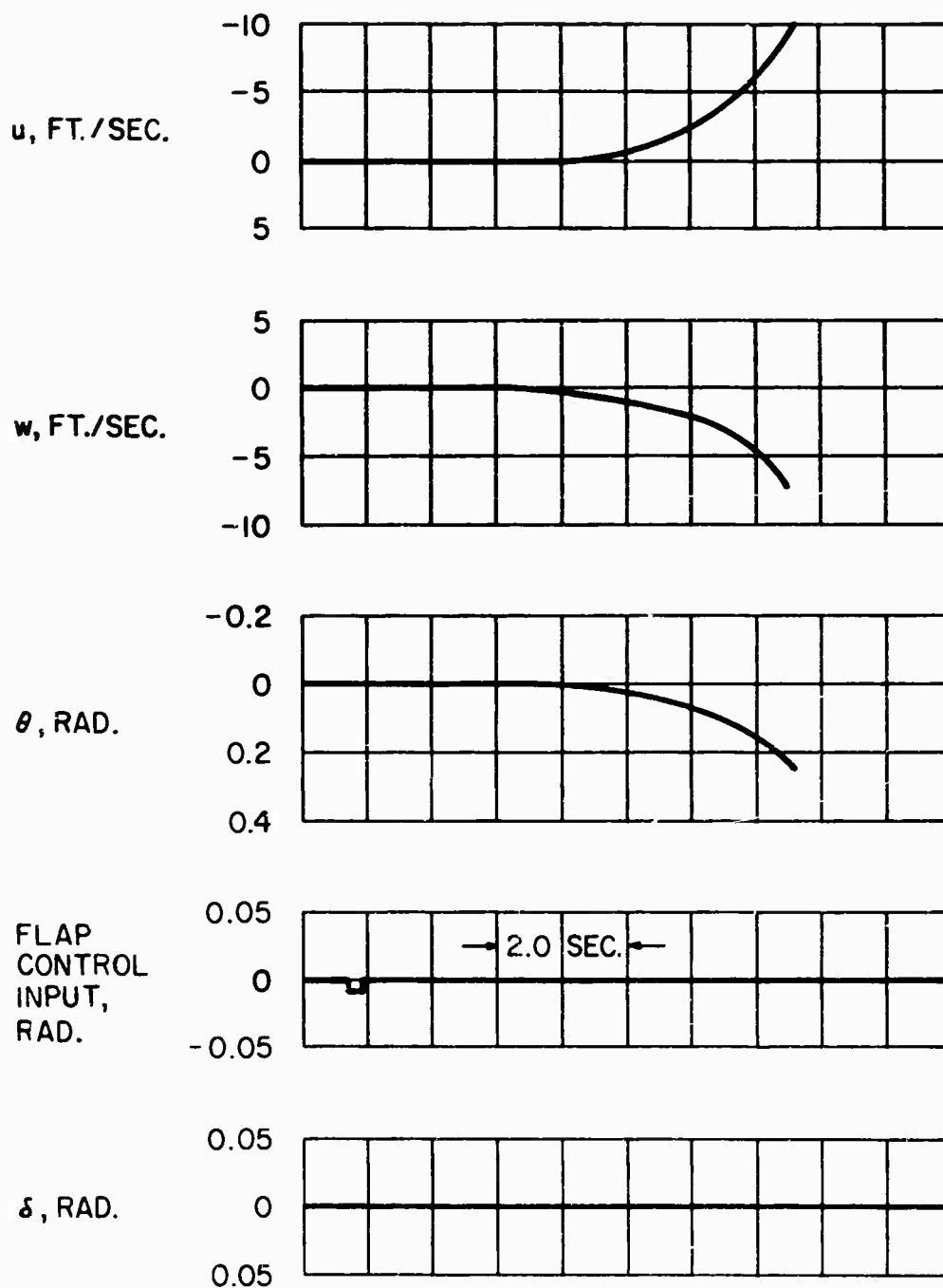
FIGURE II: TRANSIENT RESPONSE OF UNSTABILIZED AIRCRAFT TO A FLAP CONTROL INPUT (V_0 = 30 KNOTS).

27

STABILIZER: $\delta - 15\theta - 0.32w = 0$
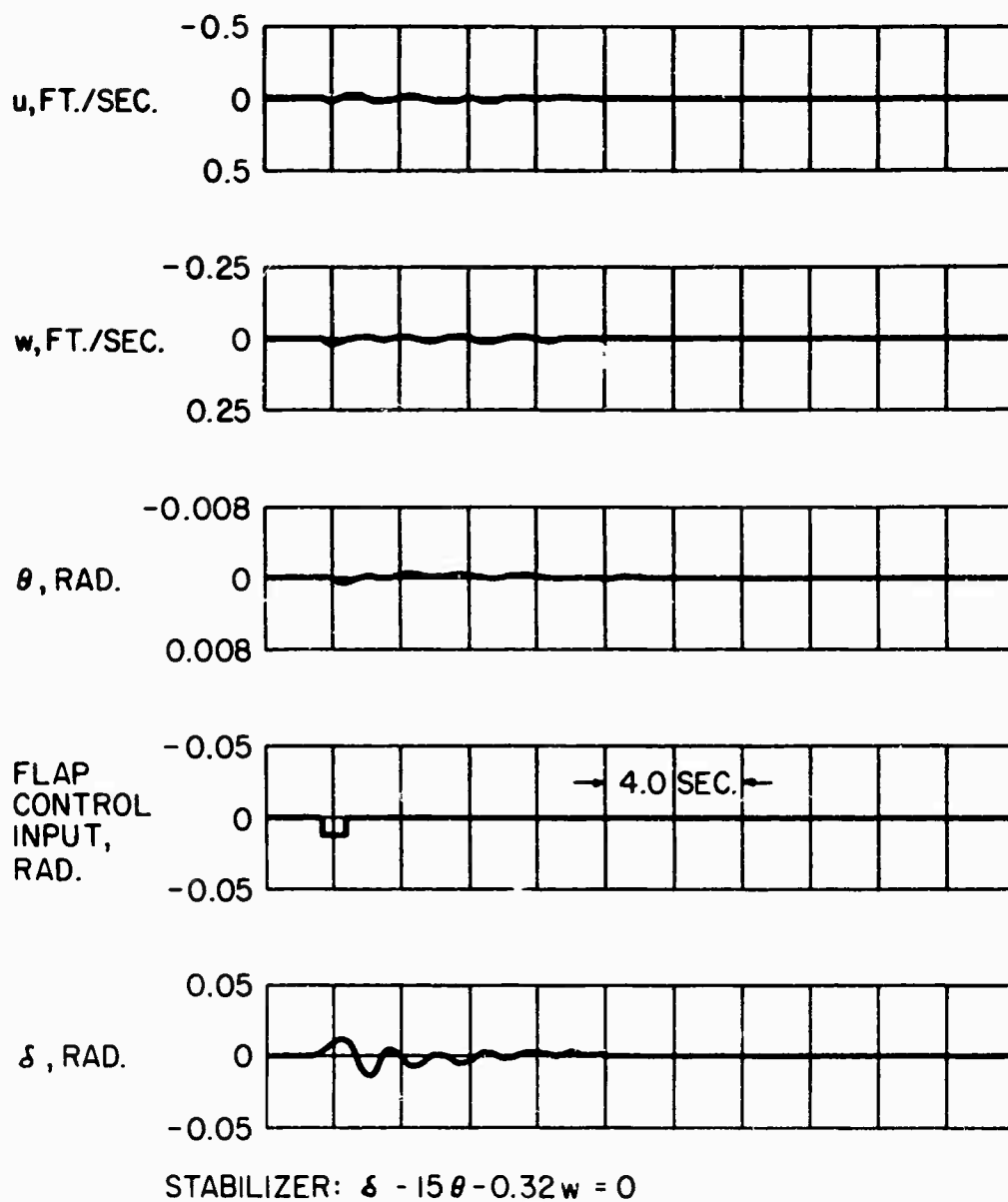
FIGURE 12: TRANSIENT RESPONSE WITH NORMAL VELOCITY AND ATTITUDE FEEDBACK STABILIZATION ($V_0 = 30$ KNOTS).

28
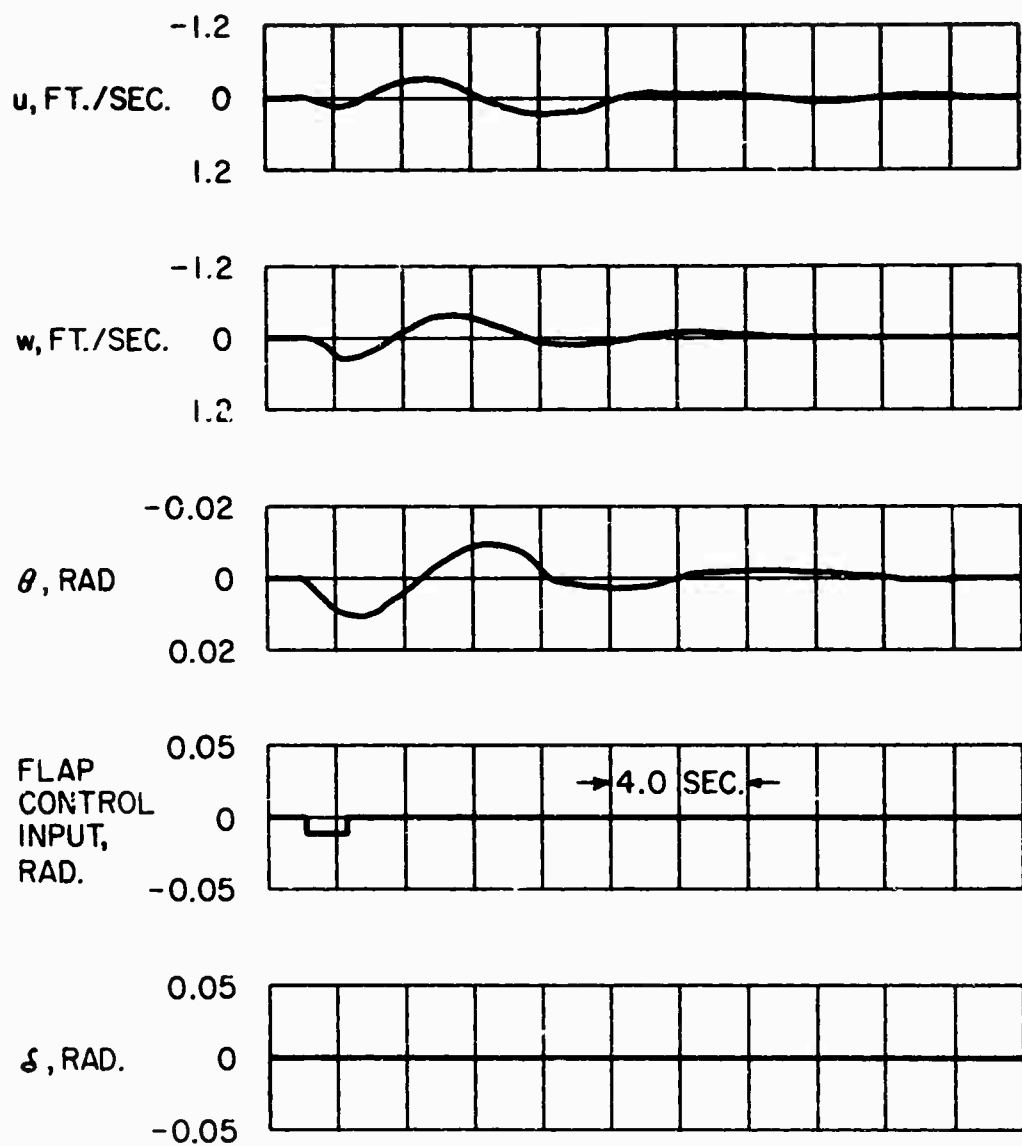
FIGURE 13: TRANSIENT RESPONSE OF THE UNSTABILIZED AIRCRAFT TO A FLAP CONTROL INPUT (V_o = 70 KNOTS).
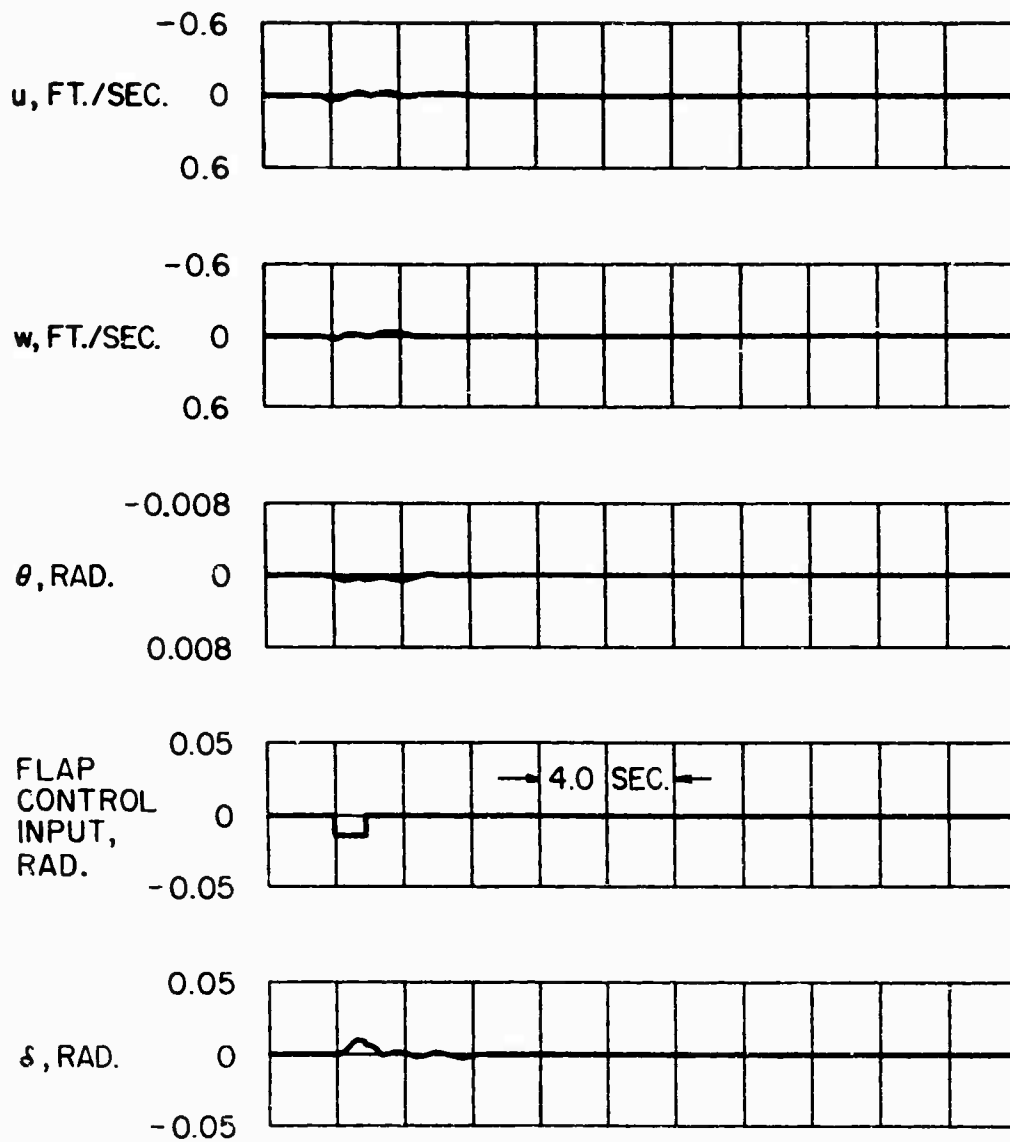
STABILIZER: $\delta - 15\theta - 0.169w = 0$

FIGURE 14: TRANSIENT RESPONSE WITH NORMAL VELOCITY AND ATTITUDE FEEDBACK STABILIZATION (V_0 = 70 KNOTS).
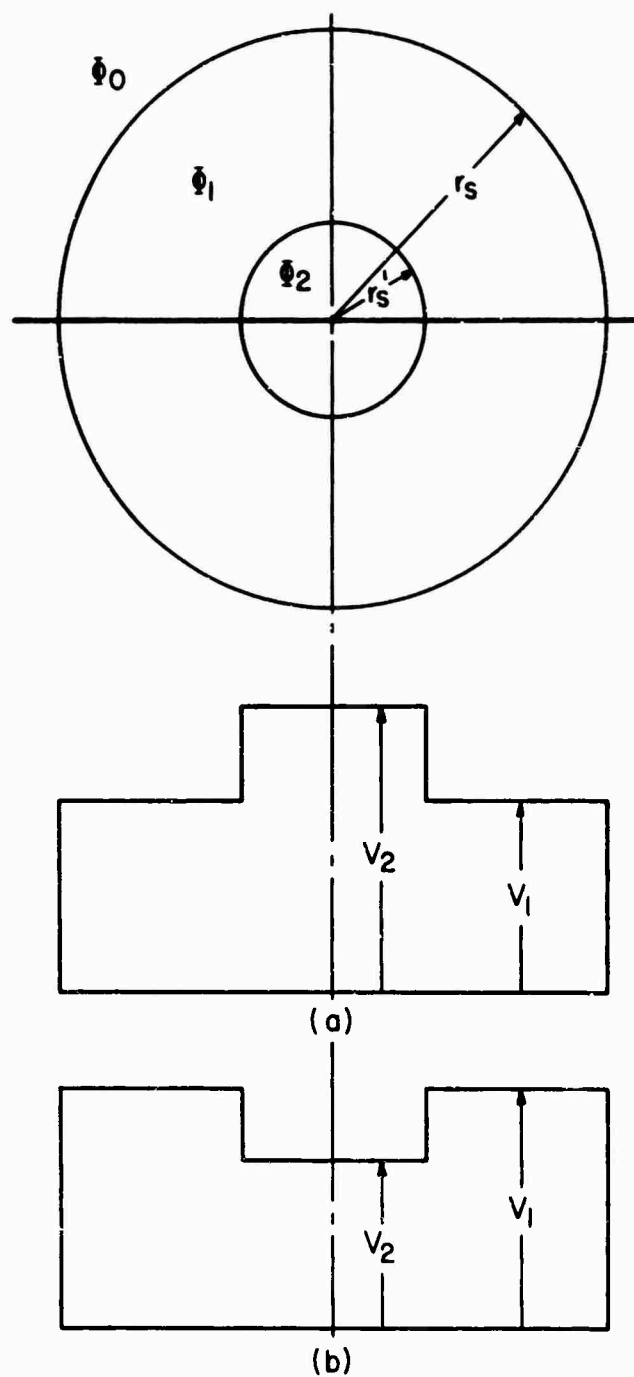
FIGURE 15: VELOCITY ZONES AND PERTURBATION POTENTIALS IN
SLIPSTREAM

31

LIST OF SYMBOLS

$\mathcal{R}$	aspect ratio
c	wing chord
C_D	total drag coefficient
C_{D_i}	induced drag coefficient of basic wing
ΔC_{D_i}	induced drag coefficient from incremental lift coefficient due to slipstream
$C_{D_{os}}$	profile drag coefficient of wing areas immersed in slipstreams
$C_{D_{ow}}$	profile drag coefficient of wing areas not immersed in slipstreams
C_l	local lift coefficient
C_{lmax}	maximum section airfoil lift coefficient
$C_{l,s}$	local lift coefficient based on slipstream dynamic pressure
C_L	total lift coefficient
ΔC_L	incremental lift coefficient due to slipstream
$\Delta C_{L,s(p)}$	incremental lift coefficient due to propeller thrust and slipstream, based on slipstream dynamic pressure
C_{L_w}	basic wing lift coefficient
$C_{T,s}$	propeller thrust coefficient based on slipstream dynamic pressure
$C_{X,s}$	longitudinal force coefficient based on slipstream dynamic pressure
D	propeller diameter

32

i_w	angle of incidence between propeller thrust axis and wing chord line
k_1	stabilizer attitude gain
k_3	stabilizer normal velocity gain
N	number of propellers
r_s	slipstream radius
r_s'	radius of inner velocity zone of slipstream
S	wing total area
S_s	portion of wing area immersed in slipstreams
u	longitudinal perturbation velocity
U	propeller induced velocity
V_o	free stream velocity
V_1	slipstream velocity in outer ring
V_2	slipstream velocity in central region
V_s	slipstream velocity (uniform)
w	normal perturbation velocity
X,Y,Z	wind axes in cartesian coordinates
y_s	spanwise distance from slipstream center
$\bar{y}_s$	nondimensionalized spanwise distance from slipstream center, y_s/r_s
α_{Lo}	angle of zero lift of basic airfoil section
α_s	effective angle of attack in slipstream
α_T	propeller thrust axis angle of attack
α_w	wing geometric angle of attack
δ	flap stabilizer deflection
δ_f	flap deflection
θ	fuselage attitude
λ	empirical factor for flap deflection

33

μ ratio of free stream velocity to slipstream velocity

μ_1 ratio of free stream velocity to slipstream velocity in outer ring

μ_2 ratio of free stream velocity to slipstream velocity in central region

ϕ deflection angle of propeller slipstream due to forward speed

Φ_o free stream perturbation velocity potential

Φ_1 slipstream perturbation velocity potential in outer ring

Φ_2 slipstream perturbatio: velocity potential in central region

Φ_{s_1} slipstream perturbation velocity potential at wing trailing edge in outer ring

Φ_{s_2} slipstream perturbation velocity potential at wing trailing edge in central region

REFERENCES

1. Koning, C., "Influence of the Propeller on Other Parts of the Airplane Structure", Aerodynamic Theory (W.F. Durand, Editor-in-Chief), Volume IV, Julius Springer, 1935.

2. Dynasciences Corporation, Effects of Propeller Slipstream on V/STOL Aircraft Performance and Stability, TRECOM Technical Report 64-47, U. S. Army Transportation Research Command, Fort Eustis, Virginia, August 1964.

3. Diederich, F.W., A Plan-Form Parameter for Correlating Certain Aerodynamic Characteristics of Swept Wings, TN 2335, NACA, April 1951.

4. Kuhn, R.E., and Draper, J.W., An Investigation of a Wing Propeller Configuration Employing Large Chord Plain Flaps and Large Diameter Propellers for Low-Speed Flight and Vertical Take-Off, TN 3307, NACA, December 1954.

5. Taylor, R.T., Wind-Tunnel Investigation of Effect of Ratio of Wing Chord to Propeller Diameter with Addition of Slats on the Aerodynamic Characteristics of Tilt-Wing VTOL Configurations in the Transition Speed Range, TN D-17, NASA, September 1959.

6. Kuhn, R.E., and Hayes, W.C., Jr., Wind-Tunnel Investigation of Longitudinal Aerodynamic Characteristics of Three Propeller-Driven VTOL Configurations in the Transition Speed Range, Including Effects of Ground Proximity, TN D-55, NASA, February 1960.

7.   Fink, M.P., Mitchell, R.G., and White, L.C., Aero-
      dynamic Da_a or !*:.:- Semispan Tilting Wing With
      0.6-Diameter Chord, Single-Slotted Flap, and Single
      Propeller Rotating Down at Tip, TN D-2412, NASA,
      August 1964.

8.   Anderson, R.F., Determination of the Characteristics
      of Tapered Wings, TR 572, NACA, 1936.

9.   Jacobs, E.N., and Sherman, A., Airfoil Section Charac-
      teristics as Effected by Variations in Reynolds Number,
      TR 586, NACA, 1939.

10.   Brenckmann, M., Experimental Investigation of the
      Aerodynamics of a Wing in a Slipstream, UTIA Technical
      Note 11, University of Toronto, Toronto, Canada, April
      1957.

11.   Butler, L., Huang, K.P., and Goland, L., An Investiga-
      tion of Propeller Slipstream Effects on V/STOL Aircraft
      Performance and Stability, USAAVLABS Technical Report
      65-81, U. S. Army Aviation Materiel Laboratories, Fort
      Eustis, Virginia, February 1966.

12.   Kuhn, R.E., and Draper, J.W., Investigation of effec-
      tiveness of Large Chord Slotted Flaps in Deflecting
      Propeller Slipstreams Downward for Vertical Take-Off
      and Low Speed Flight, TN 3364, Janauary 1955.

AERODYNAMIC PROPERTIES OF AIRFOILS
IN NONUNIFORMLY SHEARED FLOWS*

by

W. G. Brady and G. R. Ludwig

Cornell Aeronautical Laboratory, Inc.
Buffalo, New York, U.S.A.

SUMMARY

A theoretical method, which requires the use of a digital computer, was developed to predict pressure distributions on airfoils in two-dimensional nonuniformly sheared flows. The theory is applicable to airfoils of arbitrary profile, including those with flaps and other auxiliary lift devices. To verify this theory, aerodynamic characteristics of an airfoil were investigated both theoretically and experimentally in a simple nonuniformly sheared flow consisting of two segments with shears of equal magnitude but of opposite sign. Agreement between computed and experimental pressure distributions was at least as good as the agreement obtained between exact potential flow theory and experimental data for an unsheared flow.

Previous investigations have demonstrated experimentally that the lift characteristics of an airfoil in a two-dimensional nonuniformly sheared jet, similar to a section through a propeller slipstream, and in an axially symmetric nonuniformly sheared jet similar to a propeller slipstream are strongly dependent on the airfoil's location in the flow. On the basis of the present theoretical and experimental results, a mechanism is postulated by which the large changes in lift characteristics can occur. This mechanism suggests that the presence of nonuniform shear in a propeller slipstream must be considered if accurate pressure distributions and, hence, lift and

---

stalling characteristics of an airfoil immersed in a propeller slipstream with significant shear are to be obtained.

NOTATION

c Airfoil chord, feet.

c_l Uniform flow section lift coefficient; $\dfrac{\text{Lift per Unit Span}}{\frac{1}{2}\rho(U_o)^2 c}$.

$(c_l)_R$ Sheared flow section lift coefficient, referred to free-stream velocity at airfoil midchord position; $\dfrac{\text{Lift per Unit Span}}{\frac{1}{2}\rho(U_R)^2 c}$.

$(c_l)_s$ Sheared flow section lift coefficient, referred to free-stream velocity along airfoil stagnation streamline; $\dfrac{\text{Lift per Unit Span}}{\frac{1}{2}\rho(U_s)^2 c}$.

$\bar{c}_l$ Sheared flow section lift coefficient, referred to average free-stream velocity in wind tunnel section; $\dfrac{\text{Lift per Unit Span}}{\frac{1}{2}\rho(\bar{U})^2 c}$.

C_p Uniform flow pressure coefficient; $\dfrac{p-p_o}{\frac{1}{2}\rho(\bar{U}_o)^2}$.

$(C_p)_R$ Sheared flow pressure coefficient, referred to free-stream velocity at airfoil midchord position; $\dfrac{p-p_o}{\frac{1}{2}\rho(U_R)^2}$.

$(C_p)_s$ Sheared flow pressure coefficient, referred to free-stream velocity along airfoil stagnation streamline; $\dfrac{p-p_o}{\frac{1}{2}\rho(U_s)_R^2}$.

$f(\psi)$ Function defined by Equations (1).

$g(x)$ Displacement of dividing streamline (see Figure 2).

h Vertical height of airfoil midchord above tunnel centerline, feet.

$\overline{K}$ Smoothing parameter used in computer program.

L Vertical distance from tunnel centerline to wall (see Figure 2).

$p(x,y)$ Static pressure at (x, y), pounds per square foot.

p_o Static pressure in free stream, pounds per square foot.

U_o Uniform flow free-stream velocity, feet per second.

$U(y)$ Sheared flow free-stream velocity, feet per second.

2

U_R Sheared flow free-stream velocity at $y = h$, feet per second.

U_S Sheared flow free-stream velocity of stagnation streamline, feet per second.

U_1 Free-stream velocity at lower wind-tunnel wall, feet per second.

U_2 Free-stream velocity at upper wind-tunnel wall, feet per second.

U_3 Free-stream velocity along vertical centerline in wind tunnel, feet per second.

$\overline{U}$ Average free-stream velocity in wind-tunnel test section, feet per second.

u Velocity component in x-direction, feet per second.

v Velocity component in y-direction, feet per second.

x Coordinate along axis parallel to wind-tunnel walls, positive downstream; $x = 0$ at airfoil midchord.

y Coordinate perpendicular to x-axis, positive up; $y = 0$ at wind-tunnel centerline.

α Airfoil angle of attack, positive leading edge up, degrees.

$\alpha_{l=0}$ Airfoil angle of attack for zero lift.

$\overline{\alpha}$ Airfoil angle of attack measured from zero lift angle of attack; $\overline{\alpha} = \alpha - \alpha_{l=0}$.

γ_{A1} Vortex sheet singularity strength of airfoil aft lower surface.

γ_{A2} Vortex sheet singularity strength of airfoil aft upper surface.

γ_{AL} Vortex sheet singularity strength of airfoil leading edge surface.

γ_1 Vortex sheet singularity strength of lower wind-tunnel wall.

γ_2 Vortex sheet singularity strength of upper wind-tunnel wall.

ρ Air density, assumed constant, slugs per cubic foot.

ψ Stream function; see Equation (1).

3

INTRODUCTION

Many of the analytical problems of wing aerodynamics in flows at low subsonic speeds are treated successfully within the framework of potential flow theory. However, potential flow theory is inadequate for predicting analytically the interaction between a wing and a propeller slipstream when the slipstream intersects the wing and the flow in the propeller slipstream is not irrotational, i.e., when the slipstream flow has significant shear. An additional difficulty which gives rise to nonlinearities in the analytical treatment results from the interaction of the free boundaries of the slipstream flow and the wing.

A number of analytical treatments of the aerodynamics of sheared flows have been published; typical are References 1 through 4. Exact aerodynamic theories for uniform two-dimensional shear (constant vorticity) are available (References 1 and 4), but the available solutions for nonuniform shear (Reference 3, for example) are not particularly useful to the aerodynamicist because of limitations of the theoretical assumptions. These are primarily restrictions to small shear and shear gradient. Three-dimensional sheared flow theory (Reference 2, for example) has hardly advanced beyond attempts to arrive at a formulation which is mathematically tractable.

This paper reports the latest results of an experimental and theoretical program which has been concerned with the aerodynamic characteristics of airfoils in sheared flows. This work and the earlier work (References 4 through 8) were conducted for the U. S. Army Aviation Materiel Laboratories (formerly U. S. Army Transportation Research Command). A point of particular interest from the earlier studies was the discovery that nonuniform shear in a two-dimensional flow could have a marked effect on airfoil stall characteristics (Reference 6). It is noted in Reference 6 that in the specific two-dimensional nonuniformity sheared flow treated, large variations in maximum lift were obtained near the flow centerline when the airfoil vertical position was varied by distances of the order of magnitude of the airfoil thickness. The current program was designed as the initial step toward investigating the reasons for this unusual behavior.

4

Since the maximum lift and stall behavior are dependent on the properties of the boundary layer on the airfoil, and these properties, in turn, are primarily influenced by the pressure distribution, it was decided that any theoretical investigation must be one which will produce accurate pressure distributions on an airfoil in a nonuniformly sheared flow. Of course, the unusual behavior near stall may have been caused by other effects such as a dir 'nteraction of the boundary layer with the inviscid sheared flow in such a ... nner as to promote or delay boundary-layer separation, or by subtle wind-tunnel wall effects associated with the sheared flow. The direct interaction possibility has been considered previously with essentially negative results (Reference 6). The effect of wind-tunnel walls could be determined by including them in the analysis, which, if successfully completed, could be used to investigate wind-tunnel wall effects by varying the wall positions.

In keeping with the above observations, a digital computer program was developed to compute pressure distributions on a two-dimensional airfoil in a particular inviscid, nonuniformly sheared flow. The sheared flow velocity profile was kept as simple as possible for this initial development, while still incorporating what was believed to be all essential features of a nonuniformly sheared flow. The free-stream velocity profile was such that shears of equal magnitude but opposite sign occurred above and below the centerline of the flow. Wind-tunnel walls were also included in the theoretical program so that the flow model would duplicate the experiment as nearly as possible. At the same time, experimental airfoil pressure distribution data were obtained in a wind tunnel for a free-stream velocity profile nearly the same as that used in the theory. These data were obtained to enable the accuracy of the theoretical program to be verified.

Once the analytical technique is established as to its accuracy on the basis of the nonuniformly sheared flow treated in the present program, its extension to the more complicated nonuniformly sheared flow of Reference 6 is justified. The analytical technique would then provide a powerful tool for the investigation of flow mechanisms responsible for the unusual lift behavior near stall shown in Reference 6.

5

THEORETICAL PROGRAM

The main characteristic of a sheared flow which distinguishes it from a nonsheared flow is the fact that it is rotational. The powerful techniques of potential theory, including conformal mapping, that can be used for two-dimensional irrotational flow problems, are generally not applicable to rotational flows.

Rather than Laplace's equation, the stream function must satisfy

$$\nabla^2 \psi = f(\psi) \tag{Eq. 1}$$

i.e., $\nabla^2 \psi$ is a constant along a streamline (along which the stream function is also a constant). It can be shown that, in two-dimensional flow, this constant is the vorticity; that is, the vorticity is a constant along a streamline in an inviscid two-dimensional rotational flow. Except for the case of uniform shear ($f(\psi)$ = constant), or the exceptional case $f(\psi) = a\psi$, a = constant, one is faced with solving a nonlinear partial differential equation. However, if the free-stream velocity profile can be approximated by piecewise linear segments, as in Figure 1, then the streamlines passing through those points at which the velocity gradient changes (points (a), (b), and (c) in Figure 1, for example) separate regions of constant vorticity throughout the flow. This approximation can be used to change the problem of solving a nonlinear partial differential equation with known boundary conditions to one with a linear equation ($\nabla^2 \psi$ = constant) within regions with free (and, hence, unknown) boundaries.

The above approach was used to formulate a theory for finding the pressure distribution on any airfoil at angle of attack in an inviscid, incompressible, two-dimensional nonuniformly sheared flow. A digital computer program was written for a two-dimensional velocity profile like that of Figure 1(b). This velocity profile has the advantage of being one of the simplest nonuniformly sheared flows to which the theory can be applied. Application of the theory in its development stage to the more complicated sheared flow used in the experimental work of Reference 6 (which included the added complexity of free jet boundaries) was felt to be premature.

6

Wind-tunnel walls were incorporated into the program so that the computed results would be directly comparable to the results of the experimental program, and to allow the possibility of investigating wind-tunnel wall effects at a later date. The theoretical program is not limited to small magnitudes of the shear or to small flow disturbances. This latter feature is essential if inviscid pressure distributions are to be obtained for airfoil angles of attack near stall.

Details of the theory and its implementation on an IBM 7044 digital computer are presented in Reference 9. A brief outline of the basic ideas incorporated and certain numerical techniques of importance to the program are discussed in the following paragraphs.

Description of Computer Program

The two-dimensional flow model assumed for the computer program is shown in Figure 2. A Cartesian coordinate system is used. The x-axis is parallel to the wind-tunnel walls and positive in the direction of the flow. The origin is centered vertically between the walls and $x = 0$ is located at the airfoil midchord. The wind-tunnel walls and the airfoil surface are represented by bound vortex sheets of varying strength. The free-stream velocity variation in the y-direction is piecewise linear and symmetric about $y = 0$ (point (a) in Figure 2). On either side of the streamline which passes through point (a) (denoted henceforth as the "dividing streamline") the distributed vorticity is constant. If the assumed free-stream velocity profile, $U(y)$, is symmetric ($U_1 = U_2$ in Figure 2), as is the case in the work presented here, the vorticity on either side of the dividing streamline is equal in magnitude but of opposite sign. If the airfoil is of nonsymmetric profile, or is nonsymmetrically disposed in the wind tunnel, the resulting disturbance flow will distort the dividing streamline in some fashion. This distorted shape is denoted by $g(x)$ in Figure 2. Equation (1) states that the vorticity in a rotational flow is constant along streamlines; therefore, the dividing streamline still separates regions of constant vorticity. If the shape of the dividing streamline $g(x)$ were known, then it would be possible to compute the variation in strength of the bound vortex sheets representing the wind-tunnel walls and airfoil surface.

7

If, for the present, it is assumed that $q(x)$ is known, then the procedure used in calculating the singularity strength distributions on the airfoil surface and wind-tunnel walls is as follows. The surfaces are represented by small segments of vortex sheets each of which has a constant singularity strength. The integrals over segments of the vortex sheets for use in the equations for velocity components can then be evaluated in closed form. Hence, the velocity components are expressible as finite series in terms of the vortex sheet singularity strengths. The vortex sheets representing the wind-tunnel walls are assumed to have known constant strengths far upstream and downstream of the airfoil. The boundary conditions for no normal flow across the wind-tunnel walls and airfoil surface are next applied at the center of each of the vortex sheet segments. If these boundary conditions were the only conditions to be satisfied, there would result a determinant set of linear simultaneous algebraic equations. However, in addition, the Kutta-Joukowski condition at the airfoil trailing edge must be satisfied. This constraint is implemented in the computer program by requiring that the sum of the singularities representing the upper and lower airfoil surfaces vanish in the limit as the trailing edge is approached. This results in an additional equation, and the problem is now overdetermined. The overdeterminancy results from the choice of constant singularity strength for each vortex sheet segment. If it had been assumed that the singularity strength of each segment varied linearly, there would have been as many equations as unknowns. The constant strength assumption was made to limit the number of linear equations requiring solution.

The method used to solve the overdetermined set of equations followed that of Reference 10 which presents a numerical technique for obtaining smoothly varying solutions to such sets when it is known beforehand that the solutions should be smooth. The smoothing technique is required to suppress oscillations arising from small errors in the numerical computations. These oscillations can become very large as is illustrated in Figure 3 where computed pressure distributions on a symmetric Joukowski airfoil in a uniform stream are compared to the exact solution obtained through conformal mapping. It is evident that smoothing is required and that the

8

process works quite well, at least for the present model. The maximum deviation between the smoothed numerical solution and the exact solution occurred at the suction peak and amounted to a 3 percent overshoot. The size of the vortex sheet segments chosen to represent the airfoil surface in this region may have contributed to this small error. Hence, it would appear that the process used to calculate the singularity strength distribution on the surfaces provides satisfactory accuracy.

An important part of the computer program is an iterative technique for determining the function $g(x)$ numerically. Mass-flow continuity is the basis for this iterative technique in the developed computer program. If an initial shape $g_0(x)$ is assumed, the strengths of the singularity distributions (vortex sheets representing the wind-tunnel walls and the airfoil surface) can be determined as outlined above. Once these distributions are known, the first iterated streamline shape, $g_1(x)$, is determined by computing, at each value of x considered, the vertical point ($g_1^*(x)$, say) in the flow where the mass flow is equal to that on either side of the dividing streamline in the undisturbed free stream, and then by taking the average of $g_0(x)$ and $g_1^*(x)$. Thus

$$g_1(x) = \frac{1}{2}\left[g_0(x) + g_1^*(x) \right].$$

Given $g_1(x)$, again the singularity strength distributions for the bound vortex sheets representing the wind-tunnel walls and the airfoil can be obtained, from which the second iterated streamline shape, $g_2(x)$, can be determined. If the iterative process converges, $\lim_{i \to \infty} g_i(x) = g(x)$. Hopefully, the rate of convergence is such that this limit is very nearly attained after only a few iterations. For the configurations run thus far, five to six iterations appeared to be sufficient to provide an acceptable solution.

The singularity strength distributions required to satisfy the boundary conditions at the wind-tunnel walls and the airfoil surface are those which correspond to the $g(x)$ evaluated in the final iteration. The flow field is thus completely determined. Velocities on the airfoil surface can then be converted to static pressures by means of the Bernoulli equation for rotational flow,

9

$$\frac{1}{2}\rho(u^2 + v^2) + p = \frac{1}{2}\rho\left[U(y)\right]^2 + p_o \,, \qquad \text{(Eq. 2)}$$

applied along the airfoil stagnation streamline. The proper value of $U(y)$ in the freestream to be used in Equation (2) is determined by computing the mass flow between the wind-tunnel wall and the airfoil. The value of $U(y)$ which corresponds to this mass flow in the undisturbed freestream is the correct value. It should be noted that the use of mass flow continuity in the iterative process and in determining $U(y)$ requires a known reference streamline of the flow. In the present case, a wind-tunnel wall provides this reference streamline.

Using the program outlined above, pressure distributions on a symmetric Joukowski airfoil at angle of attack were computed for several locations in the simple nonuniformly sheared flow. The results are compared to experiment in a later section.

EXPERIMENTAL PROGRAM

The experimental program was designed to provide airfoil pressure distribution data by means of which the accuracy of the theoretical results could be determined. At the same time, additional experimental evidence regarding airfoil maximum lift behavior in sheared flows would be obtained.

The experiments were made in the subsonic leg of the CAL One-Foot High-Speed Wind Tunnel. This leg of the wind tunnel has a test section with a cross section of 17 inches by 24 inches and is operated as a closed-throat nonreturn tunnel. The two-dimensional airfoil used in this research has a symmetric Joukowski profile with a thickness-chord ratio of 17 percent and a chord of 6 inches. The wing was mounted in the wind-tunnel test section by a supporting structure which permitted independent change in geometric angle of attack and vertical location of the wing in the wind tunnel by means of manual adjustment.

Instrumentation was relatively simple. Flow calibrations in the wind-tunnel test section were performed with a conventional 3/16-inch-diameter pitot-static probe which included static pressure taps from which

10

flow angularity data were obtained. Static and dynamic pressures were measured with manometers. Thirty-two static pressure taps were distributed over the top and bottom surfaces of the wing at a section 0.75 inch to one side (left looking downstream) of the wind-tunnel centerline. These taps were connected to an inclined manometer bank and the resulting pressures were recorded photographically. Free-stream static pressure was obtained from a pressure tap on the ceiling of the test section. This tap was approximately 2-1/2 chord lengths upstream of the model midchord.

The sheared flow in the wind-tunnel test section was produced by a screen placed slightly more than 3 feet (between 6 and 7 wing chords) upstream of the wing. This screen consisted of an array of circular rods spanning the wind-tunnel section horizontally and secured by a frame which was clamped between two sections of the wind-tunnel circuit. The spacings between rods and the rod diameters were varied so as to introduce variable losses across the flow. By proper spacing and rod size variation, the vertical distribution of losses in the flow at the screen can be such that the desired sheared flow velocity contour is obtained in the test section.

The theory presented in Appendix II of Reference 5 was used in the design of the screen. Application of this theory is somewhat laborious and the results are dependent on the accuracy of the empirical relationship between local screen solidity and loss coefficient. Apparently the empirical curve presented in Reference 5 is not reliable at high values of solidity because the use of this curve provided a velocity distribution which was considerably different from the design velocity distribution near the centerline of the test section. The final configuration used for the shear screen was tailored by a trial and error process of small modifications to the theoretical design until it was judged that further improvement could not be obtained without undue expenditure of time.

A number of velocity profiles were measured in the test section in a vertical plane at the model axis of rotation (midchord of the wing) using the 3/16-inch-diameter pitot-static probe. Figure 4 presents velocity distributions for the final shear screen configuration used during pressure

11

data tests. It can be seen that the velocity distribution approached the design distribution with reasonable accuracy but that some irregularities were present in the experimental data in the vicinity of 5 inches above and below the tunnel centerline. These irregularities are not believed to be of importance because they were not large and because the test region only extended to 3 inches above and below the centerline.

In addition to the velocity calibrations of the sheared flow, calibrations of flow angularity in the vertical plane were obtained using the static pressure angularity taps on the 3/16-inch probe. The variation of flow angularity over the test section height was small. A total variation of 0.65 degrees was observed. The geometric angle of attack of the airfoil was corrected for this small variation in flow angularity.

The wind-tunnel airfoil tests were of three types: uniform flow, low-turbulence tests; uniform flow, high-turbulence tests; and sheared flow tests. The uniform-flow tests, with and without high turbulence, were designed as an experimental control. The shear screens used to generate the sheared flow also generate higher turbulence levels in the flow. It was possible that this higher turbulence level would, in itself, have some marked effect on airfoil separation characteristics. The low and high turbulence tests in uniform flow were to resolve this possibility. The uniform flow, low turbulence tests were performed in the clear wind tunnel and the uniform flow, high turbulence tests were performed with screens of uniform solidity mounted upstream from the test section. These screens were similar to the shear screen except that the horizontal rods used were uniformly spaced. Two such turbulence screens were used in separate tests, one with rod diameter and spacing corresponding to that portion of the shear screen with low solidity (relatively large open area ratio) and one screen corresponding to the high solidity portion of the shear screen.

12

EXPERIMENTAL RESULTS

Uniform Flow Tests

In Figure 5, pressure distributions measured on the airfoil for several conditions of free-stream velocity and turbulence are shown. The angle of attack for these measurements was 10 degrees. All three sets of data agree satisfactorily with the pressure distributions calculated from potential flow theory except in the region near the suction peak. The divergence between theory and experiment and between the various experimental conditions decreased with decreasing angle of attack. At angles of attack higher than 10 degrees, the divergence between theory and experiment increased but differences between the various experimental configurations remained about the same. The maximum sectional lift coefficient, obtained by integration of the pressure coefficient distributions, occurred at an angle of attack of 13 degrees for all cases and the numerical values ranged between 1.24 and 1.29.

In general, the uniform flow experiments showed that the addition of turbulence by means of screens influenced the data only very slightly (see Reference 9 for further details). However, since there was a small effect of turbulence on the airfoil pressure distributions in uniform flow, it was concluded that the uniform flow data used for comparison with the sheared-flow data should be those obtained with the low-solidity turbulence screen in place. These data were chosen over those with the high solidity turbulence screen in place because the velocity and angularity calibrations in the wind-tunnel test section showed that a more nearly uniform flow was obtained with the low solidity screen. The free-stream velocity used in the uniform flow control experiments was 66 fps which is approximately midway between the minimum and maximum velocities encountered in the sheared-flow tests.

Sheared-Flow Tests

A major problem in discussing the aerodynamics of airfoils in sheared flows is the question of what constitutes a proper reference velocity.

From a practical viewpoint, the lift generated is of most interest. Hence, some average velocity, taken as a constant independent of airfoil location, should be used. Another reference velocity which has been used is the velocity which would occur in the undisturbed sheared flow (with no airfoil in the flow) at the location of the midchord of the airfoil. This velocity, which will be called the midchord velocity, is convenient for data reduction since it takes approximate account of variations in velocity with variations in airfoil location in the sheared flow. Finally, a velocity can be defined which takes into complete account all variations in the effective velocity of oncoming flow, either due to changes in airfoil location in the sheared flow, or due to changes in airfoil angle of attack in the sheared flow. This velocity is the one which occurs in the undisturbed sheared flow far upstream on the stagnation streamline (the streamline which encloses the airfoil). It is this multiplicity of reference velocities in sheared flows which tends to cause confusion and may encourage misleading conclusions regarding experimental aerodynamic data obtained in sheared flows.

The dynamic pressure which corresponds to the stagnation stream-line reference velocity is equal to the difference between the pressure at the stagnation point on the airfoil and the free-stream static pressure. If pressure taps are placed sufficiently close together on the surface of the airfoil, it is possible to obtain this dynamic pressure from the experimental airfoil pressure distributions. Bernoulli's equation along the stagnation streamline is

$$p + \frac{1}{2}\rho(u^2 + v^2) = p_o + \frac{1}{2}\rho(U_s)^2$$

where p_o is the free-stream static pressure and U_s is the velocity in the undisturbed sheared flow far upstream which corresponds to the stagnation streamline. Using this relation, the pressure coefficient, $(C_p)_s$, based on the dynamic pressure of the stagnation streamline becomes

$$(C_p)_s = \frac{p - p_o}{\frac{1}{2}\rho(U_s)^2} = 1 - \frac{u^2 + v^2}{(U_s)^2}$$

14

Note that, since the maximum positive value of $(C_p)_s$ is unity, the appropriate dynamic pressure is simply the maximum positive value of $(p-p_0)$ which is reached on the airfoil. In addition, the remaining two reference velocities which were mentioned above, provide pressure coefficients $\bar{C}_p$ (based on an average velocity, $\bar{U}$) and $(C_p)_R$ (based on midchord velocity, U_R) which are defined by

$$\bar{C}_p = \frac{p-p_0}{\frac{1}{2}\rho(\bar{U})^2} = \left(\frac{U_s}{\bar{U}}\right)^2 - \frac{u^2+v^2}{(\bar{U})^2}$$

$$(C_p)_R = \frac{p-p_0}{\frac{1}{2}\rho(\bar{U}_R)^2} = \left(\frac{U_s}{U_R}\right)^2 - \frac{u^2+v^2}{(U_R)^2}$$

Section force coefficients can be referred to any of the reference velocities to obtain, for example, $\bar{c}_l$, $(c_l)_R$ or $(c_l)_s$.

The pressure distributions obtained on the Joukowski airfoil over a wide range of angles of attack for various locations in the sheared flow were reduced to the coefficient form $(C_p)_R$. These distributions were then integrated numerically to obtain the section lift coefficient $(c_l)_R$ based on midchord velocity. In addition, the section lift coefficient, $\bar{c}_l$, based on the average velocity of the undisturbed sheared flow, $\bar{U}$, was computed by using the relation $\bar{c}_l = \left(\frac{U_R}{\bar{U}}\right)^2 (c_l)$. The results obtained for $\bar{c}_l$ are shown in Figure 6 and for $(c_l)_R$ in Figure 7, both plotted versus angle of attack. In both figures, the vertical location of the midchord of the airfoil is designated by the value of h/c in the legend, where h is the height of the midchord above the sheared-flow centerline and c is the chord of the airfoil.

It is obvious from the curves of $\bar{c}_l$ versus α (Figure 6) that the magnitude of the section lift is strongly influenced by the location of the air-foil in the flow. It is equally obvious from the curves of $(c_l)_R$ versus α (Figure 7) that a simple linear correction for the variation of local (midchord) dynamic pressure with airfoil position in the sheared flow does not completely account for the large variations in sectional lift. The trends shown on both of these figures are similar, on a much reduced scale, to those found in Reference 6. In Reference 6, however, the shear in the flow was greater by

15

a factor of 4 and the velocity profile contained free boundaries as in Figure 1(c). Either of these factors, the higher shear or the free boundaries, might account for the larger effects of airfoil location on the section lift coefficient curves found in that work.

The curves of Figures 6 and 7 show that at zero angle of attack there is a positive section lift coefficient for $\frac{h}{c} > 0$ and a negative section lift coefficient for $\frac{h}{c} < 0$. This phenomenon is similar to that predicted by Tsien's theory (Reference 1) for a symmetric Joukowski airfoil in a uniformly sheared flow. Tsien's theory has been applied to the current test configuration by assuming that the local value of shear at the airfoil midchord could be used to predict the angle of attack for zero lift ($\alpha_{\ell=0}$). For this purpose, the experimental velocity profile of Figure 4 was used to estimate the mean shear at the airfoil midchord position. Comparison between values of $\alpha_{\ell=0}$ calculated in this way and experimental values of $\alpha_{\ell=0}$ provided no conclusion on the validity of the assumption that local shear may be used to compute $\alpha_{\ell=0}$ in a nonuniformly sheared flow, primarily because of the uncertainties in finding the value of local shear from the experimental velocity profiles.

In addition to the change in angle of attack for zero lift with airfoil location in the nonuniformly sheared flow, the behavior of $(c_\ell)_R$ near maximum lift appears to be dependent on the magnitude of the shear (Figure 7). At airfoil positions well below the centerline of the velocity distribution, the stall is abrupt. At positions near the centerline and above the centerline the stall is much more gradual. Some cases which exhibit abrupt stall ($\frac{h}{c} = -1/6$ and -1/3 for example) provide higher values of $(c_\ell)_R$ just before stall than those obtained when the airfoil stalls gradually ($\frac{h}{c} = +1/2$, +1/6, and +1/12).

Some degree of correlation can be brought to the c_ℓ data by referring the section lift to the stagnation streamline reference velocity as discussed previously. The results of this method of data reduction are shown in Figure 8 as $(c_\ell)_s$ versus $\bar{\alpha} = \alpha - \alpha_{\ell=0}$. The angle of attack for zero lift has been subtracted from the usual angle of attack in this figure to facilitate direct comparison of the shapes of the curves formed by the $(c_\ell)_s$ data. Note that the data shown in Figure 8 lie on or below the

16

inviscid uniform flow theoretical curve and fall into two approximate groupings; one for positions below the sheared flow centerline, and one for positions near and above the sheared flow centerline. The data group corresponding to the airfoil near and above the sheared-flow centerline exhibit a gradual stall and, generally, higher values of $(c_l)_s$ at all positive values of α than the data group corresponding to the airfoil below the centerline. This behavior, high values of $(c_l)_s$ in combination with gradual stall and low values of $(c_l)_s$ in combination with abrupt stall, is in contrast to that exhibited by the $(c_l)_R$ data, for which no correlation of stall characteristics with magnitude of $(c_l)_R$ just prior to stall was found.

Examination of the pressure distributions measured on the airfoil at the various locations in the sheared flow provides at least a partial explanation for the apparent correlation of the c_l data when reduced to the form $(c_l)_s$. The pressure distributions measured on the airfoil located at $\frac{h}{c} = +1/6$ and $-1/6$ and at an angle of attack of 12.9 degrees for each case are shown in Figure 9. These particular pressure distributions are presented because they resulted in approximately the largest differences in $(c_l)_R$ data just below stall. A major point of interest in the data of Figure 9 is that the largest contribution to the difference in $(c_l)_R$ occurs on the airfoil's lower surface, with the data for $\frac{h}{c} = -1/6$ providing the highest contribution to $(c_l)_R$. Apparently, reducing the lift data to the form $(c_l)_s$ by accounting for the differences in $(C_p)_R$ at the stagnation point on the airfoil, partially corrects the data for the differences in the lower surface pressure distribution. However, viscous effects, which are of more importance on the upper surface, and the differences due to shear in angle of attack for zero lift are not properly accounted for by reducing the data to the form $(c_l)_s$.

The upper surface pressure distribution shown in Figure 9 for $\frac{h}{c} = +1/6$ has a substantially lower suction peak and less adverse pressure gradient just downstream of the peak than that shown for $\frac{h}{c} = -1/6$. These results are typical of all the pressure distributions measured below stall but at relatively high angles of attack, except for some cases where a leading-edge bubble formed, reducing the magnitude of the suction peak which was attained. The existence of such bubbles was detected through lampblack and

17

kerosene flow visualization studies. The presence was also detectable in some cases by irregularities in the pressure distribution just downstream of the suction peak.

It was found, in general, that those configurations which exhibited an abrupt stall were also configurations which resulted in the sharpest suction peaks and most adverse pressure gradients just downstream of the peak (as for $\frac{h}{c} = -1/6$ in Figure 9) up to angles of attack where the formation of a leading-edge bubble did not severely distort the upper surface pressure distribution. The abrupt stall which was obtained resulted from the bursting of the leading-edge bubble. In contrast, the configurations which exhibited gradual stall were configurations in which bubble formation was delayed to much higher angles of attack and which resulted in the least sharp suction peaks and least adverse pressure gradients before the formation of the bubble (as for $\frac{h}{c} = +1/6$ in Figure 9). In these latter cases, stall occurred by a progressive forward movement of the upper surface separation point.

Both of the above cases appear to be consistent with the hypothesis that it is the action of the pressure distribution on the upper surface boundary layer which determines the stalling characteristics of an airfoil in a sheared flow. It is probably not necessary to consider the direct inter-action between shear in the flow external to the boundary layer and the behavior of the boundary layer when investigating the stall behavior of an airfoil in a sheared flow. It is, however, necessary to account for the manner in which the shear affects the pressure distribution on the airfoil.

In summary, the above observations suggest that the unusual lift behavior of an airfoil in a two-dimensional nonuniformly sheared flow is a consequence of at least two more or less independent effects. These are: changes in stall behavior as a result of differences in the upper surface pressure gradients, and changes in lift behavior associated with changes in stagnation pressure of the streamline which intersects the airfoil as angle of attack is varied. It is worth noting that the stagnation streamline dynamic pressure differed from the dynamic pressure referenced to the airfoil midchord by more than 50 percent in some instances.

18

COMPUTED RESULTS AND COMPARISON WITH EXPERIMENT

The computer program has been used to compute pressure distributions on the Joukowski airfoil at two vertical locations in the nonuniformly sheared flow; $\frac{h}{c}$ = -1/3 and $\frac{h}{c}$ = +1/2. At $\frac{h}{c}$ = -1/3, pressure distributions were computed for α = 7.1 degrees and α = 9.5 degrees. At $\frac{h}{c}$ = +1/2, the pressure distribution at α = 8.2 degrees was computed.

Figures 10 and 11 show comparisons between computed and experimental values of $(C_p)_R$ versus $\frac{x}{c}$ for $\frac{h}{c}$ = -1/3 and α = 7.1 and α = 9.5 degrees. Also shown on these figures are the computed pressure distributions for the airfoil in uniform flow at the same location in the wind-tunnel test section. These latter pressure distributions differ from the potential flow solutions for an airfoil in an inviscid uniform stream of infinite extent because of the presence of the wind-tunnel walls. For the particular cases computed, however, the differences were very small. In both figures, the computed sheared flow pressure distributions agree satis-factorily with the experimental data on the lower surface and both experi-mental and computed results differ appreciably from the uniform flow pressure distribution in the vicinity of the stagnation point. The moderate differences between theory and experiment near the midchord on the lower surface are about the same as those found in uniform flow, an example of which is given in Figure 5. At α = 7.1 degrees, the computed upper surface pressure distribution agrees well with the experimental data except near the suction peak. At the higher angle of attack, α = 9.5 degrees, the experi-mental data differ from the computed pressure distribution over the majority of the upper surface. In both cases, the difference between the computed pressure distributions and the experimental data for the sheared flow were comparable to the differences observed between theory and experiment in the uniform flow control tests at comparable angles of attack. These differences are, therefore, probably attributable to viscous effects which become larger as angle of attack is increased. Note that at both angles of attack, the computed pressure gradient immediately downstream of the suction peak is more adverse than that computed for uniform flow. This result is consistent with the observed abrupt stall which occurs with the airfoil at $\frac{h}{c}$ = -1/3.

Figure 12 presents a comparison of computed and experimental pressure distributions for $\frac{h}{c}$ = +1/2 and α = 8.2 degrees. The agreement between theory and experiment for this case is very good over most of the airfoil surface. The experimental data show a small loss in the suction near the peak and a small increase in stagnation pressure. The reason for the latter difference is not known at present but may be attributable to experimental error. The loss near the suction peak in this case, again probably due to viscous effects, is quite small because of the mild pressure gradient on the upper surface. Note that the computed and experimental pressure distributions lie above the computed uniform flow curve. Such behavior cannot be attributed to viscous effects. These would reduce the experimental suction pressures on the upper surface. The computed pressure gradient immediately downstream from the suction peak is less adverse for the sheared flow than for the uniform flow in this case. This is consistent with the gradual stall observed with the airfoil in this location.

The computed pressure distributions were integrated to get lift, moment, and pressure drag coefficients referenced to midchord dynamic pressure. The results are compared to appropriate experimental results in Reference 9. Agreement between computed and experimental values of $(c_\ell)_R$ and $(C_{m_{c/4}})_R$ was satisfactory, except, perhaps, for $(C_{m_{c/4}})_R$ at $\frac{h}{c}$ = -1/3, α = 9.5 degrees where the computed value was -0.011 and the experimental value -0.028. The pressure drag coefficients computed from the theory for the sheared flow and the uniform flow configurations varied between -0.01 and -0.016. The negative values may reflect the slight over prediction of leading-edge suction peak for uniform flow which undoubtedly carries over into the nonuniformly sheared flow calculations. In contrast, the experimental pressure drag coefficients had minimum values of approximately 0.005.

CONCLUDING REMARKS

The good agreement between the computed and experimental pressure distributions (allowing for viscous effects of similar magnitude to those observed in uniform flow) and the fact that the computed distributions

20

differ in important respects from computed uniform flow pressure distributions indicate that the theoretical model successfully predicts the important features of the airfoil aerodynamic characteristics in the unseparated nonuniformly sheared flow. A particular notable feature of the computed results is that they appear to account for the stall behavior solely on the basis of the inviscid flow pressure distribution.

For the particular airfoil and nonuniformly sheared flow used in the experimental portion of this program, a marked degree of correlation of the section lift data is obtained for differing vertical positions in the flow if section lift coefficients are referenced to the airfoil stagnation streamline dynamic pressure ($\frac{\rho}{2} U_s^2$), and angle of attack is measured from the zero-lift angle of attack. The two primary factors in determining the observed two-dimensional aerodynamic behavior of airfoils in nonuniformly sheared flows then appear to be the variation of stagnation streamline dynamic pressure with angle of attack for a given wing position in the sheared flow, and the inviscid influence of the nonuniformly sheared flow in determining the pressure distribution on the airfoil upper surface. The former factor determines the apparent lift-curve slope well below stall and the latter determines the stalling behavior. Both factors appear to depend on the overall distribution of shear in the flow.

The experimental results presented in this paper and in Reference 6 have indicated that airfoil location in a nonuniformly sheared flow plays a substantial role in determining the lift and stalling characteristics of the airfoil. The results presented in Reference 6, which were measured with the same airfoil in a two-dimensional nonuniformly sheared flow more representative of a section through a propeller slipstream, have shown that the differences in lift characteristics can become very large indeed. For example, relocation of the airfoil midchord in a region of large shear gradient from a position approximately one-half of its thickness above the sheared flow centerline to a position equally distant from but below the centerline increased the maximum sectional lift available before stall by a factor of more than 2. Such large differences in the sectional lift available

21

before stall plus the change in stalling characteristics in the two-dimensional nonuniformly sheared flow suggest that there may be appreciable benefits available for a wing immersed in a three-dimensional propeller slipstream with significant shear if the overall configuration is properly designed.

The theoretical model outlined briefly in this paper would, with extensions to account for additional complexities of the flow such as free boundaries, provide a powerful tool for investigation of the effec of non-uniform shear on aerodynamic characteristics of arbitrary airfoils in two-dimensional nonuniformly sheared flows. The results of these investigations could be used as a starting point to attack the more complex three-dimensional problem of a wing immersed in a propeller slipstream with significant nonuniform shear.

REFERENCES

1. Tsien, H.S., "Symmetrical Joukowski Airfoils in Shear Flow", Quarterly of Applied Mathematics, Vol. I, No. 2, 1943, pp. 130-148.

2. Lighthill, M.J., "The Fundamental Solution for Small Steady Three-Dimensional Disturbances to a Two-Dimensional Parallel Shear Flow", Journal of Fluid Mechanics, Vol. 3, 1957, pp. 113-144.

3. Jones, E.E., "The Forces on a Thin Airfoil in Slightly Parabolic Shear Flow", ZAMM, Vol. 37, 1957, pp. 362-370.

4. Sowyrda, A., Theory of Cambered Joukowski Airfoils in Shear Flow, CAL Report AI-1190-A-2, Cornell Aeronautical Laboratory, Inc., Buffalo, New York, September 1959.

5. Vidal, R.J., Hilton, J.H., and Curtis, J.T., Cornell Aeronautical Laboratory, Inc., The Two-Dimensional Effects of Slipstream Shear on Airfoil Characteristics, TREC TR60-56, U.S. Army Transportation Research Command, Fort Eustis, Virginia, September 1960.

6. Vidal, R.J., Curtis, J.T., and Hilton, J.H., Cornell Aeronautical Laboratory, Inc., The Influence of Two-Dimensional Stream Shear on Airfoil Maximum Lift, TCREC TR61-93, U.S. Army Transportation Research Command, Fort Eustis, Virginia, August 1961.

7. The Effects of Axisymmetric Slipstream Shear on Airfoil Characteristics, TCRFC TR61-138, U.S. Army Transportation Research Command, Fort Eustis, Virginia, December 1961.

8. Brady, W.G., Cornell Aeronautical Laboratory, Inc., Theoretical and Experimental Studies of Airfoil Characteristics in Nonuniform Sheared Flow, USAAML TR65-17, AD 616617, U.S. Army Aviation Materiel Laboratories, Fort Eustis, Virginia, May 1965.

9. Brady, W.G., and Ludwig, G.R., Cornell Aeronautical Laboratory, Inc., Theoretical and Experimental Investigation of the Aerodynamic Properties of Airfoils Near Stall in a Two-Dimensional Nonuniformly Sheared Flow, to be published as USAAVLABS TR66-35 by the U.S. Army Aviation Materiel Laboratories, Fort Eustis, Virginia.

10.   Twomey, S., "On the Numerical Solution of Fredholm Integral
       Equations of the First Kind by the Inversion of the Linear
       System Produced by Quadrature", Journal of the Association
       for Computing Machinery, Vol. 10, 1963, pp. 97-101.
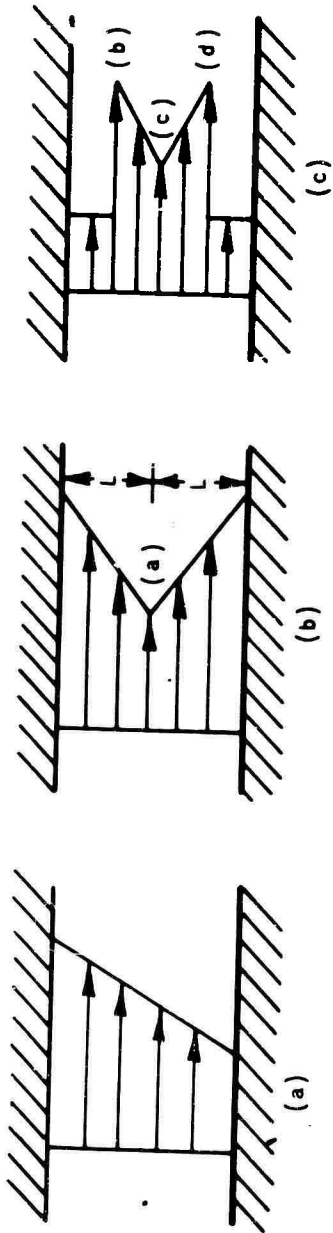
Figure 1. EXAMPLES OF FREE-STREAM VELOCITY PROFILES REPRESENTED BY PIECEWISE LINEAR SEGMENTS.
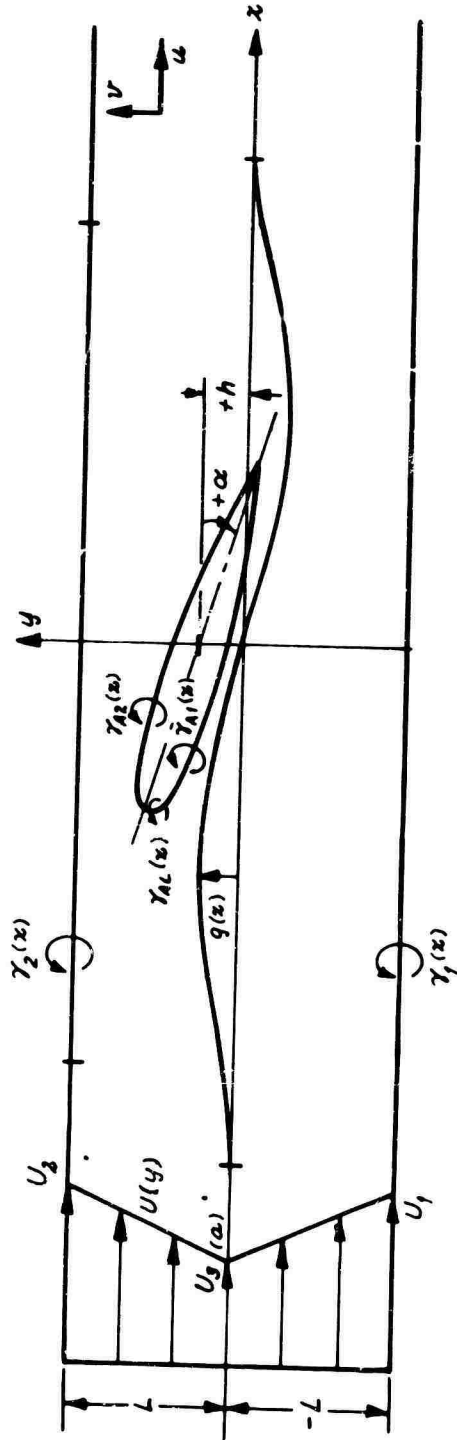
Figure 2. SCHEMATIC OF FLOW MODEL FOR IBM COMPUTER PROGRAM.

25
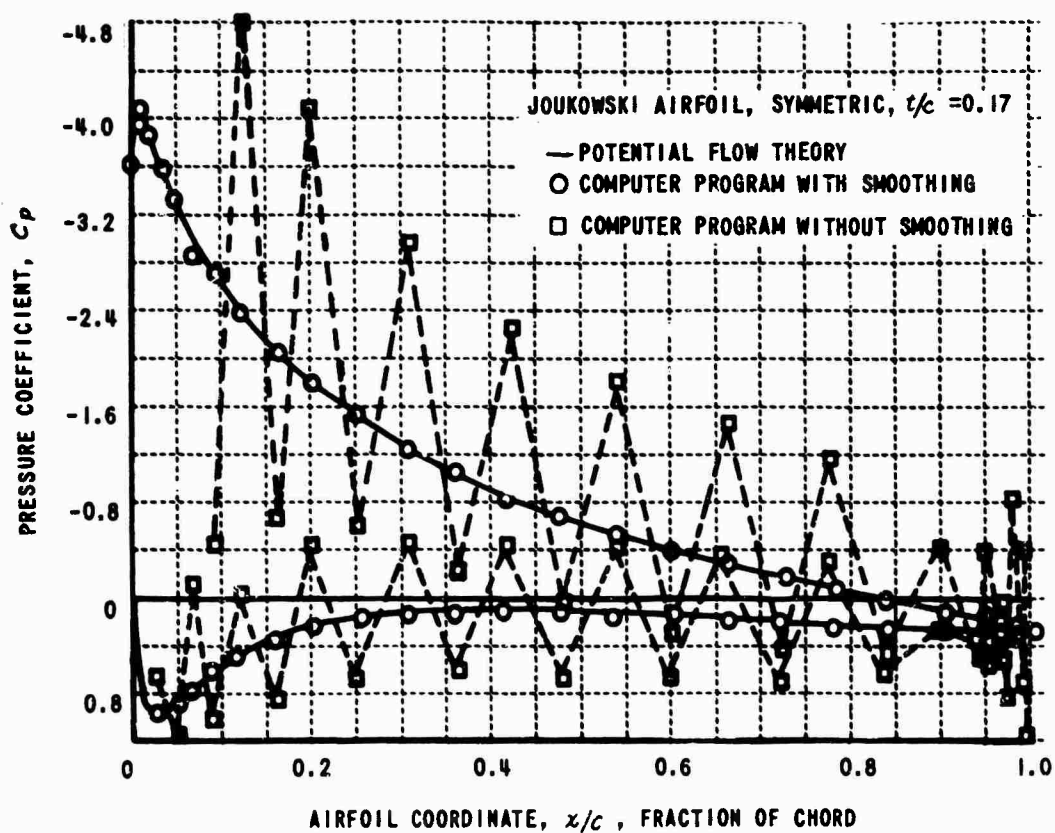
Figure 3. PRESSURE COEFFICIENT, C_p, VERSUS FRACTION OF CHORD, x/c, FOR UNIFORM FLOW FROM POTENTIAL FLOW THEORY, AND FROM COMPUTER PROGRAM WITH AND WITHOUT SMOOTHING; α=10.0 DEGREES.

26
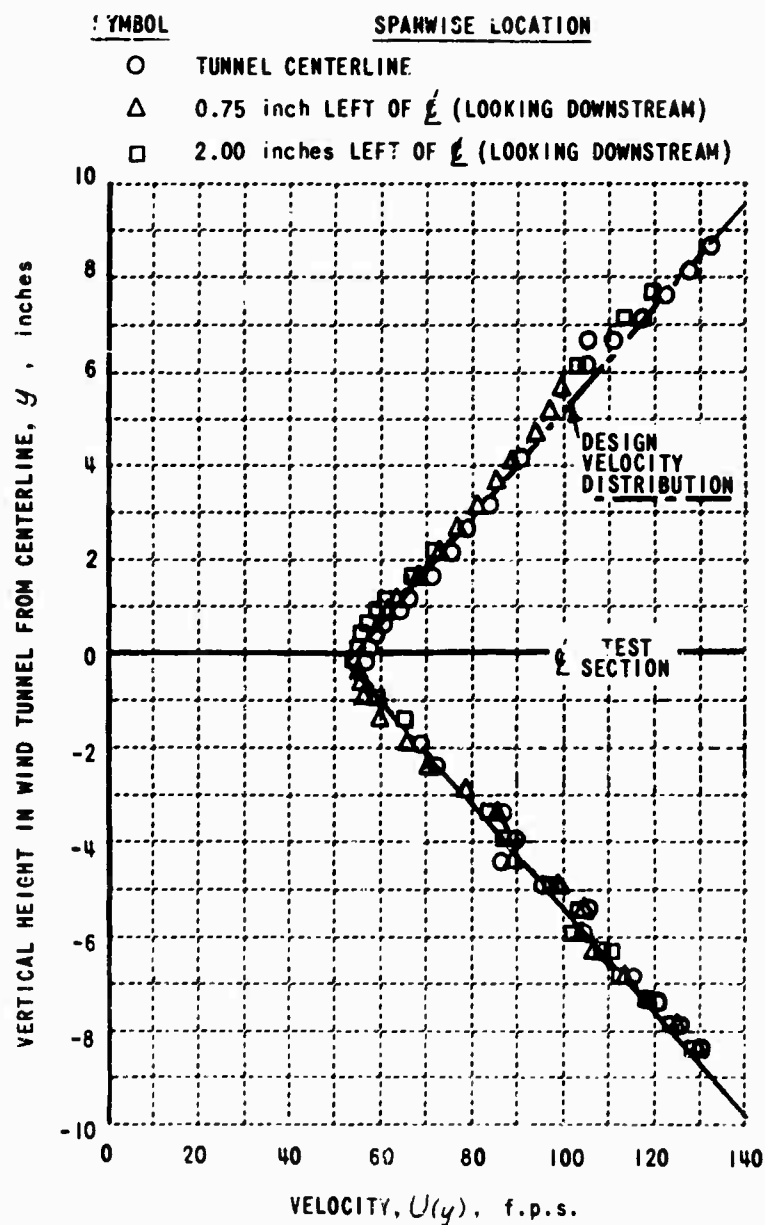
Figure 4. MEASURED FREE-STREAM VELOCITY DISTRIBUTION IN NONUNIFORMLY SHEARED FLOW AT MODEL MIDCHORD STATION.

27
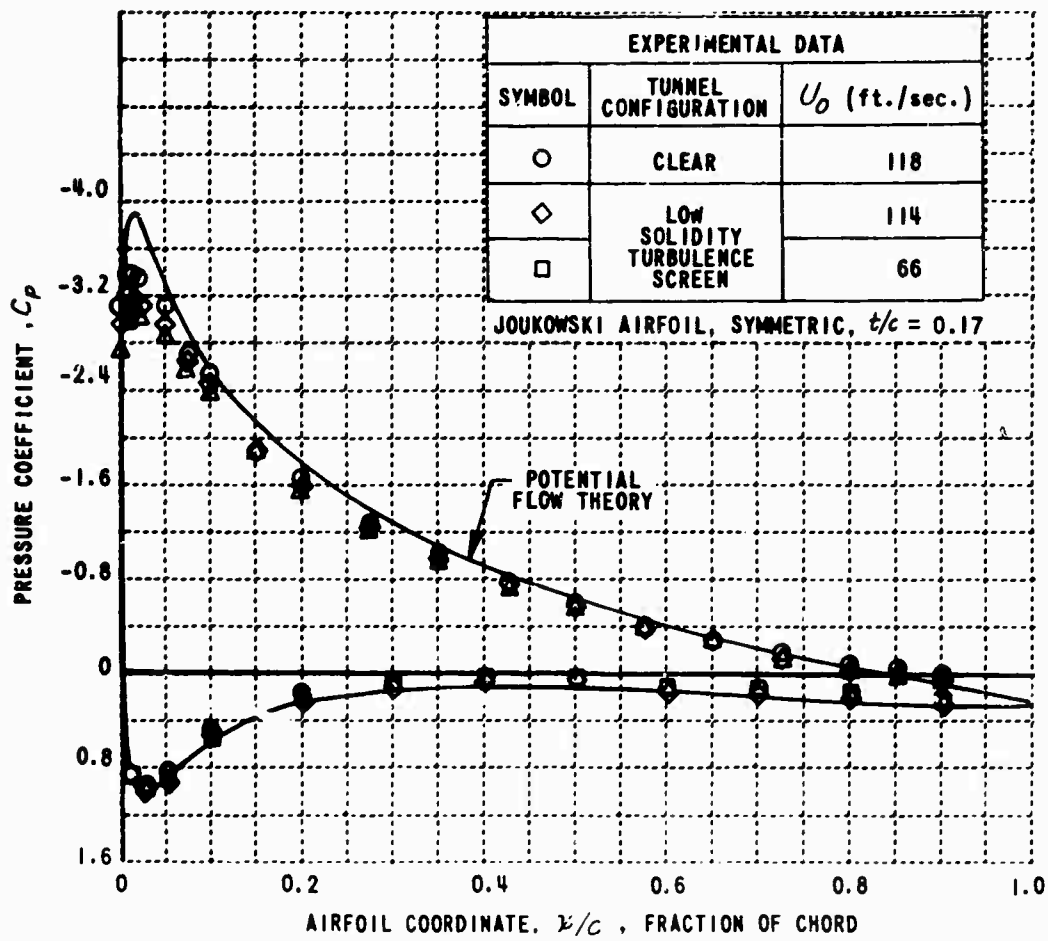
Figure 5. PRESSURE COEFFICIENT, C_p, VERSUS FRACTION OF CHORD, x/c, UNIFORM FLOW, α = 10.0 DEGREES.

28
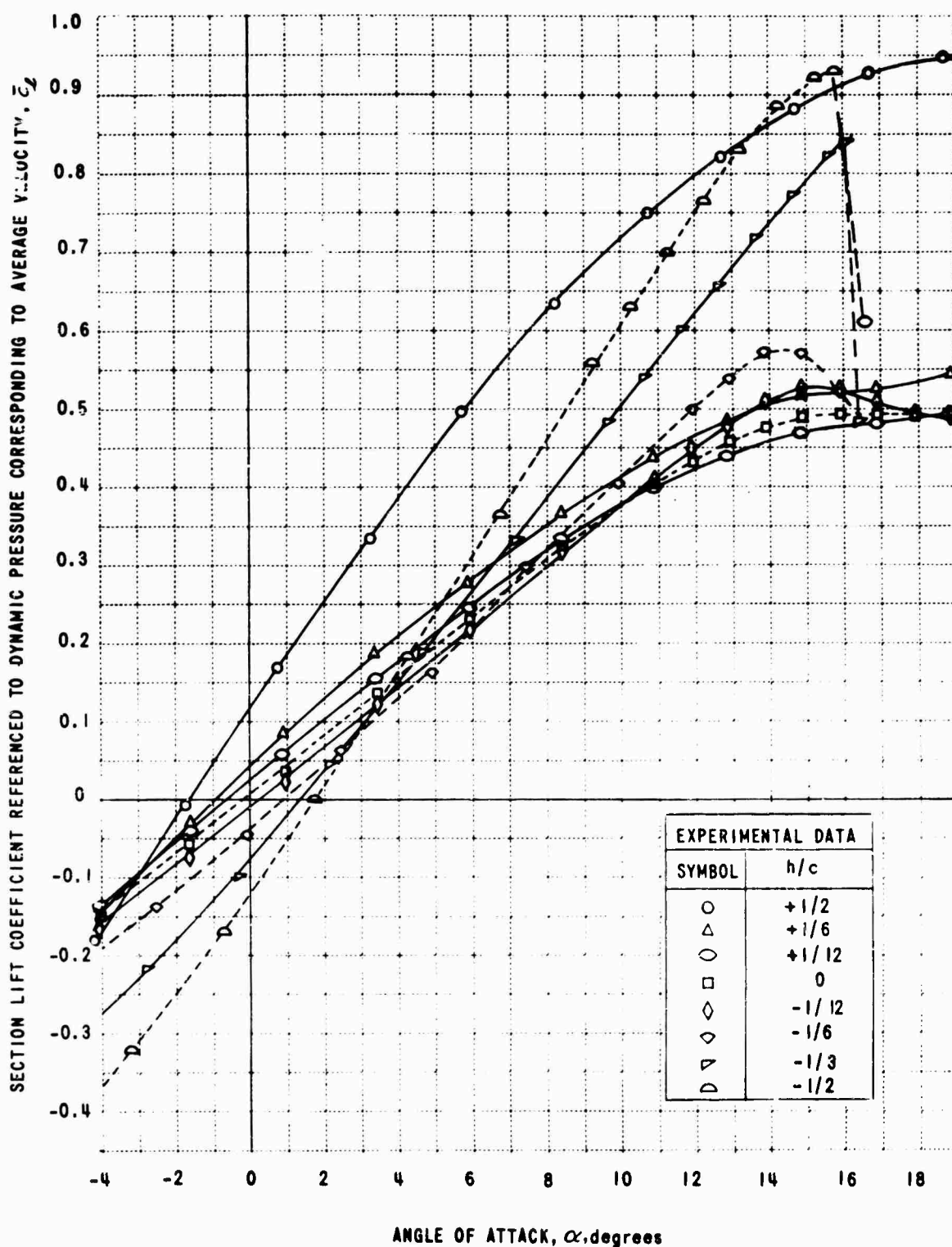
Figure 6.   NONDIMENSIONAL SECTION LIFT, $\bar{c}_\ell$, VERSUS ANGLE OF ATTACK, α,
NONUNIFORMLY SHEARED FLOW.
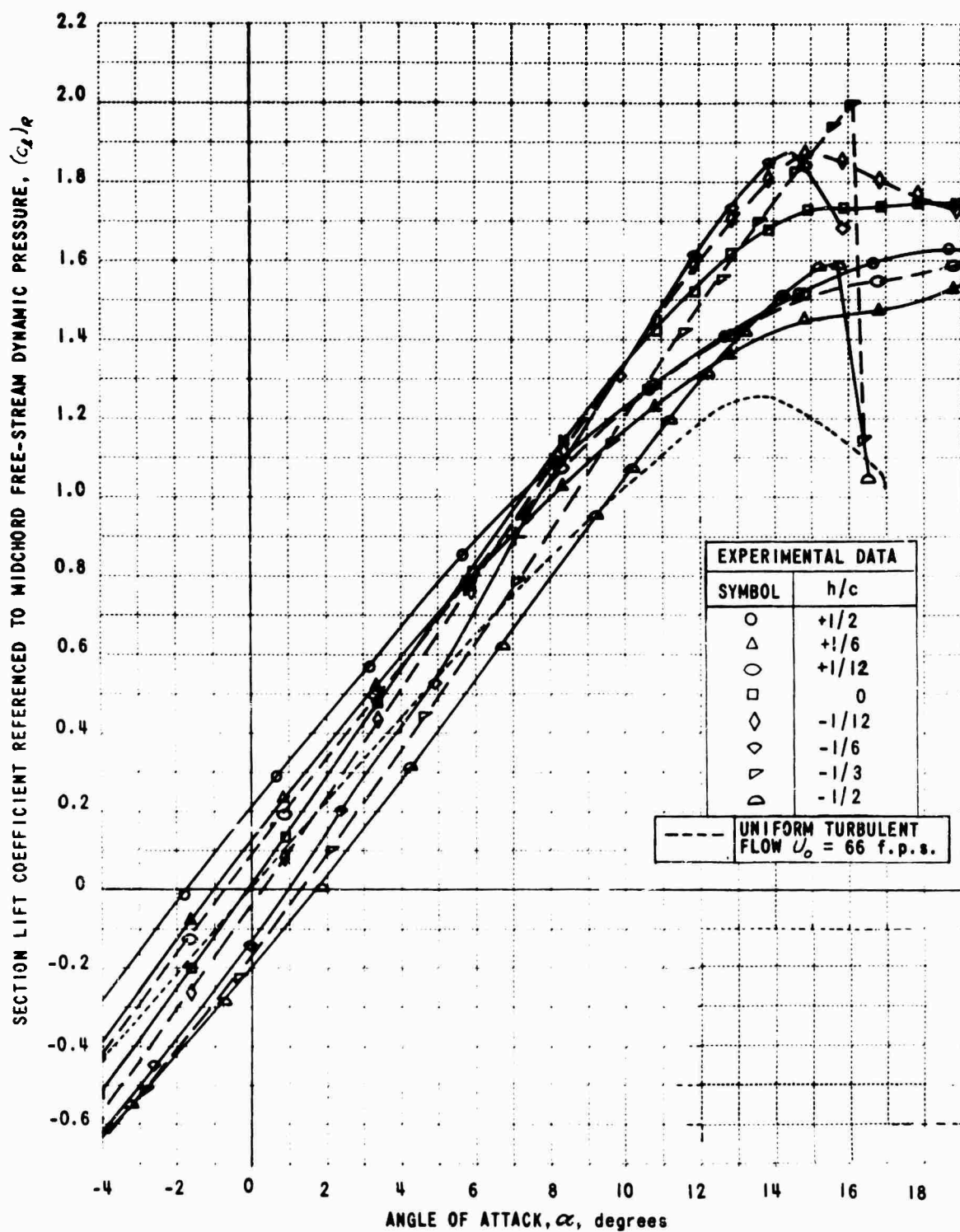
Figure 7. SECTION LIFT COEFFICIENT REFERENCED TO MIDCHORD
DYNAMIC PRESSURE, $(c_l)_R$, VERSUS ANGLE OF ATTACK, α,
NONUNIFORMLY SHEARED FLOW.

30
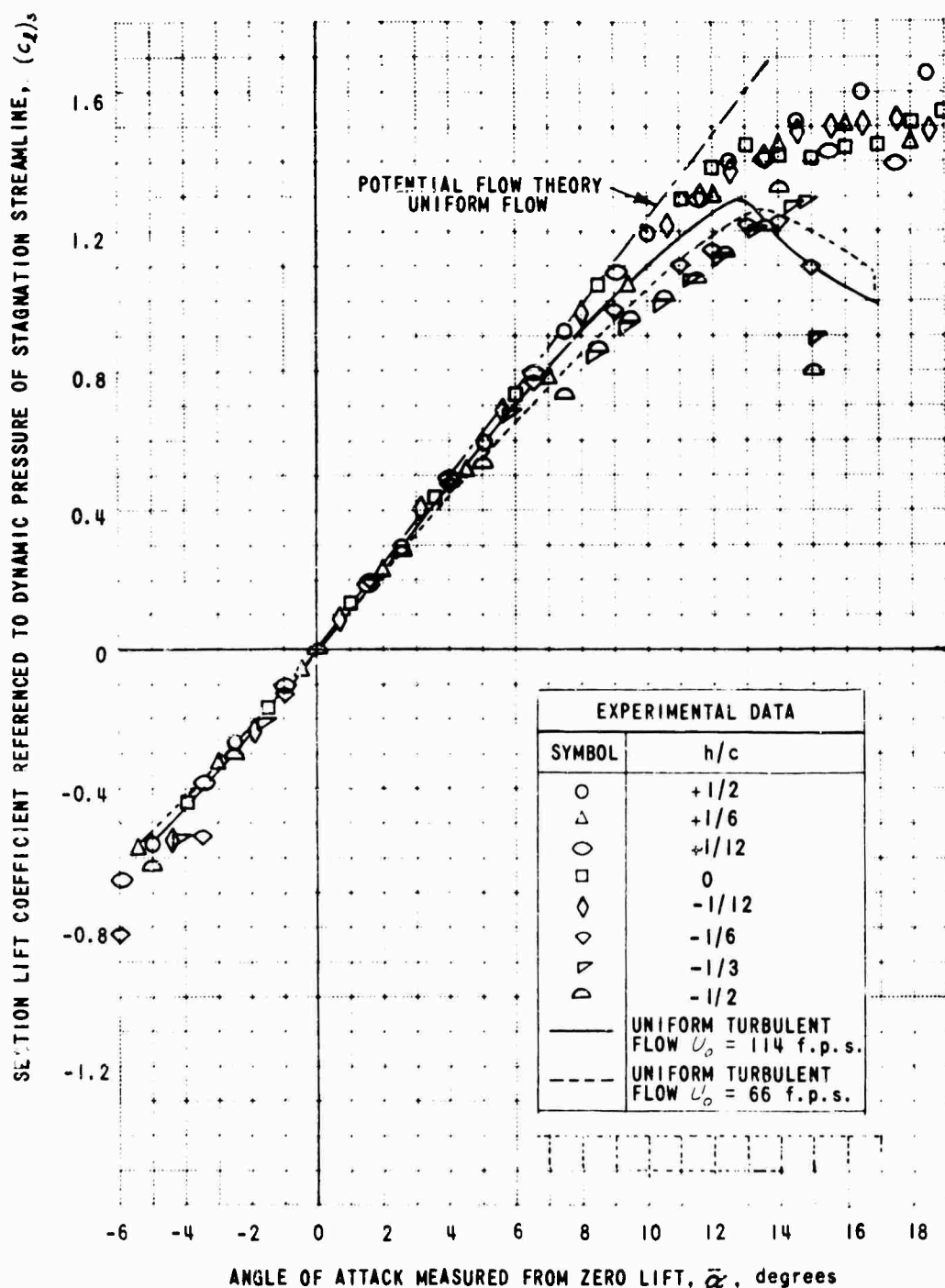
Figure 8. SECTION LIFT COEFFICIENT REFERENCED TO DYNAMIC PRESSURE OF STAGNATION STREAMLINE,$(c_l)_s$, VERSUS ANGLE OF ATTACK MEASURED FROM ZERO LIFT, $\bar{\alpha}$, NONUNIFORMLY SHEARED FLOW.

31
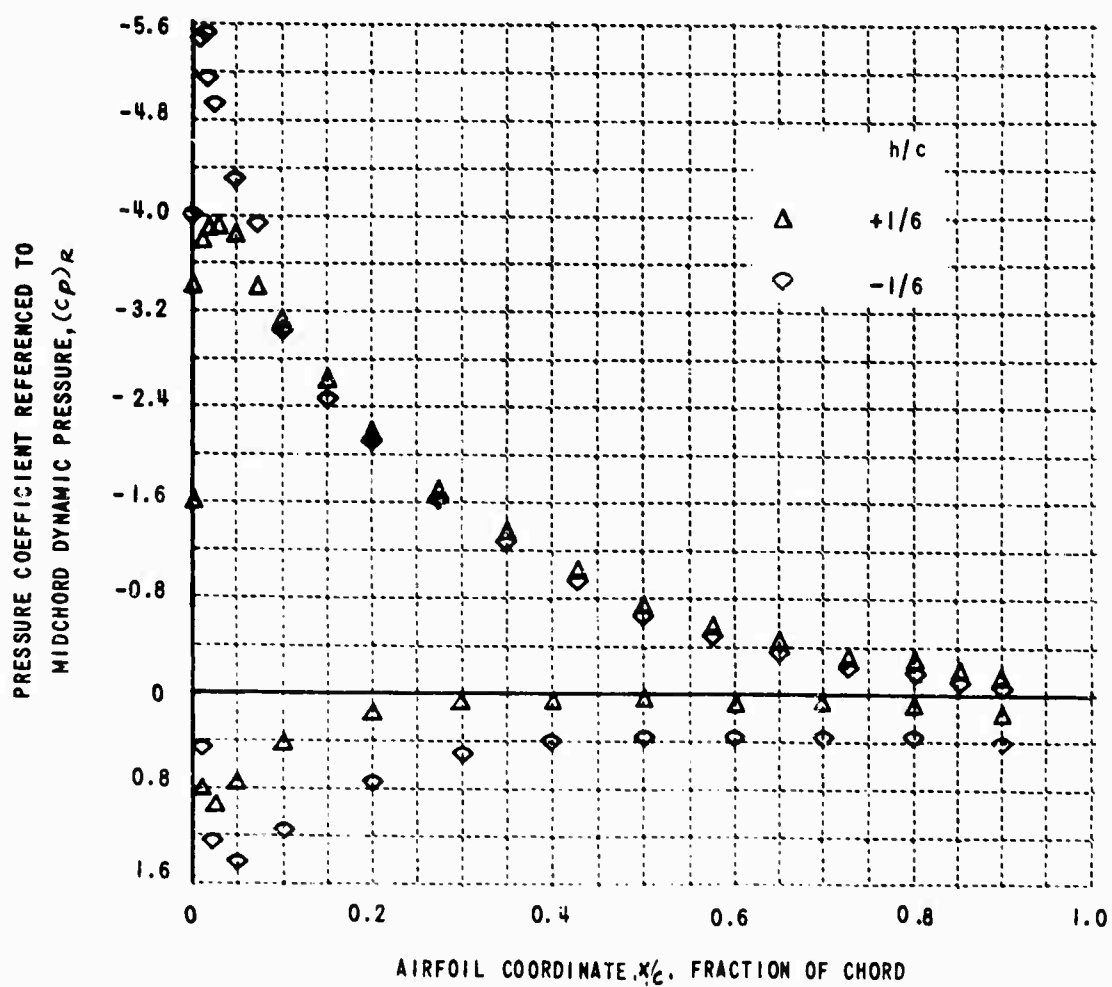
Figure 9. PRESSURE COEFFICIENT REFERENCED TO MIDCHORD DYNAMIC PRESSURE, $(c_p)_R$, VERSUS FRACTION OF CHORD, x/c, FOR NONUNIFORMLY SHEARED FLOW, $\alpha = 12.9$ DEGREES, $h/c = +1/6$ AND $-1/6$.
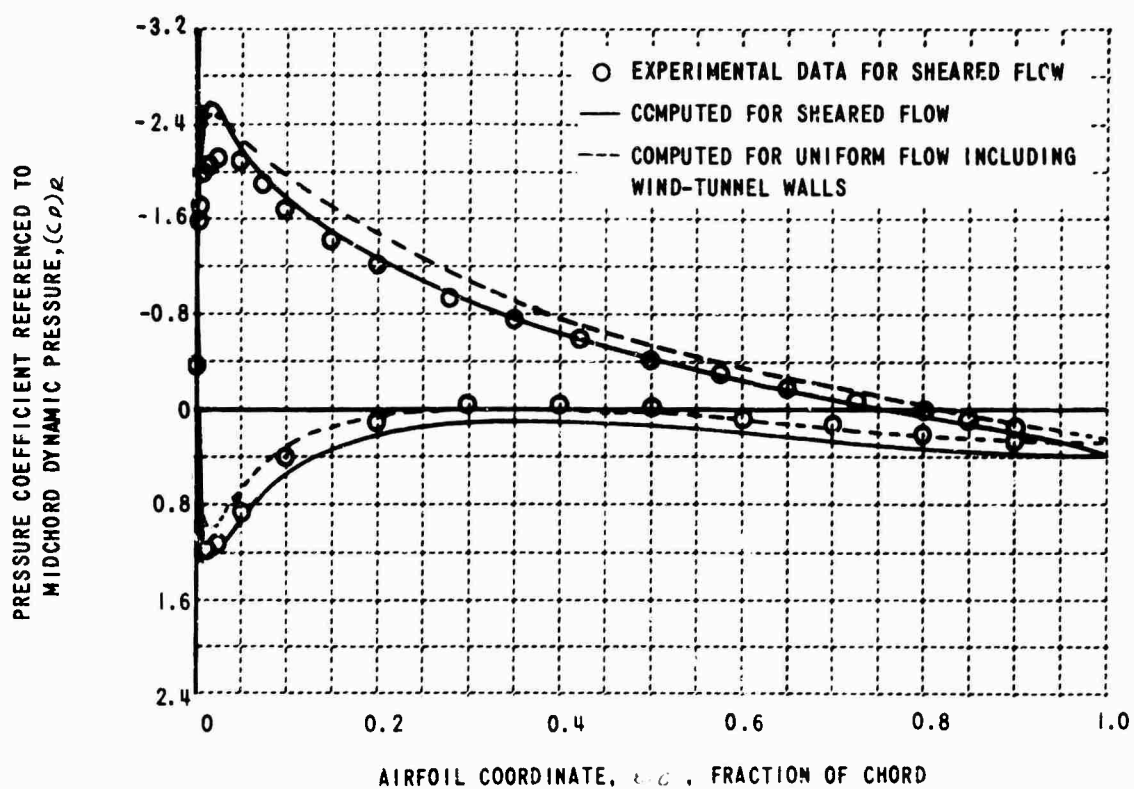
Figure 10.   COMPARISON OF COMPUTED AND MEASURED PRESSURE COEFFICIENTS,
$(c_P)_R$, VERSUS FRACTION OF CHORD, x/c, NONUNIFORMLY
SHEARED FLOW, $h/c = -1/3$, $\alpha = 7.1$ DEGREES.
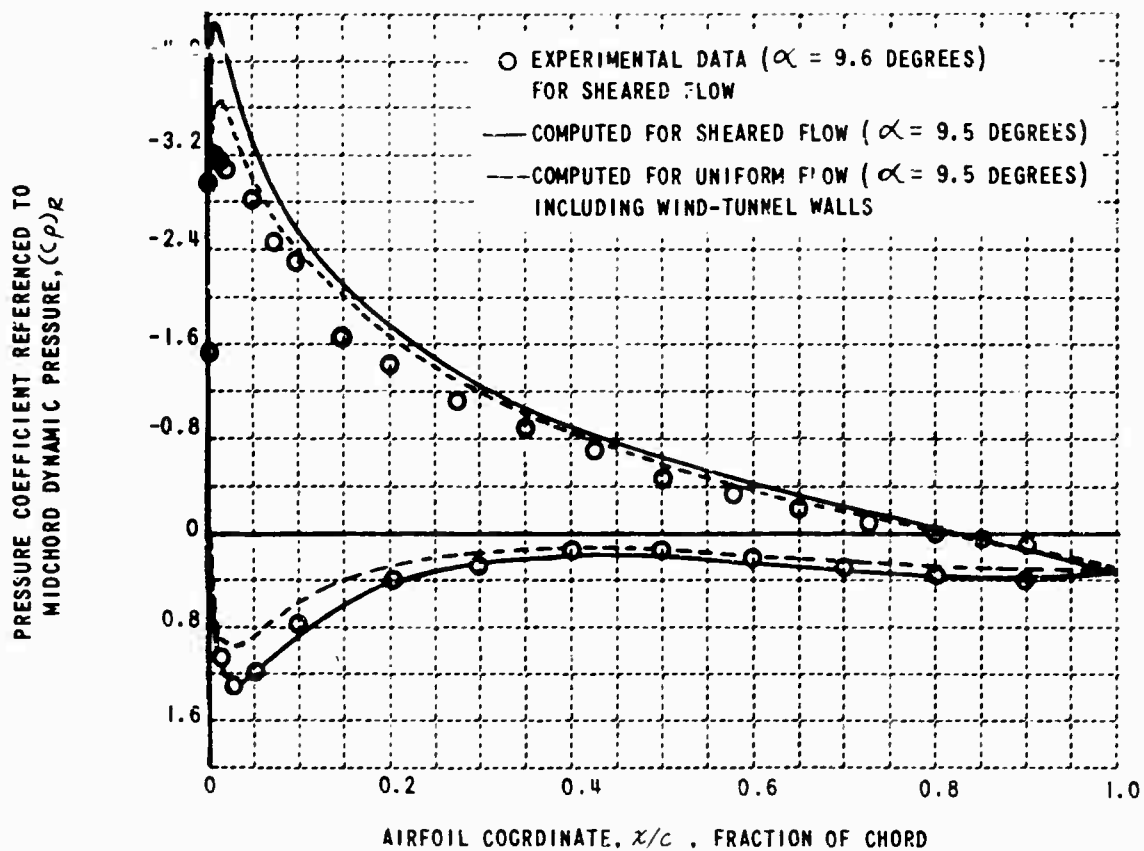
Figure 11.   COMPARISON OF COMPUTED AND MEASURED PRESSURE COEFFICIENTS,
$(c_P)_R$, VERSUS FRACTION OF CHORD, x/c, NONUNIFORMLY
SHEARED FLOW. $h/c = -1/3$, $\alpha = 9.5$ DEGREES.
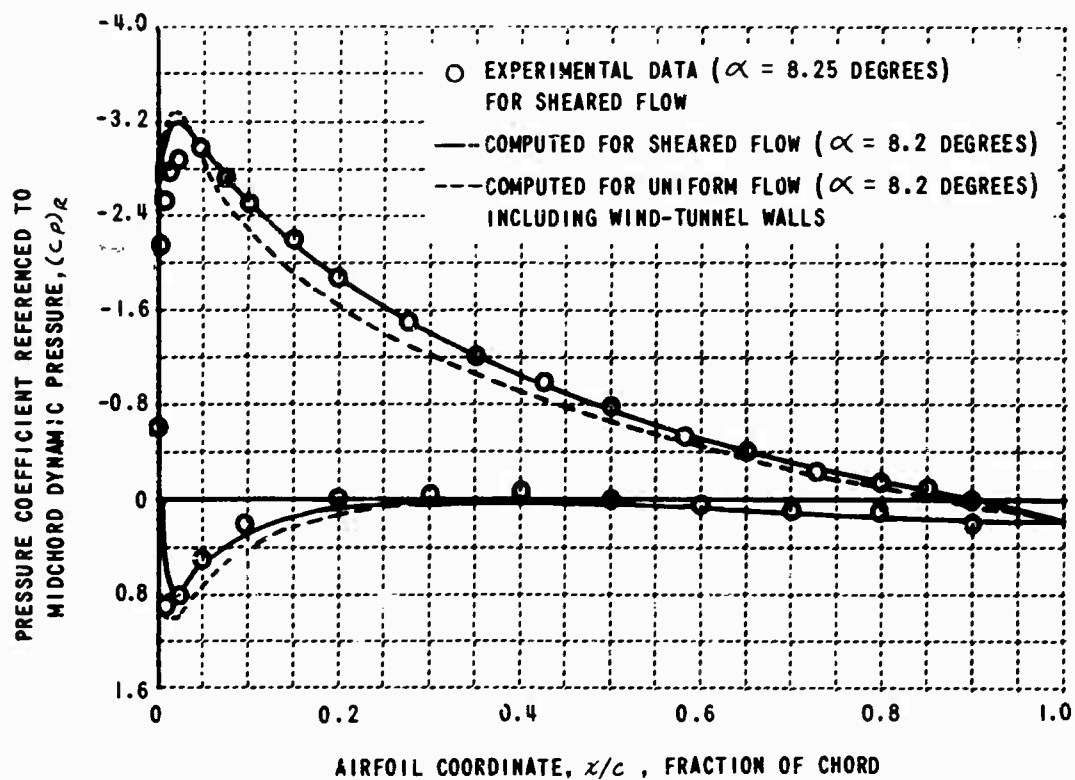
Figure 12. COMPARISON OF COMPUTED AND MEASURED PRESSURE COEFFICIENTS, $(c_p)_R$, VERSUS FRACTION OF CHORD, x/c, NONUNIFORMLY SHEARED FLOW, $h/c = +1/2$, $\alpha = 8.2$ DEGREES.

35

NOTES

EXPERIMENTAL INVESTIGATION OF COMPOUND

HELICOPTER AERODYNAMIC INTERFERENCE EFFECTS

by

RICHARD M. SEGEL
Supervisor, Advanced Rotorcraft Research Projects Group
Aircraft Advanced Research Section

LAWRENCE J. BAIN
Supervisor, Dynamics Research Group
Aircraft Advanced Research Section

ABSTRACT

The presence of numerous lifting components on a compound
helicopter results in mutual aerodynamic interferences between them.
A generalized model of a compound helicopter was tested during March,
1966 in the United Aircraft 18 Foot Wind Tunnel to investigate these
effects at speeds up to 300 knots. Three strain gage balances measured
rotor, wing and fuselage forces and moments independently. In addition,
wing static pressure distribution, oscillatory airloads, tail downwash
angle, and rotor blade flapping and stresses were measured. Configuration
variables included three wing sizes, each tested at three vertical locations
on the fuselage.

A preliminary analysis of the data is presented which shows the
decrease in wing loading induced by rotor downwash, and the influence
of wing size and position on this effect. The wing lift/drag ratio is shown
to decrease with increasing rotor lift. In the practical operating range of
compound helicopters, the influence of the wing upon rotor characteristics
was found to be small. The measured downwash at the tail conforms to
fully developed momentum values.

INTRODUCTION

The successful marriage of fixed wing and helicopter technologies in the development of the compound helicopter requires an understanding of the aerodynamic interactions among the vehicle's lifting components. The relative effects of a number of design and operating parameters such as wing size and vertical position, and rotor/wing lift sharing upon performance and handling characteristics must be determined before the concept can be fully developed. This paper describes an AVLABS sponsored experimental investigation of the interference effects occurring in compound helicopters between rotor, wing, fuselage and horizontal stabilizer over a broad range of configuration variables, Reference 1.

The existence of these interference effects was revealed in small scale wind tunnel tests which were conducted as early as 1955 and more recently in the UAC 4 x 6 foot wind tunnel. In addition, flight research in this area began with the addition of wings to an S-55 helicopter in 1957-8 and is continuing at the present with the Sikorsky S-61F research aircraft, shown in Figure 1. This aircraft is instrumented to measure rotor and wing loads independently and has attained speeds in excess of 200 knots. The S-61F program and other AVLABS sponsored flight research investigations of compound helicopters have helped to define the effects of rotor/wing lift sharing, but none has provided the flexibility or precision which may be obtained in the wind tunnel. Consequently, AVLABS awarded a contract to Sikorsky Aircraft in February 1965, to perform a comprehensive wind tunnel investigation to study the aerodynamic characteristics and interference effects of rotor-wing-fuselage combinations.

WIND TUNNEL MODEL

The wind tunnel model used in this investigation is shown in Figure 2. Representing a generalized compound helicopter, it is approximately nine feet long and is equipped with a four blade dynamically scaled rotor nine feet in diameter. Rotor power is supplied by a 19 horsepower electric motor through a reduction gearbox. The rotor controls are hydraulically actuated and are capable of duplicating all motions of a full scale control system. The model is equipped with three internal six-component strain gage balances which measure forces and moments on the rotor, wing and fuselage independently. A floating horizontal tail surface allows measurement of the mean tail downwash angle. In order to measure the various effects of wing size and vertical location, the model was constructed with a rectangular fuselage cross-section in the vicinity of the wing mounting points, thus allowing the mounting of any of the three wings

2

at any vertical location. The wings are mounted from side plates which are attached to a box structure suspended from the wing balance. The wing loads are thus measured independently of fuselage loads. The three wings have similar planforms with an aspect ratio of 6 and taper ratio of 1.5. The wing spans are equal to 30, 50 and 75 percent of rotor diameter and cover the range of interest for most compound configurations. Three wing vertical positions, determined by model geometry are 10.9, 15.7 and 20.4 percent of the rotor diameter below the rotor. Thus nine combinations of wing size and location, in addition to the wingless configuration were tested. The general arrangement and dimensions of the model are shown in Figure 3.

The fiberglass rotor blades were dynamically scaled about the three axes to allow simulation of forward speeds and rotor speeds which are twice the actual values. These blades were fully strain gaged to measure the affects of the wing upon vibratory stress. The "flight" conditions which were investigated are shown in Figure 4, a plot of rotor tip speed versus forward speed. The five test speeds simulate operation from 120 knots to high speed compound flight at 300 knots.

ANALYSIS OF TEST DATA

Effect of Rotor On Wings

The effect of rotor downwash upon wing loading and performance was investigated for the nine configurations throughout the speed range. As was anticipated, the most significant measured effect was a decrease in wing lift which was approximately proportional to the rotor momentum downwash. An example of this effect is shown for the large wing at 120 knots in Figure 5. The wing lift coefficient, C_{L_W}, is plotted as a function of rotor lift coefficient-solidity ratio, C_{L_R}/σ, for several values of fuselage angle of attack, α_f. In addition to the linear relationship between wing and rotor lift, it is seen that rotor trim condition affects the magnitude of the lift decrease. For example, at $C_{L_R}/\sigma = .04$ and $\alpha_f = 4$ degrees, an increase in collective pitch from 0 degrees, where the rotor is tilted rearward and near autorotation; to 8 degrees, where the rotor is tilted forward; results in an increase in C_{L_W} of .06. This is believed due to the change in rotor loading distribution and the corresponding change in orientation between the rotor disk and wing.

The linear decrease in wing lift may be expressed as a change in wing effective angle of attack. This effective rotor downwash angle is compared, for the large wing, with the value of the momentum downwash in the rotor disk in Figure 6. The average experimental rotor downwash

3

angle per unit $C_{L_R/\sigma}$ is presented as a function to forward velocity for the large wing at low, mid, and high positions. The downwash angle for the low wing is approximately equal to the momentum value and increases as the wing is placed nearer to the rotor. Expressing this angle as a linear function of the momentum downwash gives the expression

$$\Delta \alpha_w = K \frac{57.3\,\sigma}{2\,\mu^2} \left[C_{L_R/\sigma} \right] \qquad \text{(Eq. 1)}$$

The average experimental value of the constant, k, was determined for the medium and large wings and is shown in Figure 7 as a function of the nondimensional vertical separation between wing and rotor, Z/D. The effect of the downwash on the large wing is significantly larger than on the medium wing, and increases for both wings approximately linearly as the wing/rotor spacing is reduced in the practical range of interest shown.

Although the effect of rotor downwash on the total wing lift was expressed as a simple angle of attack change, the effect on wing drag was found to be more complex. An increase in rotor downwash caused an increase in wing drag due to the rearward inclination of the wing resultant force vector. When combined with the loss of lift, this resulted in a signficiant deterioration of the wing lift/drag ratio. An example of this effect is shown in Figure 8 for the large wing at 120 knots the lowest speed investigated. To obtain this plot, wing lift and drag coefficients were plotted against $C_{L_R/\sigma}$, and the results were crossplotted as shown. It may be seen that the decrease in L/D is due primarily to a large decrease in lift at nearly constant drag. This effect decreases rapidly with forward speed as the rotor downwash angle decreases. Consequently at high speeds, where a decrease in wing L/D would be critical, the effect is small.

In order to obtain a more complete picture of the rotor downwash effects, the medium wing was constructed with static pressure taps at 40 and 70 percent semi-span on top and bottom surfaces. The resulting static pressures were examined and the chordwise distributions integrated to obtain wing local normal force coefficients.

An interesting effect was obtained at 120 knots where the spanwise normal force distribution is shown in Figure 9 for the high and mid positions and several values of rotor lift. In the upper plot, three curves are shown for the high wing with no rotor, and for values of $C_{L_R/\sigma}$ equal to .033 and .063. The effect of the downwash is to decrease the lift on the starboard wing, beneath the advancing blade, without a large effect on the port wing. However, with the wing in the mid position, the lift is more symmetrical as shown in the lower plot. The downwash effect upon the low wing was also found to be symmetrical.

4

Effect of Wings on Rotor

A major portion of this investigation was directed toward establishing the effects of wing geometry and loading upon rotor performance and stresses. The model was initially tested without wings through the speed range and over a wide range of rotor operating conditions to obtain basic rotor characteristics. Comparison of the basic data with values measured in the presence of the wings revealed that the effect of any of the wings upon the rotor is small at speeds below 200 knots.

Figure 10 illustrates the effect of the large wing upon rotor lift and angle of attack at 120 knots. These data were obtained by trimming out first harmonic flapping with respect to the shaft. Thus the constant values of α_f are equivalent to equal tip-path plane angles of attack. The wing free stream angle of attack is equal to $\alpha_f + 4$ degrees because of the four degrees wing incidence. It may be seen that the wing, even at high angles of attack, causes only modest decreases in rotor lift. Similar data are shown for the large wing in Figure 11 and 12 for velocities of 200 and 300 knots respectively. At 200 knots, the decrease in C_{L_R}/σ is more pronounced, while at 300 knots, the interference effect is substantial. However, it should be noted that the large wing is oversized for cruise at 300 knots. The condition at $\alpha_f = 4$ degrees with four degrees incidence is equivalent to a wing lift more than twice the hovering lift capacity of the rotor.

The effect of the medium size wing upon the rotor is much smaller than that of the large wing. For example at 200 knots, Figure 13, there is no measurable loss of rotor lift at any condition. The effect of the medium and large wings upon rotor lift is summarized in Figure 14, a plot of the change in C_{L_R}/σ per degree change in wing angle of attack as a function of forward speed.

It is seen that the interference effect increases rapidly with forward speed, but that it is relatively large only for the large wing. Furthermore, since the rotor lift sensitivity with respect to changes in angle of attack also increases rapidly with forward speed, the wing induced loss in rotor lift is easily offset by a small cyclic pitch change.

Rotor blade vibratory stresses were measured at five flapwise, three chordwise and two torsion stations on one blade. Time histories and peak-to-peak values were recorded at all test conditions and analysis of a considerable portion of these data, including the large wing at the high position, has not revealed any significant effect of the wing on blade stresses.

5

Tail Downwash Angle

To investigate the downwash effects on a tail, a 0012 airfoil section with a span equal to 36 percent of the rotor diameter was mounted as a floating tail on the compound helicopter model. The integrated downwash angle at the tail was measured by means of a potentiometer which sensed the tail angle of attack. This angle was measured over simulated forward speeds from 120 to 300 knots, fuselage angles of attack, α_f, from -8 to +12 degrees and rotor lift coefficient-solidity ratios, C_{LR}/σ, from zero to 0.1.

The downwash angle resulting from the wing at the mid position and the fuselage is shown in Figure 15 as a function of α_f. Both theoretical * (Reference 2) and experimental values are included and the correlation for all three size wings is good. The measured angle for the fuselage alone is also shown. In Figure 16 the downwash angle resulting from the rotor is shown for forward speeds of 120, 200 and 300 knots as a function of C_{LR}/σ. The derivative of the downwash angle with respect to C_{LR}/σ varies inversely with the forward speed as would be expected from momentum considerations. The net angle predicted by the fully developed momentum flow can be checked, for example, at $C_{LR}/\sigma = 0.04$ and 200 knots. The calculated downwash angle is 2.6 degrees which compares with the measured value of 3.5 degrees including an effect of approximately 1 degree from the fuselage. Also shown in Figure 16 is the variation of the downwash angle with C_{LR}/σ including the effects of the small and medium wings at the mid position. At the zero rotor lift condition the angle for the medium wing is on the order of 4.5 degrees. The addition of the angle for the wing alone from Figure 15 and the angle for the rotor alone also gives approximately 4.5 degrees, when one degree is deducted to avoid double inclusion of the fuselage effect. For larger values of C_{LR}/σ this type of addition is no longer possible since the contribution of the wing to the net downwash angle decreases with increasing rotor loading. This effect is believed to be caused by the rotor downwash displacing the wing trailing vortices further below the tail, thus reducing their influence on the downwash angle. The curves show that with the small wing the downwash angle at the tail is essentially unaffected by the wing when C_{LR}/σ reaches a value of 0.06. Although operation of the rotor much beyond this point at 200 knots is not generally practical it can be seen that the medium wing curve is also tending toward a union with the rotor only curve.

* Because of the unusually large nondimensional distance of the tail behind the wing it was necessary to extrapolate the published data.

The results shown in Figures 15 and 16 are representative of the remainder of the tail downwash data, but may not be applicable to wing-tail configurations other than those used in this program.

Fuselage and wing balance measurements taken over a range of conditions with the three wings positioned at the high, mid and low points on the fuselage were reduced and compared with various published NACA test data on fuselage-wing combinations and no significant departure from those results was found. The complete analysis of these measurements will be given in the final program report.

ADDITIONAL RESEARCH

Currently being implemented under an AVLABS contract is a rotor-propeller interference investigation through the forward speed range to 300 knots. For this program dynamically scaled propellers will be mounted on the model in various configurations to obtain experimental stress and aerodynamic data necessary for correlation with theory and for the design of high performance rotary-fixed wing aircraft using propellers for auxiliary forward thrust.

Future studies with the compound helicopter model which would provide valuable data include:

a.   A repetition of a selected number of the test conditions reported in the present paper utilizing metal dynamic model rotor blade scaled for full scale Mach number. The results of this program could be compared with the present data to define the effects of compressibility on rotor-wing interference.

b.   An exploratory investigation of rotor instabilities including stall and classical flutter and torsional divergence. In addition transient rotor response due to step control inputs and angle of attack change could be studied.

CONCLUSIONS

Based on the preliminary analysis of data, the following conclusions were reached:

1.   The rotor induced downwash at the wing is approximately equal to the momentum downwash in the rotor disk. However wing size and vertical distance from the rotor are important parameters in accurately

7

determining the actual mean downwash value.

2.   In addition to the loss in wing lift caused by the rotor downwash, a small increase in wing drag occurs. The combined result is a decrease in the wing lift/drag ratio, at low speeds. However this effect decreases with forward speed and is small when wing performance becomes important.

3.   At pure helicopter speeds, the rotor downwash induces an unsymmetrical spanwise decrease in wing loading. The larger reduction in wing lift occurs beneath the advancing blade. This effect is largest for the high wing configuration.

4.   The effect of the wing is to decrease rotor lift. However the loss in lift is small at low speeds for all conditions. It becomes large only at high speeds with large wings at loading corresponding to extreme operating conditions and is not considered to be significant in the design of a compound helicopter.

5.   The presence of a wing has no significant effect on rotor blade stresses.

6.   The rotor induced downwash at the tail is approximately equal to the full developed momentum downwash in the absence of the wing. The contribution to the downwash at the tail induced by the wing, in the configurations tested, decreases rapidly as rotor lift is increased.

REFERENCES

1.   Rotor-Wing Fuselage Aerodynamic Interference Investigation, USAAML Contract DA44-177-AMC-203(T), February 1965.

2.   Silverstein and Katzoff, Design Charts For Predicting Downwash Angles and Wake Characteristics Behind Plain and Flapped Wings. NACA TR 648, 1940.
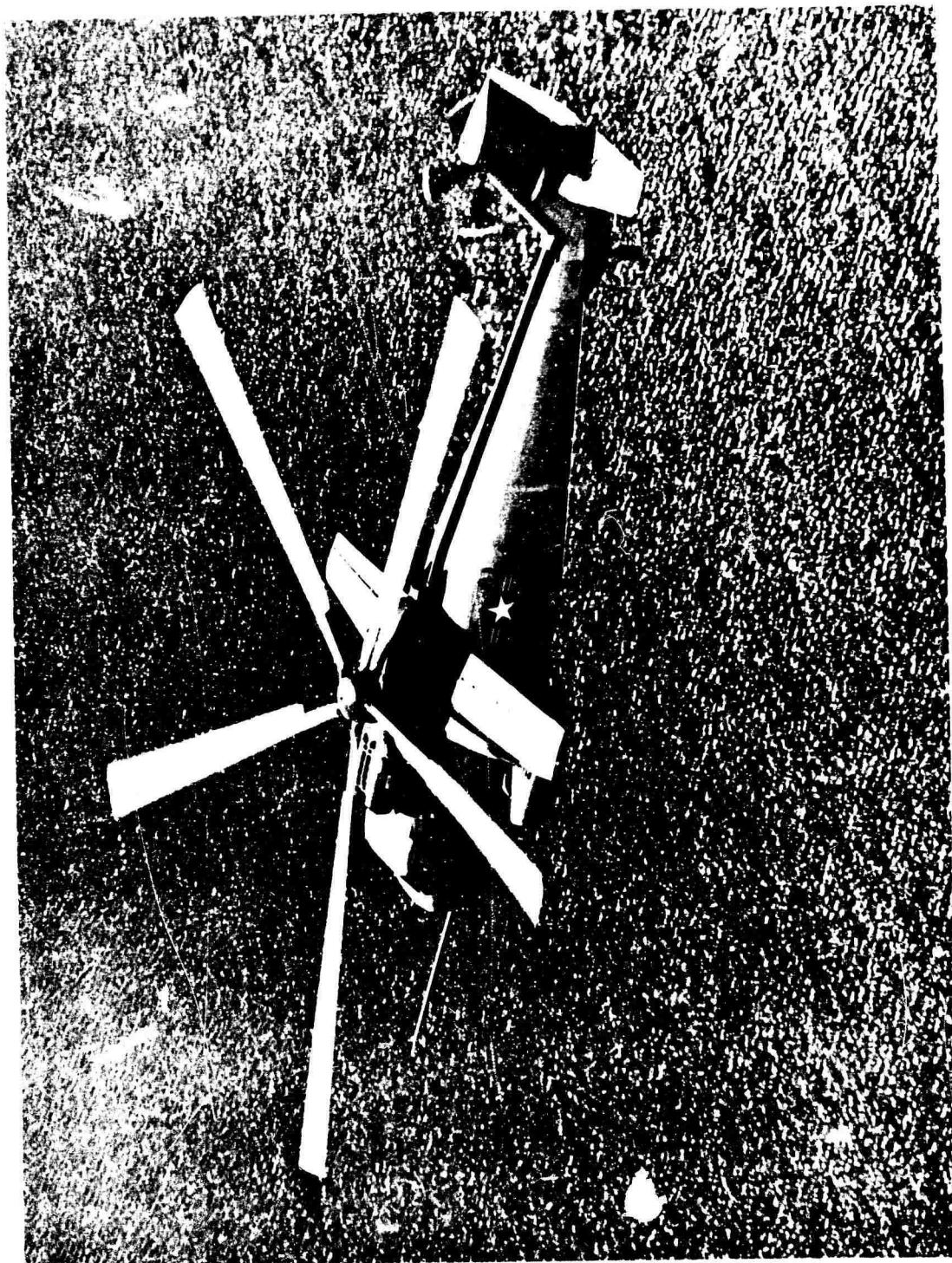
FIGURE 1. S-61F RESEARCH AIRCRAFT.
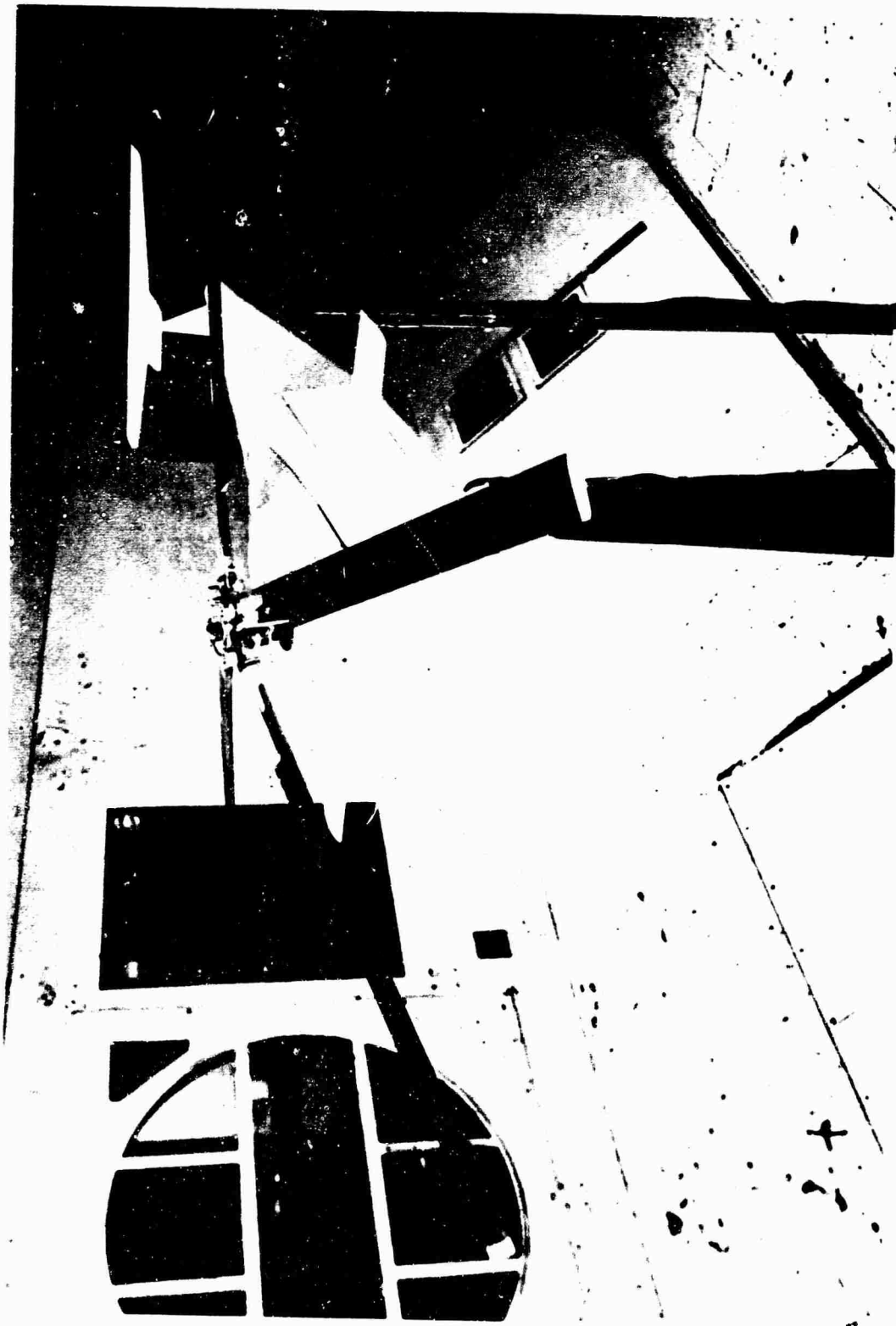
FIGURE 2. SIKORSKY COMPOUND HELICOPTER MODEL IN 18 FOOT WIND TUNNEL.

10

WING DATA

WING NO.	1	2	3
SPAN, IN	32.4	54.0	84.0
AREA IN²	175	486	1094
AR	6		
C$_{ROOT}$,IN	6.48	10.8	16.2
C$_{TIP}$,IN	4.32	7.20	10.8
AIRFOIL SECTION NACA 64₂415			

ROTOR DATA

RADIUS 54"	NO. OF BLADES 4
CHORD 4.24"	σ .010
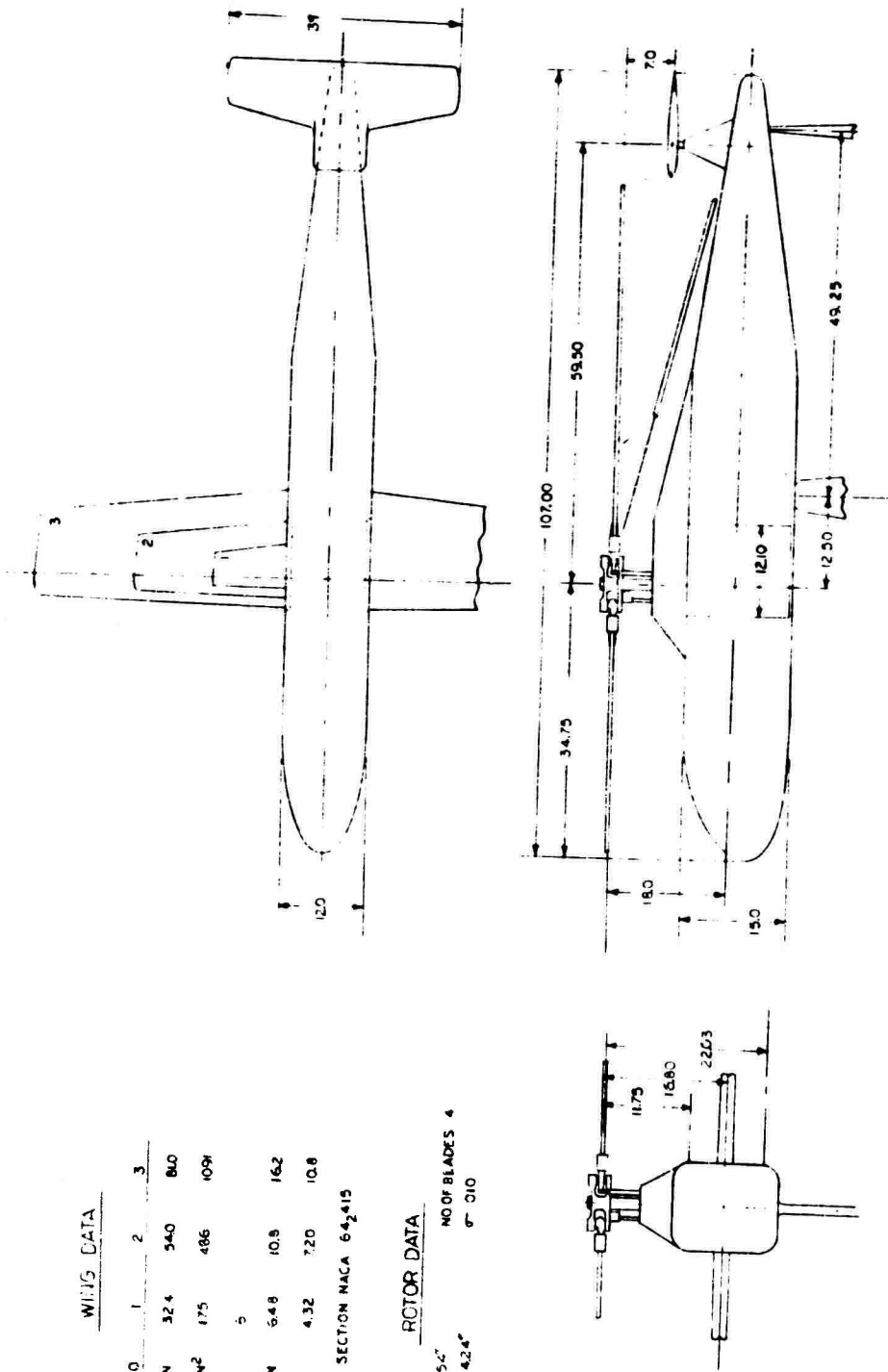
FIGURE 3. GENERAL ARRANGEMENT OF SIKORSKY COMPOUND HELICOPTER MODEL.

11
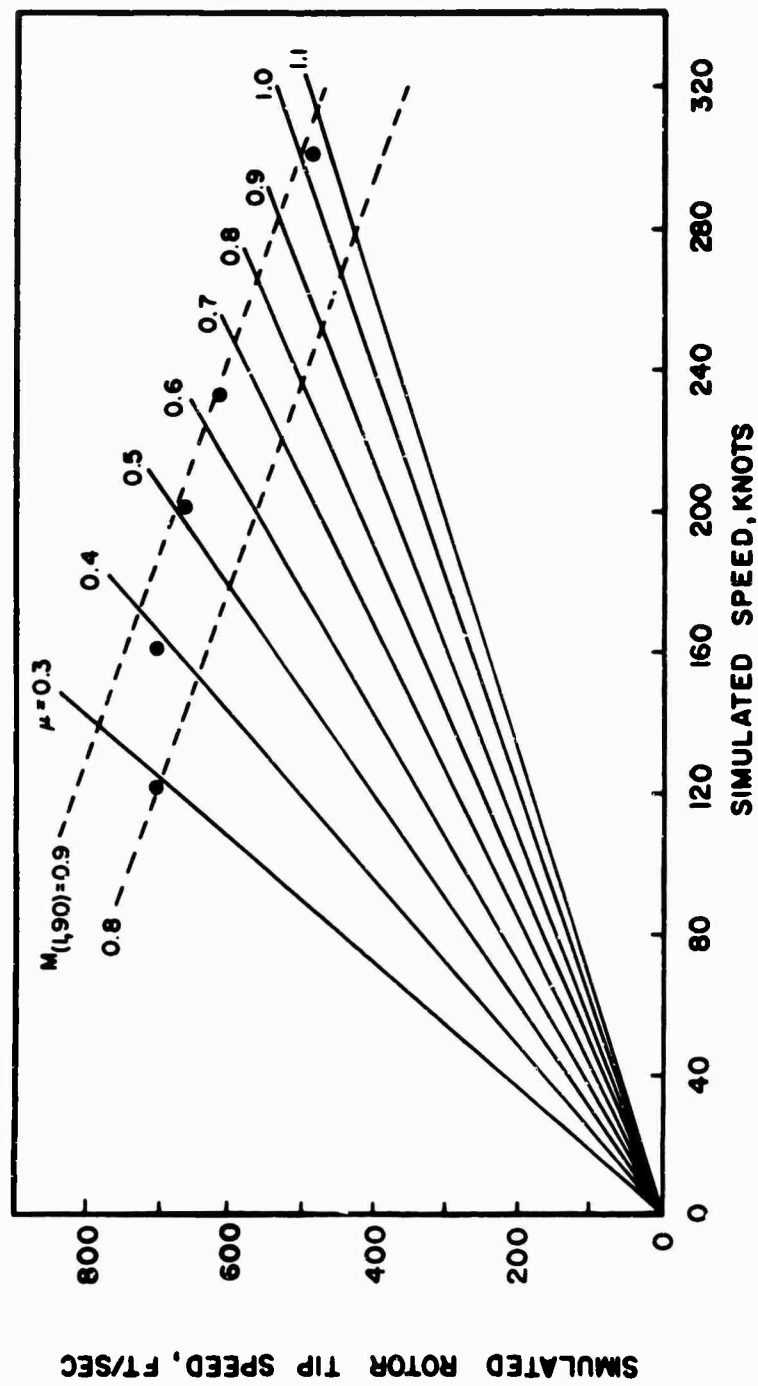
FIGURE 4. ROTOR TEST CONDITIONS.

12
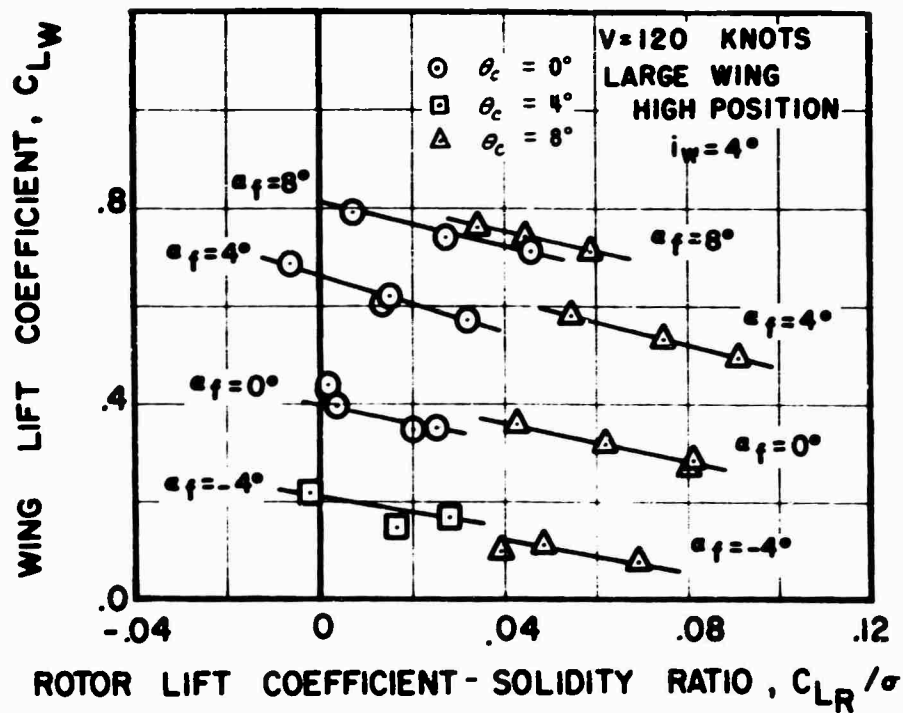
FIGURE 5. EFFECT OF ROTOR LIFT
ON WING LIFT.
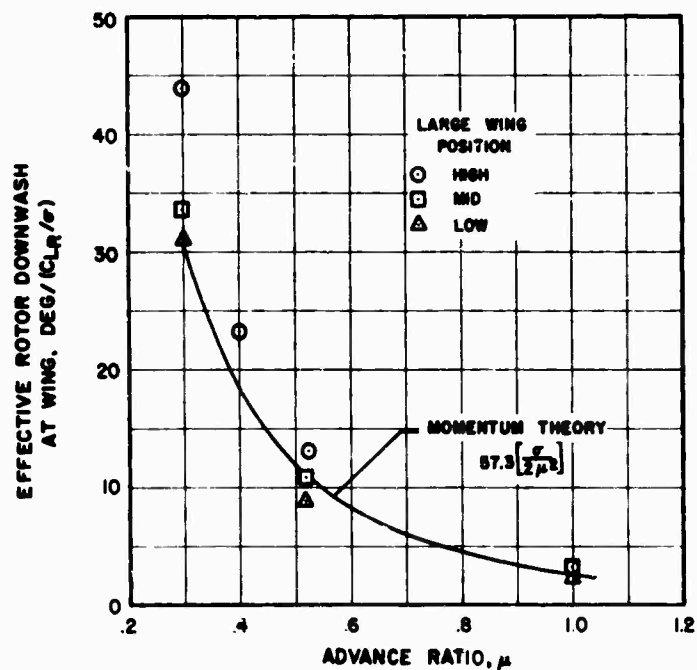
FIGURE 6. EFFECT OF FORWARD SPEED ON EFFECTIVE
ROTOR DOWNWASH ANGLE.

13
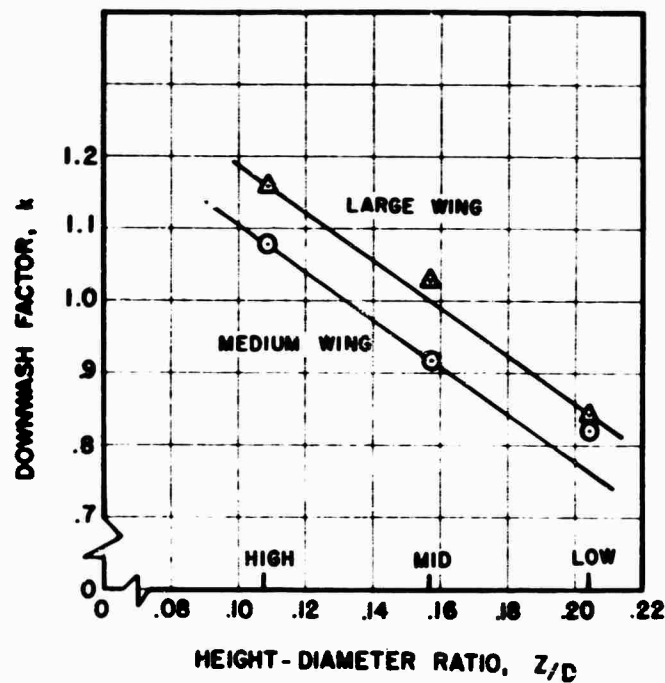
FIGURE 7. EFFECT OF WING POSITION
ON DOWNWASH FACTOR.
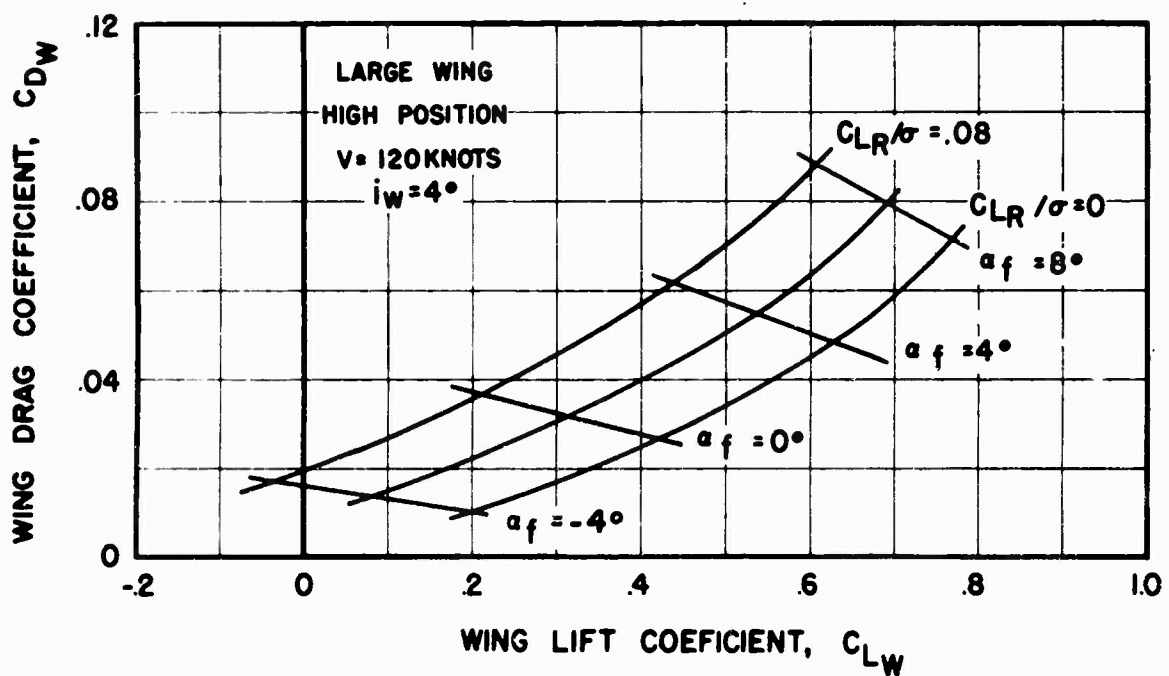
FIGURE 8. EFFECT OF ROTOR LIFT ON WING C_L AND C_D.

14
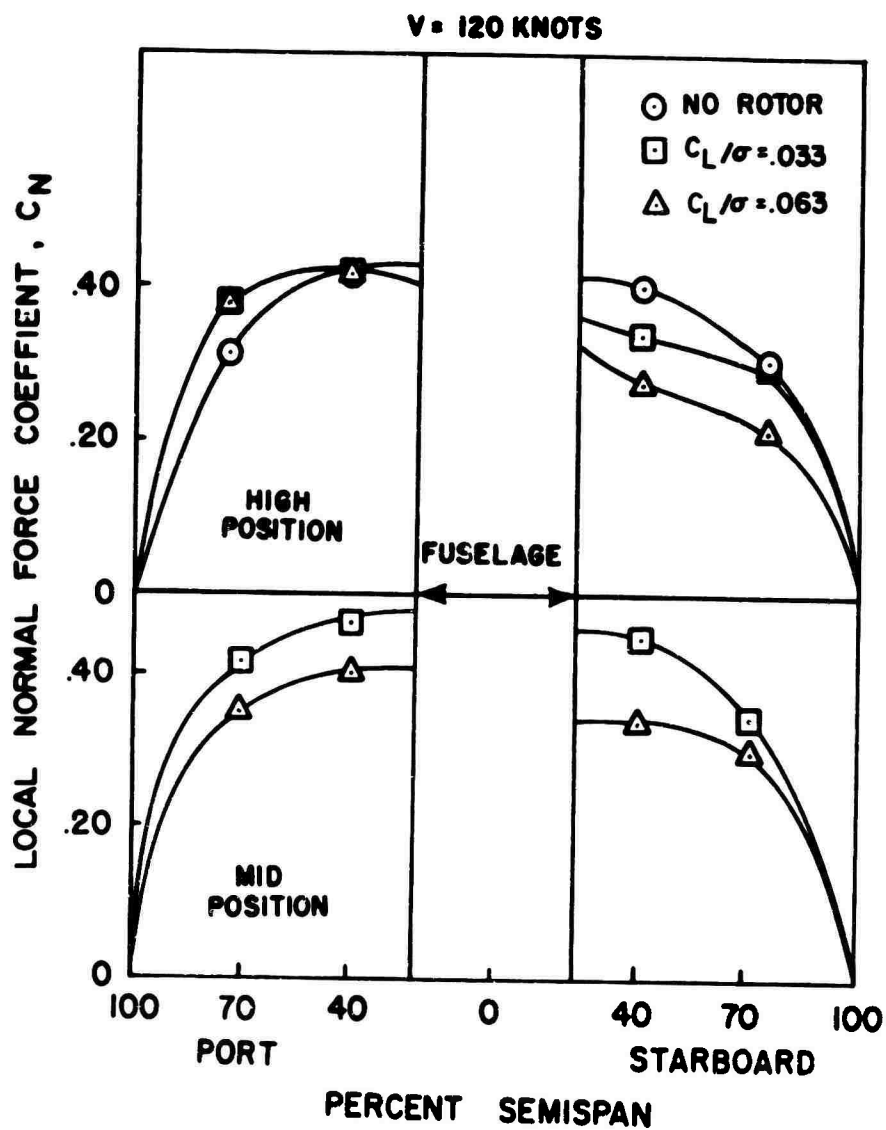
FIGURE 9. SPANWISE NORMAL FORCE DISTRIBUTION ON THE MEDIUM WING AT 120 KNOTS.
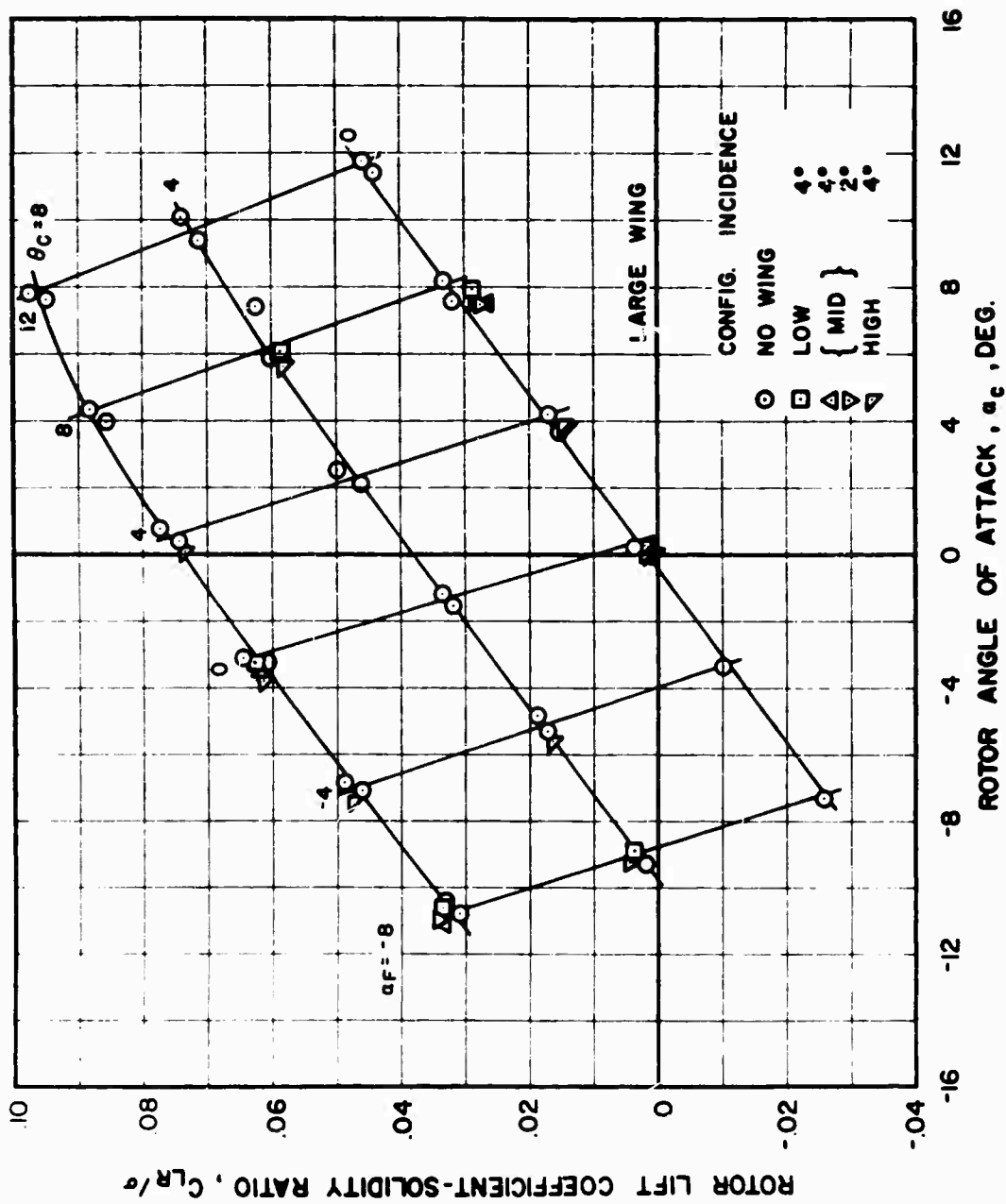
FIGURE 10. ROTOR LIFT COEFFICIENT - SOLIDITY RATIO
V.S. ROTOR ANGLE OF ATTACK AT 120 KNOTS.

16
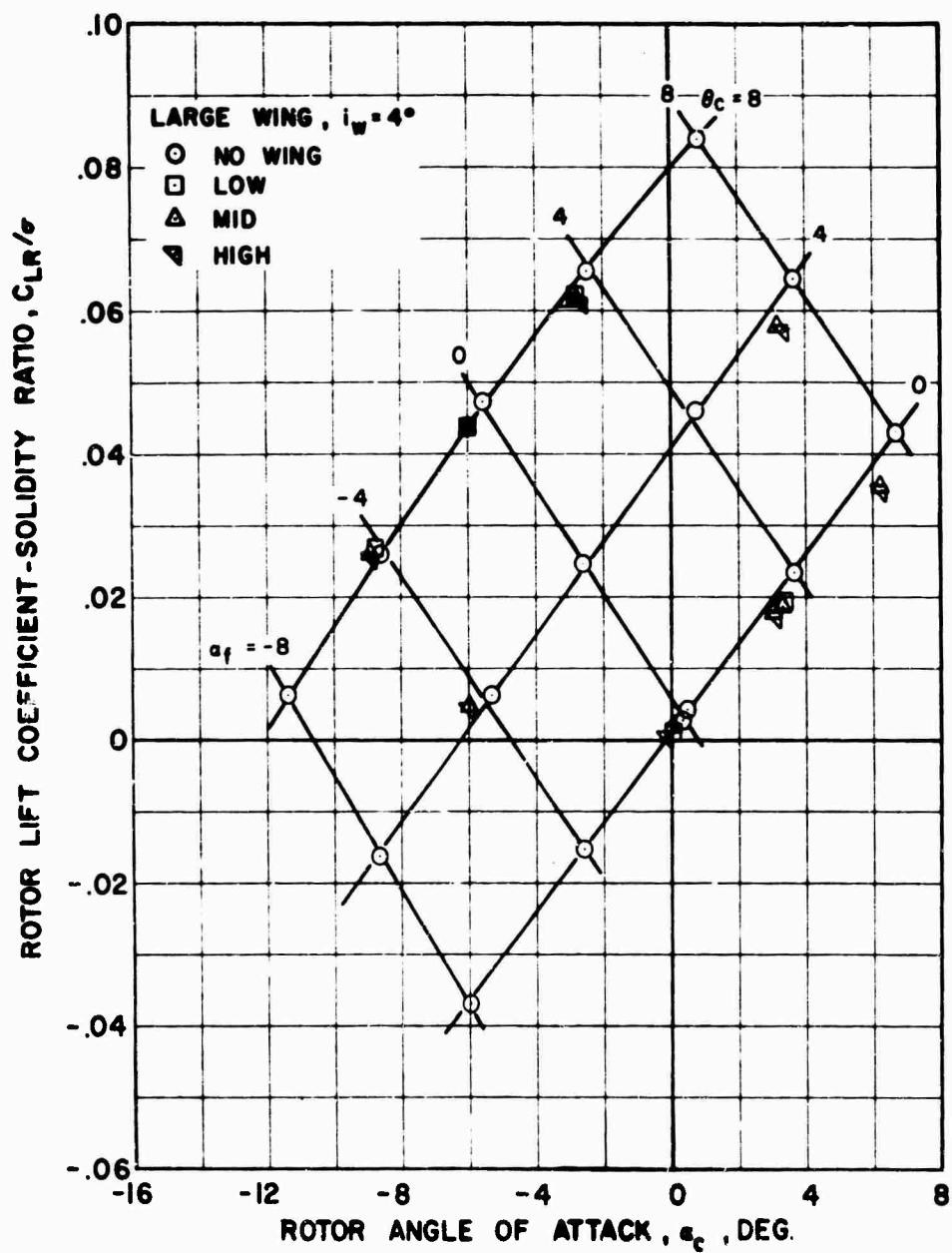
FIGURE II. ROTOR LIFT COEFFICIENT-SOLIDITY RATIO
V.S. ROTOR ANGLE OF ATTACK AT 200 KNOTS.
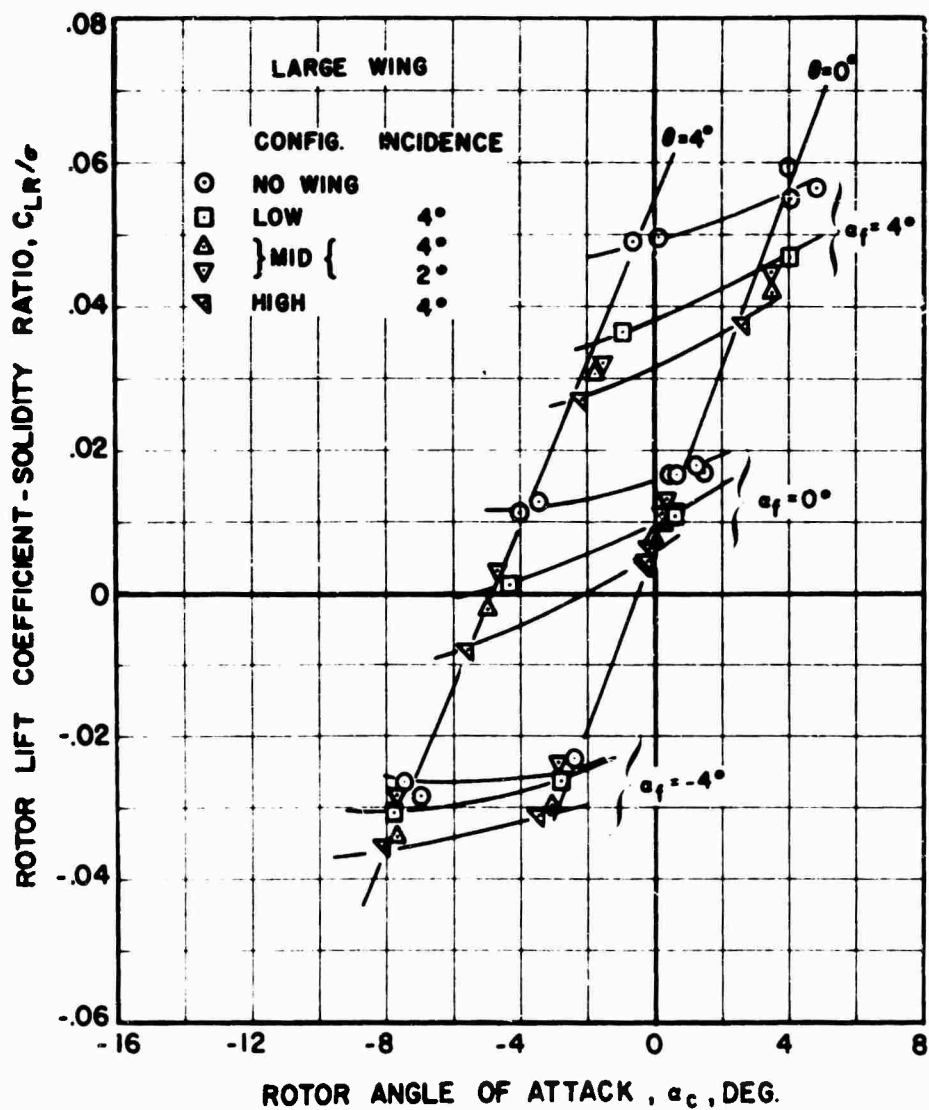
FIGURE 12. ROTOR LIFT COEFFICIENT-SOLIDITY RATIO
V.S. ROTOR ANGLE OF ATTACK AT 300 KNOTS.

18
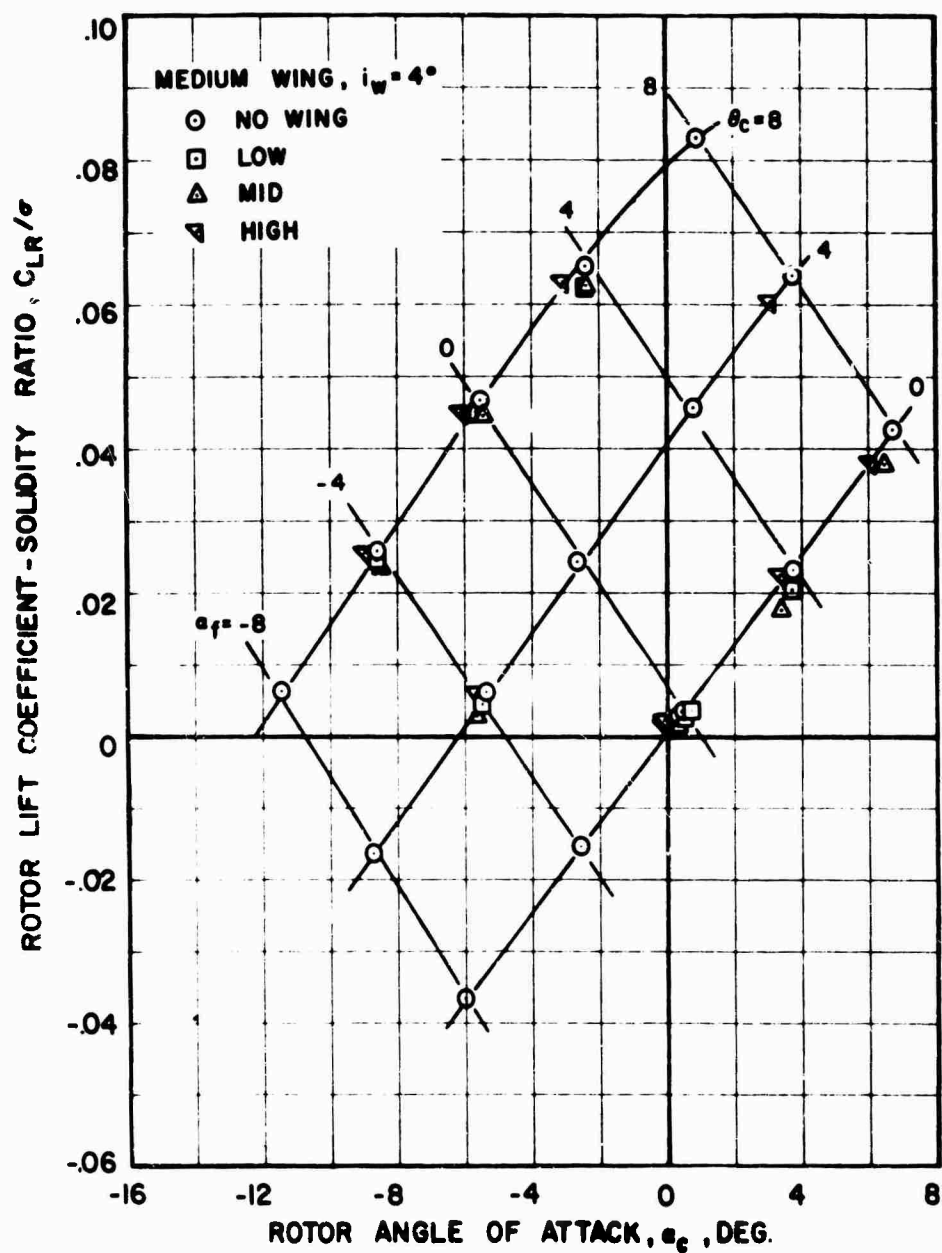
FIGURE 13. ROTOR LIFT COEFFICIENT- SOLIDITY RATIO
V.S. ROTOR ANGLE OF ATTACK AT 200 KNOTS.
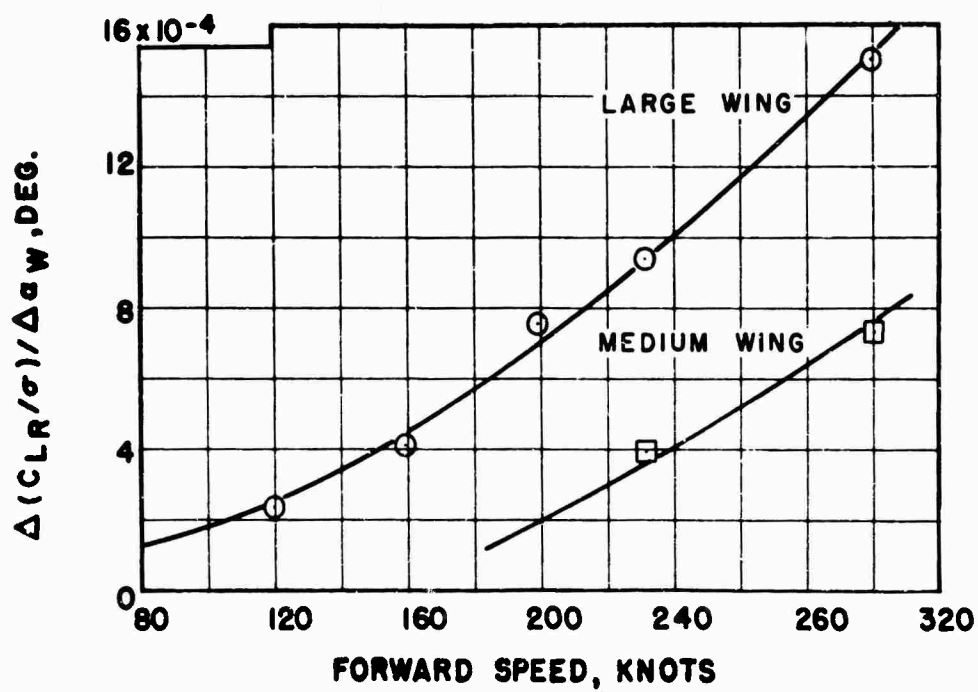
FIGURE 14. EFFECT OF FORWARD SPEED ON CHANGE IN
ROTOR LIFT PER UNIT CHANGE IN WING ANGLE OF ATTACK.
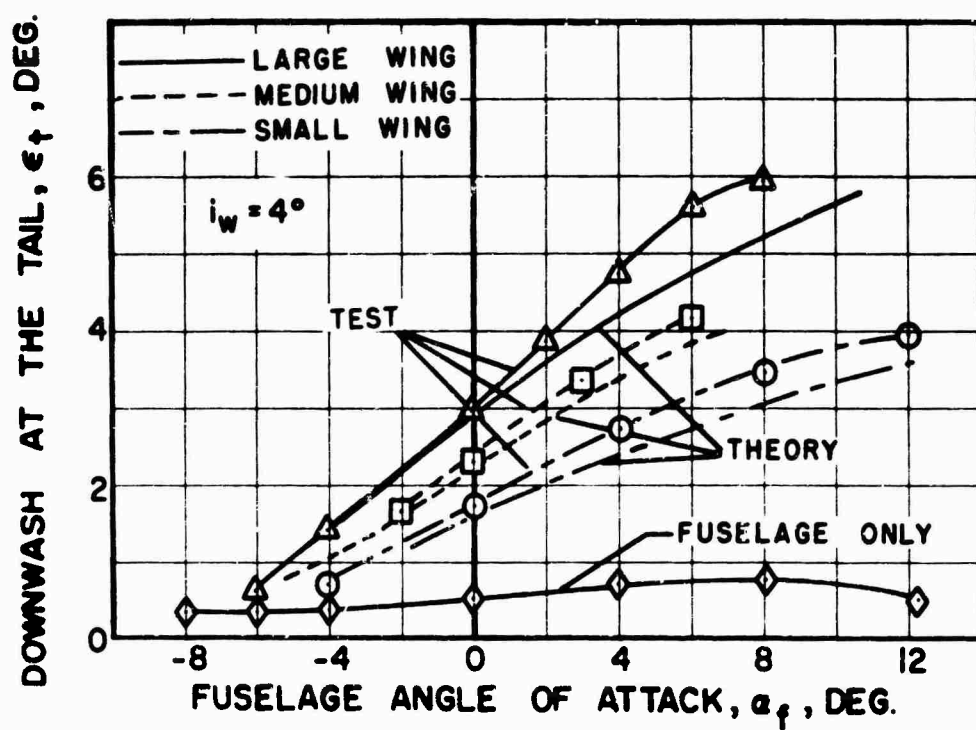
FIGURE 15. EFFECT OF FUSELAGE ANGLE OF ATTACK
ON DOWNWASH ANGLE AT THE TAIL.
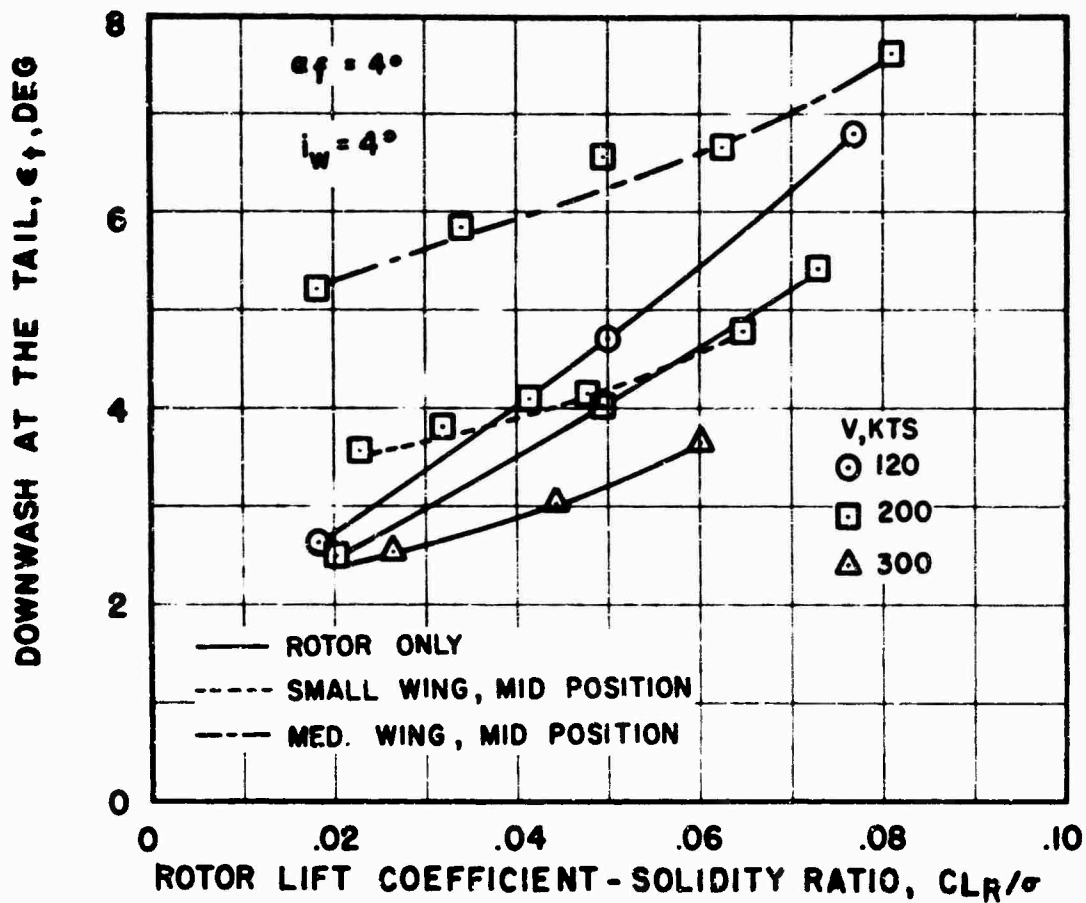
FIGURE 16. EFFECT OF ROTOR LIFT ON DOWNWASH
ANGLE AT THE TAIL.

MAXIMUM LIFT COEFFICIENT FOR STOL AIRCRAFT:

A CRITICAL REVIEW

by

D. C. Whittley

Chief Research Engineer (Aerodynamics)
The De Havilland Aircraft of Canada, Limited,
Downsview, Ontario, Canada.

INTRODUCTION

Various investigators have studied wing theory in an attempt to establish the absolute maximum lift coefficient which can be generated from a given wing of finite aspect ratio   This problem is an important one to those engaged in STOL technology because take-off and landing performance depends vitally upon it.   Also, it is important to establish the "absolute" performance potential, so that reasonable objectives can be set for research programs and proper conclusions drawn from design studies.

The present paper reviews the previous work on the subject and draws different conclusions in some respects.   Many of the ideas expressed are not regarded as absolute but are presented to promote discussion.

STATEMENT OF THE PROBLEM

It is well known that $C_{L_{max}}$ is a parameter of prime importance in the calculation of take-off performance.   It could be said that wing stall usually occurs prematurely because of boundary layer and viscous effects

so that the full potential of the wing is seldom attained in practice. However, various boundary layer control systems (suction and blowing) provide a means of largely overcoming the adverse viscous effects so that the full potential of the wing can be more nearly attained. The questions which arise are these: what is the full potential lift of a wing and how nearly can it be attained (even with the help of boundary layer control devices)? And, again, what is the drag (particularly induced drag) associated with this lift? Further to this, the question of super-circulation is considered briefly.

Various investigators have attempted to predict the limiting value of $C_{L_{max}}$ [1-5] while others have used these predictions to obtain absolute potential performance of STOL aircraft (for example, Sutcliffe, [6] and Johnston & Saint, [7]. All the investigators [1-5] who have developed "large angle" theories suggest that the absolute value of $C_{L_{max}}$ on a wing depends linearly on aspect ratio. That is, $C_{L_{max}}$ = (constant) A. The value of the constant arrived at varies from 0.855 to 1.94 and so gives very wide limits for the possible absolute value of $C_{L_{max}}$.

Also, it is quite apparent that formulae of this kind tend to quite astounding limits, as aspect ratio becomes large. For instance, the form used by Sutcliffe states that for an aspect ratio of 20, the maximum potential aerodynamic lift coefficient is 31.4!

The present note suggests that expressions of this kind do not give a sensible guide to the potential value of $C_{L_{max}}$ (except at quite low values of

2

aspect ratio outside the range of our particular interest) and suggests another limit which may be more realistic.

BRIEF REVIEW OF LARGE ANGLE WING THEORY

Various investigators have made theoretical predictions of the lift generated by finite wings at high incidence [1 - 5]. These theories are unanimous in that they predict a limit to the lift which can be achieved. This limit arises simply because, at high α , the local force vector is inclined so far backward by the local downwash that the ability of the wing to produce lift becomes seriously impaired, (the direction of the lift force being, by definition, at right angles to the distance up-stream relative wind).

For wings with elliptic spanwise loading some limiting values of lift have been given as follows:

$$C_L = .855 \ A \quad [2][3]$$
$$C_L = 1.21 \ A \quad [4]$$
$$C_L \doteq 1.90 \ A \quad [1][5]$$

Analysis shows that the differences between these various forms depend upon the assumptions which are made concerning the final inclination of the vortex wake at infinity down stream.

The first expression is based on the assumption that the vortex sheet remains flat (i. e. it does not roll up) and has a transversal velocity equal to Γ_o/b ; in this case the vortex sheet follows a convex path, the downwash at infinity down stream being greater than that at the wing.

3

In the second expression, it is assumed that the vortex sheet remains flat and follows a straight path such that the downwash at infinity down stream is the same as that at the wing. This case arose because it happened to represent a convenient mathematical approximation but it has only weak physical justification.

The third equation results from the assumption that the vortex sheet rolls up and finally attains a stable configuration in the form of two symmetrical vortex cores of opposite and equal circulation Γ_0 ; the distance between their centers being given by $\pi b/4$ where 'b' is the wing span. The transversal velocity at infinity down stream is less than that at the wing and the vortex sheet, therefore, follows a concave path as it moves down stream. The transversal velocity in this case is equal to $\left[\dfrac{2}{\pi^2} \cdot \dfrac{\Gamma_0}{b} \right]$

This latter case has ample physical justification and is equally good in terms of mathematical accuracy. It would, therefore, appear to give the preferred equation, namely, limiting $C_L \doteq 1.90\ A$.

The derivation of this equation was first given by Helmbold in 1956[5]. In retrospect, it would appear to be a brilliant piece of manipulation. The data of [3][4] which came four or five years later appear very much as an anti-climax, particularly since the first and second equations can also be derived directly from Helmbold's analysis (See Appendix "A").

The work of Cone (1961) elaborates on the "rolling up" process and describes it in much more mathematical detail so as to provide general

4

information about the downwash field in the vicinity of the empennage. He arrives at substantially the same result as Helmbold with regard to the limitation of maximum lift coefficients; namely, $C_L = 1.94 A$.

Appendices "A" and "B" deal with the large angle wing theory in more detail. Appendix "C" investigates the implications of large angle theory on the interpretation of wind tunnel test data, while Appendix "D" speculates about the possible ratio between translational and rotational energy in the wake.

THE WORK OF NICHOLS AND SUTCLIFFE

Sutcliffe [6] (page 191) reviews the simple theory put forward by Nichols [9]. It is a momentum concept in which the lift and drag of a wing of finite aspect ratio is related to the downwash, $\mathcal{E}_w$, at the wing. This would appear to be incorrect because lift and drag depend upon the final changes experienced by the associated mass and not on the local changes which occur at the wing. Consideration should be given to the final conditions of the flow at infinity down stream to obtain a correct result of simple momentum theory, (See for example, [10]). Nichols' theory, therefore, cannot be considered very seriously. Comments to this effect were made by the writer on page 231 of [6] as part of the discussion to Sutcliffe's paper. However, errors in drag are not very great, provided C_L/A is kept small; for example, Sutcliffe limited $C_L/A \leqslant 0.6$.

Nichol's equations are given for reference, as follows:

$$C_L = \frac{\pi A}{2} \sin \mathcal{E}_w \tag{1}$$

$$C_{D_i} = \frac{\pi A}{2} \left[1 - \cos \mathcal{E}_w \right] \tag{2}$$

whereas more correct results have been derived from simple momentum theory as follows: (See [6][10])

$$C_L = \frac{\pi A}{2} \sin \mathcal{E}_\infty \tag{3}$$

$$C_{D_i} = \frac{\pi A}{2} \left[\frac{\sin^2 \mathcal{E}_\infty}{2} \right] \tag{4}$$

One obvious objection to these simplified forms of momentum wing theory is that the energy dissipated in the wake is assumed to be purely translational. In fact, we know that the wake takes the form of a strong contra-rotating vortex pair having some translational motion, so that a large part of the energy is bound up in this rotational motion.

A PROPOSED LIMIT TO MAXIMUM LIFT

It has been pointed out that Helmbold's limit to maximum lift ($C_L = 1.90$ A) yields exceedingly high values of lift coefficient for moderate values of aspect ratio (say A = 10).

A more practical limit to the lift of a wing might well be obtained by assuming that the local flow at the wing is deflected to 90°; values greater than this being arbitrarily considered extreme. In effect, this corresponds to an unflapped wing at 90° angle of attack in potential flow. In practice, similar flow conditions would more probably be achieved with a flap angle of 75° with the aerofoil at 30° incidence.

This suggested limit also corresponds to the condition when the two

6

stagnation points approach coincidence (if $A = \infty$), and any further increase in circulation would cause the stagnation points to leave the surface. Under these circumstances, fluid must circulate right around the aerofoil, which it is not likely to do in practice if the trailing edge is sharp. Thus, a second limitation to lift could be considered; namely, the value of lift achieved when the stagnation points coincide. Such a limit would permit local flow angles in excess of 90° (for $A < \infty$). On the basis of these suggestions, it is possible to obtain expressions for limiting C_L. The 'lift' of an elliptic wing of finite aspect ratio may be written:

$$C_L' = 2\pi \ (1 + t/c) \sin (\alpha - \mathcal{E}_w) \tag{5}$$

where $(1 + t/c)$ is an approximate correction factor to the sectional lift-curve slope to account for wing thickness chord ratio (t/c). The 'lift', L' (to which C_L' corresponds) acts at right angles to the local free stream velocity). Let $\alpha = 90^\circ$ represent a practical limit to lift, then

$$\text{limiting } C_L' = 2\pi \ (1 + t/c) \cos \mathcal{E}_w \tag{6}$$

Now following an analysis similar to that of Appendix "B":

$$\text{Local velocity} = V \cos \mathcal{E}_w \tag{7}$$

$$\text{Also lift } L \quad = L' \cos \mathcal{E}_w \tag{8}$$

$$\text{Therefore, } C_L = \frac{L'}{\frac{1}{2}\rho V^2 \cos^2 \mathcal{E}_w S} = \frac{C_L}{\cos^3 \mathcal{E}_w}$$

and equation (6) becomes:

$$\text{limiting } C_L = 2\pi \ (1 + t/c) \cos^4 \mathcal{E}_w \tag{9}$$

giving:

$$\frac{\text{limiting } (C_L/A)}{\cos^4 \mathcal{E}_w} = \frac{2\pi \ (1 + t/c)}{A} \tag{10}$$

7

But $\mathcal{E}_w$ is a known function of C_L/A (See Figure A 2, Appendix "A"), and therefore, $\dfrac{2\pi\ (1 + t/c)}{A}$ plots uniquely against C_L/A according to equation (10) (See Figure 1). The variation of limiting C_L with aspect ratio and thickness chord ratio is shown in Figure 2, this being based on a lift-curve slope of $2\pi\ (1 + t/c)$ according to equation (5).

If coincidence of the stagnation points is used as a basis for limitation of lift, then the average local flow direction close to the wing exceeds 90° and an alternative expression for limiting C_L is given as follows:

$$\text{limiting } C_L = 2\pi\ (1 + t/c) \cos^3 \mathcal{E}_w \tag{11}$$

The implications of such an assumption are also shown in Figure 1.

It should be noted that the previous derivations have dealt with the limiting lift without physical chord extension devices.

Leading edge devices are an essential part of high lift technology (nose blowing, slats, etc.). Leading edge slats may appear to give a chord extension but seldom give an effective increase in wing area. They do, however, represent a very powerful means of extending the lift curve to higher angles of attack.

Flap extension schemes, such as the Fowler flap, have been used at moderate values of lift coefficient in spite of the large nose down pitching moment which they generate. However, since tail lift coefficient required to trim increases linearly with wing lift coefficient, it seems unlikely that high lift flaps using large flap extensions will find a place in STOL technology.

8

THE WORK OF CLARENCE D. CONE

Cone [1] makes a lengthy analysis of the vorticity in the wake and obtains a limit to lift coefficient given by:

$$CL_{max} = 1.94 A \qquad (12)$$

Once again, we note that other investigators, using similar concepts, have arrived at formulae of similar form but with a different constant. For example, both Ribner and Hancock give $C_L = 0.855 A$. The relative merits of these various expressions are discussed in the section on Large Angle Wing Theory, and in Appendix "A".

However, Cone does recognize that, in the limit, expressions such as equation (12) yield unrealistic answers in attempts to provide a more practical limit for wings of aspect ratio greater than 6.5. This he gives in [1], Page 31, as $CL_{max} = 4\pi$. Cone chose, as a limiting factor, the conditions which cause front and rear stagnation points to coincide, and considers a Joukowski profile as obtained by conformal transformation of a circle of radius 'a' with the chord of the profile being given as 'c'. He then gives an expression for lift as:

$$C_L = 8\pi \ a/c \ \sin \alpha \qquad (13)$$

This equation happens to be true for many (if not all) profiles which have been transformed from a circle of radius 'a' to a profile of chord 'c'.

Cone then goes on to state that the maximum value of a/c is 1/2, and so for this case: $\qquad C_L = 4\pi \sin \alpha \qquad (14)$

9

which in the limit yields $C_{L_{max}} = 4\pi = 12.6$.

The first thing we note here concerning equation (14) is that for small angles the lift-curve slope tends to 4π (rather than the more familiar value of 2π). On further investigation it is found that the symmetrical Joukowski aerofoil can be obtained in a full range of thickness/chord ratios. At one extreme it becomes a flat plate for which $a/c = 1/4$ (a well known result); at the other end of the range the transformation degenerates to a one to one correspondence, and the flow round the circle of radius 'a' remains unchanged. It is this case for which $a/c = 1/2$.

It would appear that Cone unwittingly chose this rather uninteresting case to obtain equation (14) - it simply expresses the lift on a circular cylinder as the stagnation points move toward one another. The lift coefficient corresponding to coincidence of the stagnation points on a circular cylinder is well known to be equal to 4π.

Cone limits the aerofoils lift coefficient of aspect ratios greater than 6.5 to $C_{L_{max}} = 4\pi$. It would seem that a value of 2π would be closer to reality for those engaged in the design of conventional types of aircraft. If limiting $C_L = 2\pi$ is accepted as a more realistic limit, then vortex considerations would limit the lift attainable at values of aspect ratio less than 3.3. (In other words, the formula $C_{L_{max}} = 1.94\,A$ would not apply above an aspect ratio of 3.3.) The use of such relationships should, therefore, be avoided in take-off calculations for conventional STOL transport

10

aircraft. Similarly, the "complete" induced drag polar shown by Cone [1], Figure 23, and discussed by Schairer, has little meaning in this context, although it might have a bearing on the Concorde, for example.

Figure 25 of Cone's report further substantiates the verity of the standard form of the induced drag equation $C_{D_i} = C_L^2/\pi A$, up to the maximum values of lift that are likely to be achieved in practice, provided, once again, that we confine attention to a moderate or high aspect ratio wing.

OTHER LIMITING FACTORS

It has been suggested, that a practical limitation to lift on a wing of moderate aspect ratio would occur when the local flow deflection reachs a value of 90° or that, in any case, it is not likely to exceed a value corresponding to coincidence of the stagnation points. Either of these conditions would appear to be quite extreme when one tries to visualize the corresponding flow patterns round the wing, and so, the useable value of lift is likely to be somewhat less. Also, lift limitations would be imposed for other quite different reasons; these are briefly:

Effect of Fuselage

Lift coefficients are normally based on gross wing area and there will be a 'lift loss' due to the blanking effect of the fuselage. Lift will not be completely lost in this region but will fall far below the peak potential as compared to other sections of the wing.

11

Effect of Trim

High lift coefficients usually create large nose-down moments, and a significant down load on the tail is then required to trim the aircraft. This down load detracts from the overall lift coefficient which would otherwise be achieved.

Part-span Flaps

It is not always convenient to employ full-span flaps. Although ailerons may be drooped, they seldom are as effective as the flap for two reasons: first, in order to retain roll effectiveness, droop angles are often limited to approximatley 40°; secondly, it is not always possible to incorporate quite such exotic high lift devices in the aileron (as compared to the flap) because the aileron is required to serve a double function. Once again, the lift tends to fall below the maximum potential value.

Effect of Flap Drag

A very large flap angle often produces a large drag: this hinders take-off and can also cause embarrassment in the event of a single engine failure. Consequently, it often turns out that the 'optimum' flap angle for take-off is considerably less than maximum.

Use of B. L. C.

It becomes increasingly costly in terms of air supply to maintain attached flow at large flap angles when using conventional blowing for boundary layer control. Once again, it may be desirable to restrict the

12

flap angle or settle for conditions in which the flow over the flap is fully attached.

No attempt has been made to estimate the loss of lift due to such effects since each design will differ and must be considered on its own merits. It is, nevertheless, interesting to note that large scale experiments have been carried out on a transport type aircraft which employed quite powerful B. L. C. flaps. The maximum lift coefficient reported with a flap angle of 70° at $\alpha = 13^{\circ}$ was approximately 3. 0 [12].

SUPERCIRCULATION AND THE JET FLAP

In the previous sections, consideration has been given to the maximum lift coefficient which can be achieved on a wing with 'potential" flow. It was assumed that potential flow conditions could be closely attained by means of conventional flap blowing schemes, together with some form of leading edge device. The amount of flap blowing was assumed to be just sufficient to meet the requirement ($C_{\mu \ critical}$) so that supercirculation effects were not significant.

Wing Lift with Jet Flap

If a jet flap (or augmentor wing) scheme is used, then the flap is said to be "over blown". This is the condition known as supercirculation and large values of lift coefficient can now be achieved that are in excess of the limit given by equation (9). The reasons for this can be described in various ways; one is to state that the lift of a two-dimensional wing depends

13

upon the circulation, which, from a mathematical point of view, is distributed along the wing chord in such a manner as to satisfy the boundary condition (zero flow normal to the wing surface). In the case of the jet flap, a jet sheet extends behind the wing and sustains a pressure change across it. Circulation in the field now extends along the wing chord and along the jet sheet so that the total integrated lift on the wing ($\Sigma \rho u \Gamma$) can now be considerably greater than for the aerofoil without jet sheet.

The variation of lift coefficient with jet strength and jet angle has been predicted by Spence [8] for a two-dimensional jet augmented flap. This theory has been reasonably well substantiated by experiment [11], and if anything, the lift tends to exceed the prediction. The jet flap in three-dimensions has been considered theoretically by various investigators, including Maskell & Spence [13]. The limitations to lift which might apply in this case are not easy to predict because the problem is now further complicated by the presence of the jet sheet. The extension of the work by Cone to include the effect of a jet sheet would be of great interest in this regard.

In the absence of an adequate theory, one might be permitted to speculate as follows:

One of the previous limits for the case without jet sheet was set by coincidence of the two stagnation points. This gave a limit to lift coefficient of 2π (approximately) for a thin aerofoil of infinite aspect ratio, but as

14

already indicated. this will no longer apply.

The equation 6-33 (c)[11] quotes Strand to give the following expression for lift of a jet flapped wing:

$$C_{L_T} = 2\pi \ \sin \alpha \ + (3.9 \ C_j^{\frac{1}{2}} + C_j) \sin (\theta + \alpha)$$

where θ is the jet angle relative to the chord line and the theory has been extended to apply for large angles of deflection.

Lift coefficient would reach a maximum for $\alpha = 90^O$, $\theta = 0^O$. Physically this is an unrealistic condition and a more realistic case is arbitrarily suggested as $\alpha = 30^O$, $\theta = 60^O$, giving $(\theta + \alpha) = 90^O$.

Thus, $(C_{L_T})_{max} = \pi + (3.9 \ C_j^{\frac{1}{2}} + C_j)$ having an aerodynamic lift component of $(\pi + 3.9 \ C_j^{\frac{1}{2}})$ as compared to 2π, approximately, without a jet sheet. This suggests an increase of about 40% in the aerodynamic lift of a two-dimensional jet flap with $C_j = 2$ as compared to the potential lift of a wing without jet sheet.

Wing Drag With Jet Flap

Consideration of the downwash at infinity down stream and the corresponding magnitude of the associated mass (according to momentum wing theory) leads to a reconsideration of the induced drag of a wing with jet flap.

The well known result given by Maskell [13] can be derived as follows:

Assuming that the jet itself is subject to the influence of the vortex system, it will acquire a downward velocity at infinity down stream equal to

15

that of the associated mass.

Then lift $= \rho \left(\dfrac{\pi b^2}{4} \right) V_0^2 \sin \mathcal{E}_\infty + M_j V_j \sin \mathcal{E}_\infty$

giving $C_{L_T} = \left(\pi A + 2 C_j \right) \dfrac{\sin \mathcal{E}_\infty}{2}$

Also, equating work done to energy in the wake,

$D_i V_c \doteq \dfrac{\rho}{2} \left(\dfrac{\pi b^2}{4} \right) V_0 \left(V_0 \sin \mathcal{E}_\infty \right)^2 + \Delta T V_0$

where ΔT is the thrust loss due to deflection of the jet sheet far below the wing.

$\Delta C_T = (1 - \cos \mathcal{E}_\infty) C_j \doteq \dfrac{\sin^2 \mathcal{E}_\infty}{2} C_j$ for $\mathcal{E}_\infty$ small

Thus, $C_{D_i} = \dfrac{\sin^2 \mathcal{E}_\infty}{4} \left(\pi A + 2 C_j \right)$

giving $C_{D_i} = \left(\dfrac{C_{L_T}^2}{\pi A + 2 C_j} \right)$

Alternatively, and in a similar manner, the results of Appendix "D" can be used to obtain a different relationship between lift and drag of a jet flapped wing with elliptic spanwise loading. The associated mass is now larger by a factor $\dfrac{\pi^2}{2}$, the downwash at infinity down stream less by a factor of $\dfrac{2}{\pi^2}$, and the ratio of total energy to translational energy carries a factor $\left(\dfrac{\pi^2}{2} \right)$.

Thus, in a similar manner as before:

Lift $= \rho \left(\dfrac{\pi^2}{2} \right) \left(\dfrac{\pi b^2}{4} \right) V_0^2 \sin \mathcal{E}_\infty + M_j V_j \sin \mathcal{E}_\infty$

giving $C_{L_T} = \left[\left(\dfrac{\pi^2}{2} \right) \pi A + 2 C_j \right] \dfrac{\sin \mathcal{E}_\infty}{2}$

Also, $D_i V_0 = \dfrac{\rho}{2} \left(\dfrac{\pi^2}{2} \right)^2 \left(\dfrac{\pi b^2}{4} \right) V_0 \left(V_0 \sin \mathcal{E}_\infty \right)^2 + \Delta T V_0$

Thus, $C_{D_i} = \dfrac{\sin^2 \mathcal{E}_\infty}{4} \left[\pi A \left(\dfrac{\pi^2}{2} \right)^2 + 2 C_j \right]$

16

$$\text{giving } C_{D_i} = \frac{C_{L_t}^2}{\pi A} \cdot \left[1 + \left(\frac{2}{\pi}\right)^2 \cdot \frac{2C_j}{\pi A}\right] \Big/ \left[1 + \left(\frac{2}{\pi}\right) \cdot \frac{2C_j}{\pi A}\right]^2$$

$$\doteq \frac{C_{L_t}^2}{\pi A} \cdot \left[1 - 8\left(\frac{2}{\pi}\right)^3 \cdot \frac{C_j}{\pi A}\right]$$

The modifying factor in the square brackets is very close to unitv

for combinations of C_j and A of interest.

REFERENCES

(1) C. D. Cone   A Theoretical Investigation of Vortex Sheet
Deformation Behind a Highly Loaded Wing and Its
Effect on Lift
NASA TN D 657, April 1961.

(2) H. S. Ribner   On the Lift and Induced Drag Associated with Large
Downwash Angles
U. T. I. A. TN No. 19, January 1958.

(3) G. J. Hancock   Comments on "Limiting Circulatory Lift of a Wing of
Finite Aspect Ratio"
J. Aero/Space Sciences, January 1960.

(4) B. W. McCormick The Limiting Circulatory Lift of Wing of Finite
Aspect Ratio

J. Aero/Space Sciences, April 1959.

(5) H. B. Helmbold   Limitations of Circulation Lift
J. Aero/Space Sciences, March 1957.

(6) P. L. Sutcliffe,   Aerodynamic and Propulsion Considerations of
V. K. Merrick   Minimum Field Aircraft
A. R. Howell   RAS/IAS Eighth Anglo-American Conference,
September 1961.

(7) G. W. Johnston Note on Optimum Lift Coefficient for STOL Take-off
N. Saint   1965.

(8) D. A. Spence   The Lift on a Thin Aerofoil with a Jet-Augmented
Flap
Aeronautical Quarterly, August 1958.

17

(9) J. B. Nichols   The Limitations of a Wing for Low Speed Flight
Proceedings Thirteenth Annual National Forum,
American Helicopter Society, May 1957.

(10) D. Kuchemann   A Simple Method of Calculating the Span and Chord-
wise Loading on Straight and Swept Wings of any
Given A. R. at Subsonic Speeds
R&M 2935, August 1952.

(11) G. K. Korbacher   A Review of the Jet Flap
      K. Sridhar   UTIA Review No. 14, May 1960.

(12) L. B. Gratzer   The Development of a B. L. C. High Lift System for
      T. J. O'Donnell   High Speed Airplanes
AIAA Paper #64-589.

(13) E. C. Maskell   A Theory of the Jet Flap in Three Dimensions
      D. A. Spence   R. A. E. Rep. Aero 2612.

APPENDIX "A"

The work of Helmbold [5] is repeated here for ease of reference and because of its fundamental value.

"With a spanwise elliptic distribution of circulation, $\Gamma = \Gamma_o \sqrt{1 - (2y/b)^2}$ the trailing-vortex system far down stream of the wing will move like a rigid flat strip with the proper velocity $w_o = \Gamma_o/b$ normal to itself, provided that its cross section is hypothetically endowed with the ability to resist the deforming stress of the pressure field. The transversal momentum carried with the vortex sheet increases per unit length by $dJ_{z_o}/dx_o = \rho(\pi b^2/4)w_o$, and the kinetic energy of the absolute motion increases per unit length by

$$dE_o/dx_o = \rho(\pi b^2/4)(w_o^2/2).$$

If the cross-sectional rigidity is instantaneously destroyed and the

sheet is left free to yield to the deforming stresses of the pressure field, the sheet will start rolling itself in from its side edges and finally attain a stable configuration in the form of two symmetrical vortex cores of opposite and equal circulation Γ_o . The distance between their centers of gravity is $\mathcal{L} = \pi b/4$, and their proper velocity is

$$W' = \Gamma_o/2\pi \mathcal{L} = 2\Gamma_o/\pi^2 b = (2/\pi^2)W_o \qquad (1)$$

at least approximately. Hence $W_0 = (\pi^2/2) W'$. Since no outer forces are acting on the vortex system during the "deformation, the transversal momentum and the total energy per unit length remain unchanged by the deformation;

$$d J_z/dx = d J_{z_o}/dx_o \quad \text{and} \quad dE/dx = dE_o/dx_o$$

(With the deformed vortex system, the total energy consists of kinetic energy and work done by pressure forces; with the undeformed vortex sheet, the kinetic energy is the total energy because then there are no perturbation velocities along the vortex sheet.)

"The completely rolled-in vortex system is inclined by the angle δ toward the undisturbed relative velocity V. This angle is determined by sin δ = w'/V. The length of the final vortex system increases per unit time by dx/dt = V cos δ . The components of the aerodynamic force on the wing are the lift.

$$L = V \cdot (dJ_z/dx) - D_i \text{tg } \delta \qquad (2)$$

and the induced drag $- D_i = (dE/dx) \cos \delta$ (3)

19

Since $D_i V = dE/dt = (dE/dx) V \cos \delta$

"According to preceding statements,

$$L = \rho(\pi b^2/4) V w_o - \rho (\pi b^2/4)(w_o^2/2) \sin \delta$$
$$= \rho(\pi/8) b^2 V^2 \sin \delta \left[1-(\pi/4) \sin^2 \delta\right] \tag{4}$$

$$D_i = \rho (\pi b^2/4)(w_o^2/2) \cos \delta$$
$$= \rho (\pi^3/32) b^2 V^2 \sin^2 \delta \cos \delta \tag{5}$$

or, after division by $\rho V^2 b^2/2$

$$C_L/A = (\pi^3/4) \sin \delta \left[1-(\pi^3/4) \sin^2 \delta\right] \tag{6}$$

$$C_{D_i}/A = (\pi^3/16) \sin^2 \delta \cos \delta \tag{7}$$
"

Here $A = b^2/S$ denotes the aspect ratio. The reduced lift coefficient C_L/A

attains its maximum value, $C_{L\ lim}/A = \pi^2/(3\sqrt{3}) = 1.90$,

for $\sin \delta = 2/(\pi\sqrt{3}) = 0.368$ with a corresponding value of the reduced

drag coefficient

$$C_{D_i}/A = (\pi^2/12)\sqrt{\pi^2-4/3} \qquad = 2.40 \qquad "$$

It will now be shown how the various assumptions concerning the

transversal velocity of the jet sheet at infinity downstream can be used to

obtain the three equations described in the section on Large Angle Wing

Theory. Helmbold's notation is retained so that the downwash angle at

infinity downstream is written as δ , rather than $\mathcal{E}_\infty$ as in other parts of

the text.

Helmbold gives:

$$L = \rho(\pi b^2/4) V w_o - \rho(\pi b^2/4)(w_o^2/2) \sin \delta \tag{A-1}$$

20

$$D_i = \rho(\pi b^2/4)(W_o^2/2) \cos \delta \qquad (A-2)$$

Three cases are now considered:

(i) $\sin \delta \cdot W_o/V$ corresponding to $C_L = 0.855A$
                                                  (A-3)

(ii) $\sin \delta = W_o/2V$ corresponding to $C_L = 1.21 A$
                                                  (A-4)

(iii) $\sin \delta = (W_o/V)(2/\pi^2)$ corresponding to Helmbold
                                            and to equation $C_L = 1.90 A$
                                              (A-5)

Substituting these values for W_0 in equation (A - 1), we obtain:

(i) $\dfrac{C_L}{A} = \dfrac{\pi}{2}\left[\sin \delta - \dfrac{\sin^3 \delta}{2}\right]$ $\sin \delta = 0.815$ (A-6)

     yielding a limiting $C_L = 0.855 A$

(ii) $\dfrac{C_L}{A} = \pi\left[\sin \delta - \sin^3 \delta\right]$ $\sin \delta = 0.576$ (A-7)

     yielding a limiting $C_L = 1.205 A$

(iii) $\dfrac{C_L}{A} = \dfrac{\pi^3}{4}\left[\sin \delta - \left(\dfrac{\pi^2}{4}\right)\sin^3 \delta\right]$ $\sin \delta = 0.368$ (A-8)

     yielding a limiting $C_L = 1.90 A$

Corresponding equations for induced drag may also be obtained thus:

Helmbold gives $D_i = \rho\left(\dfrac{\pi b^2}{4}\right)\left(\dfrac{W_o^2}{2}\right) \cos \delta$ (A-9)

Using equations (A-3), (A-4), and (A-5), we have:

(i) $\dfrac{C_{D_i}}{A} = \left(\dfrac{\pi}{4}\right) \sin^2 \delta \cos \delta$

(ii) $\dfrac{C_{D_i}}{A} = 4\left(\dfrac{\pi}{4}\right) \sin^2 \delta \cos \delta$

(iii) $\dfrac{C_{D_i}}{A} = \dfrac{\pi^4}{4}\left(\dfrac{\pi}{4}\right) \sin^2 \delta \cos \delta$

Each equation for drag, with its corresponding equation for lift gives

a lift to drag relationship shown in Figure A-1.

The variation of $\mathcal{E}_w$ with $C_{L/A}$ can be found using $\tan \mathcal{E}_w = Di/L$ (from equations A-6 to A-12), and this is shown as a plot of $\sin \mathcal{E}_w$ vs C_L/A in Figure A-2 for each of the three cases. Prandtl's linear theory gives $\sin \mathcal{E}_w = \dfrac{C_L}{\pi A}$ which is also shown in Figure A-2 for comparison.

APPENDIX "B"

Appendix "B" demonstrates how equation A-7, Appendix "A" can be derived using well known results from Prandtl's lifting theory. This serves to give a more physical insight into the mechanism of lift vector rotation which causes the limitation of lift. It also provides a basis for equations (6) to (11) of the main text.
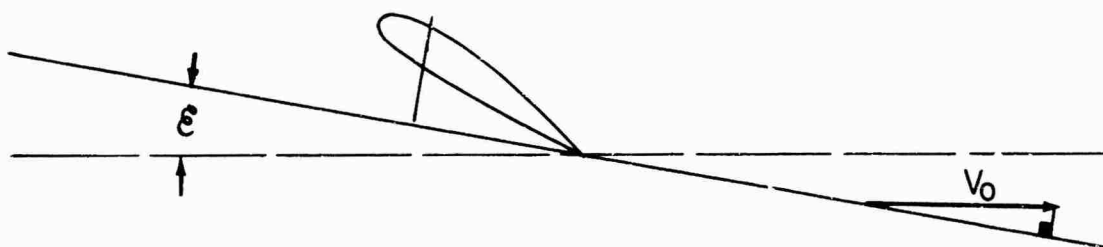
It is assumed here that the wing has elliptic spanwise loading and that the trailing vorticity lies in a plane inclined to the free stream and does not roll up - the inclination being equal to the induced downwash angle

calculated at the wing lifting line. In practice, the vortex sheet leaves the wing at this angle, and the basis of the present assumption is that the deviation from it is insignificantly close to the wing where the effect of the sheet on the wing is predominant. This is simply a convenience for the sake of mathematical simplicity but nevertheless it sounds reasonably plausible. (This assumption leads to limiting $C_L = 1.21 A$, as previously shown).

Let the local 'lift' L be inclined backward through the (downwash) angle $\mathcal{E}_w$

$$\text{Then lift } L = L' \cdot \cos \mathcal{E}_w \qquad C_L = \frac{L' \cos \mathcal{E}_w}{\frac{1}{2}\rho V_o^2 S} \tag{B-1}$$

$$\text{and drag } D = L' \cdot \sin \mathcal{E}_w \qquad C_D = \frac{L' \sin \mathcal{E}_w}{\frac{1}{2}\rho V_o^2 S} \tag{B-2}$$

$$\text{and, therefore } C_D = C_L \tan \mathcal{E}_w \tag{B-3}$$

The transversal velocity of the vortex sheet is usually given as $\dfrac{C_L V}{\pi A}$. Now, in large angle theory, these values of C_L and V must assume local values which account for inclination and for local changes in the velocity.

$$\text{Thus, } (C_L V) \text{ LOCAL } = \frac{L' V_o \cos \mathcal{E}_w}{\frac{1}{2}\rho V_o^2 \cos^2 \mathcal{E}_w S} = \frac{C_L V_o}{\cos^2 \mathcal{E}_w}$$

$$\text{therefore, } \sin \mathcal{E}_w = \frac{C_L}{\pi A} \cdot \frac{1}{\cos^2 \mathcal{E}_w} \tag{B-4}$$

$$\text{giving } C_L = \pi A \cdot \sin \mathcal{E}_w \cdot \cos^2 \mathcal{E}_w \tag{B-5}$$

$$\text{that is - } C_L = \pi A (\sin \mathcal{E}_w - \sin^3 \mathcal{E}_w) \tag{B-6}$$

This being identical to equation (A-7) which gives rise to a limiting value of $C_L = 1.205 A$.

23

APPENDIX "C"

This appendix investigates the implications of large angle theory with regard to experimental measurements of lift made on wings of finite aspect ratio when comparisons are required with two-dimensional theory. In such experiments, the measured lift for a given vorticity is less than it would be using linear theory because of the inclination of the force vector (the effect of which is usually small, and therefore ignored).

Helmbold gives:

$$L = \rho \left(\frac{\pi b^2}{4}\right) V w_0 - \rho \left(\frac{\pi b^2}{4}\right) \frac{w_0^2}{2} \cdot \sin \delta$$

where w_0 can be considered as a measure of vorticity

since $\Gamma_0 = w_0 b$

Let $L' = \rho \left(\frac{\pi b^2}{4}\right) V w_0$

where L' is the lift which would result using small angle theory.

Thus, $L = L' \left[1 - \frac{1}{\pi^2} \left(\frac{w_0}{V}\right)^2 \right]$

Now $\frac{w_0}{V} \doteq \frac{2 C_L'}{\pi A}$

$\therefore \frac{C_L}{A} = \frac{C_L'}{A} \left[1 - \frac{4}{\pi^4} \left(\frac{C_L'}{A}\right)^2 \right]$

Evaluating:

C_L'/A	.5	1.0	1.5
$(C_L'/A)^2$	.25	1.0	2.25
$\frac{4}{\pi^4}\left(\frac{C_L'}{A}\right)^2$	.01	.02	.09
C_L'/C_L	1.01	1.04	1.10

24

$$C_L/A \qquad .495 \qquad .96 \qquad 1.36$$

- thus, giving an approximate correction factor for the purpose described.

APPENDIX 'D"

Ratio of Translation to Rotational Energy in the Wake

It has been noted that one obvious objection to simple momentum wing theory is that all of the residual energy in the wake is assumed to be translational. Making this assumption, then the associated mass is given by:

$\rho\left(\frac{\pi b^2}{4}\right)V_0$, this value is consistent with equation (4) of the main text.

For δ small, Helmbold gives $C_L = \frac{\pi^2 A}{4}$ sin δ (equation A-8) as compared to $C_L = \frac{\pi A}{2}$ sin δ for Prandtl (equation A-6), where δ is the downwash angle at infinity down stream. This implies that, for a given wing lift, the associated mass given by Halmbold is greater by a factor of $\frac{\pi^2}{2}$, and, that the downwash is correspondingly smaller by a factor of $\frac{2}{\pi^2}$ approximately.

The total residual energy in the wake gives rise to induced drag and it is known that the Prandtl result is substantially correct in this regard.[*] It is, therefore, possible to deduce the ratio of translational to rotational enerty in the wake according to Halmbold's model.

$$E \text{ (translational)} + E \text{ (rotational)} = E \text{ (total)}$$

Let m represent the associated mass per unit time which is deflected according to Prandtl, and let W_0 represent its corresponding
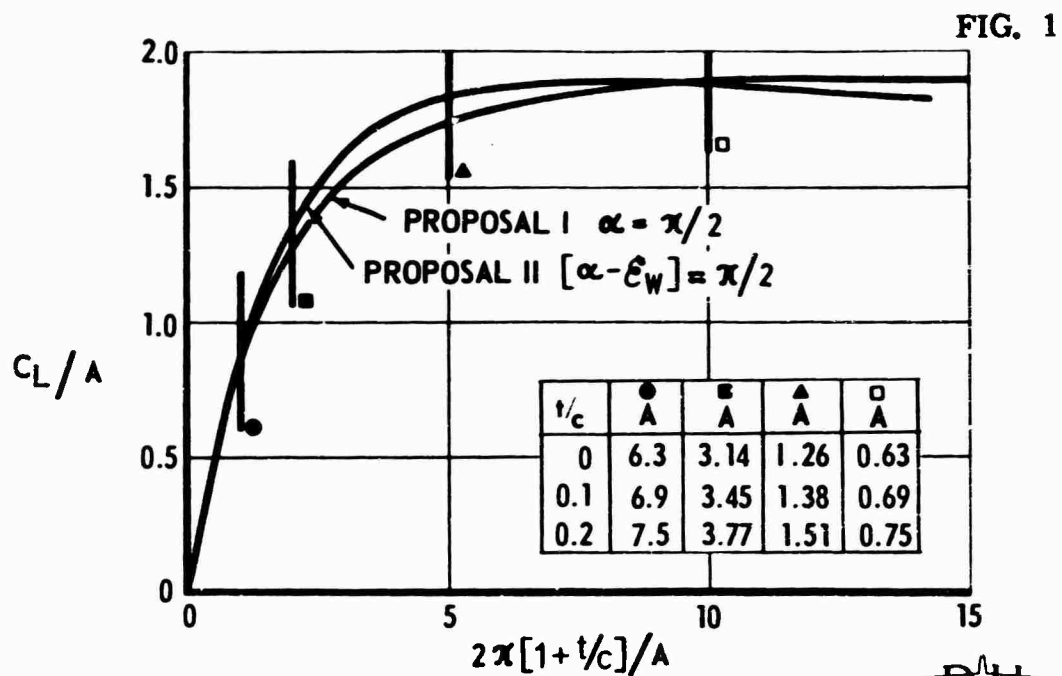
25

translational velocity:

$$\text{Then} \quad \tfrac{1}{2} m \left(\tfrac{\pi^2}{2}\right)\left[\omega_o \tfrac{2}{\pi^2}\right]^2 + E_R = \tfrac{1}{2} m \omega_o^2$$

$$\text{giving} \quad \tfrac{1}{2} m \omega_o^2 \left[\tfrac{2}{\pi^2} + k_R\right] = \tfrac{1}{2} m \omega_o^2$$
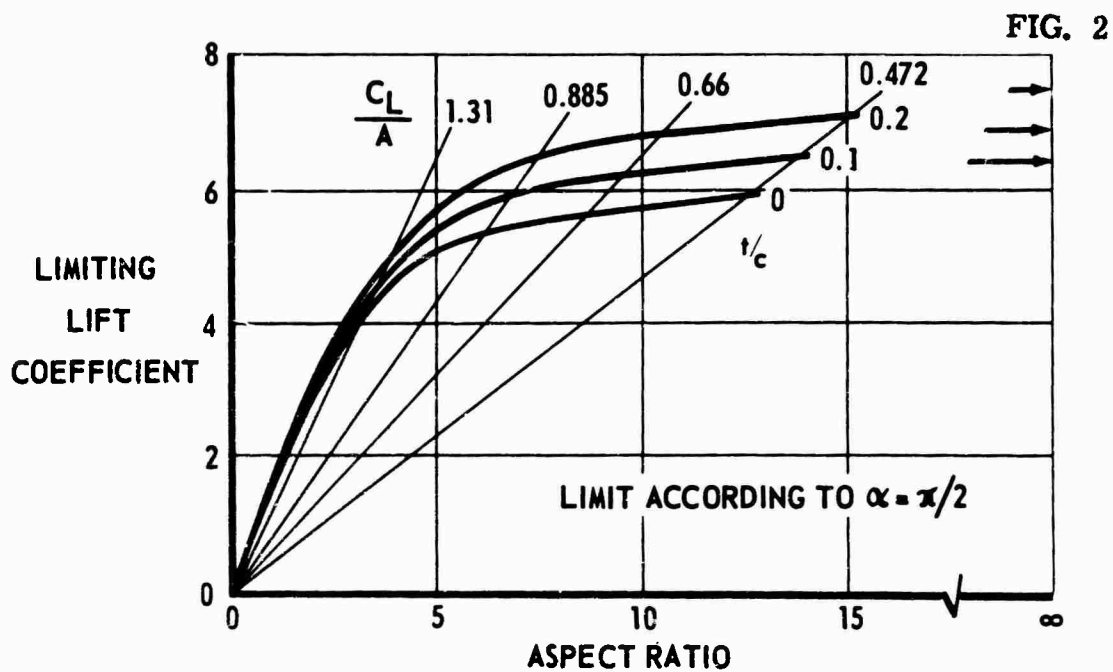
$$\text{when} \quad E_R = k_R \cdot \tfrac{1}{2} m \omega_o^2$$

Thus, k_R the fraction of rotational energy is given by $(1 - \tfrac{2}{\pi^2})$,
that is nearly 80% of the wake energy is rotational.

* The total energy in the wake, shed from an elliptically loaded wing, is known from wing theory, (for example, Sears, 1955, Page 227). This is derived from consideration of an undeformed vortex sheet at infinity down stream. The fact that the vortex sheet might roll up into a closed pair does not alter the wake energy. (This was pointed out by Halmbold). Thus, when considering momentum wing theory, the wake energy is known and does not depend upon assumed changes in the value of downwash (ϵ_∞) or corresponding changes in the associated mass.

26

FIG. 1

C_L/A

PROPOSAL I $\alpha = \pi/2$

PROPOSAL II $[\alpha - \hat{\epsilon}_w] = \pi/2$

t/c	● $\overline{A}$	■ $\overline{A}$	▲ $\overline{A}$	□ $\overline{A}$
0	6.3	3.14	1.26	0.63
0.1	6.9	3.45	1.38	0.69
0.2	7.5	3.77	1.51	0.75

$2\pi[1+t/c]/A$

PREDICTION OF LIFT LIMIT — HELMBOLD'S THEORY

17-1

FIG. 2

$\frac{C_L}{A}$ 1.31   0.885   0.66   0.472

0.2

0.1

0

t/c

LIMITING
LIFT
COEFFICIENT

LIMIT ACCORDING TO $\alpha = \pi/2$

ASPECT RATIO

PROPOSED LIMIT TO LIFT COEFFICIENT

17-2

27

FIG. A-1

INDUCED DRAG

FIG. A-2

DOWNWASH ANGLE AT THE WING